Analysis of the dynamic behavior of fluid-granular soil-structure systems in waterfront areas of high seismicity

Hayoung KIM

Analysis of the dynamic behavior of fluid-granular soil-structure systems in waterfront areas of high seismicity

March, 2005

Hayoung KIM

ABSTRACT

This thesis focuses on the dynamic behavior of fluid-granular soil-structure systems, such as composite breakwaters, in waterfront areas of high seismicity. The related important considerations include the following: (1) Extensive damage occurred to the composite breakwaters in the port of Kobe due to the 1995 Hyogoken-Nambu earthquake and called for a rational earthquake-resistant design procedure for such breakwater systems; (2) The seismic behavior of breakwater systems under moderate intensities of, yet markedly prolonged periods of shaking await a critical examination in view of the increased likelihood of occurrence of the Nankai or Tonankai earthquake or combined; (3) There is acute need for controlled disposal sites, and nearshore areas may offer optimal locations for them from environmental as well as engineering standpoints; (4) More developments will thus be needed in the studies of the performance of controlled disposal sites subjected to dynamic loading such as earthquake shaking and fluid-wave loading; and (5) Indeed, all of these issues combined strongly require the development of an integrated analysis framework that permits advanced yet physically sound representations of the fluid-soil-structure systems in nearshore areas.

With the above-mentioned in mind, the present thesis consists of three parts. Part 1 describes a workable analysis framework by which to facilitate predictions regarding the dynamic behavior of composite breakwaters, of controlled disposal sites nearshore and of such other marine structural systems. The features of the analysis procedure developed in terms of the method of finite elements include the following: (1) incorporation of a realistic cyclic-plasticity model for soil; (2) development of a realistic, elastoplastic constitutive model for interfaces between soil and solid structures; (3) fully coupled stress-flow approach; and (4) consideration of dynamic interactions with adjacent fluid columns. Also, Part I presents a range of discussions that demonstrate the validity of the proposed numerical-analysis procedure against some closed-form solutions in dynamics available.

Part II of the thesis applies the proposed analysis procedure to assessing the seismic performance of composite breakwater systems. This starts with a discussion of the plastic deformability of composite breakwater models on liquefiable sand foundation, in terms of centrifugal shaking-testing and associated predictions. Then, the seismic behavior of the Kobe port breakwater No. 7 is revisited, clarifying the mechanism of large settlements that occurred during the 1995 Hyogo-ken Nambu earthquake. This is followed by a discussion of the effect of prolonged shaking of a moderate intensity upon the deformability of composite breakwater systems. Factors contributing to marked settlement are pointed out.

In part III the thesis focuses the discussion on the performance of controlled disposal sites subjected to either earthquake shaking or fluid-wave loading. First, it clarifies the pattern and magnitude of extensional straining that was predicted to occur in the water-shielding sheet in a controlled disposal site during anticipated strong shaking. This is followed by examination of the effect of wave-induced pore pressure fluctuations in the backfill soil of a controlled disposal site. The predicted characteristics of propagation of wave pressures through the rubble mound and backfill soil compare favorably with what has been measured in the field by Kotake et al. (2004).

Also, care is called upon the possible effect of markedly long durations of fluid waves. This arises from the predictions that the wave-induced pore pressures may propagate deep into the backfill soil of the controlled disposal site, thereby affecting the performance of the water-shielding sheet there to some extent.

Acknowledgements

The author wishes to express profound gratitude to his academic supervisor, Professor Hideo Sekiguchi, at the Disaster Prevention Research Institute, Kyoto University, for his unfailing guidance, invaluable suggestions, criticisms and encouragement throughout the period of this research.

The author owes a lot to Professor Fusao Oka at the Department of Civil Engineering of Kyoto University and to Professor Susumu Iai at the Disaster Prevention Research Institute of Kyoto University for their invaluable comments and constructive suggestions in reviewing this thesis.

The author wishes to thank Associate Professor Ryutaro Yamashita at the Disaster Prevention Research Institute of Kyoto University for his constructive suggestions and generous encouragement.

The author would like to extend his thanks to Dr. Michio Miyake at the Head of Technical Research Institute, Naruo, Toyo Construction Co. Ltd., for generous encouragement.

The author wishes to express sincere thanks to Mrs. F. Lee, Mr. Amiruddin, Mr. Kriyo Sambodho, Mr. M. Minakuchi at Waterfront Geotechnics Laboratory chaired by Professor Hideo Sekiguchi.

The author would like to extend his thanks to pastor Sogoro Ogawa, sub-pastor Masanori Yamada and the other staffs of Senrinewtown Baptist Church for their pray and encouragement.

A very special gratitude is offered to his beloved wife Miyeon, daughter Miral and son Juyoung for their constant love, prayer, encouragement throughout the research period. Their constant affection and forbearance have been a source of strength.

The author humbly dedicates his piece of work to his beloved parents, without whose sacrifices and understanding he could never have reached where he is today.

Finally, the author wants to praise his God with all his heart, and to sing praise to His name with Psalm 23. " The Lord is my shepherd, I shall not be in want. He makes me lie down in green pastures, he leads me beside quiet waters, he restores my soul. He guides me in paths of righteousness for his name's sake"

Table of contents

List of tables

List of photos

List of figures

Fig. 6.5 Predicted time histories of horizontal and vertical displacements of the caisson top (Case KB2-1 with M_f=0.48 (Dr=40%))

Fig. 6.6 Predicted plastic deformation of the composite breakwater No. 7 after shaking (t=20s) (Case KB2-1 with M_f=0.48 (Dr=40%))

Fig. 6.7 Predicted deformation of interface between caisson and rubble mound after shaking (t=20s) (Case KB2-1 with M_f=0.48 (Dr=40%))

Fig. 6.8 Predicted settlement plotted against parameter M_f /M_g (or relative density Dr) of sand backfill after shaking

Fig. 6.9 Predicted distributions with depth of (a) vertical strains, (b) lateral strains and (c) volumetric strains in the foundation soil along the centerline of the caisson after shaking (t=20s) (Case KB2-1 with M_f=0.48 (Dr=40%))

Fig. 6.10 (a) Shear stress-deviator strain relation; (b)(c) stress paths; (d) time history of excess pore pressure in element EK1 below the caisson in Case KB2-1 with M_f=0.48 (Dr=40%)

Fig. 6.11 (a) Shear stress-deviator strain relation; (b)(c) stress paths; (d) time history of excess pore pressure in element EK2 below the caisson in Case KB2-1 with M_f=0.48 (Dr=40%)

Fig. 6.12 (a) Shear stress-deviator strain relation; (b)(c) stress paths; (d) time history of excess pore pressure in element EK3 below the caisson in Case KB2-1 with M_f=0.48 (Dr=40%)

Fig. 6.13 (a) Stress path; (b)time history of excess pore pressure in element EK4 in Case KB2-1 with M_f=0.48 (Dr=40%)

Fig. 6.14 Predicted distribution of excess pore pressure ratios at the end of the shaking (t=20s) in Case KB2-1 with M_f=0.48 (Dr=40%)

Fig. 6.15 Predicted time histories of (a) dynamic fluid force; (b) horizontal force; (c) vertical force in Case KB2-1 with M_f=0.48 (Dr=40%)

Fig. 6.16 Predicted relative horizontal displacements for joint element in Case KB2-1 with M_f=0.48 (Dr=40%)

Fig. 6.17 Predicted relative vertical displacements for joint element in Case KB2-1 with M_f=0.48 (Dr=40%)

Fig. 6.18 Stress path for joint element A1 (refer to Fig. 6.2) in Case KB2-1 with M_f=0.48 (Dr=40%)

Fig. 6.19 Time histories of dynamic safety factors against sliding of caisson

Fig. 6.20 Predicted dynamic safety factors plotted against parameter ratio M_f /M_g

INTRODUCTION

The seismic behavior of fluid-soil-structure systems such as composite breakwaters has received considerable attention, especially after the 1995 Hyogoken-Nambu earthquake. This is understandable in view of the extensive damage that occurred to the composite breakwaters in Kobe port, in a manner illustrated in Fig. 0.1(Port Bureau Ministry of Transport et al., 1997). Breakwater No. 7, for instance, settled as much as 2.6m leading to reduced serviceability, as implied in Photo. 0.1 (Sekiguchi et al. 1996). Several research has already been performed in various aspects of this deformation problem(Sekiguchi et al., 1996; Oka et al., 1996; Iai et al., 1998; Kawasaki, 1998; Tanaka et al., 2001).

In fact, the stability of composite breakwaters under earthquake shaking presents a comprehensive range of problems that involve dynamic fluid-soil-structure interactions, depending on the relative importance of a number of factors as illustrated in Fig. 0.2. Namely,

- Dynamic fluid pressures on either sides of the caisson
- Slippage at the caisson-rubble mound interface
- Liquefaction of soil near the toe of the rubble mound
- Cyclic shearing of the foundation soil below the caisson
- Transport of fiver particles through the interface between the rubble mound and the foundation soil

The present study is aimed at developing an integrated analysis procedure by which to consider such factors in a consistent fashion.

Recently, serious concern has been expressed about possible consequences due to strong earthquakes with prolonged shaking that may be induced by Tokai, Tonankai and Nankai earthquakes. An estimated source area of the combined Tokai, Tonankai and Nankai earthquake is shown in Fig. 0.3 (Central Disaster Prevention Council, 2003). When Tonankai earthquake or Nankai earthquake or combined occurs, strong ground motions will affect large areas of Japan and high tsunamis will attack a long section of Japan's coasts facing the Pacific ocean (Central Disaster Prevention Council, 2003). However, little is known about the performance of coastal structures when subjected to prolonged shaking due to such earthquakes. Indeed, the list of important factors mentioned above should be updated to include the following factor: Effect of prolonged shaking of moderate to strong intensities.

Furthermore, the present study discusses an emerging issue regarding performance of disposal facilities in waterfront areas (Waterfront Vitalization and Environment Research Center, 2000). Factors affecting stability of controlled disposal sites in waterfront areas are illustrated in Fig. 0.4 (Kotake et al., 2004). One of the most important considerations in the integrity of the facilities is the function of water-shielding sheet subjected to severe earthquake shaking of propagation of fluid-wave pressures. A few workers performed

researches regarding wave-resistance of water-shielding sheets for disposal sites (Baba et al. 2002, Kotake et al. 2004). However, more development is needed to lead to a thorough understanding of the performance of water-shielding sheets under dynamic loading.

With the above-mentioned in mind, the present thesis aims at proposing an integrated analysis procedure by which to encompass the dynamic behavior of composite breakwaters as well as of controlled disposal sites in waterfront areas. The emphasis of discussion is placed on assessing plastic deformability of fluid-soil-structure systems such as composite breakwaters and controlled disposal sites having water-shielding sheets.

The organization of this thesis is as follows (Fig. 0.5). In chapter 1, a plane-strain finite element code coupling for soil domain and fluid domain is developed. Chapter 2 presents a plane-strain version of Pastor model and the model parameters are calibrated by refering results of monotonic torsional shear tests with variable relative density. Chapter 3 proposes a cyclic elasto-plastic constitutive model for interface between soil and structure. In chapter 4, Influence of dynamic fluid pressures due to a layer of fluid presenting over a deposit of liquefiable soil are discussed.

Chapter 5 focus on predicting the plastic deformation of composite breakwaters that rest on sand foundations. The predicted performance are discussed and compared with the observed results in centrifugal shaking-table test. The performances of Kobe port of breakwater No. 7 subjected to the 1995 Hyogoken-Nambu earthquake and strong earthquakes with long duration shaking are discussed in chapter 6 and chapter 7, respectively.

Chapter 8 describes predicted seismic behavior of controlled disposal site with reference to the special performance of water-shielding sheet. Chareteristics of ocean-wave propagation for controlled disposal site are described in chapter 9.

Reference

Baba, S., Miyake, M., Tsurugasaki, K., Kim, H. (2002). Development of wave generation system in a drum centrifuge, *ICPMG2002, Canada, 265-270.*

Iai, S., Ichii, K., Liu, H. and Morita, T. (1998). Effective stress analyses of port structures, *Special Issue,* No.2, *Soils and Foundations*, 97-114.

Kawasaki, K., Sakai, T., Yasuda, S. and Satoh, M. (1998). Earthquake-induced settlement of an isolated footing for power transmission structures, *Centrifuge 98*, 271-276.

Kotake, Y., Turugasaki, K., Baba, S., Miyake, M., Fujiwara, R., Kaneko, K., Tezuka, T., Tokunaga, K. and Moriya, K. (2004). Field observation of pore water pressure in the backfill space of a caisson-type bulkhead for wast dispose, *Annual Journal of Coastal Engineering*, JSCE, Vol. 51, 681-685.

Ministry of Transport , The Fishing Port Bureau Ministry of Fisheries, Civil Engineering Works in Hyogo Pref., Kobe-City Harbors Maintenance Bureau, Kobe Port Wharf Public Corporations. (1997). Damage report about harbors facilities due to 1995 Hyougoken-Nambu earthquake, (In Japanese).

Oka, F., Yashima, A., Taguchi, Y., Tateishi, A., Furukawa, K. and Fukushima, K. (1996). 3-Dimensional liquefaction analysis in Port Island using borehole strong motion vertical array record, *Proc. of the conference on Hanshin-Awaji great earthquake damage, JSCE*, 137-144.

Sekiguchi, H., Kita, K., Hashimoto, K. and Katsui H. (1996). Deformation of composite breakwaters due to ground shaking, *Special issue of Soils and Foundations*, 169-177.

Special board of investigation for Tonankai and Nankai earthquakes. (2003). Report for Tonankai and Nankai earthquakes, *Central Disaster Prevention Council*, No. 2-2.

Tanaka, Y., Yagiura, Y., Shimokawa, K., Higashi, S., Kishida, T. & Mizuwake, N. (2001). Study of liquefaction damages of quay-walls and breakwaters during Kobe earthquake, *Proc. 4th Int. Conf. on Recent Advances in Geotechnical Earthquake Engineering and Soil Dynamics and Symposium in Honor of Professor W.D. Lian Finn*, Paper No. 4.44.

Waterfront Vitalization and Environment Research Center (2000). *Manual for Design, construction and management of controlled disposal site*,.1-86(in Japanese).

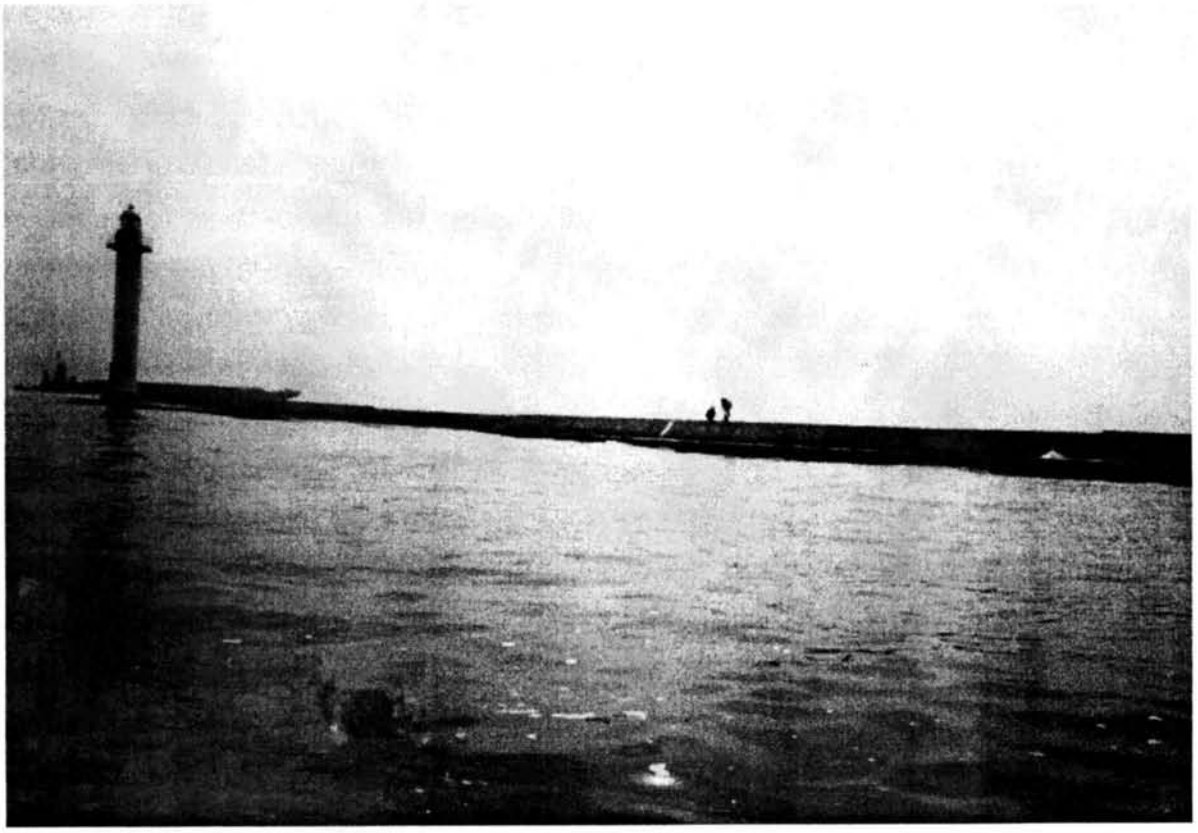

Photo. 0.1 Snapshot illustrating seismically induced large settlement of a section of composite breakwater No. 7 in Kobe Port (Sekiguchi et al., 1996)

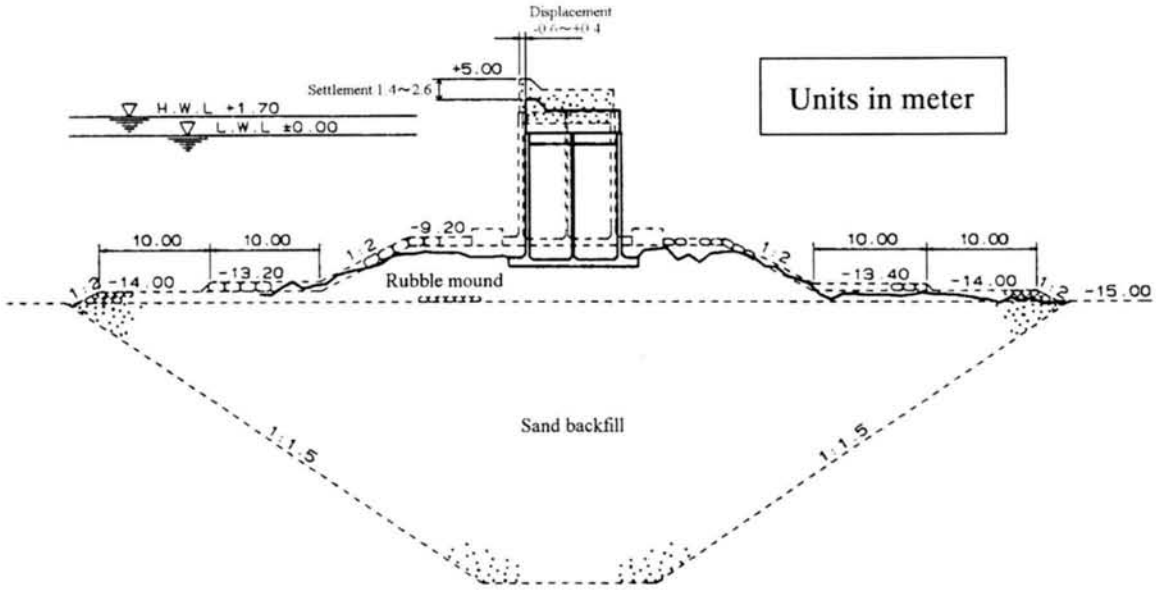

Fig. 0.1 Diagram indicating the pattern and magnitude of seismically induced deformation of composite breakwater No. 7 in Kobe Port (Port Bureau Ministry of Transport et al., 1997)

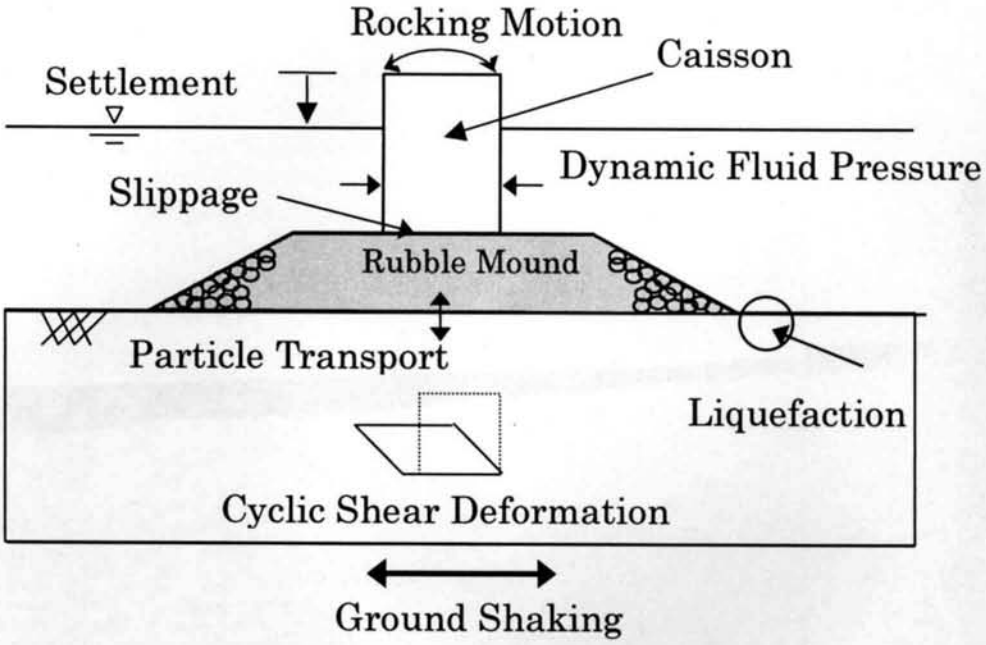

Fig. 0.2 Factors affecting the stability of composite breakwaters

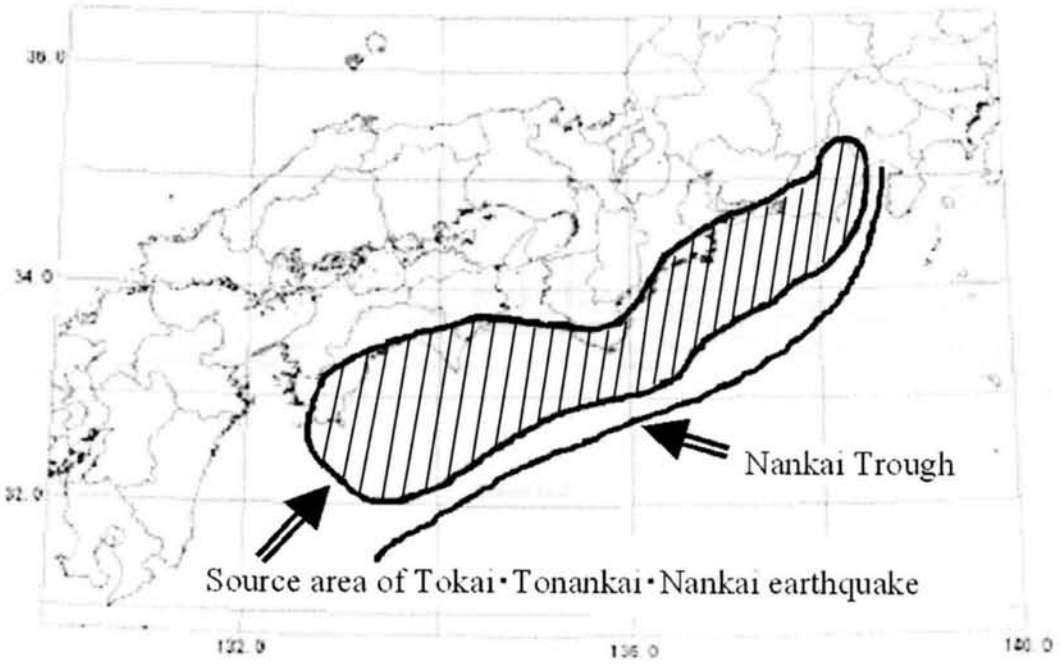

Fig. 0.3 Source area of combined Tokai,Tonankai and Nankai earthquake

(Central Disaster Prevention Council, 2003)

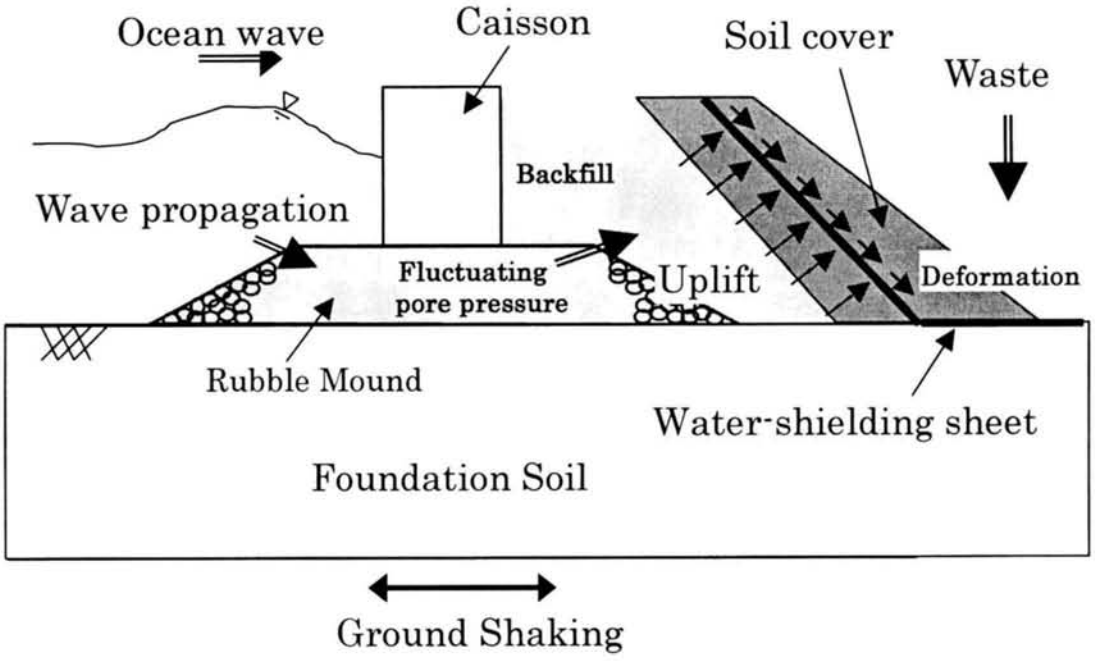

Fig. 0.4 Factors affecting the stability of controlled disposal site in waterfront area (Kotake et al., 2004)

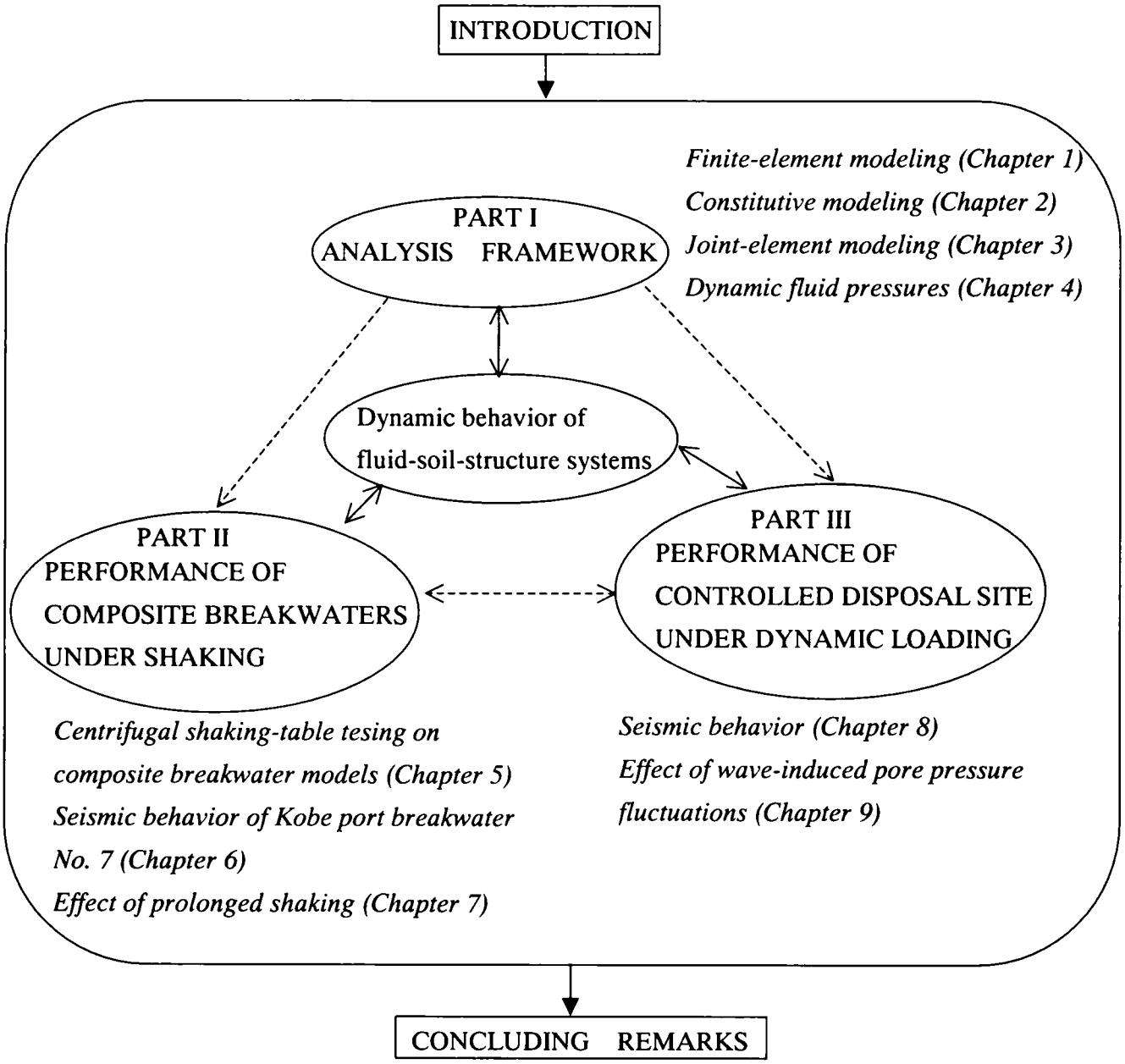

Fig. 0.5 Organization of this thesis

PART I

ANALYSIS FRAMEWORK

CHAPTER 1

Numerical formulation for the dynamics of two-phase medium under shaking

1.1 Introductory remarks

Plastic deformability of soil-structure systems has become an increasingly important issue in the safety and amenity of waterfront areas of high seismicity. However, it should be admitted that the mechanism of plastic deformation of particulate sediments under earthquake shaking is complex in nature. A comprehensive range of laboratory experiments on elemental soil behavior including liquefaction have been performed by many investigator over years, providing a wealth of knowledge for advanced constitutive modeling. In order to apply any of realistic constitutive model to a real-life dynamic problem, one may resort to numerical analysis along with sensible engineering judgement. To numerically describe liquefaction of particulate sediments, there are various types of mathematical formulations. With this statement in mind, the author will subsequently propose a workable analysis procedure for dynamic behavior of fluid-soil-structure systems in waterfront areas.

Specifically, the present study uses a coupled scheme based on Biot's two-phase mixture theory (Biot, 1960) for formulating governing equations.

Several types of formulations have been proposed according to the nature and number of unknown variables. It may be instructive herein to briefly review some of well-known approaches.

(1) Full formulation (either u-w-p or u-U-p formulation)(Zienkiewicz and Shiomi, 1984): When the displacement of the solid phase u, the pore pressure p and the relative velocity w are selected as unknown variables, this formulation is called a u-w-p formulation. Also, it is possible to express a governing equation in terms of the displacement of the fluid phase U instead of the relative velocity w. This formulation is called a u-U-p formulation.

(2) u-w or u-U formulation(Ghaboussi and Wilson, 1972; Ghaboussi and Dikmen, 1978; Zienkiewicz and Shiomi, 1984): If the fluid phase is modeled as being a compressible material, then the pore pressure p can be eliminated from the basic formulation and the number of unknowns can be reduced. This formulation is called a u-w (or u-U) formulation.

(3) Approximation formulation (u-p formulation) (Zienkiewicz et al. 1980; Zienkiewicz and Shiomi, 1984): If the relative acceleration $\ddot{w}$ is much smaller than the acceleration of the

solid phase $\ddot{u}$, the relative displacement w may be effectively deleted from governing equations. In this case, the displacement of the solid phase u and the pore pressure p are used as unknown variables. The u-p formulation can reduce the total degrees of freedom in governing equations.

Since there is an advantage that can reduce the total degrees of freedom in governing equations, many numerical analysis codes use a u-p formulation. They include LIQCA(Shibata et al., 1991; Oka et al., 1994), SWANDYNE(Zienkiewicz et al., 1999), STADAS(Yoshida, 1993b).

There is another class of numerical analysis codes that perform dynamic analysis under undrained conditions. For instance, FLIP(Iai et al., 1998). Although the numerical analysis code has been widely used for liquefaction analysis, one may note that possible dissipation of excess pore pressures during prolonged shaking cannot be taken into consideration. A summary of the effective stress analyses is shown in Table 1.1.

In the present study, a u-p formulation has been used to reproduce the liquefaction and plastic deformation processes of granular soils (Kim and Sekiguchi, 2000). A Fluid-soil-structure coupled scheme is implemented in this study for spatial discretization of the governing equations. The finite-difference technique (Akai and Tamura,1977; Shibata et al., 1991) is used for spatial discretization of the continuity or storage equation. Newmark's β method is used for time discretization of entire governing equations. The calibration of the proposed numerical analysis was performed in light of closed-form analytical solutions for two classes of linear seismic problems by Simon et al. (1984) and Idriss and Seed (1968).

In the sections that follow, the features of the analysis code developed will be described.

1.2 Finite-element modeling for soil domain

This section describes a set of governing equations and the corresponding finite-element discretization procedure. Compressive stresses and compressive strains are taken as positive.

1.2.1 Governing equations

A set of governing equations relevant to two–phase media are summarized below (Zienkiewicz, O.C. et al., 1980; Simon, B. R. et al., 1984).

Equations of motion

Let σ_{ij} be the total stress and let σ'_{ij} be the effective stress. There follows

$$\sigma_{ij} = \sigma'_{ij} + p\delta_{ij} \tag{1.1}$$

where p is the pore fluid pressure and δ_{ij} represents Kronecker's delta.

The equations of motion can be expressed as

$$\rho\ddot{u}_i + \rho_f \ddot{w}_i = -\sigma_{ji,j} + \rho b_i \tag{1.2}$$

where b_i is the body force and $\rho = (1-n)\rho_s + n\rho_f$. Here ρ_s is the mass density of solid particles, ρ_f is the mass density of the pore fluid, $\ddot{w}_i$ represents the averaged acceleration of the pore fluid relative to the solid skeleton and is defined as $n(\ddot{v}_i - \ddot{u}_i)$. Here n is the porosity, $\ddot{v}_i$ is the acceleration of the pore fluid and $\ddot{u}_i$ stands for the acceleration of the solid.

Substituting Eq. (1.1) into Eq. (1.2) for σ_{ij} yields

$$\rho\ddot{u}_i + \rho_f \ddot{w}_i = -\sigma'_{ji,j} - p_{,i} + \rho b_i \tag{1.3}$$

If the relative acceleration of the pore fluid, $\ddot{w}_i$, is negligible compared with $\ddot{u}_i$, then Eq. (1.3) can be simplified to

$$\rho\ddot{u}_i = -\sigma'_{ji,j} - p_{,i} + \rho b_i \tag{1.4}$$

Continuity equation with consideration of generalized Darcy equation

The storage equation relevant to saturated soil with a compressible pore fluid may be expressed as

$$\dot{w}_{i,i} = -\dot{u}_{i,i} - \frac{n}{K_f}\dot{p} \tag{1.5}$$

where K_f is the bulk modulus of the pore fluid.

Generalized Darcy equation for pore fluid flow reads

$$\rho_f \ddot{v}_i = -p_{,i} - \frac{\rho_f g}{k}\dot{w}_i + \rho_f b_i \tag{1.6}$$

where g and k respectively are the acceleration of gravity and the coefficient of permeability.

Substituting $\ddot{v}_i = \ddot{w}_i/n + \ddot{u}_i$ in Eq. (1.6) yields

$$\rho_f \ddot{u}_i + \frac{\rho_f}{n}\ddot{w}_i = -p_{,i} - \frac{\rho_f g}{k}\dot{w}_i + \rho_f b_i \tag{1.7}$$

If $\ddot{w}_i$ is neglected, Eq. (1.7) reduces to

$$\rho_f \ddot{u}_i = -p_{,i} - \frac{\rho_f g}{k}\dot{w}_i + \rho_f b_i \tag{1.8}$$

Taking divergence on both sides of Eq. (1.8) yields

$$\rho_f \ddot{u}_{i,i} = -p_{,ii} - \frac{\rho_f g}{k} \dot{w}_{i,i} \tag{1.9}$$

Substituting Eq. (1.5) into Eq.(1.9) for $\dot{w}_{i,i}$, one may express the continuity equation in the following form:

$$\rho_f \ddot{u}_{i,i} = -p_{,ii} + \frac{\rho_f g}{k}(\dot{u}_{i,i} + \frac{n}{K_f}\dot{p}) \tag{1.10}$$

1.2.2 Finite–element discretization

Strain rates $\dot{\varepsilon}_{ij}$ are defined in terms of displacement velocities of soil skeleton as follows.

$$\dot{\varepsilon}_{ij} = -\frac{1}{2}(\dot{u}_{i,j} + \dot{u}_{j,i}) \tag{1.11}$$

Let $\{\Delta u\}$ be the displacement increments at a generic point in a given finite element and let $\{\Delta u_N\}$ be the nodal displacement increments of that element. It then follows that

$$\{\Delta u\} = [N]\{\Delta u_N\} \tag{1.12}$$

where $[N]$ represents shape functions.

In terms of Eq. (1.12), the strain increments $\{\Delta\varepsilon\}$ and the volumetric strain increment $\Delta\varepsilon_v$ at a generic point in a finite element may be expressed as

$$\{\Delta\varepsilon\} = [B]\{\Delta u_N\} \tag{1.13}$$

$$\Delta\varepsilon_V = \{B_V\}^T\{\Delta u_N\} \tag{1.14}$$

where $[B]$ and $\{B_V\}$ respectively are the strain–displacement matrix and the volumetric strain–displacement vector. A superscript T denotes transpose of a vector or a matrix.

Elastoplastic constitutive relations of the soil skeleton may be expressed as

$$\dot{\sigma}'_{ij} = D_{ijkl}\dot{\varepsilon}_{kl} \tag{1.15}$$

where D_{ijkl} represents the coefficients of tangent stiffness matrix that generally depend on the current effective stress state, as well as on the plastic strain and stress histories.

Use of the principle of virtual work permits Eq. (1.3) to be expressed in incremental form:

$$[M_{UU}]\{\Delta\ddot{u}_N\} + [K_{UU}]\{\Delta u_N\} + [K_{UP}]\Delta p = \{\Delta Q\} \tag{1.16}$$

where

$$[M_{UU}] = \int_V [N]^T \rho [N] dV \tag{1.17}$$

$$[K_{UU}] = \int_V [B]^T [D][B] dV \tag{1.18}$$

$$[K_{UP}] = \int_V [B]_V dV \tag{1.19}$$

$$\{\Delta Q\} = \int_A [N]^T \{\Delta T\} dA + \int_V [N]^T \rho \{\Delta b\} dV \tag{1.20}$$

Here ΔT is the surface traction increment, Δb stands for the body force increment.

The procedure of deriving Eq. (1.16) is expounded in Appendix 1 of this chapter.

Equation (1.10) may be discretized using finite difference scheme (Akai and Tamura,1976) as follows.

$$[M_{PU}]\{\Delta \ddot{u}_N\} + [C_{PU}]\{\Delta \dot{u}_N\} + [C_{PP}]\Delta \dot{p} + \sum(\alpha_i \Delta p_i) + [K_{PP}]\Delta p = 0 \tag{1.21}$$

in which

$$[M_{PU}] = \frac{k}{g}(\int_V [B_V] dV) \tag{1.22}$$

$$[C_{PU}] = -(\int_V [B_V] dV) \tag{1.23}$$

$$[C_{PP}] = -(\int_V \frac{n}{K_f} dV) \tag{1.24}$$

$$[K_{PP}] = -\sum \alpha_i \tag{1.25}$$

where

$$\alpha_i = \frac{k}{\rho_f g} \alpha_i'. \tag{1.26}$$

The definition of parameter α_i' is detailed in Appendix 2 of this chapter. The procedure of deriving Eq. (1.21) is described also in Appendix 2.

If the pore fluid goes infinite ($K_f \to \infty$) is assumed incompressible, then Eq. (1.21) reduces to

$$[M_{PU}]\{\Delta \ddot{u}_N\} + [C_{PU}]\{\Delta \dot{u}_N\} + \sum(\alpha_i \Delta p_i) + [K_{PP}]\Delta p = 0 \tag{1.27}$$

In order to solve a system of Eqs. (1.16) and (1.27), it was found convenient to apply Newmark's β method to the displacement increments and also to the excess pore pressure increments. Namely,

$$\begin{Bmatrix} \Delta \dot{u} \\ \Delta \dot{p} \end{Bmatrix} = \frac{\gamma}{\beta \Delta t} \begin{Bmatrix} \Delta u \\ \Delta p \end{Bmatrix} - \frac{\gamma}{\beta} \begin{Bmatrix} \dot{u}_t \\ \dot{p}_t \end{Bmatrix} + (1 - \frac{\gamma}{2\beta}) \Delta t \begin{Bmatrix} \ddot{u}_t \\ \ddot{p}_t \end{Bmatrix} \tag{1.28}$$

$$\begin{Bmatrix} \Delta \ddot{u} \\ \Delta \ddot{p} \end{Bmatrix} = \frac{1}{\beta \Delta t^2} \begin{Bmatrix} \Delta u \\ \Delta p \end{Bmatrix} - \frac{1}{\beta \Delta t} \begin{Bmatrix} \dot{u}_t \\ \dot{p}_t \end{Bmatrix} - \frac{1}{2\beta} \begin{Bmatrix} \ddot{u}_t \\ \ddot{p}_t \end{Bmatrix} \tag{1.29}$$

where γ and β are Newmark's parameters.

Substituting Eqs. (1.28) and (1.29) into Eqs. (1.16) and (1.27) yields the following:

$$\left[\frac{1}{\beta\Delta t^2}[M_{UU}]+[K_{UU}]\right]\{\Delta u_N\}+[K_{UP}]\Delta p=\{\Delta Q\}+\frac{1}{\beta\Delta t}[M_{UU}]\{\ddot{u}_t\}+\frac{1}{2\beta}[M_{UU}]\{\dot{u}_t\} \tag{1.30}$$

and

$$\left[\frac{1}{\beta\Delta t^2}[M_{PU}]+\frac{\gamma}{\beta\Delta t}[C_{PU}]\right]\{\Delta u_N\}+[K_{PP}]\Delta p+\sum(\alpha_i\Delta p_i)$$

$$=\left(\frac{1}{2\beta}[M_{PU}]+(\frac{\gamma}{2\beta}-1)\Delta t[C_{PU}]\right)\{\ddot{u}_t\}+\left(\frac{1}{\beta\Delta t}[M_{PU}+\frac{\gamma}{\beta}[C_{PU}]\right)\{\dot{u}_t\} \tag{1.31}$$

Equations (1.30) and (1.31) hold for each of the finite elements. Thus they may be assembled to give the governing equations for an entire system. Namely,

$$\left[\frac{1}{\beta\Delta t^2}[M]+\frac{\gamma}{\beta\Delta t}[C]+[K^*]\right]\begin{Bmatrix}\Delta u\\ \Delta p\end{Bmatrix}$$

$$=\begin{Bmatrix}\Delta Q\\ 0\end{Bmatrix}+\left[\frac{1}{\beta\Delta t}[M]+\frac{\gamma}{\beta}[C]\right]\begin{Bmatrix}\dot{u}_t\\ \dot{p}_t\end{Bmatrix}+\left[\frac{1}{2\beta}[M]+(\frac{\gamma}{2\beta}-1)\Delta t[C]\right]\begin{Bmatrix}\ddot{u}_t\\ \ddot{p}_t\end{Bmatrix} \tag{1.32}$$

where

$$[M]=\begin{bmatrix}[M_{UU}] & 0\\ [M_{PU}] & 0\end{bmatrix} \tag{1.33}$$

$$[C]=\begin{bmatrix}0 & 0\\ [C_{PU}] & 0\end{bmatrix} \tag{1.34}$$

$$[K^*]=\begin{bmatrix}[K_{UU}] & [K_{UP}]\\ 0 & [K^*_{PP}]\end{bmatrix} \tag{1.35}$$

Note in Eq. (1.35) that $[K^*_{PP}]$ represents the permeability matrix.

1.2.3 Viscous boundary

Provisions of viscous boundaries (Lysmer and Kuhlemeyer, 1969) is a useful technique for considering radiation damping in a semi-infinite body. The function of a viscous boundary is schematically shown in Fig. 1.1.

$$\begin{Bmatrix}\sigma_n\\ \tau_s\end{Bmatrix}=\begin{bmatrix}\rho V_p & 0\\ 0 & \rho V_s\end{bmatrix}\begin{Bmatrix}\dot{v}_n-\dot{v}_{nf}\\ \dot{u}_s-\dot{u}_{sf}\end{Bmatrix} \tag{1.36}$$

where σ_n and τ_n be the normal and shear stresses that act on the viscous boundary. There stresses may be related to the relative velocities; $\dot{v}_n-\dot{v}_{nf}$ and $\dot{u}_n-\dot{u}_{nf}$, in the direction either

normal or tangential to the viscous boundary. $\dot{v}_n$ and $\dot{u}_s$ be the normal and tangential velocities of the boundary of the analysis region. Note that V_p and V_s represent the velocities of P-waves and S-waves, respectively.

Consideration of a viscous boundary formally requires the [C] matrix in Eq. (1.32), such that

$$[C^*] = \begin{bmatrix} [C_V] & 0 \\ [C_{PU}] & 0 \end{bmatrix} \tag{1.37}$$

$$[C^{**}] = \begin{bmatrix} [C_V] & 0 \\ 0 & 0 \end{bmatrix} \tag{1.38}$$

in which

$$[C_v] = \frac{\rho h}{6} \begin{bmatrix} 2V_p & & V_p & \\ & 2V_s & & V_s \\ V_p & & 2V_p & \\ & V_s & & 2V_s \end{bmatrix} \qquad \text{at viscous boundary} \tag{1.39}$$

where Δu_f represents the velocities in the free field. Thus Eq. (1.32) may be rewritten as

$$\left[\frac{1}{\beta\Delta t^2}[M] + \frac{\gamma}{\beta\Delta t}[C^*] + [K^*]\right]\begin{Bmatrix}\Delta u \\ \Delta p\end{Bmatrix}$$

$$= \begin{Bmatrix}\Delta Q \\ 0\end{Bmatrix} + \left[\frac{1}{\beta\Delta t}[M] + \frac{\gamma}{\beta}[C^*]\right]\begin{Bmatrix}\dot{u}_t \\ \dot{p}_t\end{Bmatrix} + \left[\frac{1}{2\beta}[M] + (\frac{\gamma}{2\beta} - 1)\Delta t[C^*]\right]\begin{Bmatrix}\ddot{u}_t \\ \ddot{p}_t\end{Bmatrix} + [C^{**}]\begin{Bmatrix}\Delta u_f \\ 0\end{Bmatrix} \tag{1.40}$$

1.3 Finite-element modeling for a fluid domain

1.3.1 Governing equations

Let us denote the fluid pressure by p_f (Zienkiewicz and Taylor, 2002). The equation of the motion of a compressible, inviscid fluid may be expressed as

$$\nabla^2 p_f = \frac{1}{c^2}\frac{\partial^2 p_f}{\partial t^2} \tag{1.41}$$

where c is the speed of sound in the fluid. If we neglect the compressibility of the fluid, there follows a Laplace equation. That is to say,

$$\nabla^2 p_f = 0 \tag{1.42}$$

1.3.2 Finite–element discretization

Use of a Galerkin discretization technique permits Eq. (1.42) to be expressed in the finite-element equation (Toki et al. 1982; Zienkiewicz and Taylor, 2002) of the form

$$[H]\{p_f\}+\{B\}=0 \tag{1.43}$$

The entries of the [H] matrix and of the {B} vector read

$$H_{ij}=\sum\int_v\left\{\frac{\partial N_i}{\partial x}\cdot\frac{\partial N_j}{\partial x}+\frac{\partial N_i}{\partial y}\cdot\frac{\partial N_j}{\partial y}\right\}dV \tag{1.44}$$

$$B_i=\sum\int_s N_i\frac{\partial p_f}{\partial n}ds \tag{1.45}$$

where N_i represents the shape function.

1.3.3 Boundary conditions in the fluid domain

Interface with a solid body(soil or structure)

The pressure gradient $\partial p_f / \partial n$ on the interface with a solid body should satisfy the following dynamical condition (Zienkiewicz and Taylor, 2002):

$$\partial p_f / \partial n = -\rho_1 \alpha_n \tag{1.46}$$

where ρ_1 stands for the mass density of the fluid and α_n represents the absolute acceleration in a direction normal to the interface concerned. In nonlinear dynamic analysis, the value of α_n may be updated using the predicted acceleration response of the solid body.

Free surface

On the free surface the simplest assumption is that

$$p_f = 0 \tag{1.47}$$

However, this does not allow for any possibility of surface gravity waves. These can be approximated by assuming the actual surface to be at an elevation η relative to the mean surface (Zienkiewicz and Taylor, 2002). Now

$$p_f = \rho_1 g \eta \tag{1.48}$$

From the dynamic equation of fluid behavior $\rho_1\frac{\partial \mathbf{v}}{\partial t}=\nabla p_f$,we have, on noting $v_z = \partial\eta/\partial t$ where v is the fluid velocity,

$$\rho_1\frac{\partial^2\eta}{\partial t^2}=-\frac{\partial p_f}{\partial z} \tag{1.49}$$

Eliminating of η, using Eq. (1.48), we have a specified normal gradient condition

$$\frac{\partial p_f}{\partial z} = -\frac{1}{g}\frac{\partial^2 p_f}{\partial t^2} = -\frac{1}{g}\ddot{p}_f \tag{1.50}$$

This allows for the generation of surface gravity waves on the free surface.

Radiation boundary

Setup a boundary physically terminates an infinite fluid domain, and some approximation to account for the effect of such a termination is necessary. The main dynamic effect is simply that the wave solution to the governing equation (1.41) must here be composed of outgoing waves only as no input from the infinite domain exists.

Suppose that the two waves F and G travel in positive and negative directions of x, respectively. The general solution of Eq. (1.41) can be written as (Zienkiewicz and Taylor, 2002)

$$p_f = F(x-ct) + G(x+ct) \tag{1.51}$$

The absence of the incoming wave G means that on a radiation boundary, we have only

$$p_f = F(x-ct) \tag{1.52}$$

Thus

$$\frac{\partial p_f}{\partial n} = \frac{\partial p_f}{\partial x} = F' \tag{1.53}$$

and

$$\frac{\partial p_f}{\partial t} = -cF' \tag{1.54}$$

where F' denotes the derivative of F with respect to (x-ct). We can therefore eliminate the unknown function F' and write

$$\frac{\partial p_f}{\partial n} = -\frac{1}{c}\dot{p} \tag{1.55}$$

1.4 Finite-element modeling for the interface between soil and a solid structure

A local coordinate system used for representing a joint element with thickness H=0 is shown in Fig. 1.2. The stored energy, ϕ, in a joint element may be expressed as (Goodman et al.; 1968, Yoshida, 1993a)

$$\phi = \frac{1}{2}\int_{-L/2}^{L/2} \{W\}^T \{P\} dx \tag{1.56}$$

in which $\{W\}$ is the relative displacement vector given by

$$\{W\} = \begin{Bmatrix} w^{top} - w^{bottom} \\ v^{top} - v^{bottom} \end{Bmatrix} \tag{1.57}$$

and $\{P\}$ is the vector of force per unit length given by;

$$\{P\} = \begin{Bmatrix} P_s \\ P_n \end{Bmatrix} \tag{1.58}$$

The vector $\{P\}$ may be expressed in terms of a product of the joint stiffness and the relative displacement, such that

$$\{P\} = [D_J]\{W\} \tag{1.59}$$

A concrete expression of the joint stiffness matrix $[D_J]$ will be described in Chapter 3 of this thesis.

Substituting Eq. (1.59) into Eq. (1.56) yields

$$\phi = \frac{1}{2}\int_{-L/2}^{L/2} \{W\}^T [D_J]\{W\} dx \tag{1.60}$$

The relative displacements $\{W\}$ may now be expressed in terms of the nodal displacements $\{u\}$ through a linear interpolation formula. Namely,

$$\{W\} = [N_j]\{u\} \tag{1.61}$$

in which

$$[N_j] = \begin{bmatrix} \frac{1}{2}-\frac{x}{L} & 0 & \frac{1}{2}+\frac{x}{L} & 0 & -\frac{1}{2}-\frac{x}{L} & 0 & -\frac{1}{2}+\frac{x}{L} & 0 \\ 0 & \frac{1}{2}-\frac{x}{L} & 0 & \frac{1}{2}+\frac{x}{L} & 0 & -\frac{1}{2}-\frac{x}{L} & 0 & -\frac{1}{2}+\frac{x}{L} \end{bmatrix} \tag{1.62}$$

and

$$\{u\}^T = \{u_I \quad v_I \quad u_J \quad v_J \quad u_K \quad v_K \quad u_L \quad v_L\} \tag{1.63}$$

Substitution of Eq. (1.61) into Eq. (1.60) yields

$$\phi = \frac{1}{2}\int_{-L/2}^{L/2} \{u\}^T \{N_J\}^T [D_J] \{N_J\} \{u\} dx \tag{1.64}$$

Let $\{R\}$ be the nodal force vector. Then the potential energy of the joint element may be expressed as

$$\chi = \phi - \{u\}^T \{R\} \tag{1.65}$$

Use of the principle of minimum potential energy permits Eq. (1.65) to be expressed as

$$\frac{\partial \phi}{\partial \{u\}} = [K_J]\{u\} = \{R\} \tag{1.66}$$

where

$$[K_J] = \int_{-L/2}^{L/2} \{N_J\}^T [D_J] \{N_J\} dx \tag{1.67}$$

The $[K_J]$ matrix is called the joint element stiffness per unit length.

1.5 Integrated analysis procedure

Suppose that solid and fluid domains constitute an entire system for which an integrated analysis will be performed.

Equations (1.40) and (1.43) for each of the finite elements may be integrated to give the governing equations for the entire system:

$$\left[\frac{1}{\beta \Delta t^2}[M^{'}] + \frac{\gamma}{\beta \Delta t}[C^{'}] + [K^{'}]\right] \begin{Bmatrix} \Delta u \\ \Delta p \\ p_{f\,t+1} \end{Bmatrix}$$

$$= \begin{Bmatrix} \Delta Q \\ 0 \\ [Q_f] \end{Bmatrix} + [A] \begin{Bmatrix} \ddot{u}_t \\ 0 \\ p_{ft} \end{Bmatrix} + \left[\frac{1}{\beta \Delta t}[M^{'}] + \frac{\gamma}{\beta}[C^{'}]\right] \begin{Bmatrix} \dot{u}_t \\ \dot{p}_t \\ \dot{p}_{ft} \end{Bmatrix} + \left[\frac{1}{2\beta}[M^{'}] + (\frac{\gamma}{2\beta} - 1)\Delta t[C^{'}] - [q^{'}]\right] \begin{Bmatrix} \ddot{u}_t \\ \ddot{p}_t \\ \ddot{p}_{ft} \end{Bmatrix}$$

$$+ [C^{'}] \begin{Bmatrix} \Delta u_f \\ 0 \\ 0 \end{Bmatrix} \tag{1.68}$$

where

$$[M'] = \begin{bmatrix} [M_{UU}] & 0 & 0 \\ [M_{PU}] & 0 & 0 \\ [B_{fU}] & 0 & [q_{ff}] \end{bmatrix} \tag{1.69}$$

$$[C'] = \begin{bmatrix} [C_V] & 0 & 0 \\ [C_{PU}] & 0 & 0 \\ 0 & 0 & 0 \end{bmatrix} \tag{1.70}$$

$$[C^*] = \begin{bmatrix} [C_V] & 0 & 0 \\ 0 & 0 & 0 \\ 0 & 0 & 0 \end{bmatrix} \tag{1.71}$$

$$[K'] = \begin{bmatrix} [K_{UU}] & [K_K] & [B_{Uf}] \\ 0 & [K^*_{PP}] & 0 \\ 0 & 0 & [H] \end{bmatrix}, \quad \begin{array}{l} K_K = K_{UP} \text{ for a soil element} \\ K_K = K_J \text{ for a joint element} \end{array} \tag{1.72}$$

$$[A] = \begin{bmatrix} 0 & 0 & 0 \\ 0 & 0 & 0 \\ [B_{fU}] & 0 & \dfrac{1}{\beta \Delta t^2} q_{ff} \end{bmatrix} \tag{1.73}$$

$$[Q_f] = [B_{fU}] \ddot{a}_g \tag{1.74}$$

$$[q'] = \begin{bmatrix} 0 & 0 & 0 \\ 0 & 0 & 0 \\ 0 & 0 & [q_{ff}] \end{bmatrix} \tag{1.75}$$

Note in Eqs. (1.73) through (1.75)

$$[B_{fU}] = \rho_1 \int_{s1} N_i N_j ds_1 \qquad \text{on an interface } s_1 \text{ between the fluid and solid} \tag{1.76}$$

$$[q_{ff}] = \frac{1}{g} \int_{s_2} N_i N_j ds_2 \qquad \text{on a fluid surface } s_2 \tag{1.77}$$

1.6 Test of the proposed analysis procedure

The finite-element program developed in this study was tested in light of some closed-form analytical solutions available.

1.6.1 Comparison with an analytical solution by Simon et al.

Simon et al. (1984) solved the response of one-dimensional saturated poroelastic columns subjecting to compression wave loading. The finite element model adopted by author is shown in Fig. 1.3. The total depth H is 100m and the width W is 1m. The domain is divided into a total of 100 quadrilateral elements. The loading conditions imposed are shown in Fig. 1.4. The material parameters used is shown in Table 1.2.

The Analytical solutions and the results of the present finite-element analyses for step loading as well as sinusoidal loading are shown in Fig. 1.5 and Fig. 1.6, respectively. The vertical axis in each figure is a non-dimensional displacement and the horizontal axis is a non-dimensional time. It is evident that the present numerical analyses can reproduce the analytical solutions.

1.6.2 Comparison with an analytical solution by Idriss and Seed

A closed-form solution is derived by Idriss and Seed (1968) regarding the response of an elastic soil layer subjected to a horizontal seismic motion. The domain was considered as a semi-infinite layer under drained conditions. In such cases the ground motions induced by a seismic excitation at the base are only the result of shear deformations in the soil, and the deposit may be considered as a one-dimensional shear beam.

The finite element models adopted in this study are shown in Fig. 1.7. Case T1 employed the rigid, smooth side boundaries together with fixed bottom boundary. In Case T2, viscous boundaries were introduced for representing radial energy dissipation. Material parameters used are shown in Table 1.3.

Each finite element model was subjected to 20 cycles of horizontal, sinusoidal excitation at a frequency of 10Hz, with a peak acceleration of 0.2 gravities.

Calculated response accelerations at node N1 on the ground surface are shown in Fig. 1.8. In Case T2 with the viscous boundaries, the response acceleration at node N1 is in good agreement with the analytical solution. For purposes of comparison, the calculated results from Case T1 are also plotted in Fig. 1.8. As expected, the performance of Case T1 without viscous boundaries is unsatisfactory.

1.7 Conclusions

A fully coupled, dynamic finite-element program for plane-strain deformation was developed. The validity of the analysis code was verified through comparisons of the predictions with the closed-form analytical solutions in the two classes of elastodynamic problems, specifically the solutions by Simon et al. (1984) and by Idriss and Seed (1968).

References

Akai, K. and Tamura, T. (1977). An application of nonlinear stress-strain relations to multi-dimensional consolidation problems. *Annuals, DPRI, Kyoto University*, No. 21 B-2, 19-35 (in Japanese).

Biot, M. A. (1960). Mechanics of deformation and acoustic propagation in porous media, *J. Appl. Phys*. Vol. 33, 1483-1498.

Ghaboussi, J. and Dikmen, S.U. (1978). Liquefaction analysis of horizontally layered sands. ASCE, Vol. 104, No. GT3, 341-356

Ghaboussi, J. and Wilson, E.L. (1972). Variational formulation of dynamics of fluid-saturated porous elastic solids. ASCE, Vol. 98, No. EM4, 947-963.

Goodman, R., Taylor, R. and Brekke, T. (1968). A model for the mechanics of jointed rock, *ASCE*, Vol. 94, No. SM3, 637-659.

Iai, S. Ichii, K., Liu, H. and Morita T. (1998). Effective stress analyses of port structures, *Special Issue of Soils and Foundations*, 97-114.

Idriss, I. M., Seed, H. (1968). Seismic response of horizontal soil layers, *ASCE*, Vol. 94, No. SM4, 1003-1031.

Kim, H. and Sekiguchi, H. (2000). Analysis of partially drained behaviour of saturated soil deposits subjected to earthquake shaking, *Annuals, Disaster Prevention Research Institute, Kyoto Univ.*, No. 43 B-2, 449-462.

Oka, F., Yashima, A., Shibata, T., Kato, M. and Uzuoka, R. (1994). FEM-FDM coupled liquefaction analysis of a porous soil using an elasto-plastic model, *Applied Scientific Research*, Vol.52, pp.209-245.

Sekiguchi, H., Kita, K., Hashimoto, K. and Katsui, H. (1996). Deformation of composite breakwaters due to ground shaking, *Soils and Foundations*, Special Issue,169-177.

Shibata, T., Sato, T., Uzuoka, R., Oka, F., Yashima, A. and Kato, M. (1991). FEM-FDM coupled liquefaction analysis of a fluid-saturated ground, *Computer methods and advances in Geomechanics*, 869-874.

Simon, B. R., Zienkiewicz, O. C. and Paul, D. K. (1984). An analytical solution for the transient response of saturated porous elastic solids, *International Journal for Numerical and Analytical Methods in Geomechanics*, Vol. 8, 381-398.

Yoshia, N. (1993a). Sujestion of joint element appling liquefaction analysis, *Proceedings of the 22th JSCE Earthquake Engineering Symposium*, Vol. 22, 31-34.

Yoshia, N. (1993b). STADAS, a computer program for static and dynamic analysis of ground and soil-structure interaction problems, *Report, Soil Dynamics Group, The University of British Columbia, Vancouver, Canada*.

Zienkiewicz, O. C., Chang, C. T. and Bettess, P. (1980). Drained, undrained, consolidating and dynamic behaviour assumptions in soils, *Géotec-nique*, Vol. 30, No. 4, 385-395.

Zienkiewicz, O. C. and Shiomi, T. (1984). Dynamic behaviour of saturated porous media; The generalized biot formulation and its numerical solution, *International Journal for Numerical and Analytical Methods in Geomechanics*, Vol. 8, 71-96.

Zienkiewicz, O. C., Chan, A.H.C., Pastor M., Schrefler, B.A. and Shiomi, T. (1999). Computational Geomechanics with Special Reference to earthquake engineering, John Wiley and Sons, 53-84.

Appendix 1: Discretization of the equations of motion

The equations of motion, Eq. (1.3) can be derived using the principle of virtual work.

The left-hand side on Eq. (1.3) stems from:

$$\int_V \delta u_i \rho \ddot{u}_i dV = \{\delta u_N\}^T \int_V [N]^T \rho [N] dV \{\ddot{u}_N\} \tag{1.78}$$

The first term on the right-hand side of Eq. (1.3) :

$$\begin{aligned} \int_V \delta u_i \sigma'_{ji,j} dV &= \int_V \{(\delta u_i \sigma'_{ji})_{,j} - \delta u_{i,j} \sigma'_{ji}\} dV \\ &= \int_A \delta u_i \sigma'_{ji} n_j dA + \{\delta u_N\}^T \int_V [B]^T \{\sigma'\} dV \\ &= -\{\delta u_N\}^T \int_A [N]^T \{T'\} dA + \{\delta u_N\}^T \int_V [B]^T \{\sigma'\} dV \end{aligned} \tag{1.79}$$

where surface force T is expressed as $T = T' + T_p$. Here T' and T_p are the surface traction vectors for solid and pore fluid respectively.

The second term on the right-hand side of Eq. (1.3) :

$$\begin{aligned} \int_V \delta u_i p_{,i} dV &= \int_V \{(\delta u_i p)_{,i} - \delta u_{i,i} p\} dV \\ &= \int_A \delta u_i p n_i dA + \{\delta u_N\}^T (\int_V [\nabla N]^T dV) p \\ &= -\{\delta u_N\}^T \int_A [N]^T \{T_p\} dA + \{\delta u_N\}^T (\int_V [B_V]^T dV) p \end{aligned} \tag{1.80}$$

The third term on the right-hand side of Eq. (1.3) :

$$\int_V \delta u_i \rho b_i dV = \{\delta u_N\}^T \int_V [N]^T \rho \{b\} dV \tag{1.81}$$

Substituting Eqs. (1.78)-(1.81) into Eq. (1.3) yields

$$\int_V [N]^T \rho[N] dV \{\ddot{u}_N\} + (\int_V [B]^T \{\sigma'\} dV + \int_V [B_V]^T dV) p$$

$$= \int_A [N]^T \{T\} dA + \int_V [N]^T \rho \{b\} dV \tag{1.82}$$

Since Eq. (1.82) holds for any time $t + dt$, one can rewrite Eq. (1.82) in the form:

$$(\int_V [N]^T \rho[N] dV)\{\ddot{u}_N\}|_{t+dt} + (\int_V [B]^T \{\sigma'\}|_{t+dt}\, dV) + (\int_V [B_V]^T dV) p|_{t+dt}$$

$$= \int_A [N]^T \{T\} dA + \int_V [N]^T \rho \{b\} dV \tag{1.83}$$

Similarly, Eq. (1.82) for time t takes the form:

$$(\int_V [N]^T \rho[N] dV)\{\ddot{u}_N\}|_t + (\int_V [B]^T \{\sigma'\}|_t\, dV) + (\int_V [B_V]^T dV) p|_t$$

$$= \int_A [N]^T \{T\} dA + \int_V [N]^T \rho \{b\} dV \tag{1.84}$$

Subtracting Eq. (1.84) from Eq. (1.83) yields

$$(\int_V [N]^T \rho[N] dV)\{\Delta\ddot{u}\} + (\int_V [B]^T \{\Delta\sigma'\} dV) + (\int_V [B_V]^T dV)\Delta p$$

$$= \int_A [N]^T \{\Delta T\} dA + \int_V [N]^T \rho \{\Delta b\} dV \tag{1.85}$$

The finite element equations that deal with a two-phase medium may be expressed in matrix form, with constitutive relations (1.15) incorporated. Namely,

$$[M_{UU}]\{\Delta\ddot{u}_N\} + [K_{UU}]\{\Delta u_N\} + [K_{UP}]\Delta p = \{\Delta Q\} \tag{1.86}$$

where

$$[M_{UU}] = \int_V [N]^T \rho[N] dV \tag{1.87}$$

$$[K_{UU}] = \int_V [B]^T [D][B] dV \tag{1.88}$$

$$[K_{UP}] = \int_V [B_V] dV \tag{1.89}$$

$$\{\Delta Q\} = \int_A [N]^T \{\Delta T\} dA + \int_V [N]^T \rho \{\Delta b\} dV \tag{1.90}$$

Appendix 2: Discretization of the storage equation

Discretization of the continuity equation of pore fluid may be accomplished in a manner that is described below.

The left–hand side on Eq. (1.10) :

$$\int_V \rho_f \ddot{u}_{i,i} dV = (\int_V \rho_f [\nabla N] dV)\{\ddot{u}_N\}$$

$$= (\int_V \rho_f [B_V] dV)\{\ddot{u}_N\} \tag{1.91}$$

The first term on the right–hand side of Eq. (1.10) :

$$\int_V p_{,ii} dV = \int_S p_{,i} n_i dS \tag{1.92}$$

The right–hand side on Eq. (1.92) (refer to Fig. 1.9) :

$$\int_S p_{,i} n_i dS = \int_{1\to 2} p_{,i} n_i dS + \int_{2\to 3} p_{,i} n_i dS + \int_{3\to 4} p_{,i} n_i dS + \int_{4\to 1} p_{,i} n_i dS \tag{1.93}$$

where

$$\begin{aligned}\int_{1\to 2} p_{,i} n_i ds &= \frac{p_{m1} - p_m}{x_G^{m1} - x_G} \int_{1\to 2} n_x ds + \frac{p_{m1} - p_m}{y_G^{m1} - y_G} \int_{1\to 2} n_y ds \\ &= \frac{p_{m1} - p_m}{x_G^{m1} - x_G}(y_2 - y_1) + \frac{p_{m1} - p_m}{y_G^{m1} - y_G}(x_2 - x_1) \\ &= -(\frac{y_2 - y_1}{x_G^{m1} - x_G} - \frac{x_2 - x_1}{y_G^{m1} - y_G})p_m + (\frac{y_2 - y_1}{x_G^{m1} - x_G} - \frac{x_2 - x_1}{y_G^{m1} - y_G})p_{m1}\end{aligned} \tag{1.94}$$

Similarly,

$$\int_{2\to 3} p_{,i} n_i ds = -(\frac{y_3 - y_2}{x_G^{m2} - x_G} - \frac{x_3 - x_2}{y_G^{m2} - y_G})p_m + (\frac{y_3 - y_2}{x_G^{m2} - x_G} - \frac{x_3 - x_2}{y_G^{m2} - y_G})p_{m2} \tag{1.95}$$

$$\int_{3\to 4} p_{,i} n_i ds = -(\frac{y_4 - y_3}{x_G^{m3} - x_G} - \frac{x_4 - x_3}{y_G^{m3} - y_G})p_m + (\frac{y_4 - y_3}{x_G^{m3} - x_G} - \frac{x_4 - x_3}{y_G^{m3} - y_G})p_{m3} \tag{1.96}$$

$$\int_{4\to 1} p_{,i} n_i ds = -(\frac{y_1 - y_4}{x_G^{m4} - x_G} - \frac{x_1 - x_4}{y_G^{m4} - y_G})p_m + (\frac{y_1 - y_4}{x_G^{m4} - x_G} - \frac{x_1 - x_4}{y_G^{m4} - y_G})p_{m4} \tag{1.97}$$

where x1,x2,x3,x4 are horizontal coordinates of node 1, node2, node3, and node4, respectively. y1,y2,y3,y4 are vertical coordinates of node 1, node2, node3, and node4, respectively. x_G, y_G denote vertical and horizontal coordinates of the center in the center element and x_G^{m1}, y_G^{m1}, x_G^{m2}, y_G^{m2}, x_G^{m3}, y_G^{m3}, x_G^{m4}, y_G^{m4} denote vertical and horizontal coordinates of the center in the adjacent element m1~m4. p_m is pore fluid pressure at the center in the center element and p_{m1}, p_{m2}, p_{m3}, p_{m4}, are pore fluid pressure at the center in the adjacent element m1 ~m4, respectively.

Substituting Eqs. (1.94)-(1.97) into Eq. (1.93), one can obtain the following:

$$\int_s p_{,i} n_i ds = -(\alpha_1' + \alpha_2' + \alpha_3' + \alpha_4')p_m + \sum_{i=1}^{4} (\alpha_i' p_i) \tag{1.98}$$

where

$$\alpha_1' = \frac{y_2 - y_1}{x_G^{m1} - x_G} - \frac{x_2 - x_1}{y_G^{m1} - y_G} \tag{1.99}$$

$$\alpha_2' = \frac{y_3 - y_2}{x_G^{m2} - x_G} - \frac{x_3 - x_2}{y_G^{m2} - y_G} \tag{1.100}$$

$$\alpha_3' = \frac{y_4 - y_3}{x_G^{m3} - x_G} - \frac{x_4 - x_3}{y_G^{m3} - y_G} \tag{1.101}$$

$$\alpha_4' = \frac{y_1 - y_4}{x_G^{m4} - x_G} - \frac{x_1 - x_4}{y_G^{m4} - y_G} \tag{1.102}$$

The second term on the right-hand side of Eq. (1.10) :

$$\int_V \frac{\rho_f g}{k} \dot{u}_{i,i} dV = (\int_V \frac{\rho_f g}{k} \{\nabla N\} dV)\{\dot{u}_N\}$$

$$= (\int_V \frac{\rho_f g}{k} [B_V] dV)\{\dot{u}_N\} \tag{1.103}$$

The third term on the right-hand side of Eq. (1.10) :

$$\int_V \frac{\rho_f g}{k} \frac{n}{K_f} \dot{p} dV = (\int_V \frac{\rho_f g}{k} \frac{n}{K_f} dV)\dot{p} \tag{1.104}$$

Substituting Eqs. (1.91)–(1.104) into Eq. (1.10), one can obtain the following:

$$(\int_V \rho_f [B_V] dV)\{\ddot{u}_N\} - (\int_V \frac{\rho_f g}{k} [B_V] dV)\{\dot{u}_N\} - (\int_V \frac{\rho_f g}{k} \frac{n}{K_f} dV)\dot{p} + \sum(\alpha'_i p_i) - \sum \alpha'_i p$$

$$= 0 \tag{1.105}$$

For time $t + dt$, Eq. (1.105) takes the form:

$$\frac{\rho_f g}{k}\{\frac{k}{g}(\int_V [B_V] dV)\{\ddot{u}_N\}|_{t+dt} - (\int_V [B_V] dV)\{\dot{u}_N\}|_{t+dt} - (\int_V \frac{n}{K_f} dV)\dot{p}|_{t+dt}$$

$$+ \sum(\alpha_i p_i)|_{t+dt} - \sum \alpha_i p|_{t+dt}\} = 0 \tag{1.106}$$

Similarly for any time t, Eq. (1.105) becomes

$$\frac{\rho_f g}{k}\{\frac{k}{g}(\int_V [B_V] dV)\{\ddot{u}_N\}|_t - (\int_V [B_V] dV)\{\dot{u}_N\}|_t - (\int_V \frac{n}{K_f} dV)\dot{p}|_t$$

$$+ \sum(\alpha_i p_i)|_t - \sum \alpha_i p|_t\} = 0 \tag{1.107}$$

Subtracting Eq. (1.107) from Eq. (1.106) yields

$$\frac{\rho_f g}{k}\{\frac{k}{g}(\int_V [B_V] dV)\{\Delta\ddot{u}_N\} - (\int_V [B_V] dV)\{\Delta\dot{u}_N\} - (\int_V \frac{n}{K_f} dV)\Delta\dot{p}$$

$$+ \sum(\alpha_i \Delta p_i) - \sum \alpha_i \Delta p\} = 0 \tag{1.108}$$

Multiplying Eq. (1.108) by $k/(\rho_f g)$ permits the finite element equation for pore fluid to

be expressed as

$$\frac{k}{g}(\int_V [B_V]dV)\{\Delta\ddot{u}_N\} - (\int_V [B_V]dV)\{\Delta\dot{u}_N\} - (\int_V \frac{n}{K_f}dV)\Delta\dot{p}$$

$$+ \sum(\alpha_i \Delta p_i) - \sum \alpha_i \Delta p = 0 \qquad (1.109)$$

where $\alpha_i = \frac{k}{\rho_f g}\alpha'_i$.

Table 1.1 Summary of analysis code

Code name	Basic model	Constitutive model	Joint element	Fluid element
ADIFSS (Present study)	u-p	Plane-strain version of Pastor model	○	○
SWANDYNE	u-p	Pastor model	○	-
FLIP	Undrained	Iai Model	○	○
LIQCA	u-p	Oka Model	○	-
STADAS	u-p	Yoshida Model	○	-

Table 1.2 Material parameters for analytical solution by Simon et al.

Density	ρ	0.306kg/m^3
Density of fluid	ρ_f	0.2977kg/m^3
Porosity	n	0.333
Permeability	K	0.01425m/s
Lame's constant	λ	8.333N/m^2
Lame's constant	μ	1250N/m^2
Bulk modulus (Fluid)	Kf	39990N/m^2
Bulk modulus (Soil)	Ks	∞
Unit weight (Fluid)	γ_w	2.917N/m^3

Table 1.3 Material parameters for analytical solution of Idriss and seed

Density	ρ	1.85Mg/m^3
Shear modulus	G	7000kN/m2
Porosity	n	0.333

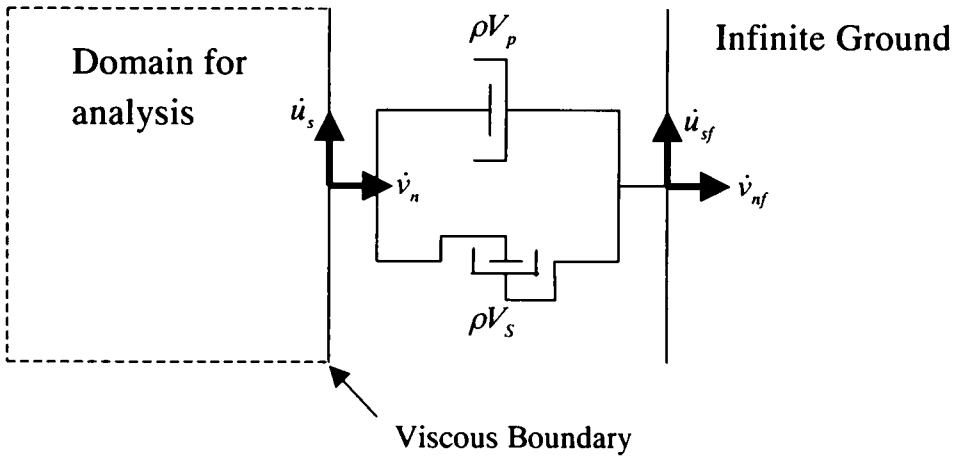

Fig. 1.1 A sketch illustrating the idea of a viscous boundary

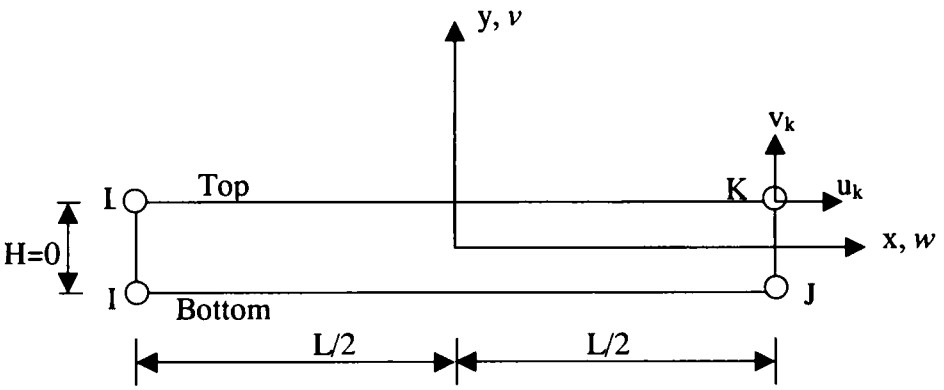

Fig. 1.2 A joint element represented using a local coordinate system

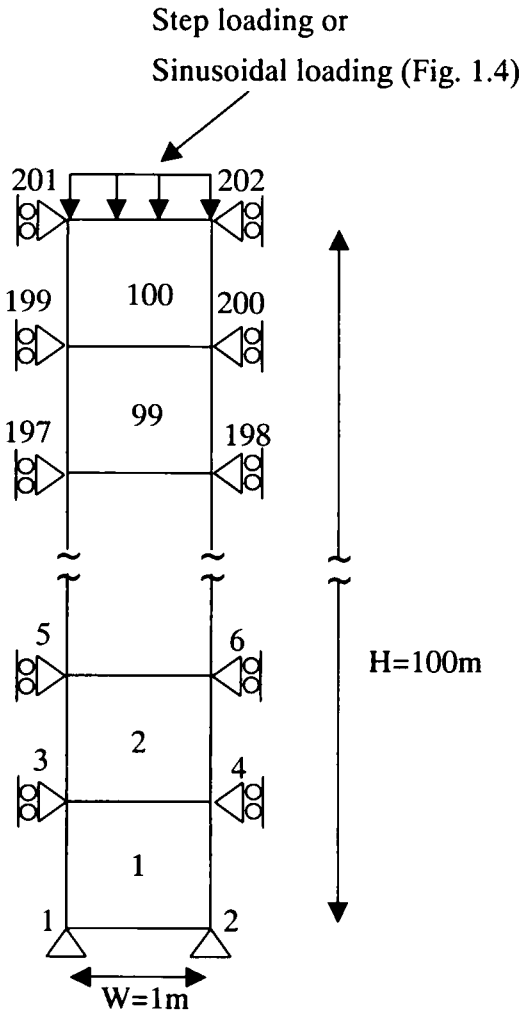

Fig. 1.3 Finite element model subjecting to compression wave loading

(a) Step loading

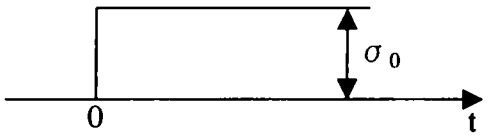

(b) Sinusoidal loading

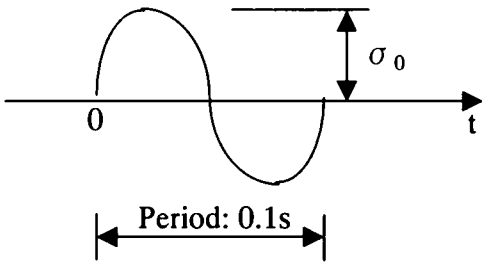

Fig. 1.4 Loading conditions

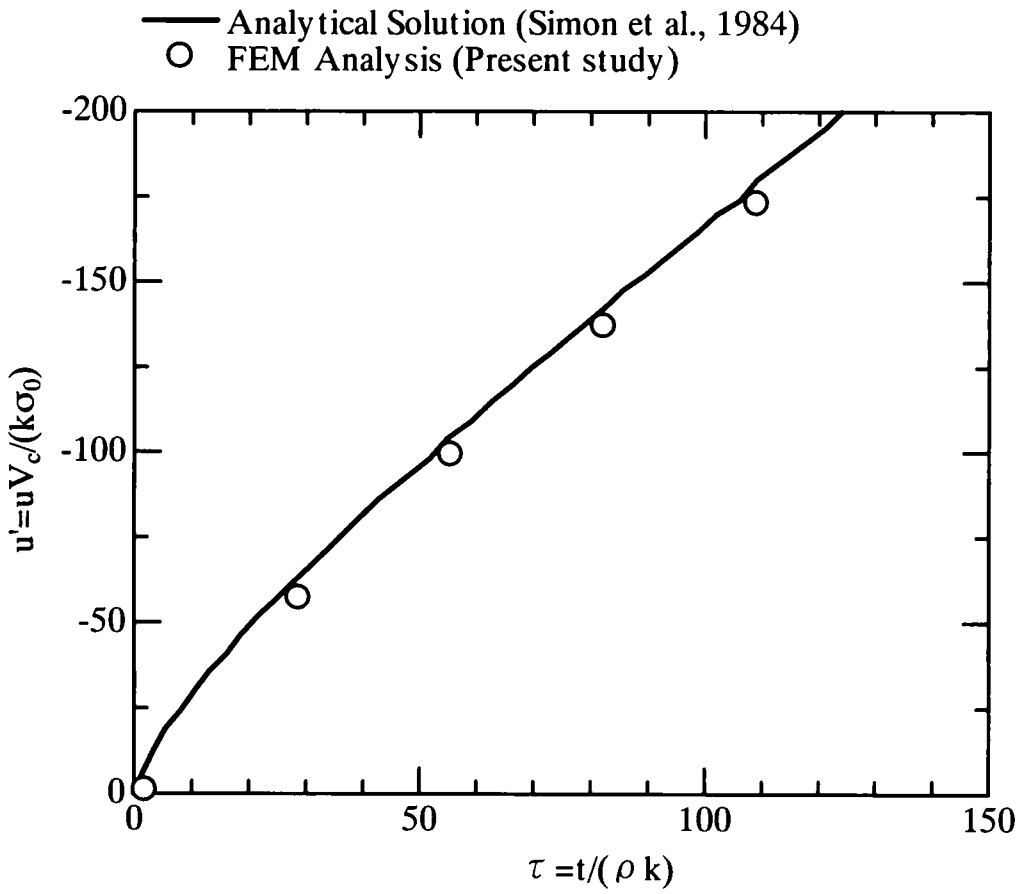

Fig. 1.5 Vertical surface movement of a poroelastic column subjected to step loading

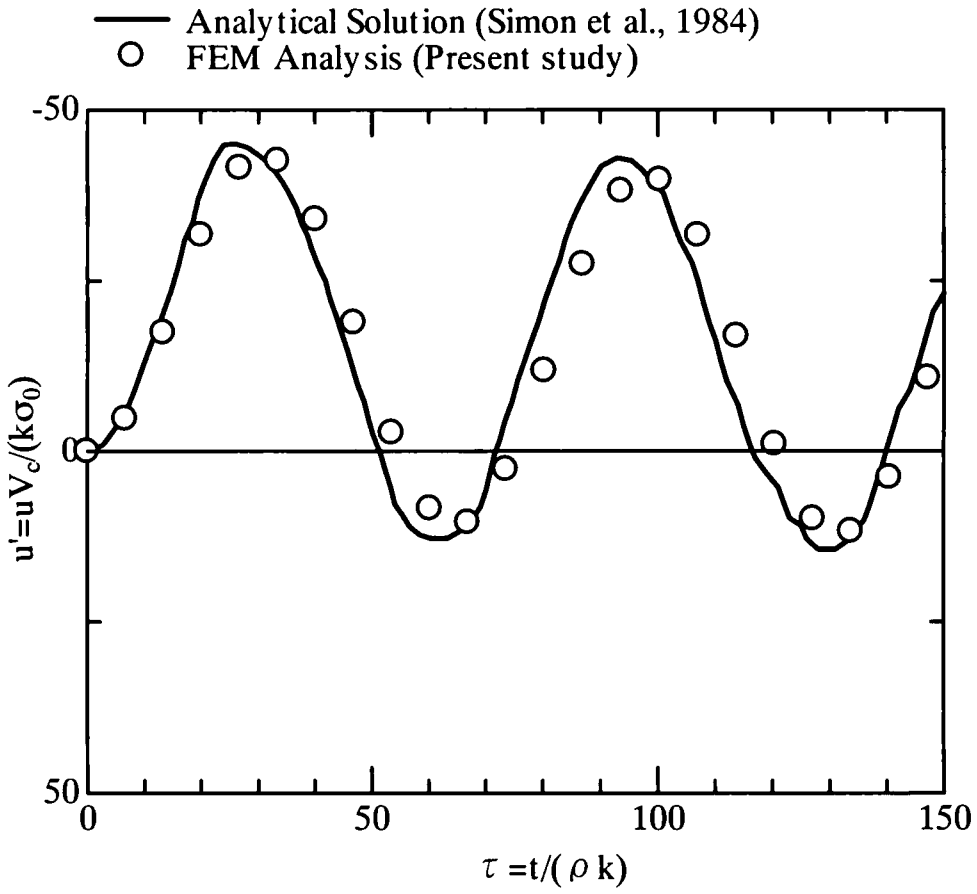

Fig. 1.6 Vertical surface movement of a poroelastic column subjected to sinusoidal loading

(a) Case T1 with rigid side walls

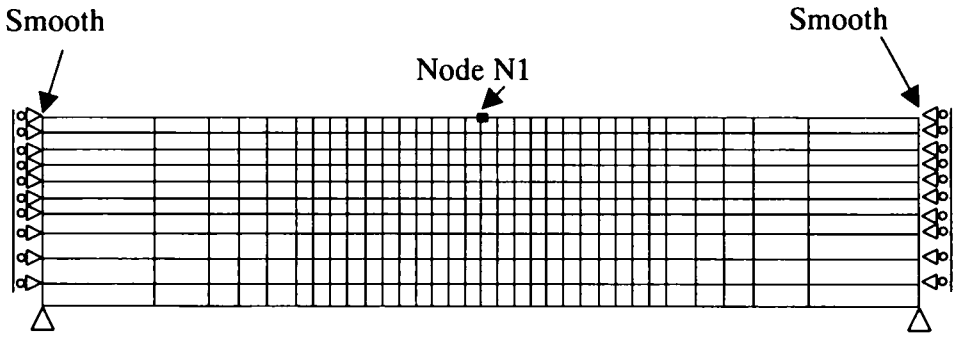

(b) Case T2 with viscous boundaries incorporated

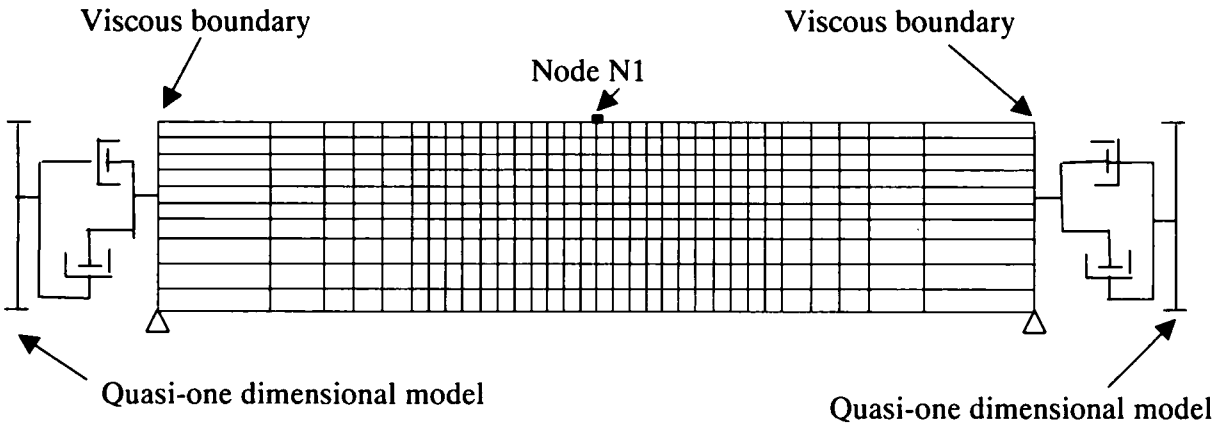

Fig. 1.7 Finite element meshes used in two-dimensional analyses

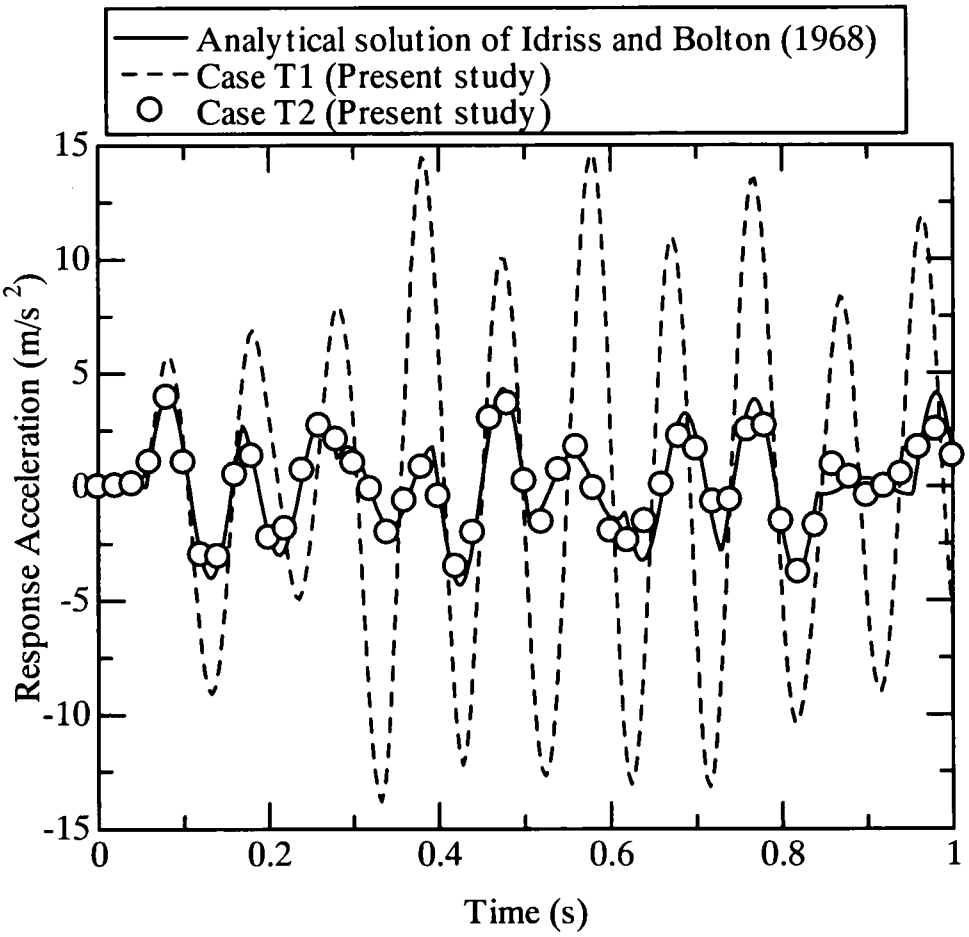

Fig. 1.8 Time histories of response acceleration at node N1

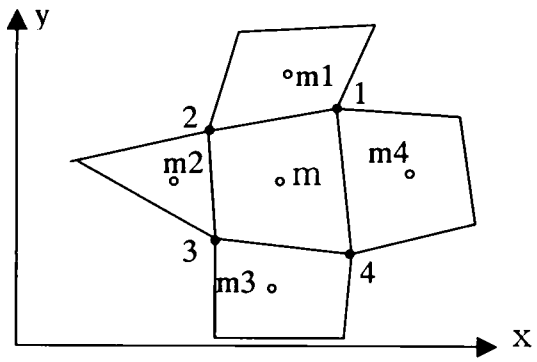

Fig. 1.9 A typical arrangement of a centered and four neighboring elements when considering discretization of storage equation

CHAPTER 2

Elastoplastic constitutive modeling for soils

2.1 Introductory remarks

The analysis of seismic wave propagation in soils can be considered as one of the major fields of research in waterfront areas. The need to predict the response of granular soil and structure systems subjected to seismic loading is increasingly important to ensure their safety and reliability.

Milestones of constitutive laws for the elasto-plastic deformation of granular soils were placed by D.C. Drucker et al. (1957) and by Roscoe et al. (1963). To facilitate accurate predictions, many advanced constitutive models have been proposed (Matsuoka and Nakai, 1974; Hashiguchi and Ueno, 1977; Dafalias, 1975; Hashiguchi, 1978; Pastor et al., 1990; Iai et al., 1992; Oka et al., 1999 among others).

A strain space plasticity model was developed by Iai et al. (1992). This is a multiple mechanism model defined in strain space and can take the effect of principal stress axis rotation on plastic deformation into account; the stress-axis rotation effect plays an important role in the cyclic behavior of sand under anisotropic stress conditions. A numerical analysis code FLIP has incorporated this constitutive model (Iai et al., 1993).

Oka et al. (1992) derived a cyclic elasto-plastic constitutive model for sand. Oka et al. (1999) modified the cyclic elasto-plastic constitutive model so that the plastic-strain dependence of the shear modulus may be allowed for. The constitutive model has been incorporated into a numerical analysis code LIQCA (Shibata et al., 1991).

Also, Oka, F. (1992) proposed a cyclic elasto-viscoplastic constitutive model for clay based on a non-linear hardening rule. This model can describe the difference in cyclic behavior of clay depending on the loading ratio imposed.

Pastor et al. (1990) proposed an elasto-plastic constitutive model for sands and clays. The main feature of the Pastor model lies in that plastic potential and yield surfaces need not to be explicitly defined, and that the consistency rule need not be applied. This facilitates a relatively simple description of behavior. In a sense the Pastor model may be regarded as an extension of Cam-clay model (Roscoe et al., 1963) in view of the flow rule incorporated. Observed phenomena to be achieved without the necessity of a rigid framework of a complex theory.

In this study, a plane-strain version of the Pastor model was incorporated into the

finite-element code developed.

What follows features of plane-strain version of the Pastor model is described. Then the constitutive model parameters were calibrated by referring to laboratory tests. The organization of subsequent sections is as follows. Section 2.2 will detail the mathematical structure of the plane-strain version of the Pastor model. Section 2.3 will describe the importance of generalized loading criteria in dealing with softening behavior of soil. In section 2.4, a physically sound procedure for determining the constitutive parameters will be presented.

2.2 A plane-strain version of the Pastor model

In order for an analysis of the dynamic-loading problem involving strong shaking to be meaningful, it is vital to incorporate a realistic constitutive model that allows for cyclic plasticity of soil. With this statement in mind the present study utilizes a plane-strain version of the elastoplastic constitutive model by Pastor et al. (1990).

2.2.1 A generalized plasticity model for granular soils

Let $d\varepsilon_v^p$ be the plastic volumetric increment and let $d\varepsilon_s^p$ be the plastic deviatoric increment. Then flow rule may be expressed as

$$\frac{d\varepsilon_v^p}{d\varepsilon_s^p} = (1+\alpha)(M_g - \eta) \tag{2.1}$$

where

$$p' = (\sigma_1' + \sigma_3')/2; \qquad q = \sigma_1' - \sigma_3'; \qquad \eta = \frac{q}{p'} \tag{2.2}$$

where the α is a material constant. M_g is a material constant that represents the slope of the phase transformation line (PTL) (refer to Fig. 2.1) and is independent of the shearing mode (compression or extension).

Note that when $\alpha = 0$, Eq. (2.1) reduces to the flow rule initially proposed by Roscoe et al. (1963) for Cam clay.

It proves convenient to express the direction of the plastic strain increments in terms of a unit normal **m** to the plastic potential surface (Fig. 2.1). There follows

$$\mathbf{m} = \frac{1}{\sqrt{(d\varepsilon_v^p)^2 + (d\varepsilon_s^p)^2}} \begin{pmatrix} d\varepsilon_v^p \\ d\varepsilon_s^p \end{pmatrix} = \frac{1}{\sqrt{1+d_g^2}} \begin{pmatrix} d_g \\ 1 \end{pmatrix} \tag{2.3}$$

where $d_g \equiv d\varepsilon_v^p / d\varepsilon_s^p$. Also, it is convenient to introduce a unit vector **n** to the yield surface

(f = 0). Namely,

$$\mathbf{n} = \frac{1}{\sqrt{1+d_f^2}}\begin{pmatrix} d_f \\ 1 \end{pmatrix} \tag{2.4}$$

where $d_f \equiv (1+\alpha)(M_f - q/p')$ and M_f is a material parameter characterizing an aspect of soil resistance.

The direction of plastic straining during "unloading", specified by a unit normal $\mathbf{m}_u$, has been selected in such a way as to permit a plastically contractive soil behavior under "unloading". Namely,

$$\mathbf{m}_u = \frac{1}{\sqrt{1+d_g^2}}\begin{pmatrix} -|d_g| \\ 1 \end{pmatrix} \tag{2.5}$$

The condition for unloading to occur will be described in Section 2.3.

The plastic modulus H_L has been assumed to take following form

$$H_L = H_0 \cdot p' \cdot \left(1 - \frac{\eta}{\eta_f}\right)^4 \cdot H_{vs} \tag{2.6}$$

where H_0 is a material constant,

and

$$H_{vs} = 1 - \frac{\eta}{M_g} + \beta_0\beta_1 \exp(-\beta_0\xi); \qquad \xi(=\int|d\varepsilon_s^p|) \tag{2.7}$$

and

$$\eta_f = (1+1/\alpha)M_f \tag{2.8}$$

where η_f limit the possible states, and in Eq. (2.7), β_0 and β_1 are the parameters which influence stress-strain relation after stress state closed phase transformation. Parameter ξ stands for the accumulated deviatoric plastic strain and is non-negative by definition.

The author has observed that the value of plastic modulus H_L depends on the degree of compaction of a given soil. It is interesting in this connection to note that the value of the constitutive parameter M_f also depends on the degree of compaction in a given soil. Thus it was found convenient to modify Eq. (2.6) into the following form:

$$H_L = H_0^* \cdot M_f \cdot p' \cdot \left(1 - \frac{\eta}{\eta_f}\right)^4 \cdot H_{vs} \tag{2.9}$$

where H_0^* is a material constant with no dependency of compaction.

The effect of discrete memory factor during cyclic loading may be introduced according to Pastor et al.(1990), such that

$$H_L = H_0^* \cdot M_f \cdot p' \cdot \left(1 - \frac{\eta}{\eta_f}\right)^4 \cdot H_{vs} \cdot H_{DM} \tag{2.10}$$

where the discrete memory factor H_{DM} has been assumed to take the following specific form:

$$H_{DM} = \left(\frac{\zeta_{max}}{\zeta}\right)^{\gamma_D} \tag{2.11}$$

Here γ_D are material constants and parameter ζ represents the mobilized stress function that is defined as follows:

$$\zeta = p' \cdot \left(1 - \frac{\alpha}{1+\alpha} \cdot \frac{\eta}{M_f}\right)^{-1/\alpha} \tag{2.12}$$

An important feature of the actual sand behavior is the occurrence of contractive volume changes under unloading or stress reversal. Also, experimental results have shown that unloading from a high stress ratio results in marked plastic straining. Thus plastic modulus H_U for unloading has been introduced, with reference to the stress ratio $\eta_u = (q/p')_u$ at the starting point of unloading. That is to say,

$$H_U = \begin{cases} H_{U0}\left(\dfrac{M_g}{\eta_u}\right)^{\gamma_u} & for \quad \left|\dfrac{M_g}{\eta_u}\right| > 1 \\ H_{U0} & for \quad \left|\dfrac{M_g}{\eta_u}\right| \le 1 \end{cases} \tag{2.13}$$

The elastoplastic constitutive relations can finally be expressed in the following form:

$$\dot{\sigma}_{ij} = L\delta_{ij}\dot{\varepsilon}_{kk} + 2G\dot{\varepsilon}_{ij}$$

$$- \frac{[(L+G)d_g\delta_{ij} + \dfrac{2\sigma_{ij} - \delta_{ij}\sigma'_{kk}}{q} 2G][(L+G)d_f\delta_{lm} + \dfrac{2\sigma_{lm} - \delta_{lm}\sigma'_{kk}}{q} 2G]}{H \| n \| \cdot \| m \| + (L+G)d_f d_g + 4G} \dot{\varepsilon}_{lm} \tag{2.14}$$

Here L is the Lamé constant and G stands for the shear modulus. Also, note that since the plane strain condition is dealt with, the following relation holds

$$\dot{\sigma}'_2 = \nu' \cdot \left(\dot{\sigma}'_1 + \dot{\sigma}'_3\right) \tag{2.15}$$

where σ_2' is the intermediate effective principal stress and ν' is Poisson's ratio in terms of effective stress.

2.2.2 A generalized plasticity model for clays

The Plastic modulus H_L for clay has been introduced in the following form (Pastor et al., 1990):

$$H_L = H_0 \cdot p' \cdot f(\eta) \tag{2.16}$$

where

$$f(\eta) = \left(1 - \frac{\eta}{M}\right)^2 \frac{\left(1 + d_0^2\right)}{\left(1 + d^2\right)} sign\left[1 - \frac{\eta}{M}\right] \tag{2.17}$$

where $d_0 = (1+\alpha)M$ and $d = (1+\alpha)(M - \eta)$.

In the case of applying to overconsolidated clays the plastic moduli HL has been modified into the following form:

$$H_L = H_0 \cdot p' \cdot \left(f(\eta) + g(\xi)\right) \cdot H_{DM} \tag{2.18}$$

in which

$$g(\xi) = \beta_0 \left(1 - \frac{\zeta}{\zeta_{\max}}\right) \exp(-\beta\xi) \tag{2.19}$$

2.3 Loading criteria

It may readily be observed that loading criteria constitute one of the most important aspects of constitutive modeling for plastically deforming media. On of conventional loading/unloading criteria, since the plastic modulus should always be positive during loading. The perfect plasticity state is put aside. More importantly, the states of softening and elastic-unloading may be undistinguishable according to conventional loading criteria.

Thus the present analysis applies, we introduce generalized loading criteria to the Pastor model. For purposes of description, a mathematical formulation of conventional loading criteria will subsequently be referred to first.

2.3.1 Conventional loading criteria

A scalar Λ is introduced

$$\Lambda = \frac{1}{H_{L/U}} N_{ij} d\sigma_{ij}^{'} \tag{2.20}$$

Elastoplastic equation can be expressed by following form

$$d\sigma_{ij}^{'} = D_{ijkl}(d\varepsilon_{kl} - d\varepsilon_{kl}^{p}) \tag{2.21}$$

where

$$d\varepsilon_{kl}^{p} = M_{kl} \frac{1}{H_{L/U}} (N_{ij} d\sigma_{ij}^{'}) \tag{2.22}$$

Let Lc denote a conventional loading function such that $L_c = N_{ij} d\sigma_{ij}^{'}$. Then the loading criteria in conventional sense read

Eq. (2.20) is expressed as

$$L_c = N_{ij} d\sigma_{ij}^{'} > 0 \qquad \text{loading} \tag{2.23}$$

$$L_c = N_{ij} d\sigma_{ij}^{'} = 0 \qquad \text{neutral loading} \tag{2.24}$$

$$L_c = N_{ij} d\sigma_{ij}^{'} < 0 \qquad \text{unloading} \tag{2.25}$$

In the case of Pastor model, the Lc function becomes

$$L_c = (1+\alpha)\left(M_f - q/p'\right) \cdot dp' + dq \tag{2.26}$$

It is important herein to observe that the states of softening (H_L<0) and unloading may be undistinguishable according to conventional loading criteria. That is, the Lc function in Eq. (2.26) become negative during the softening process although A scalar Λ in Eq. (2.20) become positive.

2.3.2 Generalized Loading criteria

To account for softening behavior of the material, when H_L is negative, definitions of generalized loading criteria L_g have to be introduced as following.

Both sides of Eq. (2.21) are now multiplied by N_{ij} and substitute Eq (2.22), we obtain

$$N_{ij} d\sigma_{ij}^{'} = \frac{N_{op} D_{opqr} d\varepsilon_{qr}}{1 + (1/H_{L/U}) N_{st} D_{stuv} M_{uv}} \tag{2.27}$$

Substituting Eq. (2.27) into Eq. (2.20) yields the following:

$$\Lambda = \frac{N_{op} D_{opqr} d\varepsilon_{qr}}{H_{L/U} + N_{st} D_{stuv} M_{uv}} = \frac{L_g}{X} \tag{2.28}$$

where

$$N_{op} D_{opqr} d\varepsilon_{qr} = \frac{1}{\left\| \partial f / \partial \sigma' \right\|} \left\{ (K + G/3) \cdot d_f \delta_{qr} + \frac{2\sigma_{qr} - \delta_{qr}\sigma_{kk}}{q} 2G \right\} d\varepsilon_{qr} \tag{2.29}$$

$$N_{st} D_{stuv} M_{uv} = \left((\mathrm{K+G/3}) \cdot \mathrm{d}_f \cdot \mathrm{d}_g \cdot +4\mathrm{G} \right) / \left\| \partial f / \partial \sigma' \right\| \left\| \partial g / \partial \sigma' \right\| \tag{2.30}$$

Generally, parameter X in Eq. (2.28) is always positive although $H_{L/U}$ become negative. Therefore, generalized loading criteria with parameter X>0 may be expressed as

$$L_g = N_{op} D_{opqr} d\varepsilon_{qr} > 0 \qquad \text{loading} \tag{2.31}$$

$$L_g = N_{op} D_{opqr} d\varepsilon_{qr} = 0 \qquad \text{neutral loading} \tag{2.32}$$

$$L_g = N_{op} D_{opqr} d\varepsilon_{qr} < 0 \qquad \text{unloading} \tag{2.33}$$

Note that the loading criterion, Eq. (2.31), is applicable to a softening process.

2.3.3 Example analysis

The marked differences in predicted performances in terms of conventional and generalized loading criteria demonstrated in Fig. 2.2 with reference to element A for finite-element model of Chapter 5. In terms of conventional loading criteria (refer to Fig. 2.2(b)), stress path for element A shows an unnatural performance and finally, calculation becomes impossible closed to $q = \eta_f \cdot p'$ line which limit the possible stress states. However, in terms of generalized loading criteria, stress path for element A shows natural performance (refer to Fig. 2.2(c)). It is evident that generalized loading criteria could be needed to calculate finite-element process.

2.4 Selection of constitutive parameters with special reference to the effect of the degree of compaction

Let us consider selection of constitutive parameters with special reference to the effect of the degree of compaction. Firstly, author selected constitutive parameter M_g with no dependency of compaction. And then parameters α, β_0, β_1 and H_0^* were assumed as the value which cover the features of behavior under monotonic loading (Fukushima, 1982; Tatsuoka, 1994). The values of the constitutive parameter M_f depending on the degree of compaction in a given soil were selected with the varied degrees of compaction. The constitutive parameters used in

the present case studies are shown in Table 2.1.

A series of simulation for a element with monotonic torsional shear tests (Fukushima, 1982; Tatsuoka, 1994) was performed on saturated sand. Observed and predicted shear stress ratio-shear strain relations for monotonic drained torsional shear tests are shown in figures Fig. 2.3(a) and Fig. 2.3(b), respectively. Predicted performance of soil behavior conforms well to the experimentally observed soil behavior.

Observed and predicted stress paths for monotonic undrained torsional shear are shown in Fig. 2.4. Predicted results represent static liquefaction and dilatancy performance of observed results.

Non-associativeness parameter M_f/M_g used in predicted performance versus relative density of observed soil element are shown in Fig. 2.5. Best fitting between the predicted and measured performances leads to the following equation of correlation:

$$M_f / M_g = e^{(A \cdot Dr + B)} \tag{2.34}$$

where A=1.07, B=-1.35.

In Eq. (2.34), non-associativeness parameter M_f/M_g was expressed on the entire degree of compaction in a given soil.

2.5 Conclusions

A plane-strain version of the elastoplastic constitutive model by Pastor et al. (1990) was reformulated, with consideration of generalized loading criteria. This permitted parameter M_g, related to the angle of the phase-transformation line, to be a true material constant in the sense that the value is independent of the shearing mode (compression or extension) and may be determined for a given soil. The introduction of generalized loading criteria permitted a consistent description of softening behavior in the present framework as being a loading process. Furthermore, particular emphasis was placed for developing a workable yet physically sound procedure for determining the plastic constitutive parameters concerned. The outcome of this approach is such that the non-associativeness parameter M_f/M_g correlates well with the degree of compaction or relative density Dr of sand, providing a useful equation of correlation as represented by $M_f / M_g = \exp(1.07Dr - 1.35)$.

Reference

Dafalias, Y.F. and Popov, E.P. (1975). A model of non-linearly hardening materials for complex loading, *Acta Mechanics*, Vol. 21, 173-192

Drucker, D.C. (1957). Soil Mechanics and work-hardening theories of plasticity, *Trans. ASCE*, Vol. 122, 338-346.

Fukushima, S. (1982). Experimental study into deformation and strength properties of sand by torsional shear tests, *Dr. of Engineering thesis*, University of Tokyo (in Japanese).

Hashiguchi, K. and Ueno, M. (1977). Elastoplastic constitutive laws of granular materials, Constitutive equations of soils, *Proc. 9th Int. Conf. SMFE*, Spec. Session 9, Tokyo, JSSMFE, 73-82.

Hashiguchi, K. (1978). Plastic constitutive equations of granular materials, *US-Japan Seminar on Continum Mech. & Stast. Approaches in Granular Materials*, Sendai, JSSMFE, 321-329.

Iai, S., Matsunaga, Y. and Kameoka, T. (1992). Strain space plasticity model for cyclic mobility, *Soils and Foundations*, Vol. 32, No.2, 1-15.

Iai, S. and Kameoka, T. (1993). Finite element analysis of earthquake induced damage to anchored sheet pile quay wall, *Soils and Foundations*, Vol. 33, No.1, 71-91.

Matsuoka, H. and T. Nakai (1974). Stress-deformation and strength characteristics of soil under three different principal stresses, *JSCE*, No. 232, 59-70.

Oka, F. (1992). A cyclic elasto-viscoplastic constitutive model for clay based on the non-linear hardening rule, *Proceedings of Fourth International Symposium on Numerical Models in Geomechanics, Swansea*, 105-114

Oka, F., Yashima, A., Kato, M. and Sekiguchi, K. (1992). A constitutive model for sand based on the non-linear kinemativ hardening rule and its application, Proc. 10th World Conf. On earthquake engineering, Madrid, pp. 2529-2534.

Oka, F., Yashima, A., Tateishi, A., Taguchi, Y. and Yamashita, S. (1999). A cyclic elasto-plastic constitutive model for sand considering a plastic-strain dependence of the shear modulus, *Geotechnique*, Vol 49, No. 5, 661-680.

Pastor, M., Zienkiewicz, O.C. & Chan, A.H.C. (1990). Generalized plasticity and the modeling of soil behaviour. *Int. J. Numer. Anal. Methods Geomech*. Vol. 14, 151-190.

Roscoe, K.H., Schofield, A. N. and Thurairajah, A. (1963). Yielding of clays in state wetter than critical, *Geotechnique*, Vo. 13, 211-240.

Shibata, T., Sato, T., Uzuoka, R., Oka, F., Yashima, A. and Kato, M. (1991). FEM-FDM coupled liquefaction analysis of a fluid-saturated ground, *Computer methods and advances in geomechanics*, 869-874.

Tatsuoka, F. (1994). Discussion on "Undrained shear strength of liquefied sands for stability analysis", *Journal of Geotehnical Engineering*, Vol. 120, No.7, 1284-1287.

Table 2.1 The constitutive parameters used for simulation of torsional shearing (Tatsuoka, 1994)

Mg	M_f	α	β_0	β_1	H_0^*
1.2	0.42-0.88	0.35	20	0.04	500

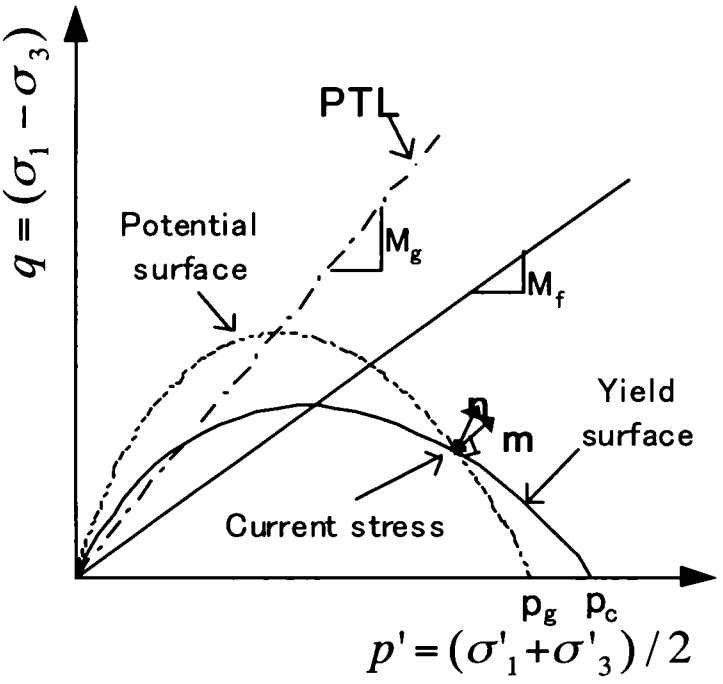

Fig. 2.1 Yield and plastic potential surfaces

(a) Reference to Element A for finite-element model

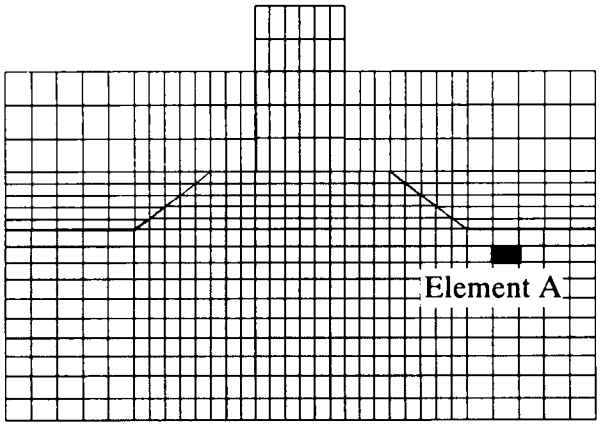

(b) In terms of conventional loading criteria

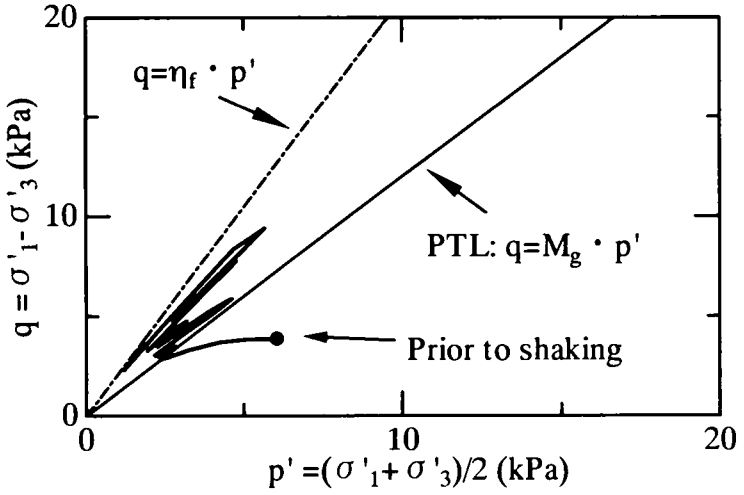

(c) In terms of generalized loading criteria

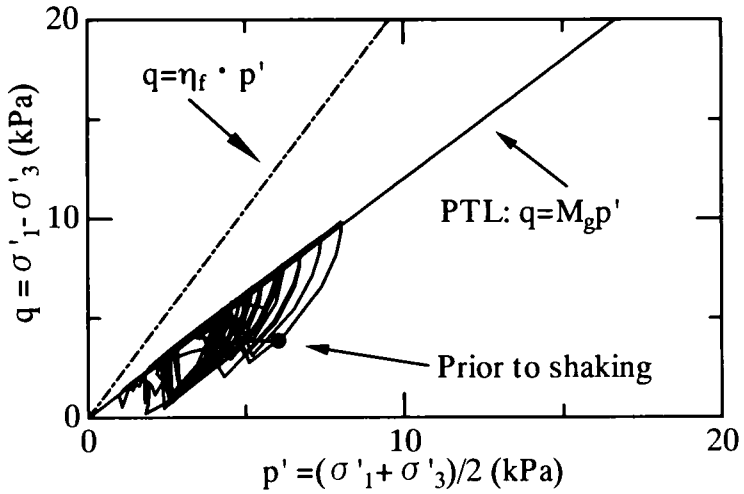

Fig. 2.2 Comparison of predicted effective stress paths performances: (a) reference to Element A for finite-element model; (b) in terms of conventional loading criteria; (c) in terms of generalized loading criteria

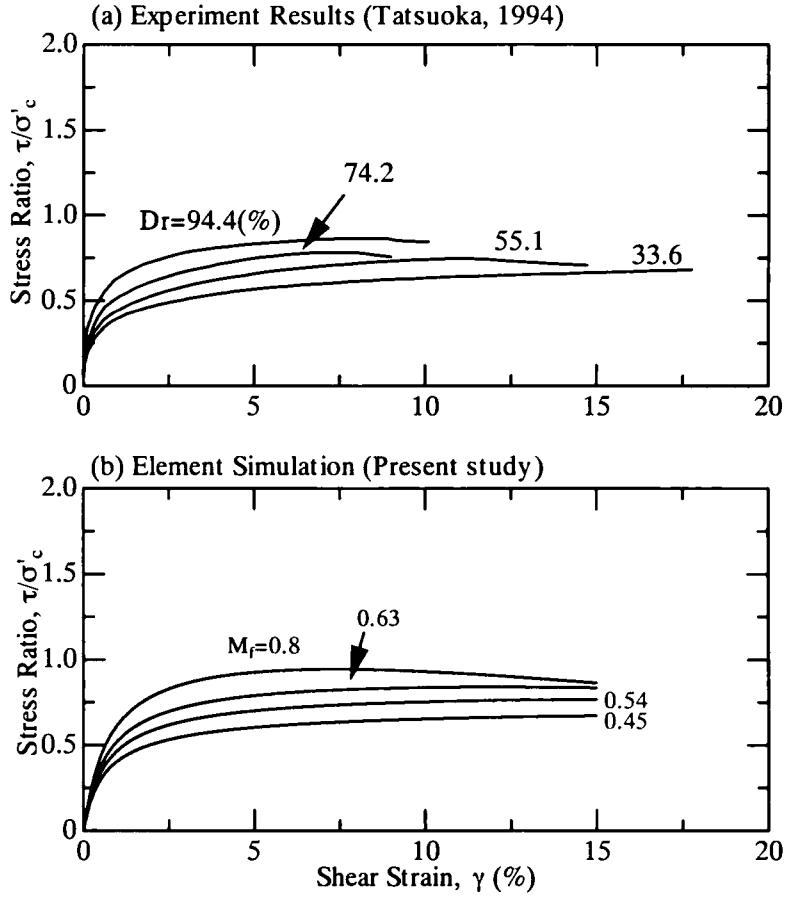

Fig. 2.3 Observed and predicted shear stress ratio-shear strain relations for monotonic drained torsional shear

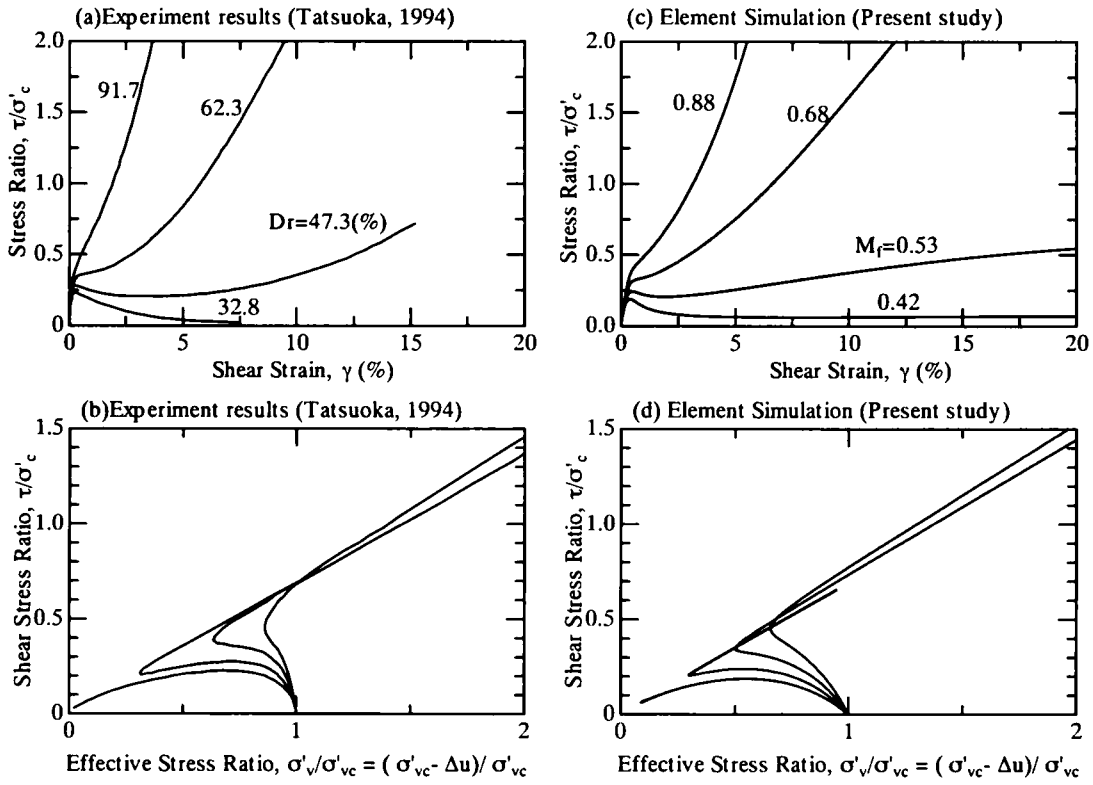

Fig. 2.4 Observed and predicted stress path for monotonic undrained torsional shear

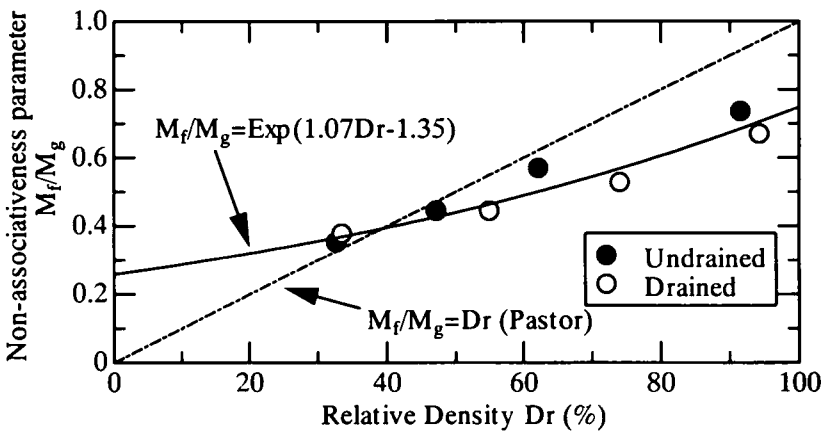

Fig. 2.5 Non-associativeness parameter M_f/M_g versus relative density Dr from monotonic undrained torsional shear

CHAPTER 3

Elastoplastic constitutive modeling for interface between soil and structure

3.1 Introductory remarks

The deformation response of soil-structure systems is influenced by stress-displacement relations of interfaces between soil and solid structures. This is particularly true of systems subjected to cyclic loading conditions. Experimental and numerical studies of the behavior of interfaces have received increasing attention.

Goodman et al. (1968) presented a concept of joint element to describe the motion at the interface between two solid matters. The joint stiffness per unit length in the tangential and normal directions were formulated. Nakai (1985) proposed an elastoplastic model for the interface between soil and structures. The elastoplastic model becomes operational only stress ratio at the interface reaches a specified coefficient of friction. Desai et al. (1985) performed tangential-displacement-controlled cyclic tests on interfaces between Ottawa sand and concrete under constant normal stress conditions. The device used was a direct shear apparatus permitting two-way shearing of small-amplitude. It was found that the rate of stiffening decreases as the number of cycles increases. Fakharian and Evgin (1997) carried out monotonic and cyclic simple shear tests on sand-steel interfaces. The experimental results showed the occurrence of contractive/dilation behavior of sand-steel interfaces during cyclic simple shear. Miyata et al. (2003) conducted a series of plate-loading tests to investigate contact pressure characteristics of a caisson/rubble mound system for composite breakwaters. The test results show that the vertical loading exerted through the caisson transmits to a small number of contact points, and that the contact forces have a wide range of magnitudes.

In what follows, the formulation of a cyclic elastoplastic model for the soil-structure will be made, along with its validation against a range of laboratory test results.

3.2 Elastoplastic constitutive modeling for a joint element

This section proposes a workable elastoplastic constitutive model for a joint element. The definitions of stress and relative displacements in a typical joint are shown in Fig. 3.1. Compressive stresses and relative compressive displacements are taken as positive.

Let us introduce the stress ratio $\eta_j (= \tau / \sigma_n')$ that is mobilized on the interface. In view of Eq. (2.1) in chapter 2, we assume the following relative-flow rule.

$$\frac{dv^p}{dw^p} = (1+\alpha_j)(\mu_g - \eta_j) \tag{3.1}$$

where dv^p is the components in normal direction of plastic displacement increment, dw^p is the components in tangential direction of plastic displacement increment, α_j is a material constant and μ_g represents the slope of the phase transformation line (PTL) when plotted in the σ_n'-τ space (refer to Fig. 3.2).

Let **m** be a unit normal vector to the plastic potential surface (Fig. 3.2). It follows that

$$\mathbf{m} = \frac{1}{\sqrt{(dw^p)^2 + (dv^p)^2}} \begin{pmatrix} dw^p \\ dv^p \end{pmatrix} = \frac{1}{\sqrt{1+d_{gj}^2}} \begin{pmatrix} 1 \\ d_{gj} \end{pmatrix} \tag{3.2}$$

where $d_{gj} \equiv dv^p / dw^p$. Let **n** be a unit normal vector to the yield surface (f = 0). Namely,

$$\mathbf{n} = \frac{1}{\sqrt{1+d_{fj}^2}} \begin{pmatrix} d_{fj} \\ 1 \end{pmatrix} \tag{3.3}$$

where $d_{fj} \equiv (1+\alpha_j)(\mu_f - \eta_j)$ and μ_f is a material parameter.

The direction of plastic straining during unloading, $\mathbf{m}_u$, is formulated in such a way as to permit contractive soil behavior under unloading. Namely,

$$\mathbf{m}_u = \frac{1}{\sqrt{1+d_{gj}^2}} \begin{pmatrix} 1 \\ -|d_{gj}| \end{pmatrix} \tag{3.4}$$

The plastic modulus H_{Lj} for the joint element under loading is assumed to take the following form:

$$H_{Lj} = H_{0j} \cdot \sigma_n' \cdot \left(1 - \frac{\eta_j}{\eta_{fj}}\right)^4 \cdot H_{vs}^* \tag{3.5}$$

where

$$\left.\begin{aligned} \eta_{fj} &= (1+\frac{1}{\alpha_j})\mu_f \\ H_{vs}^{*} &= 1-\frac{\eta_j}{\mu_g}+\beta_{0j}\exp(-\beta_{1j}\xi_j) \end{aligned}\right\} \quad (3.6)$$

Here H_{0j}, β_{0j} and β_{1j} are material constants, and parameter $\xi_j (= \int |dw^p|)$ stands for the accumulated plastic displacement in the tangential direction.

A discrete memory factor H_{DMj} for the joint element under cyclic loading reads

$$H_{Lj} = H_{0j} \cdot \sigma_n^{'} \cdot \left(1-\frac{\eta_j}{\eta_{fj}}\right)^4 \cdot H_{vs}^{*} \cdot H_{DMj} \quad (3.7)$$

in which

$$H_{DMj} = \left(\frac{\zeta_{\max_j}}{\zeta_j}\right)^{\gamma_{Dj}} \quad (3.8)$$

where γ_{Dj} are material constant and parameter ζ_j represents the mobilized stress function that is defined as follows:

$$\zeta_j = \sigma_n^{'} \cdot \left(1-\frac{\alpha_j}{1+\alpha_j}\cdot\frac{\eta_j}{\mu_f}\right)^{-1/\alpha_j} \quad (3.9)$$

The plastic modulus H_{Uj} for the joint element undergoing unloading may be represented as follows

$$H_{Uj} = \begin{cases} H_{U0j}\left(\dfrac{M_{gj}}{\eta_{uj}}\right)^{\gamma uj} & for \quad \dfrac{\mu_g}{\eta_{uj}} > 1 \\ H_{U0j} & for \quad \dfrac{\mu_g}{\eta_{uj}} \le 1 \end{cases} \quad (3.10)$$

Here η_{uj} represents the stress ratio, $(\tau/\sigma_n^{'})_U$, at the start of unloading.

The constitutive relations for the joint element can finally be expressed in the following form:

$$\begin{Bmatrix} d\tau \\ d\sigma_n^{'} \end{Bmatrix} = [D]\begin{Bmatrix} dw \\ dv \end{Bmatrix} \quad (3.11)$$

where

$$\mathbf{D} = \mathbf{D}^e - \frac{\mathbf{D}^e \mathbf{m} \mathbf{n}^T \mathbf{D}^e}{H_{Lj/Uj} + \mathbf{n}^T \mathbf{D}^e \mathbf{m}} \tag{3.12}$$

in which

$$\mathbf{D}^e = \begin{bmatrix} K_s^e & 0 \\ 0 & K_n^e \end{bmatrix} \tag{3.13}$$

Note that K_s^e and K_n^e represent elastic stiffness in the tangential and normal directions.

3.3 Generalized loading criteria for joint elements

Essentially the same discussion as section 2.3 in chapter 2 can be made for joint elements.

Note that a scalar multiplier Λ is of the following form:

$$\Lambda = \frac{\mathbf{n}^T \mathbf{D}^e \mathbf{de}}{\left[H_{Lj/Uj} + \mathbf{n}^T \mathbf{D}^e \mathbf{m}\right]} = \frac{L_g}{X} \tag{3.14}$$

where

$$\mathbf{N}^T \mathbf{D}^e \mathbf{de} = \frac{1}{\left\| \partial f / \partial \sigma' \right\|} \left(K_s^e dw + d_{fj} K_n^e dv \right) \tag{3.15}$$

$$\mathbf{n}^T \mathbf{D}^e \mathbf{m} = \left(K_s^e + d_{fj} d_{gj} K_n^e \right) / \left\| \partial f / \partial \sigma' \right\| \left\| \partial g / \partial \sigma' \right\| \tag{3.16}$$

Under conditions of X>0, generalized loading criteria for joint elements may now be expressed as

$$L_g = \mathbf{n}^T \mathbf{D}^e \mathbf{de} > 0 \qquad \text{loading} \tag{3.17}$$

$$L_g = \mathbf{n}^T \mathbf{D}^e \mathbf{de} = 0 \qquad \text{neutral loading} \tag{3.18}$$

$$L_g = \mathbf{n}^T \mathbf{D}^e \mathbf{de} < 0 \qquad \text{unloading} \tag{3.19}$$

3.4 Predicted performance of a joint element under cyclic shearing

Fakharian and Evgin (1997) investigated the monotonic and cyclic shear behavior of a sand-steel interface using a simple shear-type soil container. Their typical test results from monotonic simple shear testing under constant normal stress are shown in Fig. 3.3 (Fakharian and Evgin, 1997). The normal stress was kept at a constant value 100kPa throughout shearing. The peak and residual shear strengths were equal to 80.3 and 62.0 kPa, respectively. The

normal displacement was initially in compression during shearing and became dilative when the tangential displacement exceeded 0.8mm.

The predicted performance of a joint element subjected to monotonic simple shear under $\sigma_n^{'}$=100kPa are shown in Fig. 3.4. The model parameters used is shown in Table 3.1. The elastic interfacial stiffness was assumed as $K_s^e = K_n^e = 1 \times 10^6$ kPa/m. It is seen that the predicted behavior conforms well to the experimentally observed behavior shown in Fig. 3.3.

The results of a cyclic simple shear test under constant normal stress ($\sigma_n^{'}$=100kPa) are shown in Fig. 3.5 (Fakharian and Evgin, 1997). The amplitude of the tangential displacement was set at 0.75mm. The predicted cyclic behavior of a joint element under $\sigma_n^{'}$=100kPa are shown in Fig. 3.6. The model parameters used is listed in Table 3.1. It is seen the predicted performance of the joint-element behavior compares favorably with the observed interfacial behavior.

3.5 Conclusions

A new cyclic elastoplastic constitutive model for a soil-structure interface has been described along with generalized loading criteria. The interface joint-element model is a counterpart of the previously introduced elastoplastic constitutive model for soil. The performance of the joint-element modeling was favorably tested in light of the monotonic and cyclic shearing tests on a sand-steel interface reported by Fakharian and Evgin (1997).

Reference

Desai, C. S., Drumm, E.C. and Zaman, M. M. (1985). Cyclic testing and modeling of interfaces, *Journal of Geotechnical and Geoenvironmental Engineering, ASCE*, Vol. 111, No. 6, 793-815.

Fakharian, K. and Evgin, E. (1997). Cyclic simple-shear behavior of sand-steel interfaces under constant normal stiffness condition, *Journal of Geotechnical and Geoenvironmental Engineering, ASCE*, Vol. 123, No. 12, 1096-1105.

Ghionna, V. N. and Mortara, G. (2002). An elastoplastic model for sand-structure interface behaviour, Geotechnique, Vol. 52, No. 1, 41-50.

Goodman, R., Taylor, R. and Brekke, T. (1968). A model for the mechanics of jointed rock, *ASCE*, Vol. 94, No. SM3, 637-659.

Miyata, M., Sugano, T., Nagao, T., Nakagawa, M., Mustoe, G. G. W., Tanaka, T. and Kikuchi, N. (2003). Experimental study on load support systems of rubble rock foundations, *J. Geotech. Eng., JSCE*, No.750/III-65, 1-14.

Nakai T. (1985). Finite element computations for active and passive earth pressure problems of retaining wall, *Soils and Foundations*, Vol. 25, No. 3, 98-112.

Uesugi., Kishida, H. and Tsubakihara, Y. (1989). Friction between sand and steel under repeated loading, Soils and Foundations, Vol. 29, No. 3, 127-137.

Table 3.1 The interfacial constitutive parameters used for simulating simple shear tests on a sand-steel interface

μ_g	μ_f	α_j	β_{0j}	β_{1j}	H_{0j}	H_{U0j} (kPa/m)	γ_{uj}	γ_{Dj}
0.6	0.5	0.35	0.4	20	2000	1000000.0	2	4

(a)

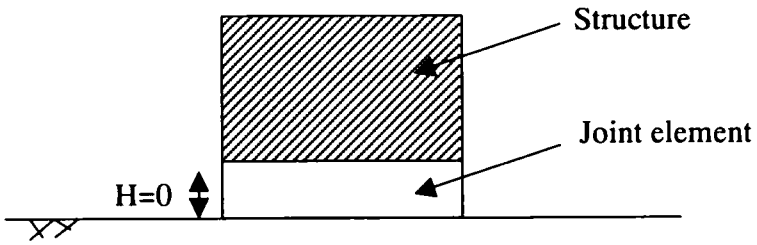

Foundation soil

(b)

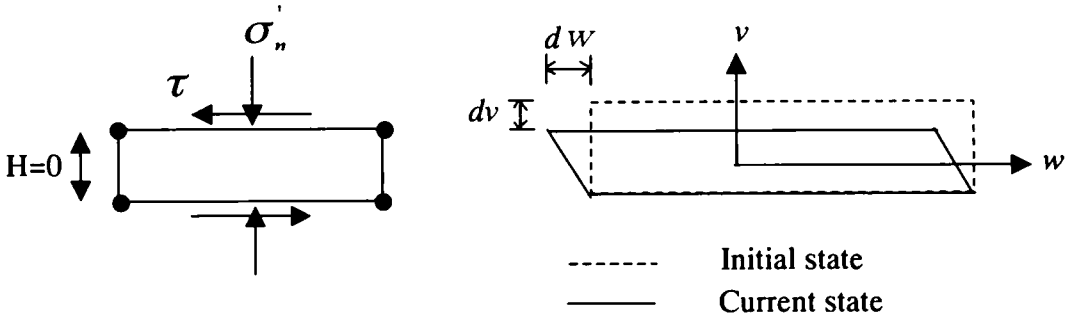

Fig. 3.1 (a) A physical idea of joint-element for a soil-structure interface; (b) definitions of stress and relative-displacement components in a joint element

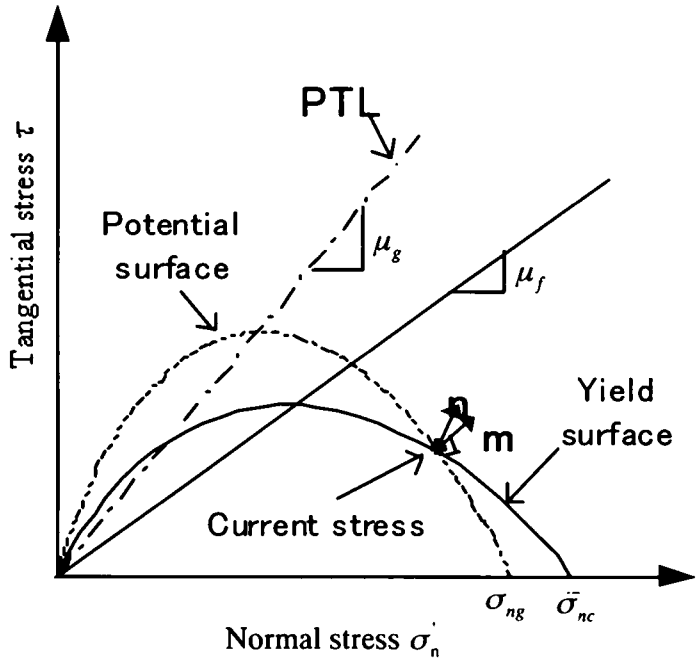

Fig. 3.2 Yield and plastic potential surfaces for joint element in a $\sigma_n - \tau$ space

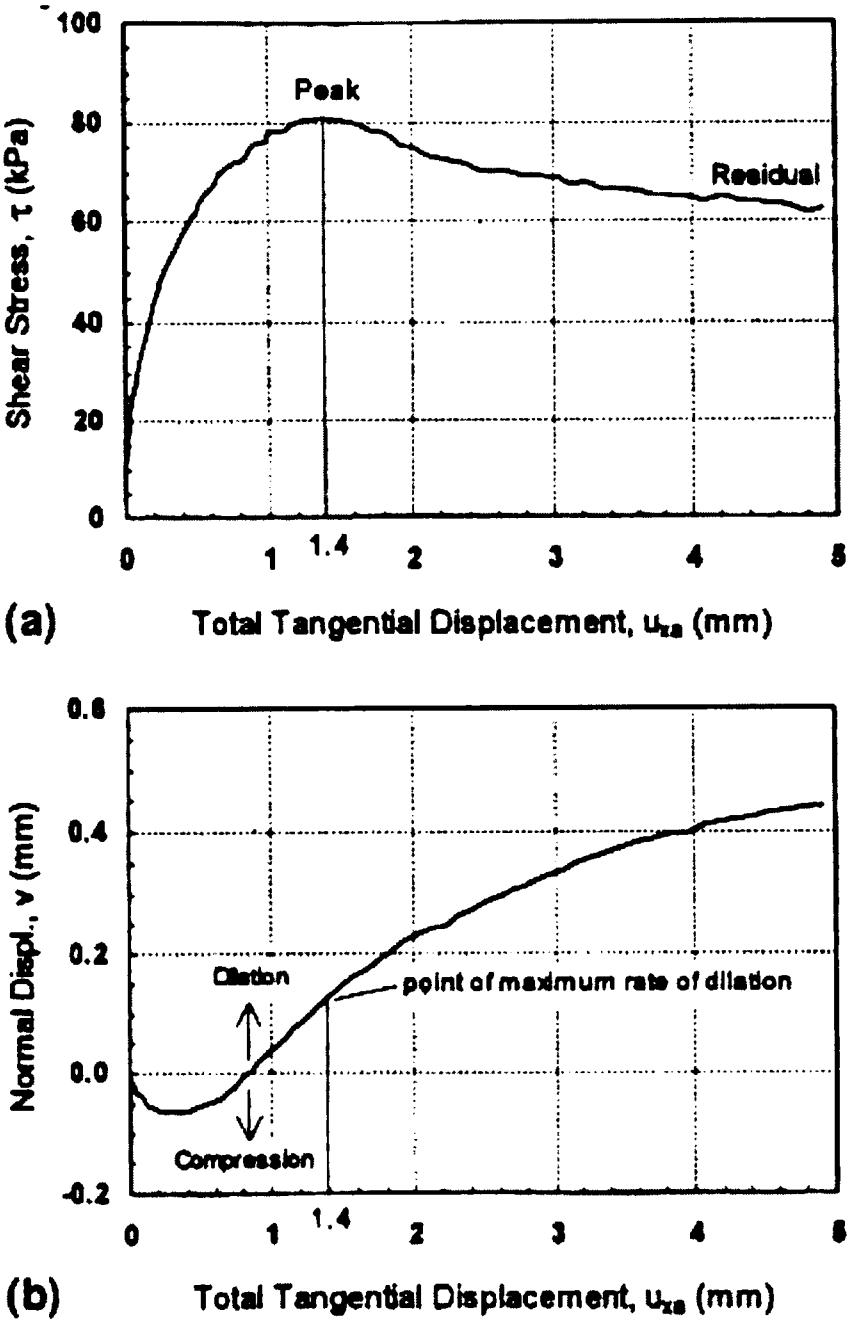

Fig. 3.3 Results of monotonic simple shear test on a sand-steel interface under constant normal stress (Fakharian and Evgin, 1997)

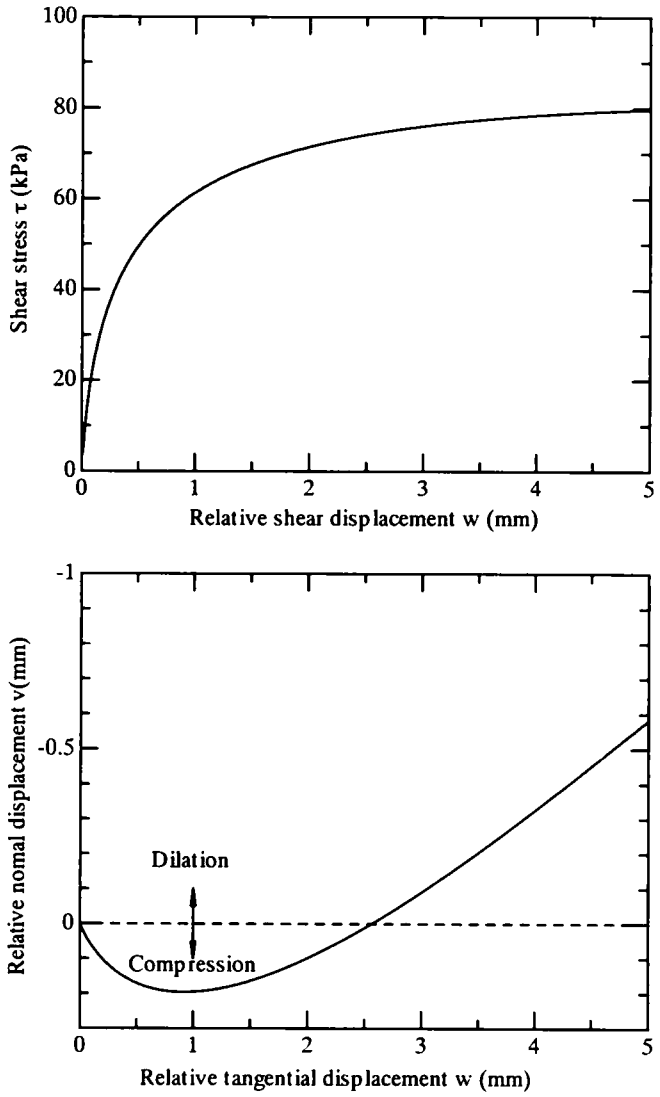

Fig. 3.4 Predicted performance of a joint element under constant normal stress condition subjected to monotonic simple shear

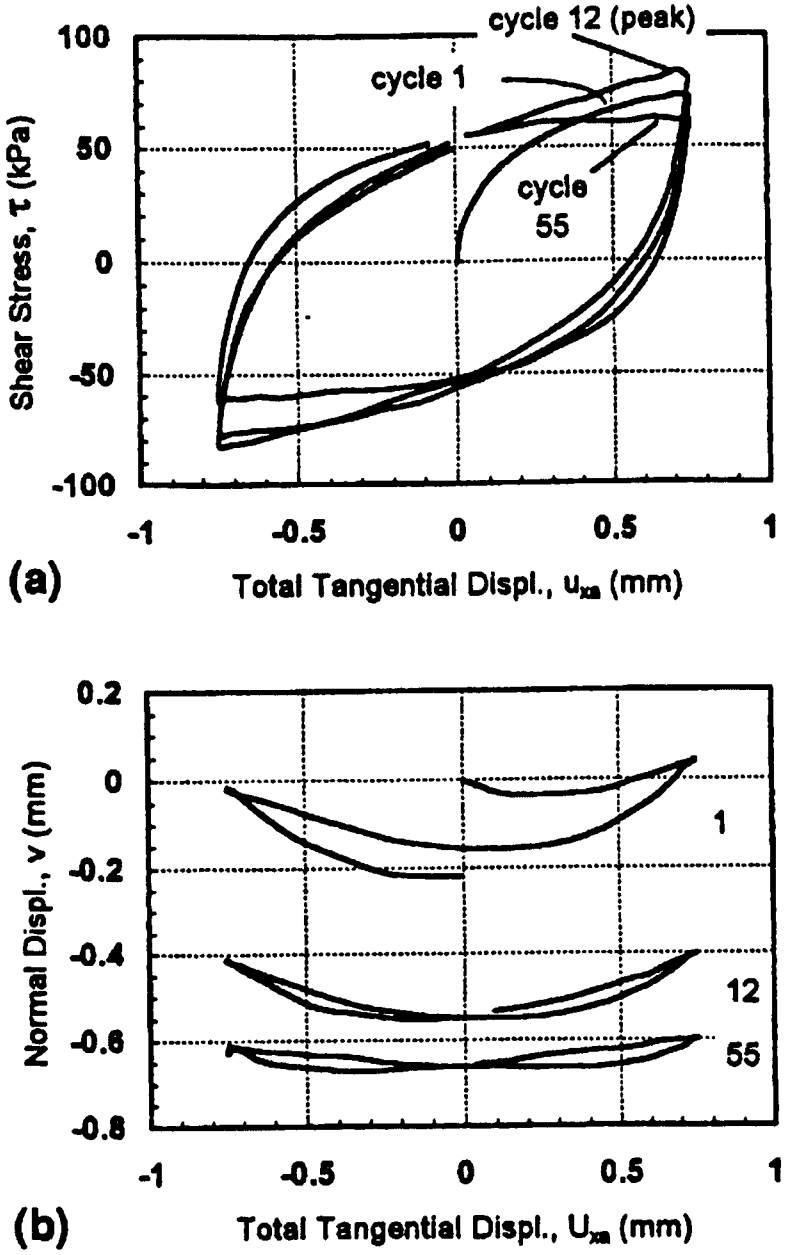

Fig. 3.5 Experimental results obtained from cyclic shear test under constant normal stress condition (Fakharian and Evgin, 1997)

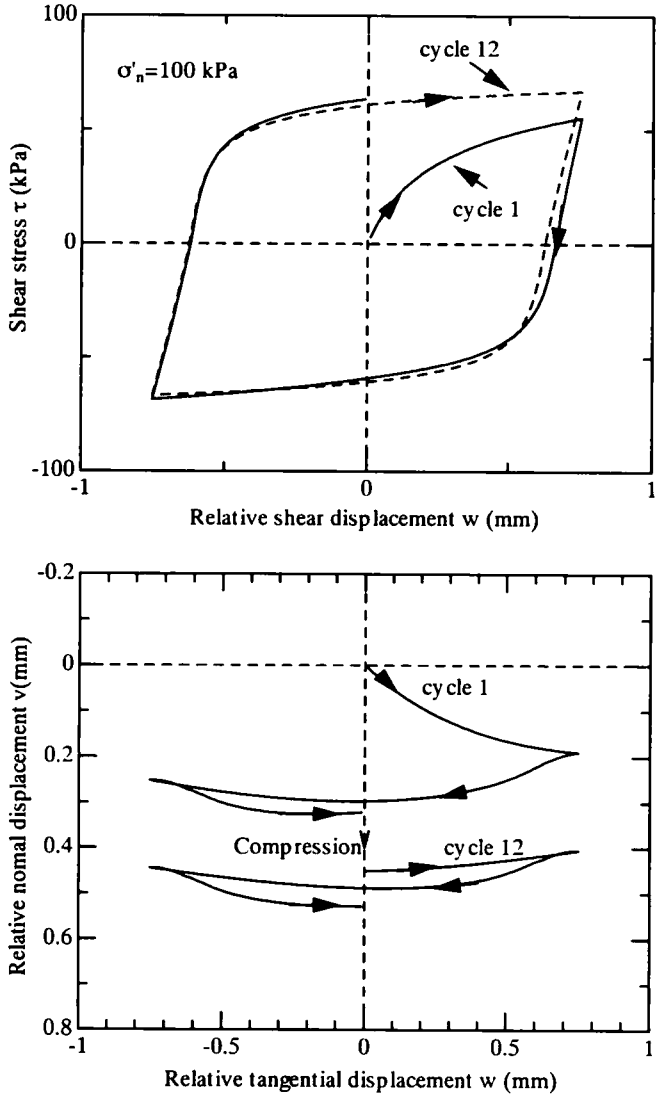

Fig. 3.6 Predicted performance of a joint element subjected to cyclic shearing under constant normal stress condition

CHAPTER 4

Discussion of dynamic fluid pressures

4.1 Introductory remarks

Saturated sand deposits in loose compaction are one of the most vulnerable environments to earthquake shaking. Extensive studies have been made of the liquefaction potential and consequences of liquefaction. However, the characteristics of dynamic or fluctuating pore pressures in a liquefied sand layer have been relatively less explored, compared with the performance of residual excess pore pressures.

In fact, there is an acute call for studies leading to a full understanding of the dynamics of liquefied soil in the vicinity of embedded rigid walls or stiff structural elements (Tsuchida, 1968; Kohama et al., 1998; among others). The interaction between soil and structural elements will become even more complex and intriguing if a layer of fluid is present over a deposit of liquefiable soil. With the just-mentioned in mind, we shall subsequently focus the discussion on the behavior of a submerged deposit of sand that is contained in a rigid rectangular box and is subjected to horizontal shaking. The targeted problem is simple in presentation and will serve as a sort of benchmark problem in dynamic fluid-soil interaction.

Three interrelated approaches were made in the present study. The first is finite-element modeling for integrated treatment of the fluid and soil domains. The second is an application of a two-fluid-layer theory where liquefied sand may be idealized as a heavy, inviscid fluid. The third approach is a physical one making use of centrifugal shaking-table testing. The predictions from the former two approaches will be examined in light of the performance observed in a geo-centrifuge (Sekiguchi et al., 2003).

4.2 An analytical solution for dynamic fluid pressures

If the sand is completely liquefied, it may be approximated to an incompressible, inviscid fluid with a density ρ_2 (refer to Fig. 4.1). Suppose that a rectangular container is subject to a horizontal shaking of A · sinωt, where A is the amplitude of dynamic horizontal displacement, and ω is the angular frequency of shaking. Then the basic equations in terms of the velocity potentials Φ_1 and Φ_2 in region I and region II may be expressed as

$$\frac{\partial^2 \Phi_i}{\partial x^2} + \frac{\partial^2 \Phi_i}{\partial z^2} = 0 \quad (i = 1, 2) \tag{4.1}$$

The boundary conditions involved are as follows:

$$\frac{\partial^2 \Phi_1}{\partial t^2} + Ng\frac{\partial^2 \Phi_1}{\partial z} = 0 \quad \left(\text{on } -\frac{l}{2} < x > \frac{l}{2},\ z = 0\right) \tag{4.2}$$

$$\frac{\partial \Phi_2}{\partial z} = 0 \quad \left(\text{on } -\frac{l}{2} < x > \frac{l}{2},\ z = -(h_1 + h_2)\right) \tag{4.3}$$

$$\rho_1 \frac{\partial \Phi_1}{\partial t} + \rho_1 Ng\eta_2 = \rho_2 \frac{\partial \Phi_2}{\partial t} + \rho_2 Ng\eta_2 \quad \left(\text{on } -\frac{l}{2} < x > \frac{l}{2},\ z = -h_1\right) \tag{4.4}$$

$$\frac{\partial \eta_2}{\partial t} = \frac{\partial \Phi_2}{\partial z} = \frac{\partial \Phi_1}{\partial z} \quad \left(\text{on } -\frac{l}{2} < x > \frac{l}{2},\ z = -h_1\right) \tag{4.5}$$

$$\frac{\partial \Phi_i}{\partial x} = -A\omega\cos\omega t \quad (i = 1,2) \quad \left(on\ \ x = -\frac{l}{2}, \frac{l}{2},\ -(h_1 + h_2) < z < 0\right) \tag{4.6}$$

Here Ng is the centrifugal acceleration, h_1 is the thickness of fluid I, h_2 is the thickness of liquefied soil, l is the width of the rectangular container, ρ_1 is density of fluid in region I and η_2 is surface displacement of completely liquefied sand. Equation (4.2) is the dynamic and kinematic boundary conditions on the free surface, with generation of surface gravity waves being taken into consideration. Equation (4.3) represents impermeable condition on the base of the container. Equations (4.4) and (4.5) are the dynamic and kinematic boundary conditions for the interface of the two fluid layers. Equation (4.6) represents the compatibility condition between the side walls of the container and the fluid in it.

The solutions that satisfy the basic equations described above are obtained as follows.

$$\Phi_1 = -A\omega(\cos\omega t)x + \sum_{n=0}^{\infty}\left[A_n \sin\frac{(2n+1)\pi x}{l}\left\{B_n \cosh\frac{(2n+1)\pi z}{l} + \sinh\frac{(2n+1)\pi z}{l}\right\}\right]\cos\omega t \tag{4.7}$$

$$\Phi_2 = -A\omega(\cos\omega t)x + \sum_{n=0}^{\infty}\left[C_n \cosh\left\{\frac{(2n+1)\pi(z + h_1 + h_2)}{l}\right\}\sin\frac{(2n+1)\pi x}{l}\right]\cos\omega t \tag{4.8}$$

where

$$A_n = A\omega^3 \frac{4l(-1)^n}{\pi^2(2n+1)^2} \cdot \frac{1}{\left\{B_n\omega^2 - Ng\dfrac{(2n+1)\pi}{l}\right\}} \tag{4.9}$$

$$B_n = \frac{\left(\dfrac{\rho_2}{\rho_1} - 1\right)Ng\dfrac{(2n+1)\pi}{l} + \left[\omega^2\dfrac{\rho_2}{\rho_1}\cdot\dfrac{1}{\tanh\{(2n+1)\pi h_2\ l\}} - \left(\dfrac{\rho_2}{\rho_1} - 1\right)Ng\dfrac{(2n+1)\pi}{l}\right]\cosh\dfrac{(2n+1)\pi h_1}{l} + \omega^2\sinh\dfrac{(2n+1)\pi h_1}{l}}{\left(\dfrac{\rho_2}{\rho_1} - 1\right)\omega^2 + \left[\omega^2\dfrac{\rho_2}{\rho_1}\cdot\dfrac{1}{\tanh\{(2n+1)\pi h_2\ l\}} - \left(\dfrac{\rho_2}{\rho_1} - 1\right)Ng\dfrac{(2n+1)\pi}{l}\right]\sinh\dfrac{(2n+1)\pi h_1}{l} + \omega^2\cosh\dfrac{(2n+1)\pi h_1}{l}} \tag{4.10}$$

$$C_n = \frac{A_n\left[-B_n \sinh\left\{(2n+1)\pi h_1 / l\right\} + \cosh\left\{(2n+1)\pi h_1 / l\right\}\right]}{\sinh\left\{(2n+1)\pi h_2 / l\right\}} \tag{4.11}$$

Then the dynamic pressure fields in the fluid regions I and II may be obtained as

$$p_1 = \rho_1 \cdot \frac{\partial \Phi_1}{\partial t} \tag{4.12}$$

$$p_2 = \rho_2 \cdot \frac{\partial \Phi_2}{\partial t} \tag{4.13}$$

When $\rho_2=\rho_1$, the two-layer-fluid solution reduces to the solution for a one-layer fluid (Graham and Rodriguez 1952). These solutions allow for the generation of surface gravity waves on the free surface and differ from Westergaard's (1933) treatment where only the condition p=0 was imposed on the free surface.

4.3 Centrifugal Shaking-Table Testing

A series of centrifugal shaking-table tests were performed on deposits of loosely packed sand with a sea of silicone oil over the sand surface. All the shaking-table tests were conducted at a steady-state centrifugal acceleration of 30 gravities. Viscous scaling was introduced so as to match the time scaling laws of vibration and consolidation. Specifically, silicon oil with a viscosity coefficient of 30cSt was used as the pore fluid as well as the exterior fluid. Each centrifuge model was subjected to 20 cycles of horizontal, sinusoidal excitation at a frequency of 30Hz, with a peak acceleration of about 3 gravities.

A typical cross-section of the centrifuge model is shown in Fig. 4.2, together with the arrangement of the transducers used.

4.4 Comparison between predicted and measured performances

4.4.1 Statement of the problem

Consider a fluid and soil system in a rigid rectangular container that is subjected to horizontal sinusoidal shaking (Fig. 4.3). The fluid domain, with free surface AF, is represented by region ABEF. This is underlain by a deposit of saturated liquefiable sand (region BCDE). The side boundaries ABC and FED are assumed to be smooth and impermeable. The bottom boundary CD is assumed to be impermeable. Since the base of the container is assumed to be a fully rough boundary, no relative motions of soil particles occur on it.

The entire system will deform in plane strain condition. Dynamic fluid pressures will develop in the fluid and soil domains. It will be of prime interest to see how they interact while the soil domain undergoes liquefaction due to build-up of residual pore pressures.

The elastoplastic constitutive parameters for sand that were used in the present study are listed in Table 4.1.

The values of ρ_1 andρ_2 used in the subsequent two-layer-fluid solutions are as follows:ρ_1=1000kg/m^3; ρ_2= 1820kg/m^3.

4.4.2 Evolutions of excess pore pressures and effective stress states in sand during shaking

The predicted and measured evolutions of excess pore pressure in the center of the sand deposit (element 1) are shown in Fig. 4.4. It is seen that the excess pore pressure increased rapidly in the early stage of shaking and developed to a value very close to the level of the initial vertical effective stress σ'_{zz0}, indicating the occurrence of liquefaction there. The fluctuations in the excess pore pressure in the liquefied soil (element 1) were very small in value. In contrast, the excess pore pressures in the proximity of the wall of the container developed with significant fluctuations as shown in Fig. 4.5. The predicted accumulation of the residual pore pressure and the marked pressure fluctuations correspond well to the observed performance.

The predicted effective stress path that element E1 followed, is shown in Fig. 4.6(a). It is seen that the mean effective stress decreased markedly in the early stage of shaking, and then the effective stress path crossed the phase transformation line(PTL) from below, exhibiting the tendency for dilatancy. Further cyclic shearing was sufficient, however, to bring the state of effective stress of this element to a point very close to the origin of the diagram, indicating the occurrence of liquefaction there. Element E2 located in the proximity of the wall of the container exhibited essentially the same pattern of effective stress changes as Element E1, confirming the occurrence of liquefaction over a wide area in the soil domain.

4.4.3 Spatial distributions of dynamic fluid pressures in the fluid and soil domains

The horizontal distributions of the amplitudes of fluctuating pore pressure in the liquefied soil are typified in Fig. 4.7 along a soil horizon z=-0.125m. The amplitude of the fluctuating pore pressure is largest on the side walls (x=±0.2m), decreases with the distance away from the wall and becomes zero at the center of the sand deposit (x=0). The predicted performances from the finite-element analyses and two-layer-fluid theory compare favorably with the measured performance from the centrifugal shaking table tests.

The distributions, with depth, of the amplitudes of dynamic fluid pressure along the side walls(x=±0.2m) are shown in Fig. 4.8. The dotted line in this figure represents the theoretical profile of the dynamic fluid pressure if the fluid domain were underlain by a rigid,

impermeable base at z=-0.06m. It is noteworthy that the dynamic fluid pressure on the fluid-soil interface increased appreciably due to the dynamic interaction between the liquefied sand and the overlying fluid.

4.5 Conclusions

The principal results obtained from the analyses and centrifugal shaking table tests may be summarized as follows:

1. The elastoplastic finite-element modeling for the submerged deposit of sand captured the build-up of seismically induced residual pore pressures leading up to liquefaction and the significant dynamic pressure changes following liquefaction.
2. There occurred a marked interaction between the liquefied sand and the overlying fluid, enhancing the dynamic pressure changes on the fluid-soil interface.
3. The predicted dynamic pressure changes from the finite-element analyses and two-layer-fluid theory compare favorably with those measured in the centrifugal shaking-table tests on the fluid and saturated sand systems.

References

Graham, E.W. and Rodriguez, A.M. (1952). Characteristics of fuel motion which affect airplane dynamics, *Jour. Applied Mechanics*, Vol. 19, No.3, 381-388.

Kohama, E., Miura, K., Yoshida, N., Ohtsuka, N. and Kurita, S. (1998). Instability of gravity type quay wall induced by liquefaction of backfill during earthquake, *Soils and Foundations*, Vol. 38, No. 4, 71-83.

Sekiguchi, H., Kim, H., Miyamoto, J. and Tomohiro, Y. (2003). Dynamic interaction between fluid and liquefying soil under earthquake shaking, *Proc. 12th Asian Regional Conf. On Soil Mech. Geotech. Eng.*, Singapore, Vol. 1, 331-334.

Tsuchida, H. (1968). Pressure of liquefied sand deposits affecting wall during shaking, *Tsuchi to Kiso, JGS,* No.526, 3-10 (in Japanese).

Westergaard, H. M. (1933). Water pressures on dams during earthquakes, *Trans. ASCE*, Vol.98, 418-433.

Table 4.1 The elastoplastic constitutive parameters for sand

Mg	M_f	α	β_0	β_1	H_0^*	H_{u0} (kPa)	γ_u	γ_D	K_0	k m/s
1.2	0.44	0.35	20	0.04	1500	8000	4	3	0.56	0.0001

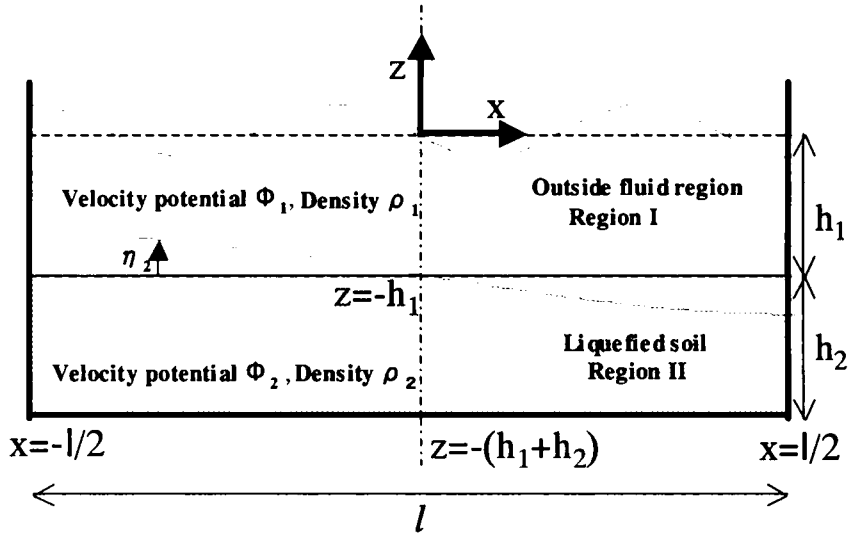

Fig. 4.1 Two-layer fluid in a rigid rectangular container subjected to horizontal shaking

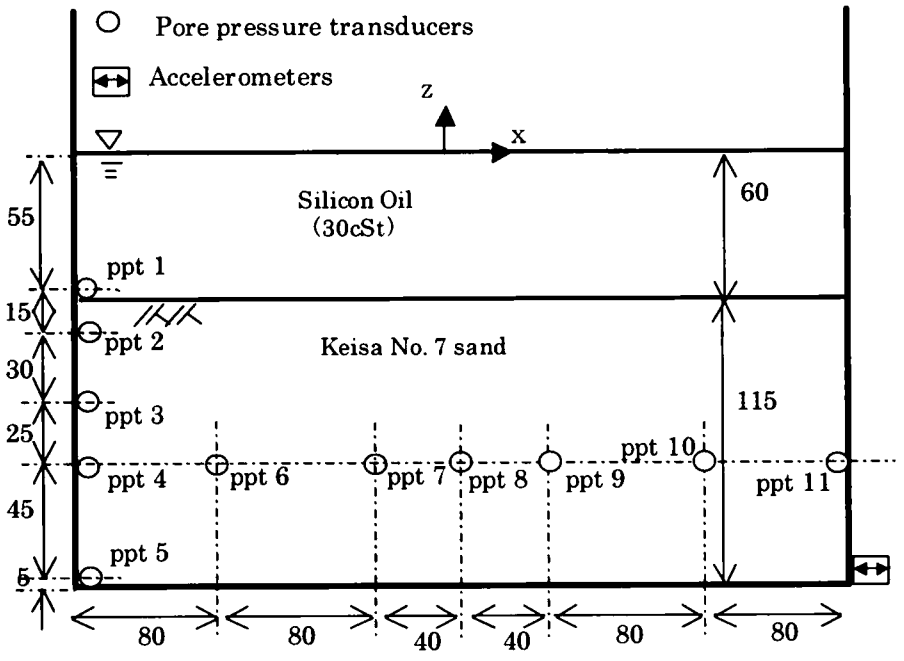

Fig. 4.2 Cross-section of a centrifuge model subjected to horizontal shaking

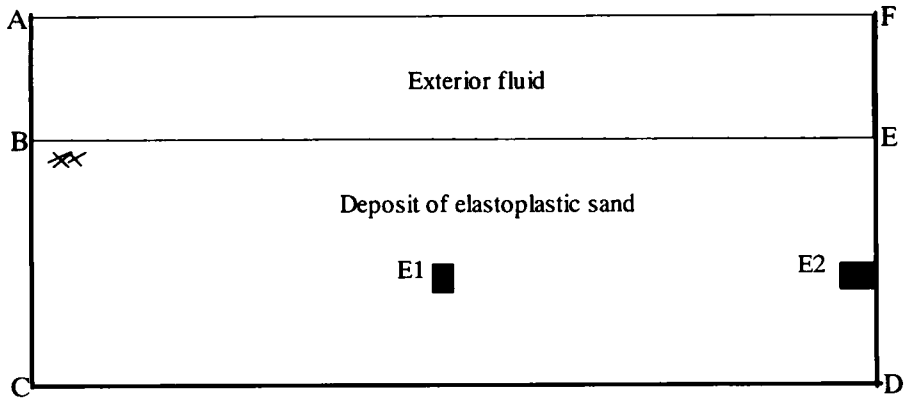

Fig. 4.3 A two-layer system in a rigid rectangular container subjected to horizontal shaking, with two representative elements of soil indicated

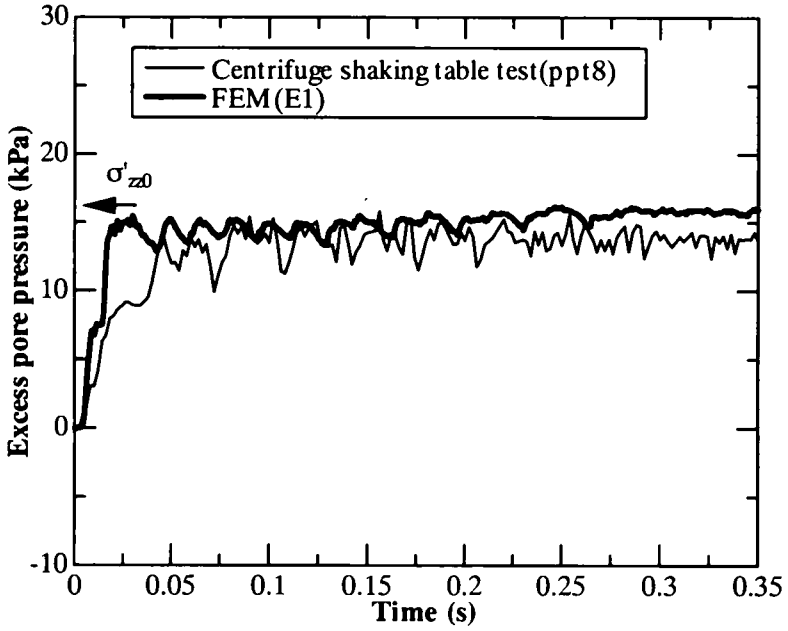

Fig. 4.4 Predicted and measured time histories of excess pore pressure in the center of sand deposit

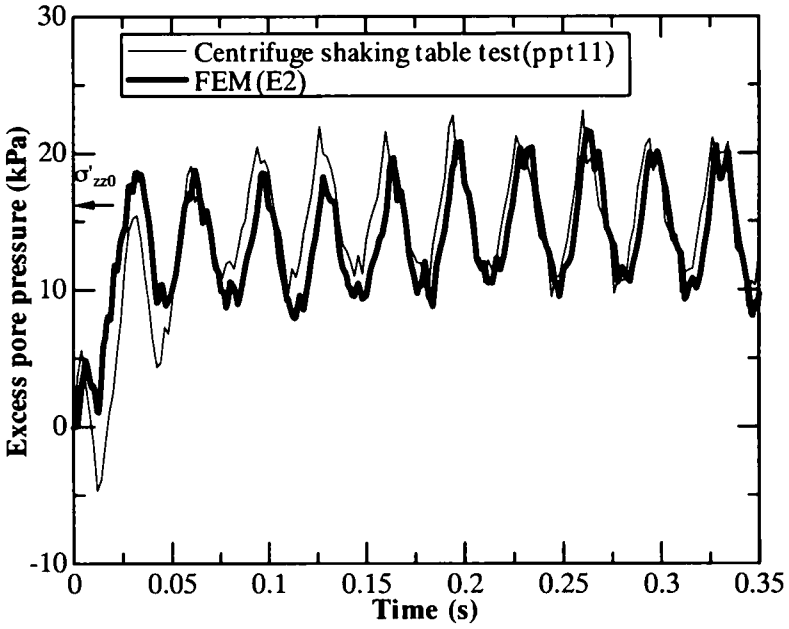

Fig. 4.5 Predicted and measured time histories of excess pore pressure in the proximity of the wall of the container

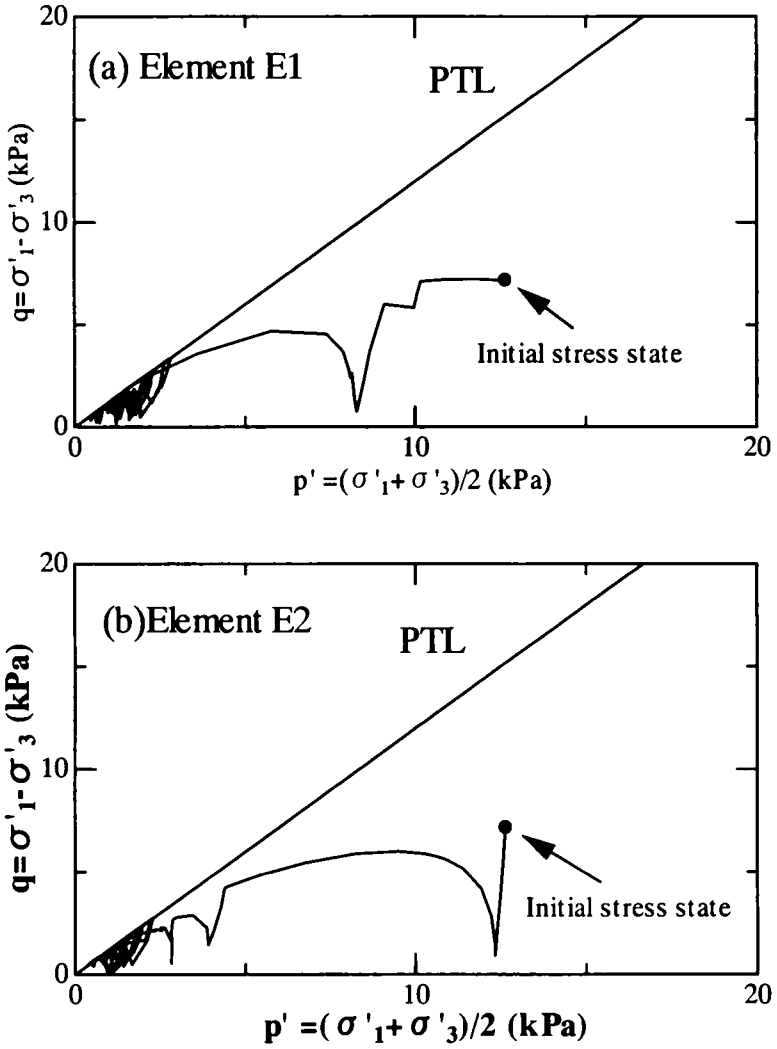

Fig. 4.6 Predicted effective stress paths in elements E1 and E2 leading up to liquefaction

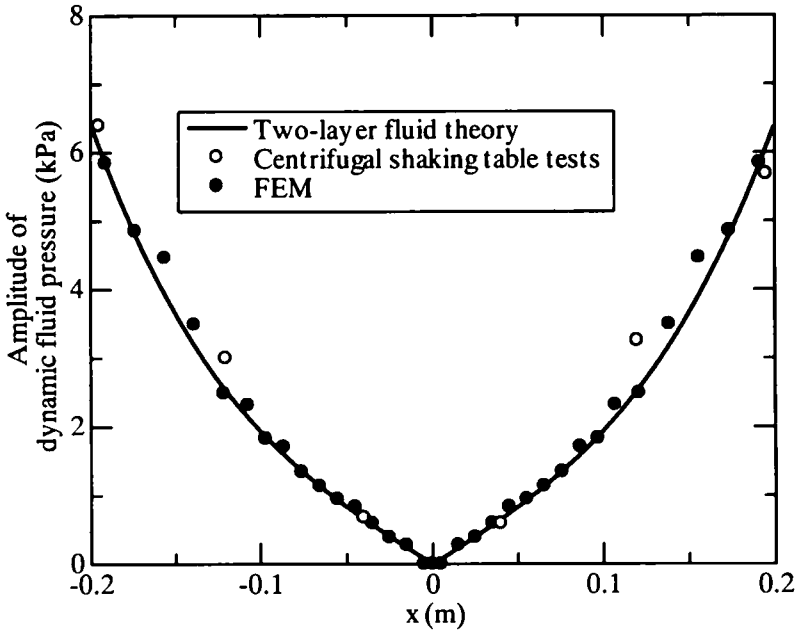

Fig. 4.7 Horizontal distributions of dynamic fluid pressures at z=-0.125m

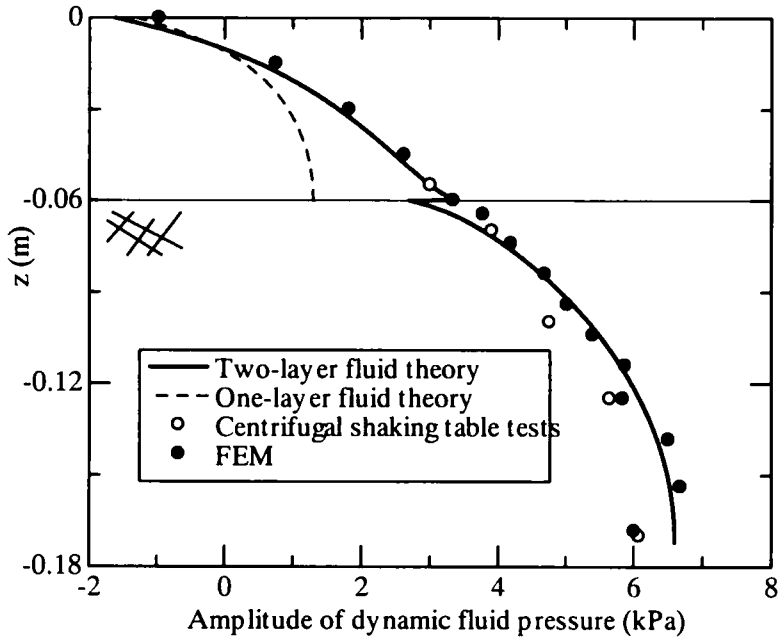

Fig. 4.8 Vertical distributions of dynamic fluid pressures on the wall

PART II

PERFORMANCE OF COMPOSITE BREAKWATERS UNDER SHAKING

CHAPTER 5

Performance of composite breakwater models in centrifugal shaking-table tests

-Comparison between analyses and experimentations-

5.1 Introductory remarks

The seismic stability of breakwater systems has received increasing attention from engineers. One of the related key issues is the need to develop a rational way in which one can predict the seismic plastic deformation of composite breakwaters that rest on liquefiable sand deposits. Note that composite breakwaters are a type of gravity foundations, and their seismic behavior has relevance to discussing the settlement behavior of spread foundations on land subjected to earthquake shaking.

Iai et al. (1998) performed a nonlinear, undrained effective stress analysis to investigate the behavior of composite breakwaters under earthquake shaking. The calculated results indicate that the effective stress state of a typical soil element beneath the caisson structure had been somewhere between the phase transformation and failure lines prior to the earthquake shaking, and that during the shaking, it fluctuated in the range closer to the failure line. The state of zero effective stress was not reached, but an appreciable amount of vertical compression ensued in the foundation sand due to a sort of repeated shear failure.

Yoshimi and Tokimatsu (1977) paid attention to the settlement of buildings on saturated sand during earthquake shaking (refer to Fig. 5.1(a)). They performed a series of shaking table tests on models of rigid structures that were placed on saturated sand, and observed the pore pressure development, up to liquefaction in the sand near the structure. Also, they pointed out some factors, which influenced the settlement of buildings during the 1964 Niigata earthquake.

Kawasaki et al. (1998) performed a series of centrifuge shaking table tests on sand-supported with isolated footings for power transmission lines (refer to Fig. 5.1(b)). The occurrence of differential settlements among isolated footings was a focus of their study. The

experimental results indicated that the footing for the power transmission tower settled considerably when the soil beneath the footing was thick and underwent seismic liquefaction.

The author considers that more developments are necessary to clarify the problem of the seismic plastic deformation of structure that rest on liquefiable sand deposits. With the above-mentioned in mind, the emphasis of the following sections will be placed on investigating into the effect of the degree of compaction of the foundation sand, through physical numerical and modeling (Kim and Sekiguchi, 1999).

5.2 Centrifuge shaking-table testing

A range of shaking-table tests was conducted on composite breakwater models resting on sand, at a steady-state centrifugal acceleration of 30 gravities. Viscous scaling was introduced so as to match the time scaling laws of vibration and consolidation. Specifically, silicon oil with a viscosity coefficient of 30cSt was used as the pore fluid as well as the exterior fluid. Each centrifuge model was subjected to 20 cycles of horizontal, sinusoidal excitation at a frequency of 30Hz, with a peak acceleration of about 3 gravities.

A typical cross-section of the centrifuge model is shown in Fig. 5.2, together with the arrangement of the transducers used. Fine-grained sand (Silica sand No. 7) was used for the foundation soil, and coarse-grained sand (Silica sand No.4) was used for the mound that supported the caisson structure. The specific gravity, the minimum void ratio and the maximum void ratio of Silica sand No. 7 are 2.69, 0.67 and 1.15, respectively. The sand foundations were formed to achieve specified degrees of compaction. A trapezoidal mound was made on a deposit of sand, which had been consolidated for about 30 minutes in a steady-state centrifugal acceleration. The mound was 120mm wide at the crest, 35mm high and had side slopes of 1:1.5. The mound was heavily densified. A rigid rectangular caisson measuring 60mm x 100mm x 100mm with a mass of 1.42kg rested on the mound. Two laser-type displacement gauges were used to measure the vertical displacements at two points on top of the caisson. Another laser-type displacement gauge was used to measure the horizontal displacement of the caisson at a specified elevation.

5.3 Analysis of seismic deformation behavior of composite breakwaters in centrifuge

5.3.1 Problem definition

A series of finite-element analyses were performed with reference to the centrifugal shaking-table tests described above. For purposes of presentation, all the predictions were made on a prototype scale that corresponded to the centrifuge model. A finite-element mesh used for dynamic analyses is shown in Fig. 5.3. The side boundaries were set to be smooth

and impermeable. The bottom boundary was fixed and impermeable. The fluid domain exists on either sides of caisson.

The material parameters used in the present case studies are shown in Table 5.1. We selected the constitutive parameters following the procedure, which was in Chapter 2. The normal and tangential stiffness for joint elements were adopted as follows: $Kn=Ks=1\times10^{4}\left(\sigma_n^{'}\right)^{0.4}$ where $\sigma_n^{'}$ represents normal effective stress that develops in a joint element.

5.3.2 Acceleration response

The predicted performance from a case with M_f=0.543 is presented in Fig. 5.4 together with the measured performance with Dr=52%, with report to the horizontal acceleration waveforms at the crest and at node N5 in the foundation sand. In this figure the input waveform of horizontal acceleration, specified at the base of the rigid container, is also plotted. It is seen that the predicted time histories of response accelerations at node N5 in the foundation sand compare favorably with the observed results.

5.3.3 Seismic plastic deformation of sand foundations

Predicted, final plastic deformations of two composite breakwater systems after shaking are shown in Fig. 5.5. The caisson in either case settled almost vertically, and the supporting sand below the caisson compressed markedly. Vertical compression was accompanied by the lateral extension of the soil beneath the caisson structure and the upheaval of the ground surface in the free field. The predicted pattern of plastic deformation corresponded well to the observed results. Note that the settlement of the caisson decreased with increasing in relative density Dr of the foundation sand.

Observed and predicted settlements of the two edges on top of a caisson are plotted in Fig. 5.6 against time during the main shaking. It is seen that the caisson rocked almost evenly and settled significantly. The predicted distributions, with depth, of the lateral strain ε_{xx} and the vertical strain ε_{yy} in the foundation soil along the centerline of the caisson after ten cycles of shaking are shown in Fig. 5.7 for the four different values of M_f indicated. It is noteworthy that as the value of parameter M_f becomes smaller, the vertical compression in the foundation sand developed more markedly. Another interesting aspect of the seismic plastic deformation of the foundation sand is that it occurred under nearly constant-volume conditions. This aspect proves to be clearer if one compares the profiles of lateral strains ε_{xx} with those of vertical strains ε_{yy} in Fig. 5.7.

The effects of varying the M_f value of the foundation soil upon the predicted plastic

settlement of the caisson are summarized in Fig. 5.8. Here the caisson settlement S after ten cycles of shaking is normalized by dividing by the thickness D of the foundation soil and is plotted against the value of parameter M_f adopted.

The question now arises as to how one can compare the predicted performance with the measured performance from the centrifugal shaking-table tests, on a quantitative basis. Remember that a total of eight shaking-table tests were performed on the sand beds with different values of relative density Dr. One can then notice that essentially the same pattern of soil behavior holds true for the predicted relationship between S/D and Dr when the afore-mentioned correlation, Eq. (2.34), holds true herein. It is evident that a procedure for selecting the constitutive parameters was physically sound.

5.3.4 Excess pore pressure responses and effective stress states in the foundation sand

The predicted (M_f=0.543) and the measured (Dr=52%) time histories of excess pore pressure in the free field are shown in Fig. 5.9. It is seen that the excess pore pressure increased rapidly in the early stage of the main earthquake shaking. Then the excess pore pressure developed to a value very close to the level of the initial vertical effective stress. The predicted accumulation of residual pore pressure corresponds well to the observed performance.

The predicted (M_f=0.543) and the measured (Dr=52%) time histories of excess pore pressure in the foundation sand beneath the caisson are shown in Fig. 5.10. It is interesting to that negative pore pressures developed in the early stages of shaking.

In order to fully understand the excess pore pressure responses in the free field and in the foundation sand directly below the composite breakwater, let us look at the effective stress changes plotted in Fig. 5.11 and Fig. 5.12. In the free field, the mean effective stress decreased markedly in the first two loading cycles and then the effective stress path crossed the phase transformation line, exhibiting the tendency for dilatancy (Fig. 5.11).

In the foundation sand directly below the composite breakwater, the soil element E1 was initially in the state of anisotropic stresses (refer to Fig. 5.12). Due to the earthquake shaking, the state of effective stress reached the phase transformation line (PTL) and varied in a region close to the phase-transformation line. Note that the negative excessive pore pressure developed when the stress point crossed and rose up along the phase transformation line. Also, it is noteworthy that each time when the effective stress path crossed the phase transformation line from below, the foundation sand underwent a significant vertical compression, together with a significant horizontal extension (refer to Fig. 5.15).

5.3.5 Energy dissipation characteristics

Let E be the accumulated energy dissipation for a element. Namely,

$$E = \int \sigma_{ij}' d\varepsilon_{ij}^{p} = \int \left(p' dv^{p} + q d\varepsilon^{p} \right) \tag{5.1}$$

where

$$p' = (\sigma_1' + \sigma_3')/2 , q = (\sigma_1' - \sigma_3'), dv^{p} = (d\varepsilon_1^{p} + d\varepsilon_3^{p}), d\varepsilon^{p} = (d\varepsilon_1^{p} - d\varepsilon_3^{p})/2 \tag{5.2}$$

The mechanical work W done in a soil element may be expressed as

$$W = \int \sigma_{ij}' d\varepsilon_{ij} = \int \left(p' dv + q d\varepsilon \right) \tag{5.3}$$

The time history of energy dissipation in a soil element during the first 1.5 second of shaking is shown in Fig. 5.13, together with the effective stress path that the element followed during the period. Note that energy dissipation was significant in period (1)-(2), (4)-(5) and (7)-(8) during all of which the effective stress path crossed PTL and the increased shear resistance due to dilatancy.

The spatial distributions of energy dissipation in the entire system over one cycle of shearing are shown in Fig. 5.14. In the foundation sand directly below the caisson, energy dissipation per unit volume is significant, in comparison with energy dissipation in the free field. This may be ascribed to the difference in soil states.

5.4 Discussion

Let us now discuss the settlement mechanism of the composite breakwaters. The seismic plastic deformation of the foundation sand occurred under nearly constant-volume conditions ($\varepsilon_v = 0$) through comparing the profiles of lateral strains ε_{xx} with those of vertical strains ε_{yy} in Fig. 5.7. Schematic shear deformation of soil element beneath the caisson for the situation, $\varepsilon_v = 0$, is shown in Fig. 5.15. The soil elements beneath the caisson undergo significant vertical compression that was accompanied by significant lateral expansion. The settlement mechanism of composite breakwaters is explained below using elastoplastic constitutive model.

Vertical compression increment $d\varepsilon_{yy}$ for plane strain cyclic shear under undrained condition ($\varepsilon_{xx} + \varepsilon_{yy} = 0$) may be expressed as

$$d\varepsilon_{yy} = \frac{d\varepsilon_{yy} - d\varepsilon_{xx}}{2} \tag{5.4}$$

For elastoplastic constitutive relations, deviator strain increment may be expressed as

$$\frac{d\varepsilon_{yy} - d\varepsilon_{xx}}{2} = \frac{d\varepsilon^{e}_{yy} - d\varepsilon^{e}_{xx}}{2} + \frac{d\varepsilon^{p}_{yy} - d\varepsilon^{p}_{xx}}{2} \tag{5.5}$$

where

$$\frac{d\varepsilon^{e}_{yy} - d\varepsilon^{e}_{xx}}{2} = \frac{1}{4G} \cdot \left(d\sigma'_{yy} - d\sigma'_{xx} \right) \tag{5.6}$$

$$\frac{d\varepsilon^{p}_{yy} - d\varepsilon^{p}_{xx}}{2} = \frac{1}{H \cdot \left| \partial f / \partial s \right| \cdot \left| \partial g / \partial s \right| + (K + G/3) \cdot df \cdot dg} \cdot \left(\frac{\left(\sigma'_{yy} - \sigma'_{xx} \right)^2}{q^2} \cdot \left(d\sigma'_{yy} - d\sigma'_{xx} \right) + \frac{4\left(\sigma'_{yy} - \sigma'_{xx} \right)\sigma_{yx}}{q^2} \cdot d\sigma_{yx} \right) \tag{5.7}$$

Simulation of a soil element with undrained condition

A cyclic simple shear with an amplitude of τ_{yx} =10kPa was applied to the soil element to simulate the effect of earthquake shaking. The initial axial stress difference of $\sigma'_{yy} - \sigma'_{xx}$ =29.36kPa was kept unchanged throughout the cyclic shearing. The initial stress was values in a soil element E1 beneath the caisson with M_f=0.543.

The axial strain difference, shown in Fig. 5.16(a), exhibits a cumulative increase during cyclic loading. The axial strain difference was accentuated when the effective stress path crossed the phase transformation line from below during cyclic loading (Fig. 5.16(b)). Also, axial strain difference accumulated when the value of the plasticity modulus H became small (Fig. 5.16(c)).

Seismic response analysis

Seismic response analyses, which fully takes into account fluid-soil-caisson interaction, was performed to identify the deformation mode. Time history of axial strain differences in a soil element E1 beneath the caisson as calculated from Eqs. (5.5), (5.6) and (5.7) are shown in Fig. 5.17(a) (M_f=0.543). Accumulation of elastic axial strain difference is very small in comparison with accumulation of total axial strain difference under shaking. Value of elastic axial strain difference after ten cycles of shaking was only 0.0005. Thus it can be concluded that the significant vertical settlement during shaking has induced principally by plastic

straining. Axial stress difference $\sigma'_{yy} - \sigma'_{xx}$ fluctuates under shaking (refer to Fig. 5.17(d)).

When value of stress closed to PTL (Fig. 5.17(c)), axial stress difference increase and the value of the plasticity modulus H becomes small (in region (1)-(2),(4)-(5),(7)-(8)) (Fig. 5.17(b)). Also, axial strain difference accumulated when the value of the plasticity modulus H became small. It is evident that the deformation mode was accentuated when the effective stress path crossed the phase transformation line from below and accounted for a significant portion of the accumulated settlement of the caisson during shaking.

5.5 Conclusions

The principal results obtained from the finite-element analyses and centrifuge shaking table tests may be summarized as follows:

1 The soil elements beneath the caisson underwent significant amounts of vertical compression that were accompanied by equally significant lateral expansion. The deformation mode was accentuated when the effective stress path crossed the phase transformation line from below and accounted for a significant portion of the accumulated settlement of the caisson during shaking.

2. The centrifuge shaking-table tests indicated that the settlement of the caisson decreased approximately linearly with increasing relative density Dr of the foundation sand.

3. The finite-element analyses showed that the caisson settlement decreased with increasing value of the non-associativeness parameter M_f/M_g.

4. The predicted performance of caisson settlements compares favorably with the measured performance when the M_f/M_g versus Dr relationship proposed in Eq. (2.34) is allowed for in the procedure of determination of the material parameters.

References

Iai, S., Ichii, K., Liu, H. and Morita, T. (1998). Effective stress analyses of port structures, Special Issue, No.2, *Soils and Foundations*, 97-114.

Kawasaki, K., Sakai, T., Yasuda, S. and Satoh, M. (1998). Earthquake-induced settlement of an isolated footing for power transmission structures, *Centrifuge 98*, 271-276.

Morio, S. (1992). Foundation of breakwater, *The foundation engineering and equipment*, Vol. 20, No. 5, 19-21 (in Japanese).

Kim, H. and Sekiguchi, H. (1999). Deformation mechanism of composite breakwaters under earthquake shaking, *Proc. 11th Asian Regional Conference on Soil Mechanics and Geotechnical Engineering*, 499-502.

Port Bureau Ministry of Transport, Aviation Bureau Ministry of Transport. Ports and Harbor Research Institute in the Ministry of Transport, The 3rd District Port Construction Bureau Ministry of Transport , The Fishing Port Bureau Ministry of Fisheries, Civil Engineering Works in Hyogo Pref., Kobe-City Harbors Maintenance Bureau, Kobe Port Wharf Public Corporations. (1997). Damage report about harbors facilities due to 1995 Hyougoken-Nambu earthquake, (In Japanese).

Yoshimi, Y. and Tokimatsu, K. (1977). Settlement of buildings on saturated sand during earthquakes, *Soils and Foundations*, Vol. 17, No. 1, 23-38.

Table 5.1 Material parameters used in the present case studies

(a) Foundation soil and rubble mound

Material	Mg	M_f	α	β_0	β_1	H_0^*	Hu0 (kPa)	γ_u	γ_D	K_0	k m/s
Foundation soil	1.2	0.44-0.9	0.35	20	0.04	1500	8000	4	3	0.56	0.0001
Rubble mound	1.2	0.9	0.35	20	0.04	1500	8000	4	3	0.56	1.0

(b) Joint Element

μ_g	μ_f	α_j	β_{0j}	β_{1j}	H_{0j}	H_{U0j} (kPa/m)	γ_{uj}	γ_{Dj}
0.6	0.5	0.35	0.4	20	1000	1000000.0	2	4

(a) Building

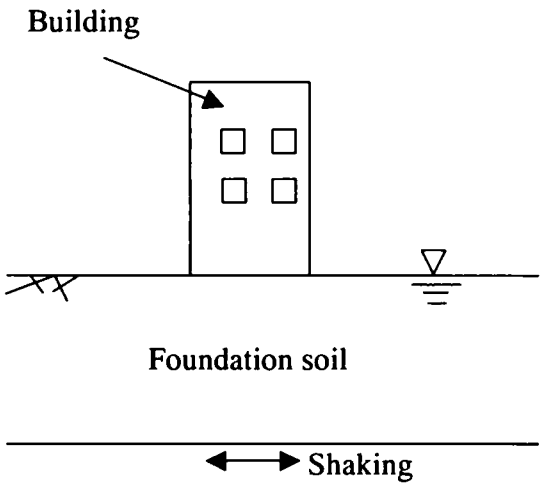

(b) Isolated footing for power transmission line

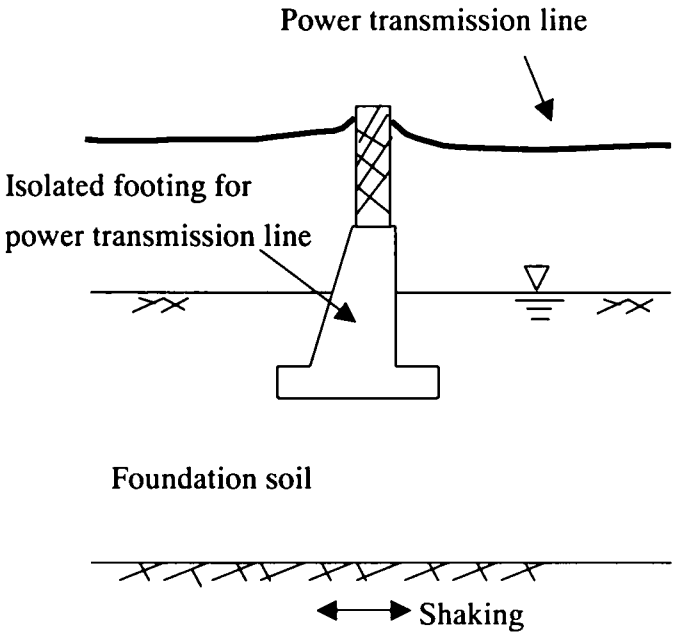

Fig. 5.1 Schematic cross sections of (a) building; and (b) isolated footing for power transmission line

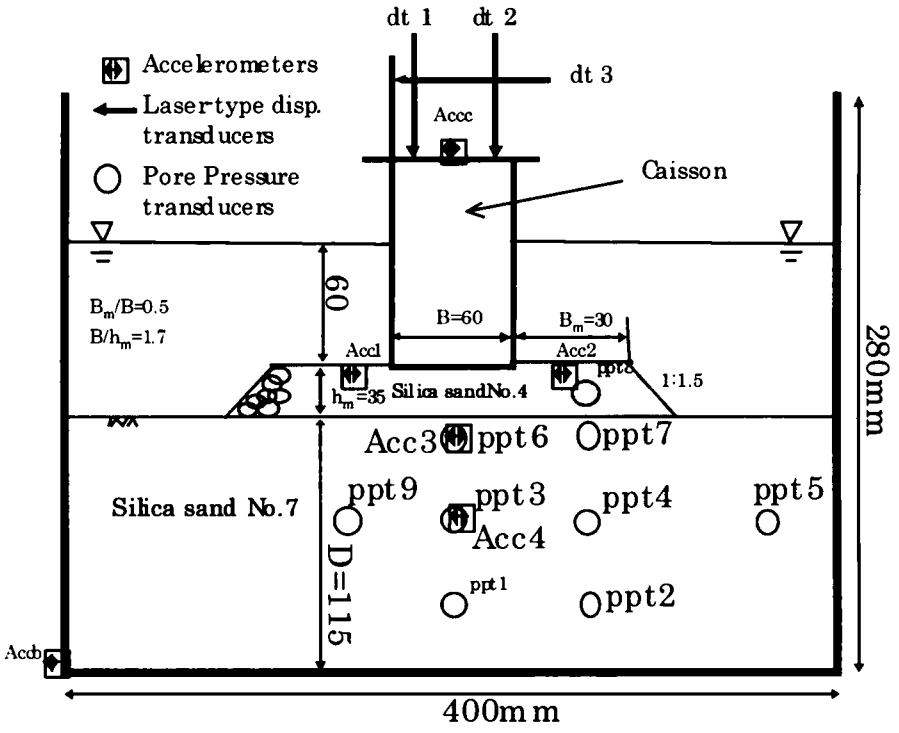

Fig. 5.2 Cross-section of a centrifuge model

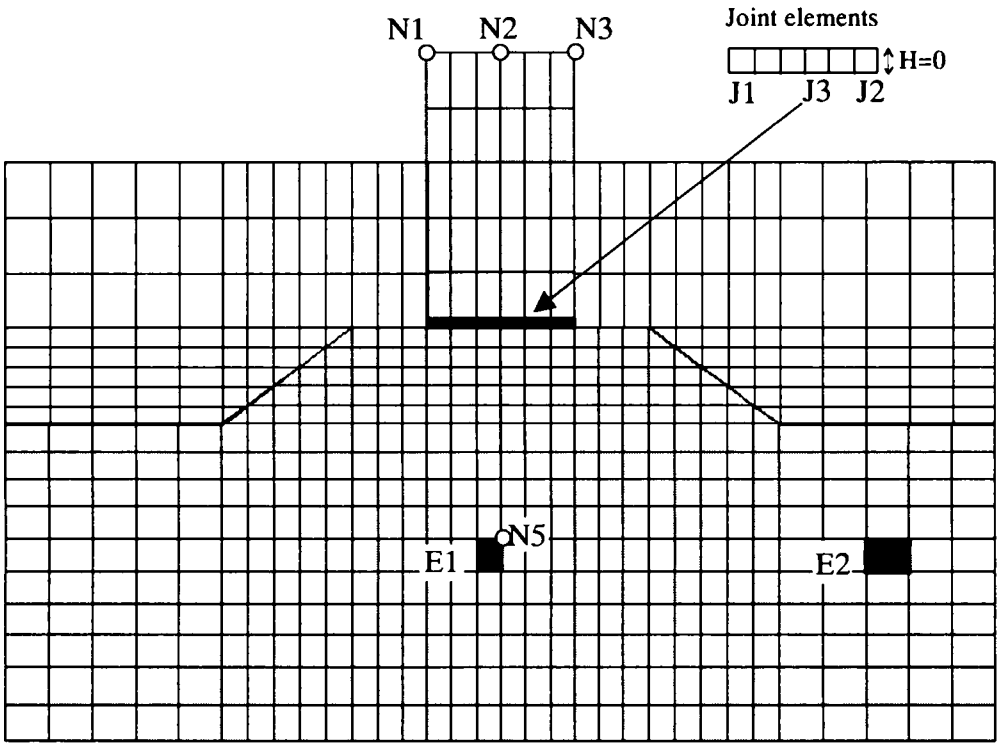

Fig. 5.3 A finite-element mesh used for dynamic analyses

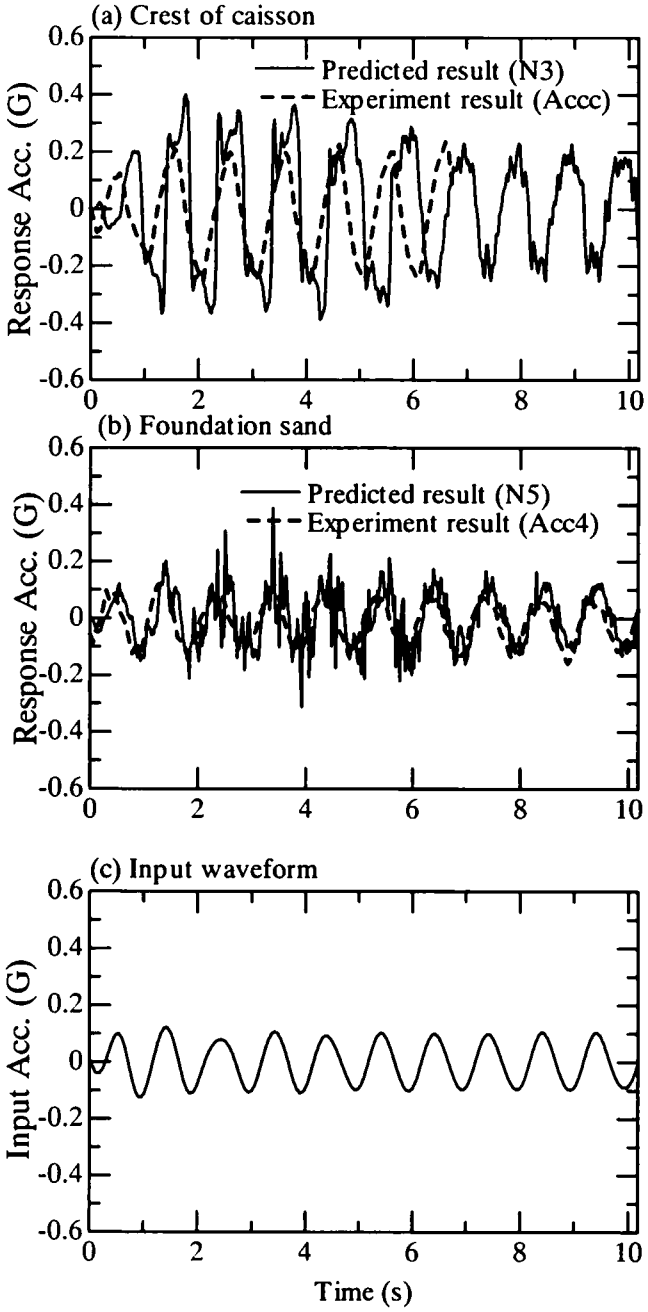

Fig. 5.4 Predicted and measured waveforms of horizontal accelerations (M_f=0.543); Dr=52%

(a)M_f=0.44

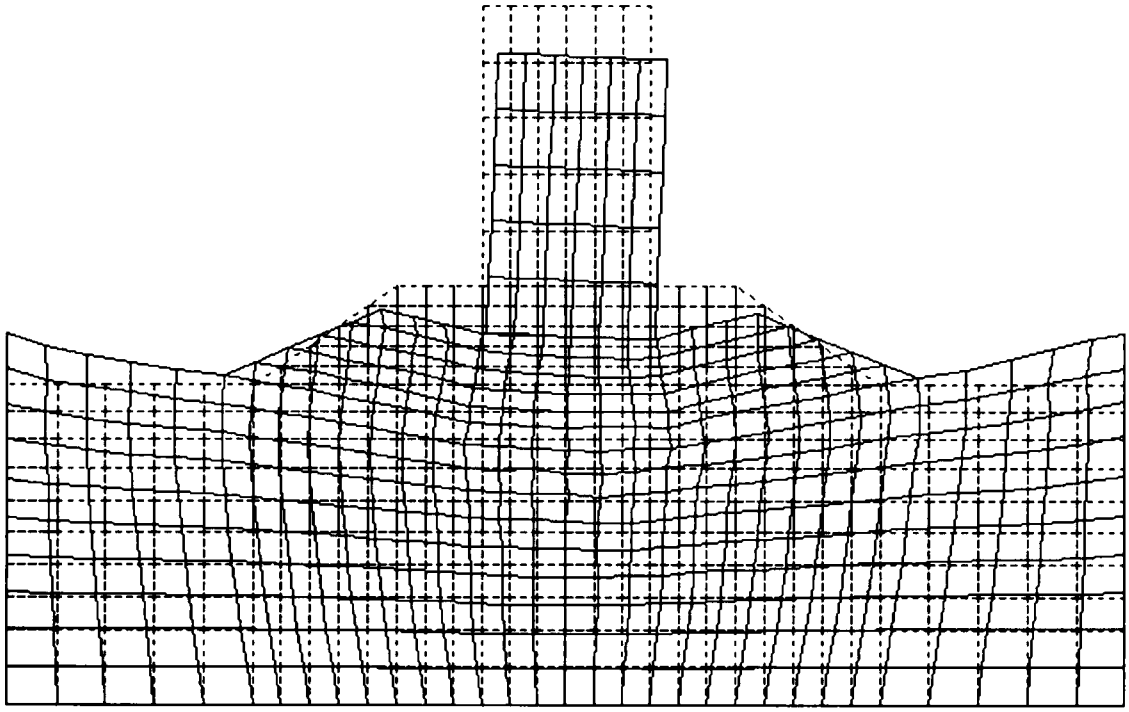

(b)M_f=0.543

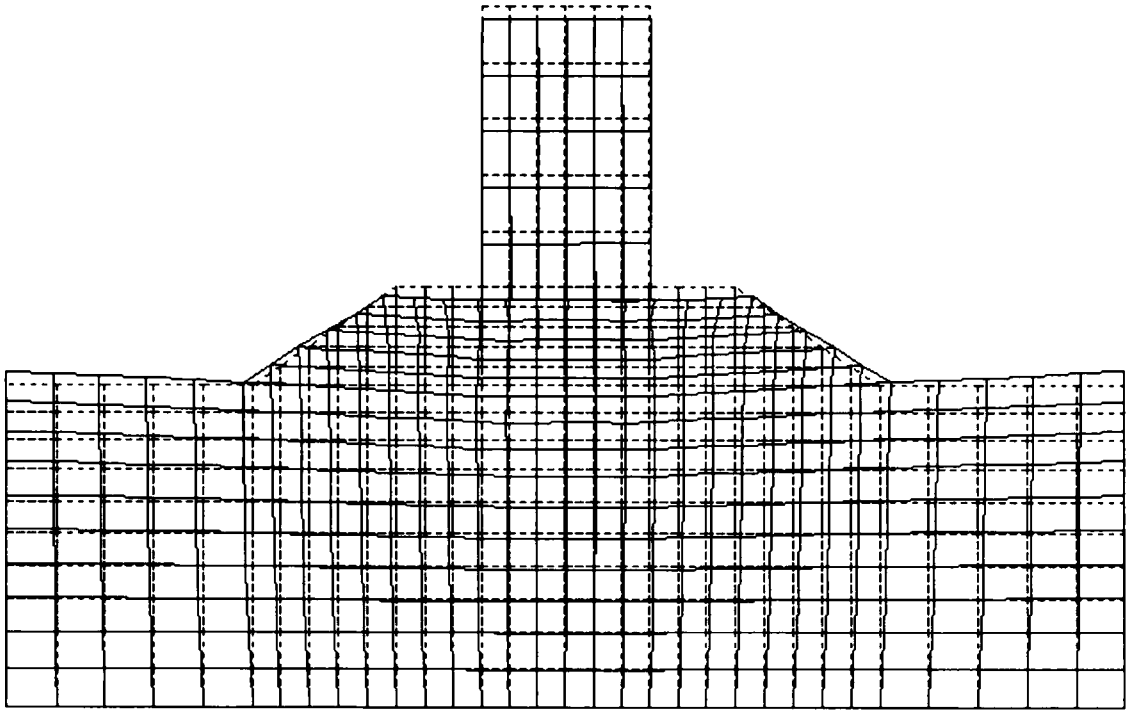

Fig. 5.5 Predicted plastic deformation of the composite breakwater model after ten cycles of shaking

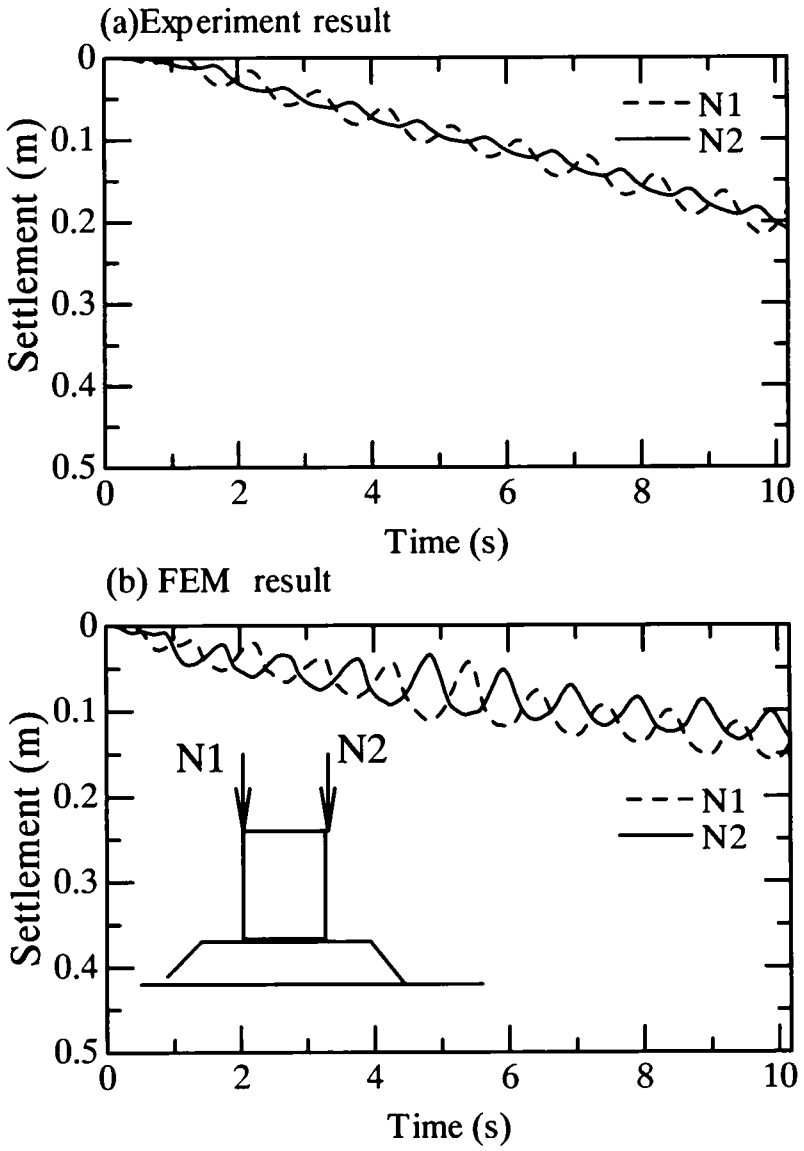

Fig. 5.6 Observed and predicted time histories of vertical displacements of the caisson top(Mf=0.543; Dr=52%)

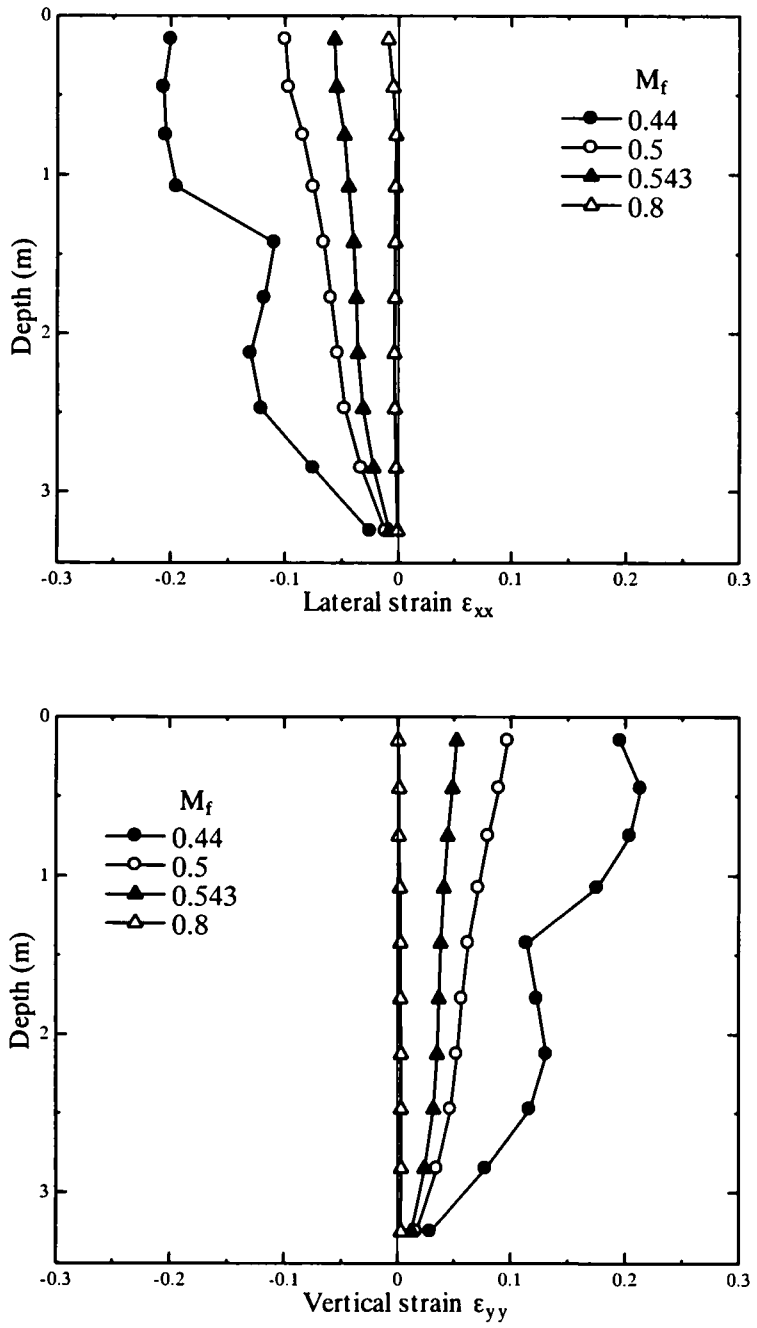

Fig. 5.7 Predicted distributions with depth of lateral and vertical strains in the foundation soil along the centerline of the caisson after ten cycles of shaking

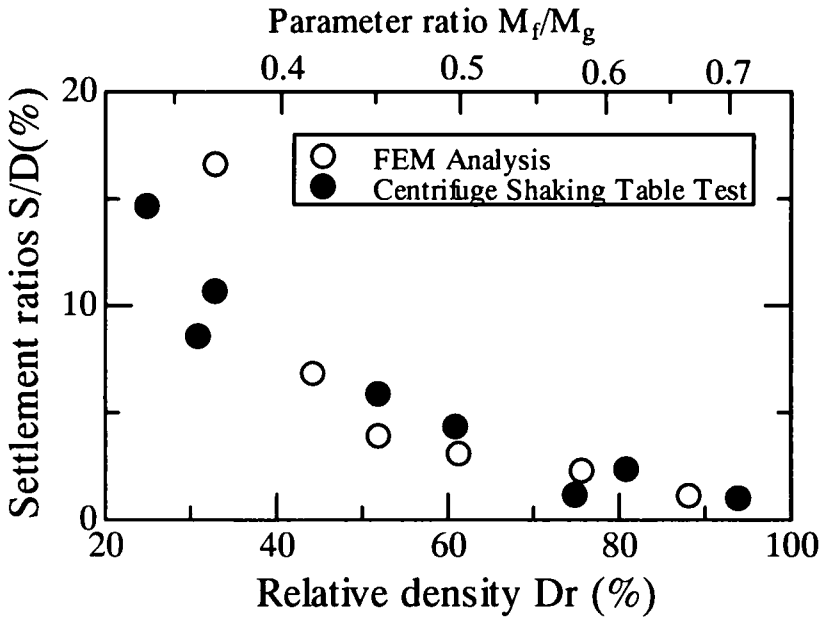

Fig. 5.8 Predicted settlement ratio (S/D) plotted against parameter M_f, together with the measured settlement ratio (S/D) plotted against the relative density of the foundation soil (after ten cycles of shaking)

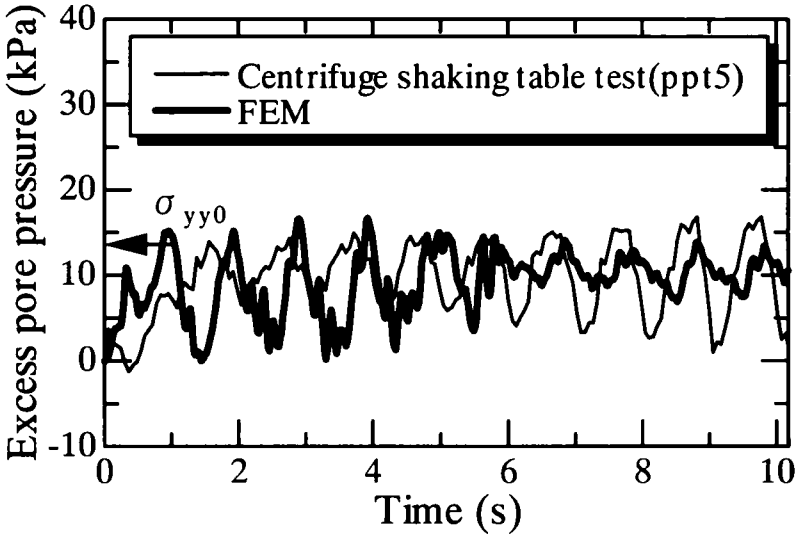

Fig. 5.9 Predicted and measured time histories of excess pore pressure in the free field (M_f=0.543)

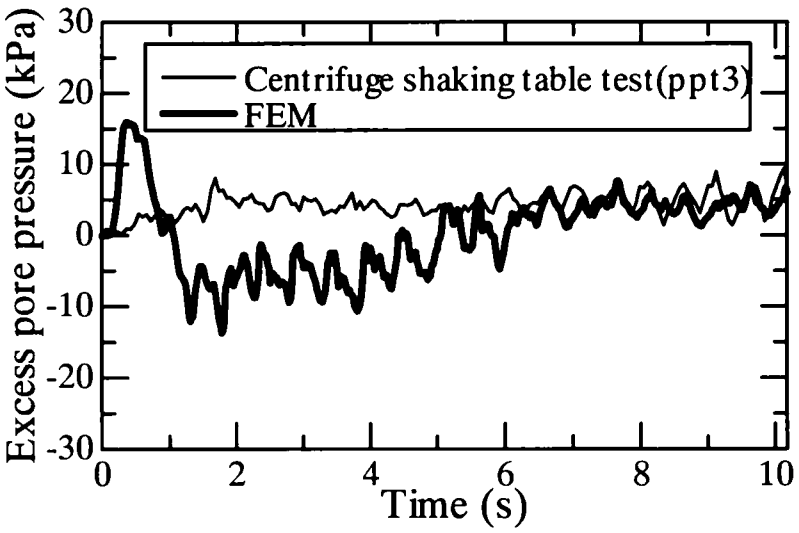

Fig. 5.10 Predicted and measured time histories of excess pore pressure in the foundation sand beneath the caisson(M_f=0.543)

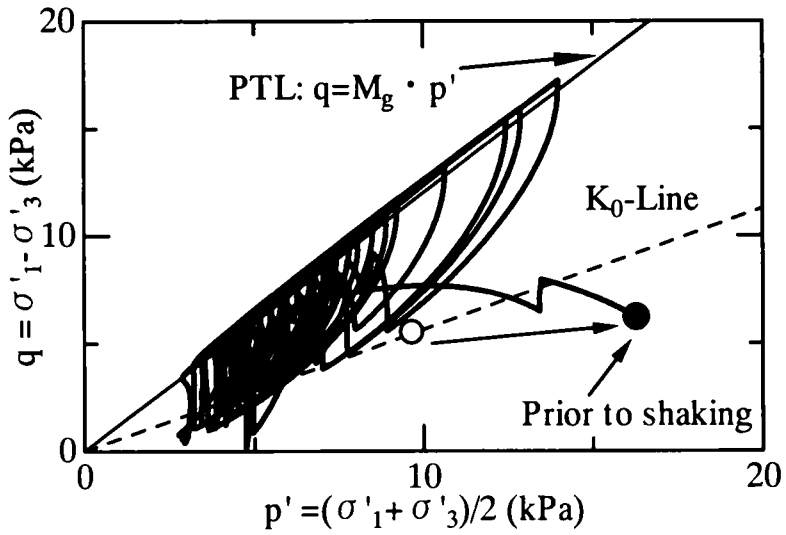

Fig. 5.11 Predicted stress paths in element E2 in the free field(M_f=0.543)

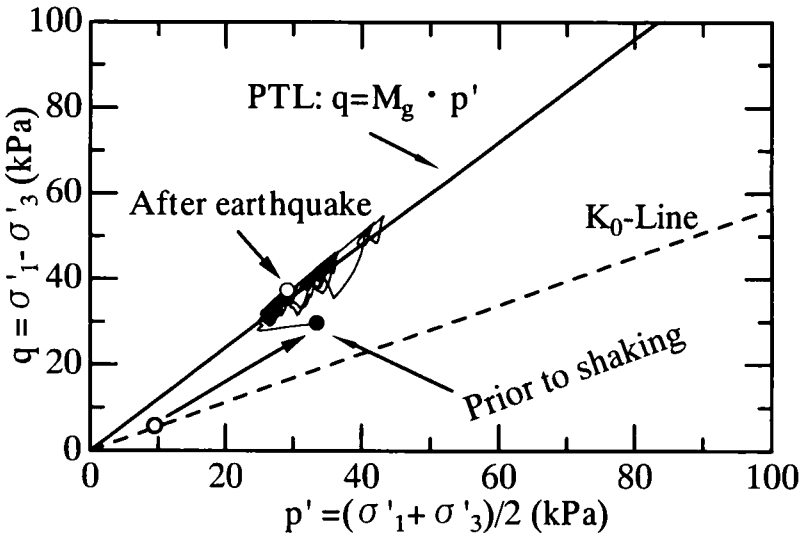

Fig. 5.12 Predicted stress paths in element E1 below the caisson(M_f=0.543)

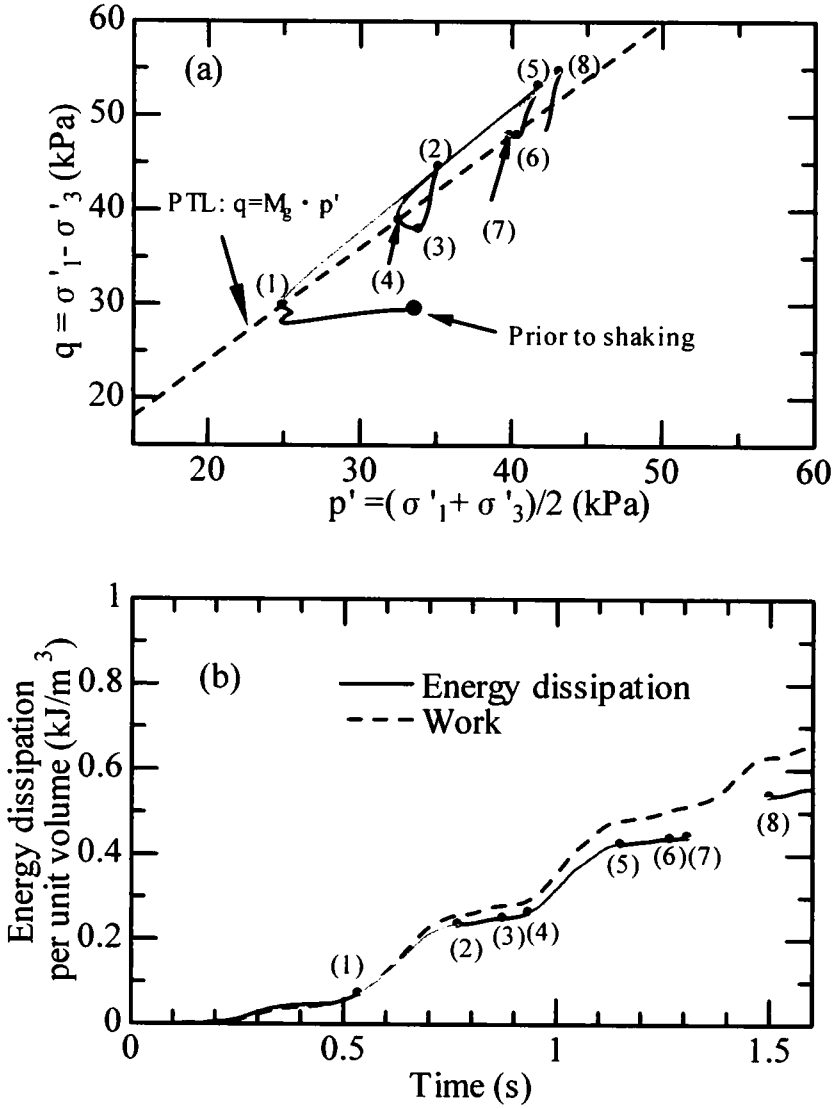

Fig. 5.13 (a) Effective stress path; (b) energy dissipation and work in element E1 below the caisson(M_f=0.543)

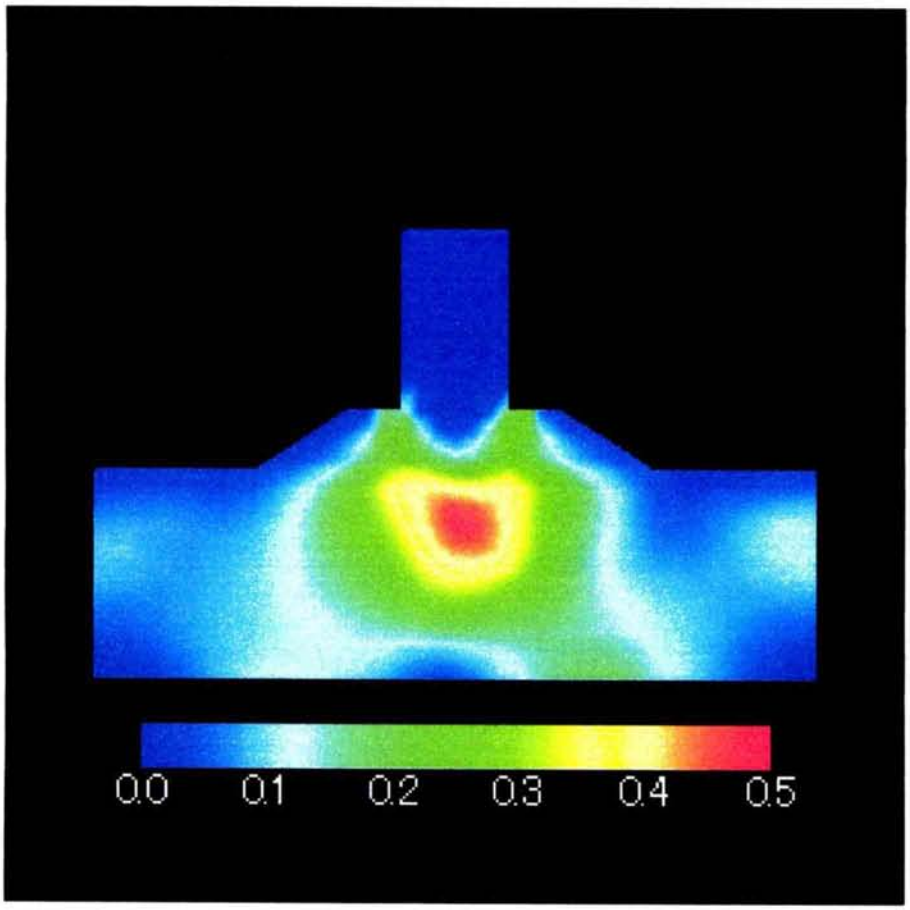

Fig. 5.14 Distribution of the amount of energy dissipation in entire system (M_f=0.543)

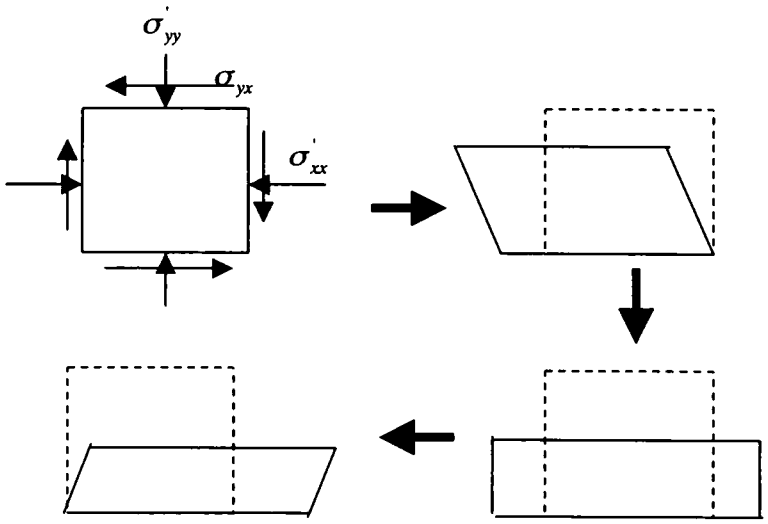

Fig. 5.15 Schematic shear deformation of soil element beneath caisson

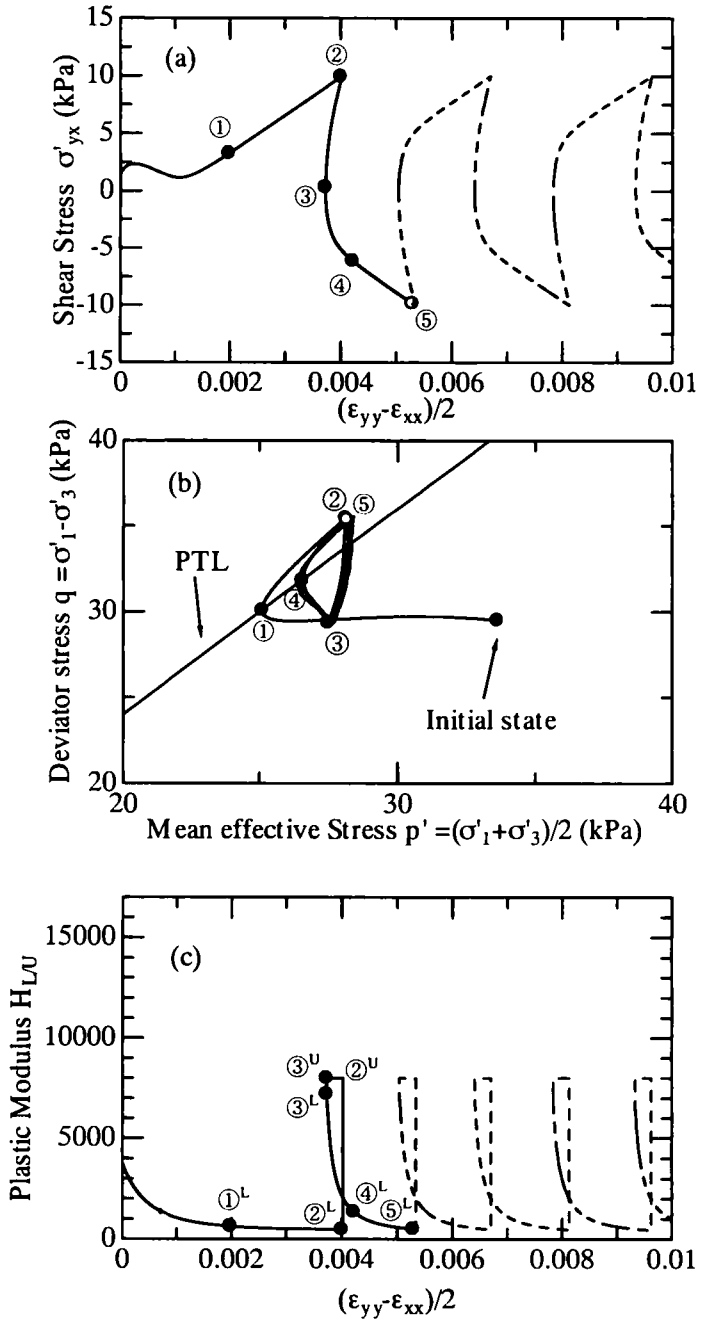

Fig. 5.16 (a) Shear stress – axial stress difference relation; (b) deviator stress –mean effective stress relation; (c) plastic modulus – axial stress difference relation (Present study)

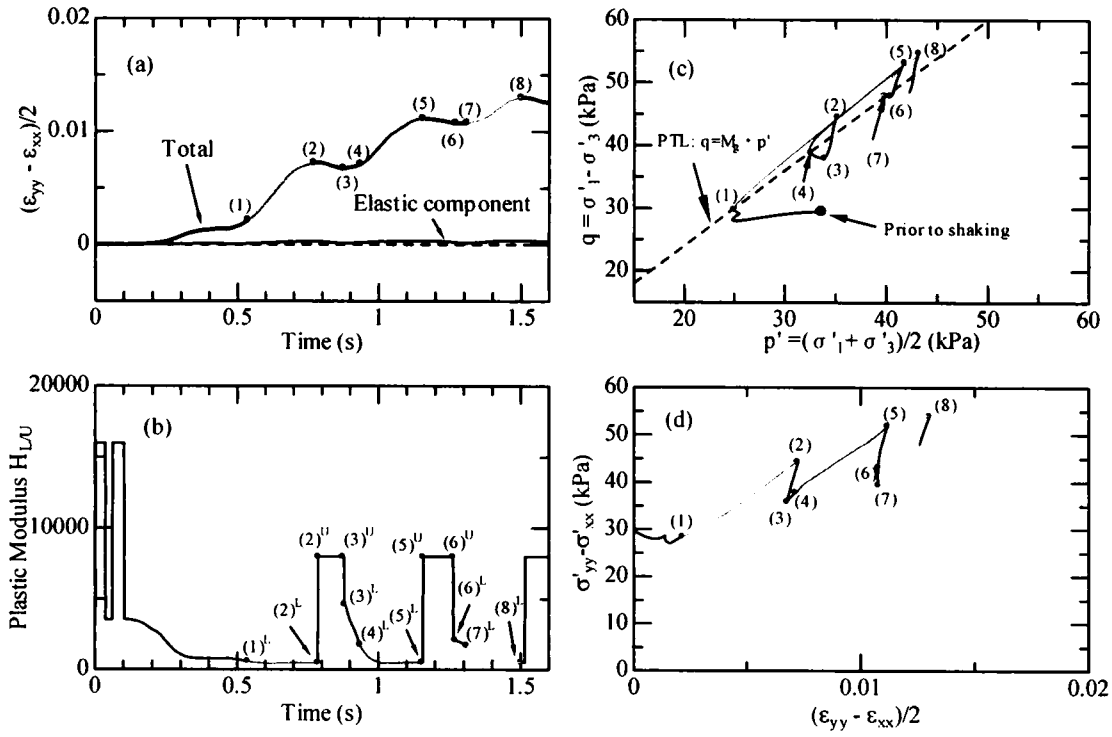

Fig. 5.17 (a) Time histories of deviator strains; (b) time history of plastic modulus; (c) stress paths (d) axial stress difference-axial strain difference relation in element E1 during 1.5s of shaking (M_f=0.543)

CHAPTER 6

Revisit to the performance of Kobe port breakwater No. 7 subjected to the 1995 Hyogoken-Nambu earthquake

6.1 Introductory remarks

The purpose of this chapter is to reproduce the seismic behavior of the Kobe port breakwater No. 7 during the 1995 Hyogoken-Nambu earthquake based on the proposed analysis framework, and to present practical implications that have relevance to the future design of composite breakwaters or such coastal structures in areas of high seismicity. Although it is understandable that the standard engineering practice has put a great deal of attention on the wave-resistant design of breakwaters, consideration of seismic performance of breakwater systems will become equally important in view of increased likelihood of occurrence of large earthquakes such as Nankai or Tonankai earthquake or combined.

It should be noted herein that extensive damage occurred to the composite breakwaters in the port of Kobe due to the 1995 Hyogoken-Nambu earthquake. Breakwater No. 7, for instance, settled as much as 2.6m, with minor tilt and horizontal displacements of the caisson structure occurring (Sekiguchi et al. 1996; Port Bureau Ministry of Transport et al., 1997). The seabed soil in Kobe Harbor is featured by a thick deposit of soft alluvial clay. Thus it was common practice that when heavy marine structures such as composite breakwaters were built, the soft clay layer had been partially excavated deep and backfilled with local granular soil (decomposed granite soil) to give less compressible foundations. By taking note of such soil conditions, Tanaka et al. (2001) drew attention to the seismic behavior of the granular fill as well as of the soft clay layer, on the basis of dynamic response analyses. Sugano et al. (1996) performed a series of large-scale shaking-table tests on models of port facilities including composite breakwater models and obtained detailed deformation data that were in compatible

with the observed deformation behavior of the composite breakwaters in the port of Kobe. They pointed out that the cause of the large caisson settlement was due to severe shear deformation of the foundation soil beneath the caisson.

Toki et al. (1981) incorporated into dynamic finite-element analysis procedure and examined the response of soil-structure systems to earthquake shaking, with consideration of the effect of separation and sliding at the soil-structure interface joint-element modeling (Goodman,1976).

In what follows, the outcome of the present analysis for seismic performance of the Kobe port breakwater No. 7 will be described in detail.

6.2 Ground conditions and material parameters

A typical cross section of breakwater No.7 is shown in Fig. 6.1(Morio, 1992; Sekiguchi et al., 1996). The Holocene clay layer at the construct site was partially replaced with backfill (decomposed granite soil), in such a way that the surface of the sand fill was flush with the surface of the adjacent clay layer.

A finite-element mesh used for the dynamic analyses of breakwater No.7 is shown in Fig. 6.2. The side and bottom boundaries were represented with the viscous boundaries. The material parameters used for the analyses of breakwater No. 7 are listed in Table 6.1. The normal and tangential stiffness for joint element were selected such that $Kn=Ks=1\times10^{4}\left(\sigma_{n}^{'}\right)^{0.4}$. Where $\sigma_{n}^{'}$ represents the normal effective stress that develop in a joint element under discussion. In order to investigate the best prediction in terms of the final caisson settlement, the parameter M_f was varied over a wide range (Table 6.2). Series I represents cases study under external fluid. Series II represents cases study without external fluid.

The input time history of the basal acceleration in the present analysis is due to the NS-component of the acceleration record observed at Port Island (GL. -32m) (Iwasaki and Tai, 1996), in NS direction. The time history of the input acceleration is shown in Fig. 6.3.

6.3 Comparison between predicted and measured performances

One of the important yet unknown factors is the degree of compaction of the sand backfill below the caisson structure. In order to obtain an idea about the importance of the state of compaction of the sand fill, the present study varied the value of parameter M_f in a wide range 0.44 to 0.6 (Table 6.2). Note here that the value of M_f/M_g adopted may effectively be convert into the value of relative density Dr, based on the previously discussed correlation, which reads:

$$M_f / M_g = e^{(1.07Dr - 1.35)} \quad (2.34)$$

6.3.1 Back analysis relevant M_f/M_g ratio for finding most

Three cases are taken up here to demonstrate the difference in the acceleration responses of top of caisson (Fig. 6.4). It is seen that the level of amplification in the acceleration of a caisson structure increase with increasing degree of compaction of the foundation sand.

The predicted time histories of horizontal and vertical displacements of the caisson top in Case KB2-1 with M_f=0.48 are shown in Fig. 6.5. The caisson rocked almost evenly and settled significantly. The predicted maximum settlement of caisson top was 1.7m and residual horizontal displacement of caisson top was 0.07m. The predicted plastic deformation of the composite breakwater systems after shaking (t=20s) in Case KB2-1 is shown in Fig. 6.6. The caisson settled almost vertically and the rubble mound has settled and deformed. Rubble mound at the foot of the caisson settled significantly, whereas a smaller settlement presented near the shoulder. This predicted plastic deformation corresponded well to the observed result (Sekiguchi et al. 1996). A typical predicted pattern (M_f=0.48) of the deformation of interface between caisson and rubble mound after shaking (t=20s) in Case KB2-1 is shown in Fig. 6.7. Relative horizontal displacement occurred at interface between caisson and rubble mound.

The predicted plastic settlements of the caisson are plotted in Fig. 6.8 against the M_f /M_g ratios adopted. Note here that the foregoing discussions in this thesis permit the parameter M_f /M_g to be correlated with the relative density Dr for a given sand. It is now evident from Fig. 6.8 that the best match between the observed and predicted performance of the caisson settlement is obtainable when relative density Dr is assumed to be equal to 40%(M_f=0.48) or so.

The predicted distributions with depth, of the vertical strain ε_{yy}, the lateral strain ε_{xx} and the volumetric strain ε_v in foundation soil along the centerline of the caisson after shaking(t=20s) in best matched Case KB2-1 with M_f=0.48 are shown in Fig. 6.9. The soil elements below the caisson structure underwent significant amounts of vertical compression (Fig. 6.9(a)) that were accompanied by equally significant lateral expansion (Fig. 6.9(b)). It is indicated that the plastic deformation of foundation soil occurred under nearly constant-volume conditions (Fig. 6.9(c)).

6.3.2 Excess pore pressure responses and effective stress states in the foundation sand

The predicted performance of elements below the caisson in best matched Case KB2-1 with Mf=0.48 (Dr=40%) are shown in Fig. 6.10, Fig. 6.11 and Fig. 6.12. The deviator strain accumulated during earthquake shaking and presented finally 7 percent at the shallow level (EK3) in Fig. 6.12(a) although the deviator strain become small in Fig. 6.10(a). The state of

effective stress reached the phase transformation line(PTL) and fluctuated in the range closer to the phase-transformation line (Fig. 6.10(c), Fig. 6.11(c) and Fig. 6.12(c)). The negative excessive pore pressure developed when the stress point crossed and rose up along the phase transformation line (Fig. 6.10(d), Fig. 6.11(d) and Fig. 6.12(d)). Excess pore pressure at the shallow level (EK3) in Fig. 6.12(d) indicated markedly negative value due to dilatancy. Excess pore pressures of the foundation soil below the caisson were considerably smaller than the corresponding initial effective vertical stress σ'_{yy0} values (Fig. 6.10(d), Fig. 6.11(d) and Fig. 6.12(d)).

The predicted stress paths (EK4) and time history of excess pore pressure in the sand backfill of the free field in Case KB2-1 with Mf=0.48 (Dr=40%) are shown in Fig. 6.13. The mean effective stress decreased markedly in the first two loading cycles and then the effective stress path crossed the phase transformation line, exhibiting the tendency for dilatancy (Fig. 6.13(a)). The predicted excess pore pressure was very closed on initial effective vertical stress σ'_{yy0} values (Fig. 6.13(b)).

The predicted distribution of excess pore pressure ratios pw/σ'_{yy0} at the end of the shaking (t=20s) in Case KB2-1 with Mf=0.48 (Dr=40%) are shown in Fig. 6.14. The excess pore pressure ratios are higher than 0.7 for the area relatively far away from the caisson structure. However, the foundation soils below the caisson shown excess pore pressure ratios less than 0.4. That is, effective stress state of the foundation soil below the caisson was far from being the state of liquefaction. The large settlements of the order of 2m in the composite breakwater system may be ascribed to a sort of repeated shear failure in the foundation soil whose effective stress state was far from being the state of liquefaction.

6.3.3 Performance of interface between rubble mound and caisson

The predicted time histories of horizontal force and vertical force with dynamic fluid force in Case KB2-1 with Mf=0.48 (Dr=40%) are shown in Fig. 6.15. Here, the value of external horizontal force was expressed with the sum of shear force beneath the caisson to dynamic fluid force on both sides of caisson. Shear force is defined by (Toki et al., 1981):

$$\text{Shear force} = \sum_{j=1}^{n} \tau_j A_j \tag{6.1}$$

where n is the total number of subdivisions for joint element beneath the caisson and τ_j and A_j represents mobilized shear stress and the area of a subdivision j for joint element.

The external horizontal force is equal to the value, which multiplied acceleration $\ddot{x}$ of x-direction by mass M of caisson.

The external vertical force represents with effective vertical force defined by

$$\text{Effective vertical force} = \sum_{j=1}^{n} \sigma_{nj} A_j \tag{6.2}$$

where $\sigma_{nj}^{'}$ is effective vertical stress of subdivisions j for joint element. The external vertical force is equal to the value, which multiplied acceleration $\ddot{y}$ of y-direction by mass of caisson. The dynamic equilibrium was satisfied in Fig. 6.15. In Fig. 6.15, dynamic fluid force Fig. 6.15(a) acts on the caisson to same direction with the inertial force of the caisson that reversed direction of acceleration.

The predicted relative horizontal displacements for joint element in Case KB2-1 are shown in Fig. 6.16. On both sides (A1 and A2) of joint element, predicted relative horizontal displacements was accompanied by the lateral extension of the rubble mound beneath the caisson. However, on element A3 for centerline, small relative horizontal displacements occurred.

The predicted relative vertical displacements for joint element in Case KB2-1 are shown in Fig. 6.17. The relative vertical displacements of elements A1 and A3 in both sides beneath caisson developed with significant fluctuations as shown in Fig. 6.17.

Stress path for joint element A1 during shaking is shown in Fig. 6.18. Relative shear displacement accumulated significantly closed to phase transformation line. Separation of interface between caisson and rubble mound occurred repeatedly (refer to Fig. 6.18).

6.3.4 Dynamic safety against sliding at the interface of the caisson and rubble mound

The dynamic safety of the caisson against sliding can be examined by the stress state of joint element beneath caisson. The dynamic safety factor is defined by (Toki et al., 1981):

$$\text{Dynamic safety factor} = \left| \frac{\sum_{j=1}^{n} \tau_{yj} A_j}{\sum_{j=1}^{n} \tau_j A_j} \right|_{\min,T} \tag{6.3}$$

where min,T means the minimum value with respect to the entire time analyzed and τ_{yj} represents yield shear stress of a subdivision j that is expressed by: $\tau_{yj} = \sigma_{nj}^{'} \cdot \mu_g$.

Time histories of the dynamic safety factor against sliding of caisson with value of

parameter M_f are shown in Fig. 6.19. All the dynamic safety factors are greater than 1.0 (refer to Fig. 6.19).

The predicted dynamic safety factor plotted against parameter ratio M_f/M_g and relative density Dr is shown in Fig. 6.20. Minimum safety factors of model under external fluid (Series I) and model without external fluid (Series II) are expressed to this figure. "The model without external fluid" is the model that considered only the influence of static fluid pressure, without the influence of dynamic fluid pressure.

In comparison of the model without external fluid as the model under external fluid, the safety factor of model under external fluid becomes slightly small value. Specially, when relative density is 60%, minimum safety factor of model under external fluid is lower 0.2 than that of model without external fluid.

In Fig. 6.20, dynamic safety factor decreased with increasing value of parameter M_f (or relative density Dr) and when relative density is 60%, minimum safety factor of model under external fluid is 1.5. It is important herein to note that the possible decrease in safety against sliding of the caisson due to densified foundation sand is in the range permissible from engineering considerations. In fact, the standard wave-resistant design of composite breakwaters permits the ratio of the design horizontal loading H to the effective caisson weight W' to reach a level as high as 0.6 or so. The required bearing capacity of a standard caisson structure subjected to horizontal (wave) loading will well accommodate the seismic amplification effects stated above.

The moderate compaction in the foundation sand or such means will be one of the practical choices when dealing with composite breakwater systems in areas of high seismicity.

6.4 Discussion

In order to obtain an idea about the importance of the state of compaction of the sand fill, the present study varied the value of parameter M_f in a wide range 0.44 to 0.6. The best match between the observed and predicted performance of the caisson settlement was obtainable when relative density Dr was assumed to be equal to 40%(M_f=0.48) or so (Fig. 6.8). This represents a relatively low level of compaction in the foundation sand, yet it is thought to be a realistic estimate for the degree of compaction that should have taken place in the field. Indeed, before the occurrence of the 1995 Hyogoken-Nambu earthquake, decomposed granite soil was regarded as being a good engineering material, and no particular compaction efforts underwater were required when using it as being backfill material for the dredged portion of seabed clay in the site of breakwater No. 7 in the port of Kobe.

It was fortunate that the estimated degree of compaction of the backfill narrowly reached a level of Dr=40% or thereabouts. If the degree of compaction were somewhat lower, the breakwaters would have suffered much more severe damage due to the seismically induced

deformation. Also, the performance shown in Fig. 6.8 suggests that the moderate compaction efforts to bring Dr to a level of 60% or so will yield a marked beneficial effect regarding settlement reduction.

6.5 Conclusions

A revisit was made to the seismic performance of Kobe port breakwater No.7 during the 1995 Hyogoken-Nambu earthquake, in terms of the proposed finite-element analysis procedure. The outcome of the analyses performed may be summarized as follows.

1. The best prediction in terms of the final caisson settlement proved to be the case where the non-associativeness parameter M_f/M_g was equal to 0.48. This prediction is of considerable practical interest, since the identified case points to the relative density Dr of the sand fill being equal to 40%, provided that Eq. (2.34) holds true for the deposits of decomposed granite soil.
2. The large settlements of the order of 2m in the composite breakwater system may be ascribed to a sort of repeated shear failure in the foundation soil whose effective stress state was far from being the state of liquefaction.
3. The factors of safety against sliding at the interface of the caisson and rubble mound during shaking could be assessed by closely examining the effective stress states in the joint elements incorporated. The factor of safety against sliding tends to take a smaller minimum in the course of shaking in the cases where parameter M_f (or Dr) takes a larger value, suggesting an adverse effect of increased degree of compaction in the sandfill.

References

Iwasaki, Y. and Tai, M. (1996). Strong motion records at Kobe port island, *Special issue of Soils and Foundations*, Japanese Geotechnical Society, 29-40.

Morio, S. (1992). Foundation of breakwater, *The foundation engineering and equipment*, Vol. 20, No. 5, 19-21 (in Japanese).

Port Bureau Ministry of Transport, Aviation Bureau Ministry of Transport. Ports and Harbor Research Institute in the Ministry of Transport, The 3rd District Port Construction Bureau Ministry of Transport , The Fishing Port Bureau Ministry of Fisheries, Civil Engineering Works in Hyogo Pref., Kobe-City Harbors Maintenance Bureau, Kobe Port Wharf Public Corporations. (1997). Damage report about harbors facilities due to 1995 Hyougoken-Nambu earthquake, (In Japanese).

Goodman, R. E. (1976). Method of geological engineering in discontinuous rocks, *West*

Publishing Company.

Sekiguchi, H., Kita, K., Hashimoto, K. and Katsui H. (1996). Deformation of composite breakwaters due to ground shaking, *Special issue of soils and foundations*, 169-177.

Sugano, T., Miyata, M., Mito, M., Inagaki, H., Oikawa, K. and Iizuka, E. (1996). Study on behavior of harbors and coast facilities subjecting to Hyogoken-Nambu earthquake, *Proc. of coastal engineering*, JSCE, Vol. 43, No. 2, 1331-1315 (In Japanese).

Tanaka, Y., Yagiura, Y., Shimokawa, K., Higashi, S., Kishida, T. and Mizuwake, N. (2001). Study of liquefaction damages of quay-walls and breakwaters during Kobe earthquake, *Fourth Int. Conference on Recent Advances in Geotechnical Earthquake Engineering and Soil Dynamics and Symposium in Honor of Professor W.D. Lian Finn,* Paper No. 4.44.

Toke, K., Sato, T. and Miura, F. (1981). Separation and sliding between soil and structure during strong ground motion, *Earthquake engineering and structural dynamcis,* Vol. 9, 263-277.

Table 6.1 The material parameters used for the analysis of breakwater No. 7

(a) Sand backfill and rubble mound

Material	Mg	M_f	α	β_0	β_1	H_0^*	Hu0 (kPa)	γ_u	γ_D	K_0	k m/s
Sand backfill	1.2	0.44-0.6	0.35	20	0.04	1500	8000	4	3	0.56	0.0001
Rubble mound	1.2	0.9	0.35	20	0.04	1500	8000	4	3	0.56	1.0

(b) Clay

Material	M	α	β_0	H_0	Hu0 (kPa)	γ_u	γ_D	K_0	k
Clay	1.2	0.35	0.1	160	8000	4	8	0.56	Undrain

(c) Joint Element

μ_g	μ_f	α_j	β_{0j}	β_{1j}	H_{0j}	H_{U0j} (kPa/m)	γ_{uj}	γ_{Dj}
0.65	0.55	0.35	0.4	20	1000	1000000.0	2	4

Table 6.2 Finite-element analyses performed

Series	Case No.	M_f of sand backfill	M_f/M_g	External fluid
I	KB1-1	0.44	0.37	O
	KB2-1	0.48	0.40	O
	KB3-1	0.5	0.42	O
	KB4-1	0.543	0.45	O
	KB5-1	0.6	0.50	O
II	KB1-2	0.44	0.37	-
	KB2-2	0.48	0.40	-
	KB3-2	0.5	0.42	-
	KB4-2	0.543	0.45	-
	KB5-2	0.6	0.50	-

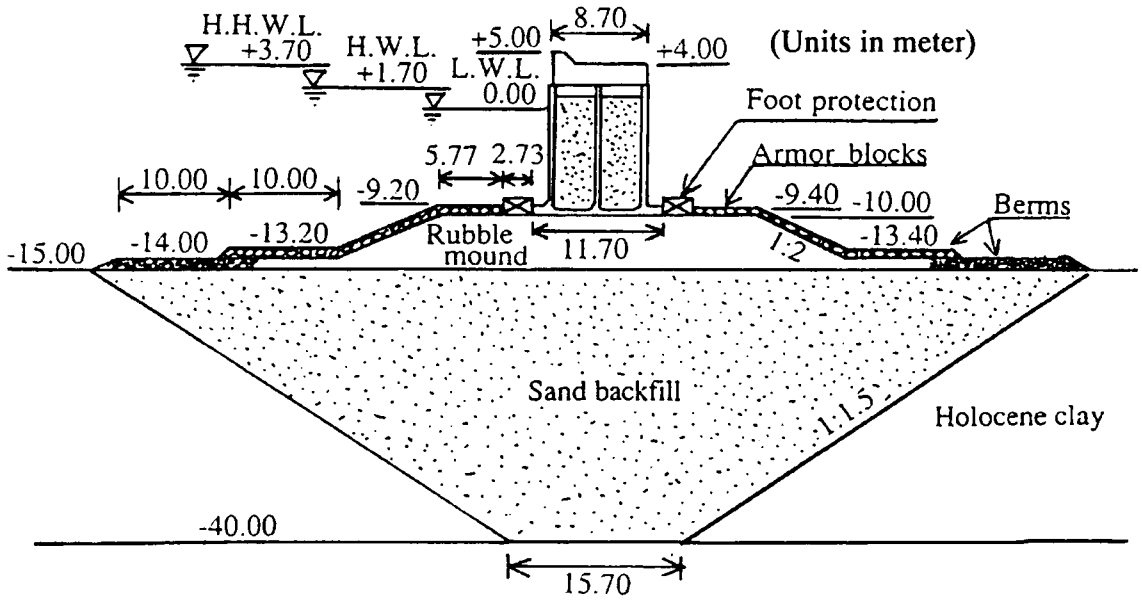

Fig. 6.1 Standard cross section of breakwater No.7

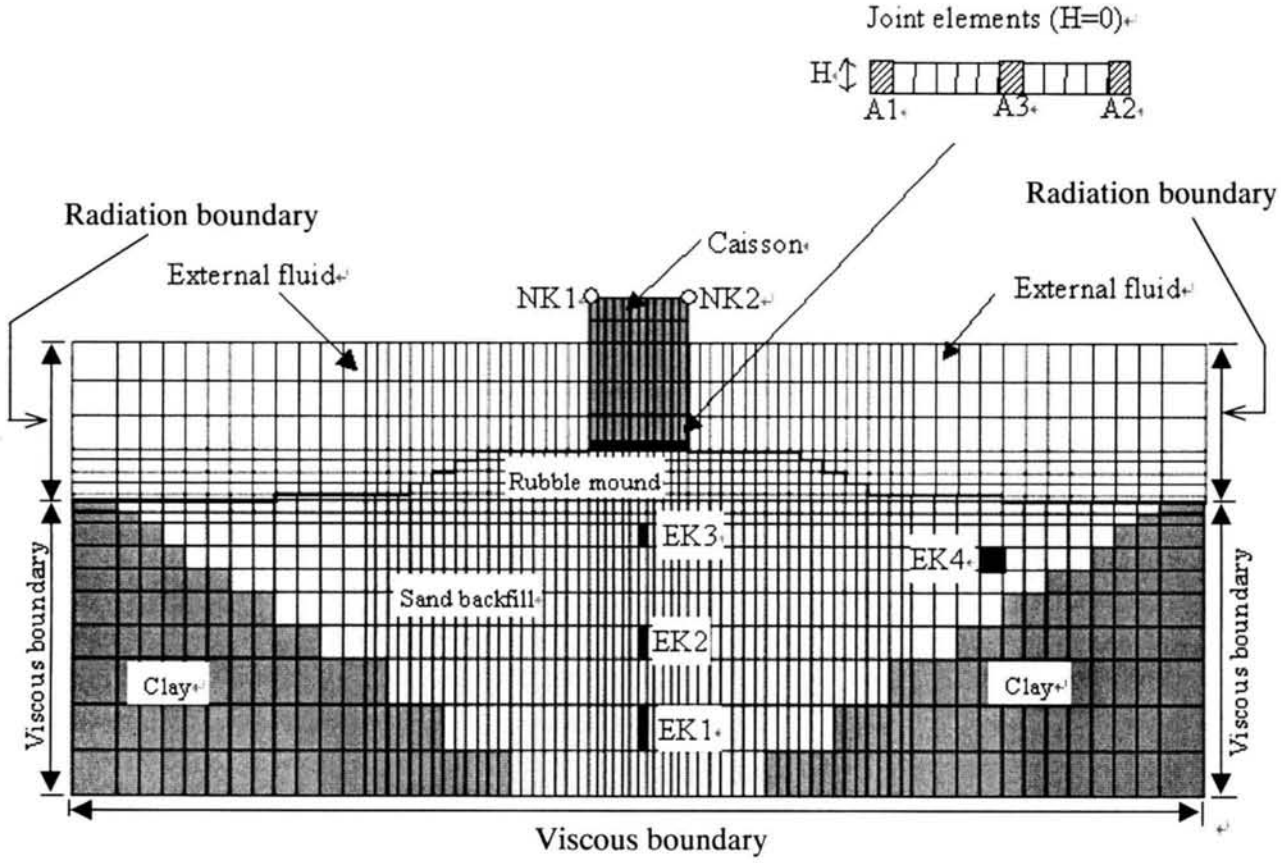

Fig. 6.2 A finite-element mesh used for dynamic analyses of breakwater No. 7

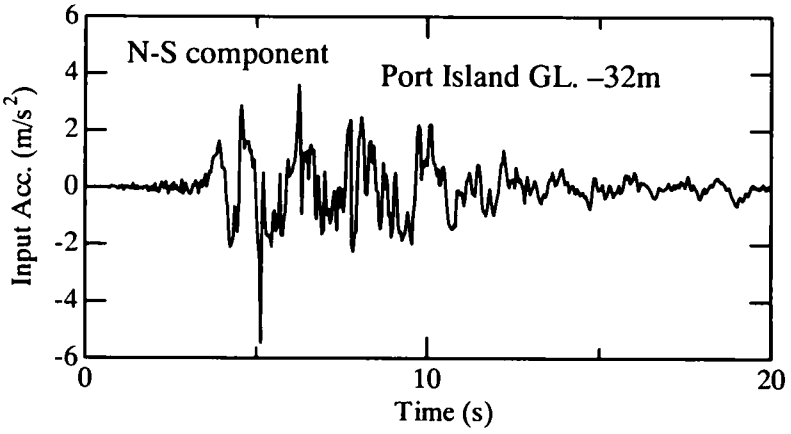

Fig. 6.3 Input horizontal acceleration (Iwasaki and Tai, 1996)

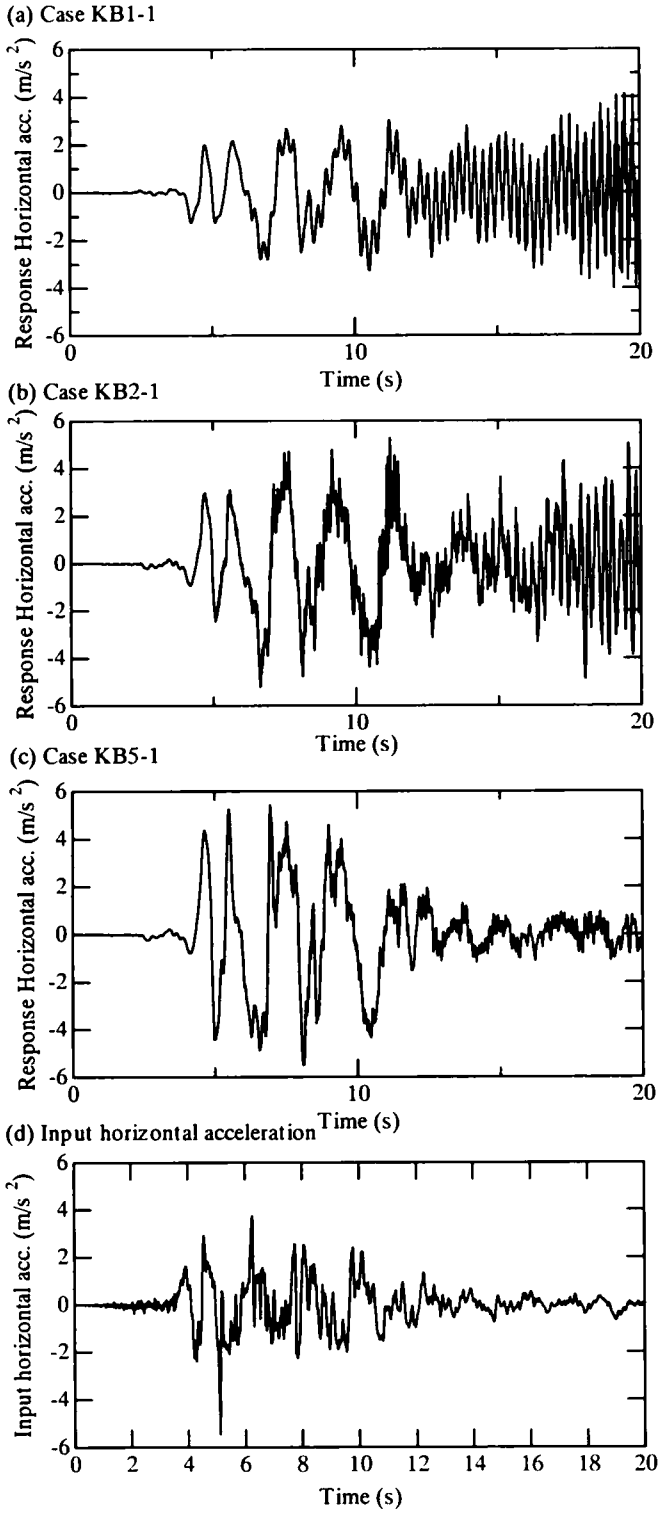

Fig. 6.4 The difference in response horizontal accelerations: (a) in Case KB1-1 with M_f=0.44 (Dr=33%); (b) in Case KB2-1 with M_f=0.48 (Dr=40%); (c) in Case KB4-1 with M_f=0.6 (Dr=61%); (d) input horizontal acceleration

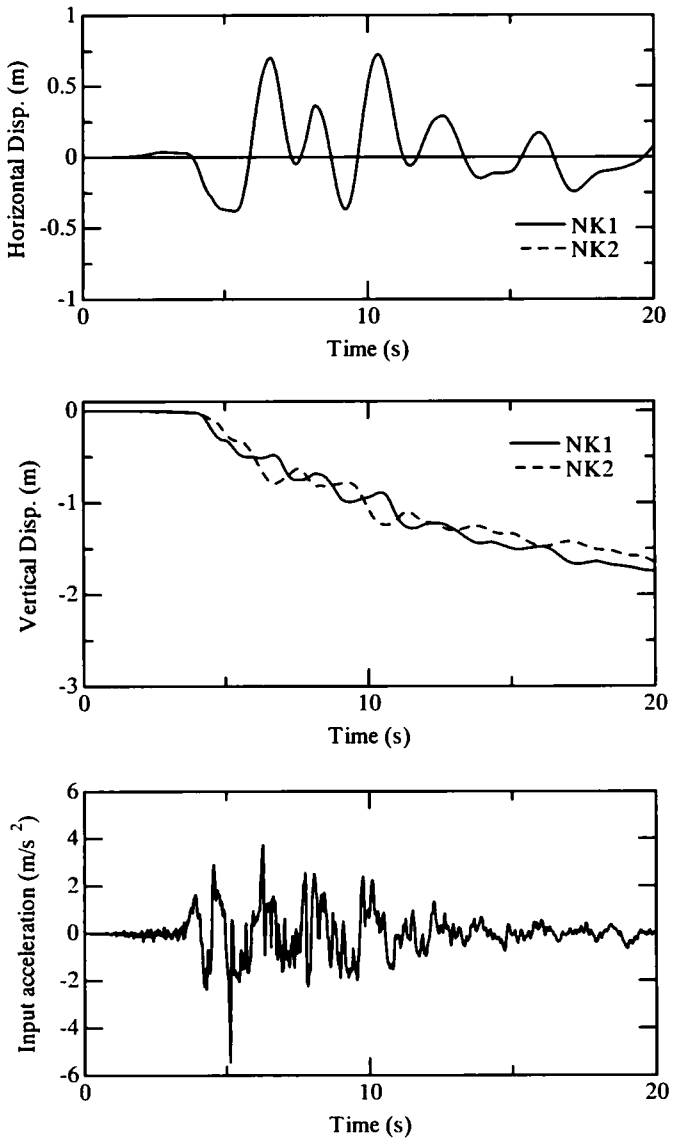

Fig. 6.5 Predicted time histories of horizontal and vertical displacements of the caisson top (Case KB2-1 with M_f=0.48 (Dr=40%))

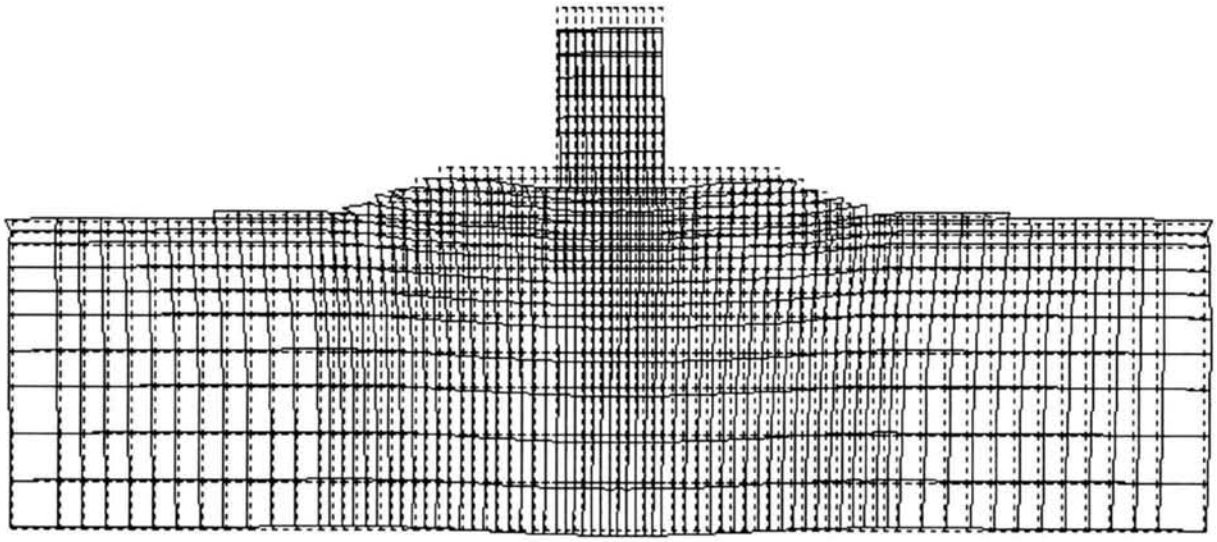

Fig. 6.6 Predicted plastic deformation of the composite breakwater No. 7 after shaking (t=20s) (Case KB2-1 with M_f=0.48 (Dr=40%))

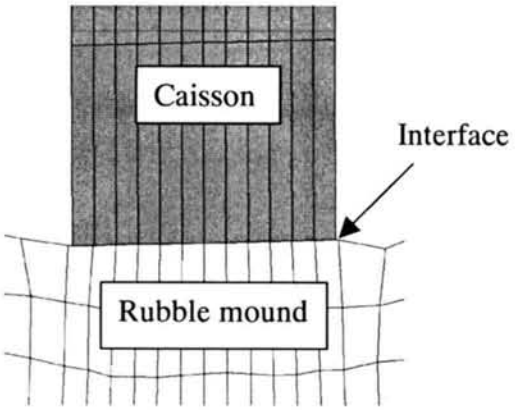

Fig. 6.7 Predicted deformation of interface between caisson and rubble mound after shaking (t=20s) (Case KB2-1 with M_f=0.48 (Dr=40%))

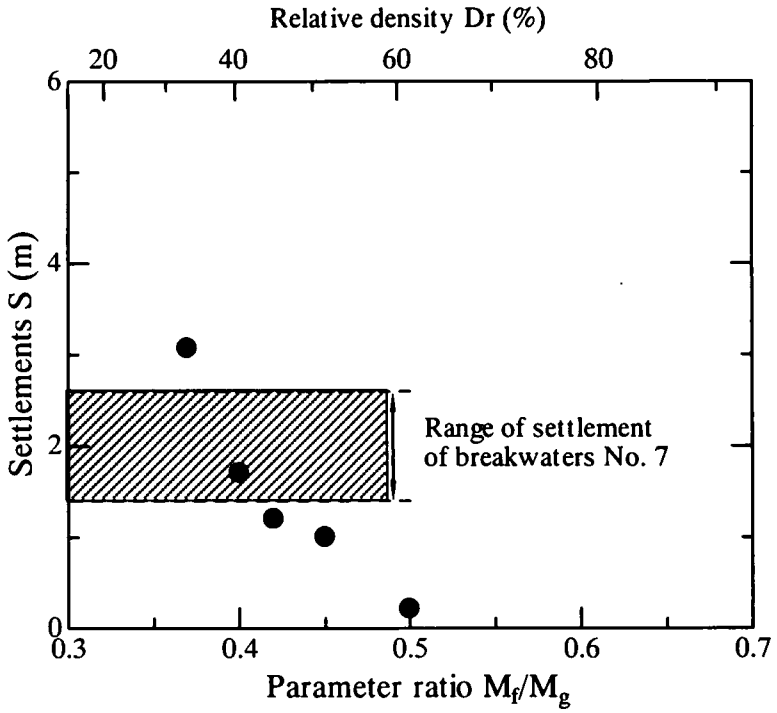

Fig. 6.8 Predicted settlement plotted against parameter M_f /M_g (or relative density Dr) of sand backfill after shaking

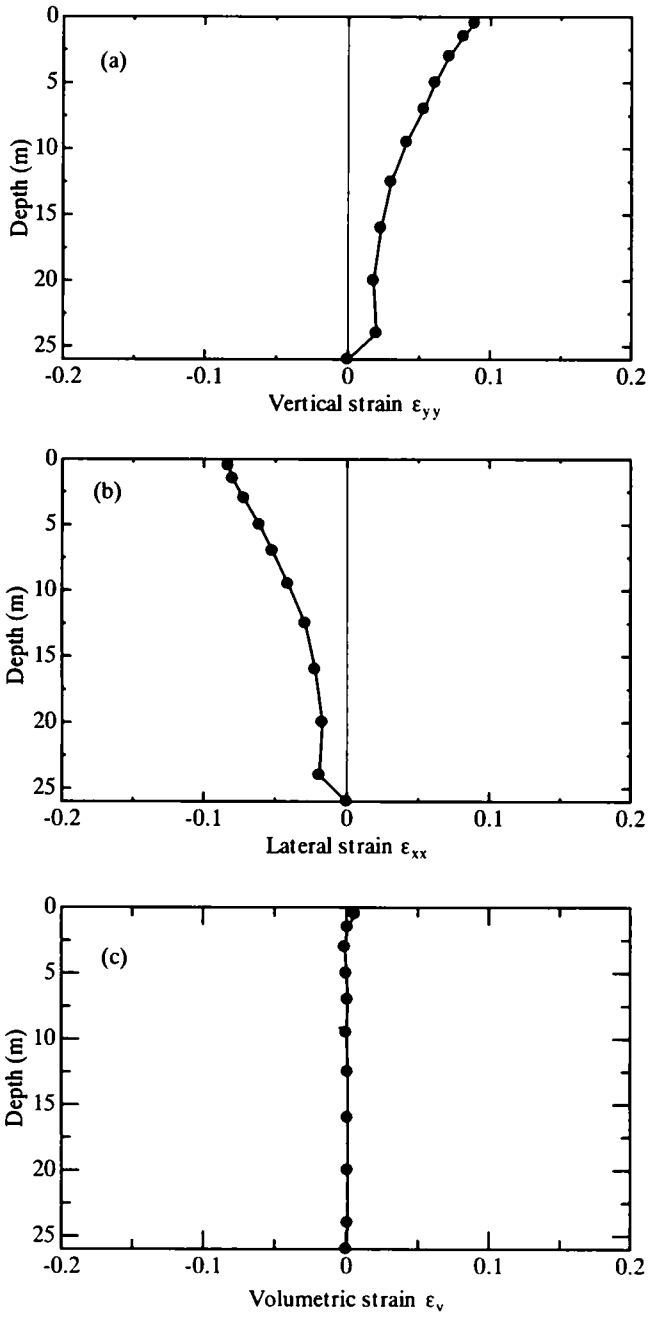

Fig. 6.9 Predicted distributions with depth of (a) vertical strains, (b) lateral strains and (c) volumetric strains in the foundation soil along the centerline of the caisson after shaking (t=20s) (Case KB2-1 with M_f=0.48 (Dr=40%))

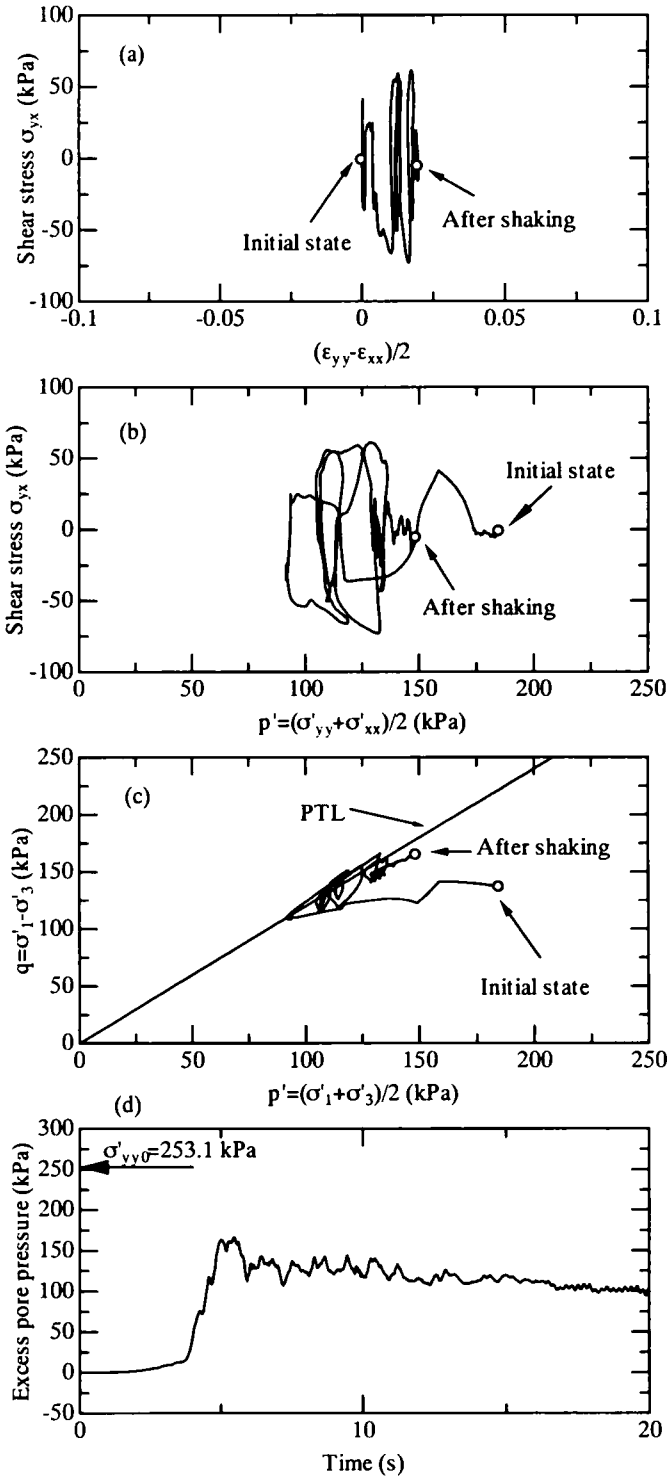

Fig. 6.10 (a) Shear stress-deviator strain relation; (b)(c) stress paths; (d) time history of excess pore pressure in element EK1 below the caisson in Case KB2-1 with M_f=0.48 (Dr=40%)

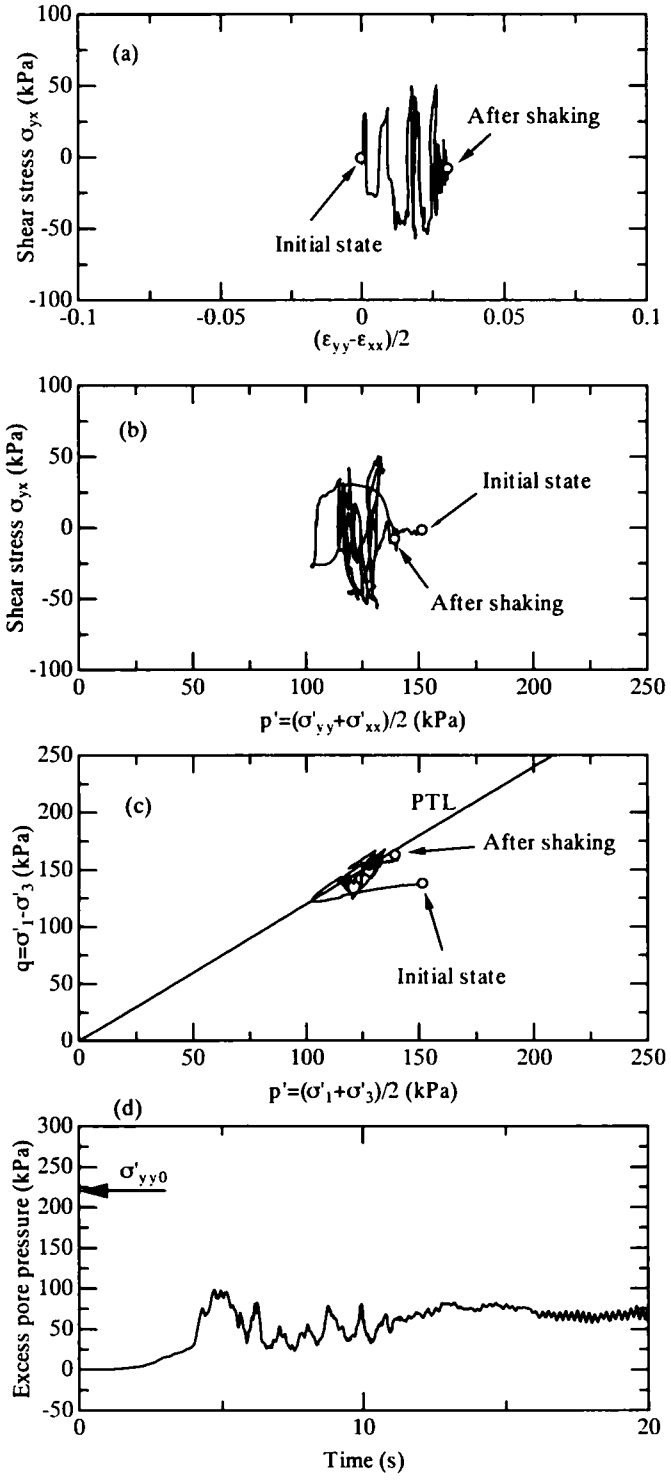

Fig. 6.11 (a) Shear stress-deviator strain relation; (b)(c) stress paths; (d) time history of excess pore pressure in element EK2 below the caisson in Case KB2-1 with M_f=0.48 (Dr=40%)

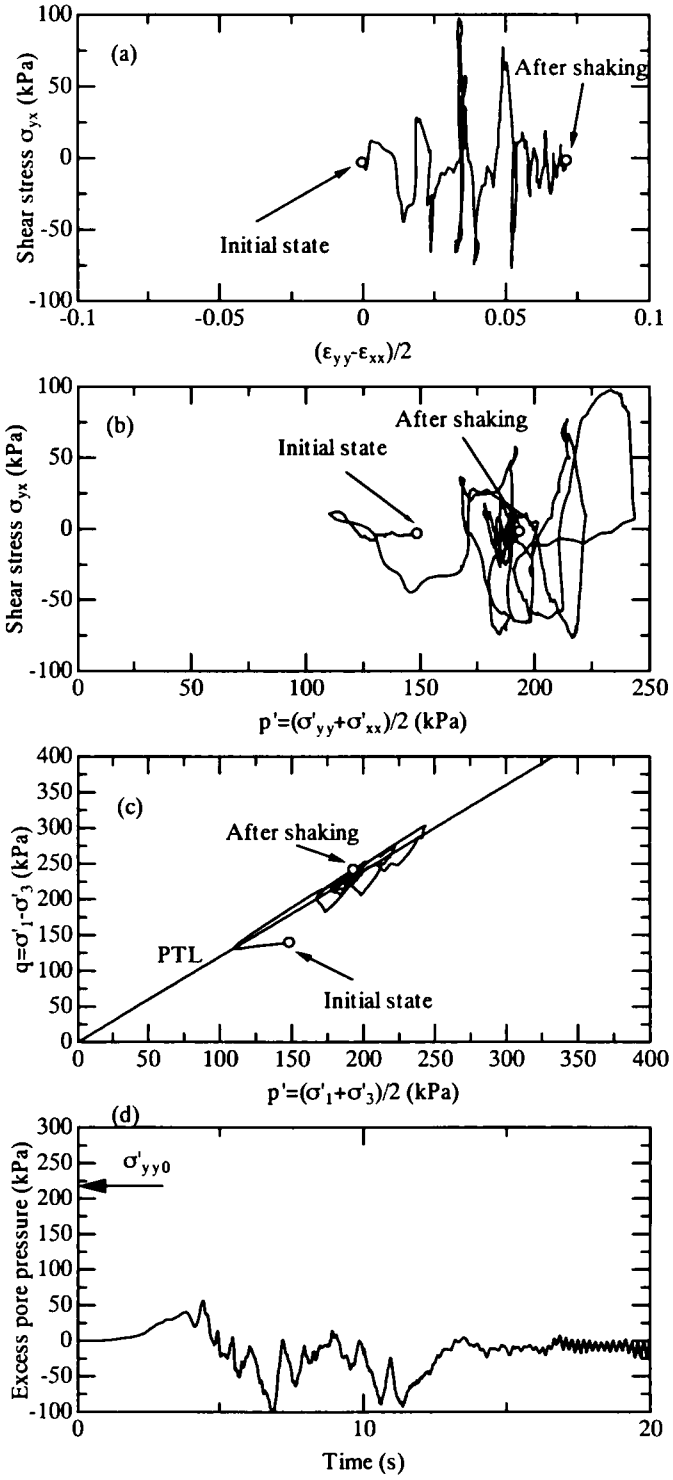

Fig. 6.12 (a) Shear stress-deviator strain relation; (b)(c) stress paths; (d) time history of excess pore pressure in element EK3 below the caisson in Case KB2-1 with M_f=0.48 (Dr=40%)

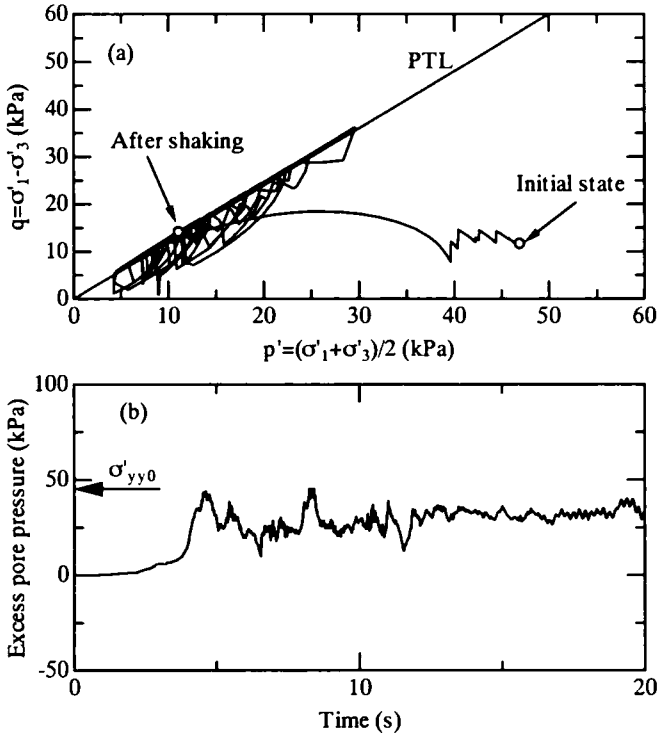

Fig. 6.13 (a) Stress path; (b)time history of excess pore pressure in element EK4 in Case KB2-1 with M_f=0.48 (Dr=40%)

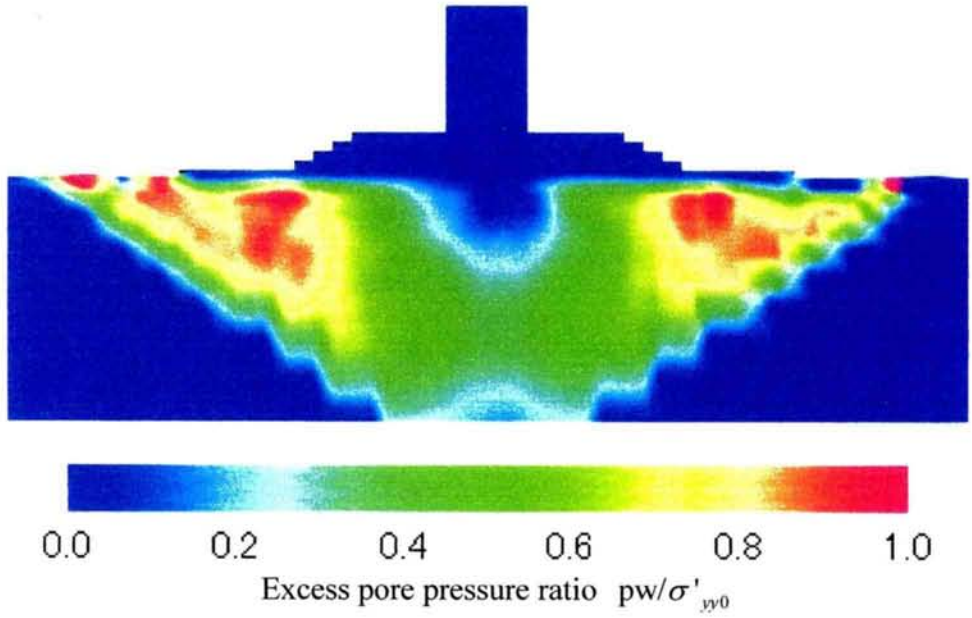

Fig. 6.14 Predicted distribution of excess pore pressure ratios at the end of the shaking (t=20s) in Case KB2-1 with M_f=0.48 (Dr=40%)

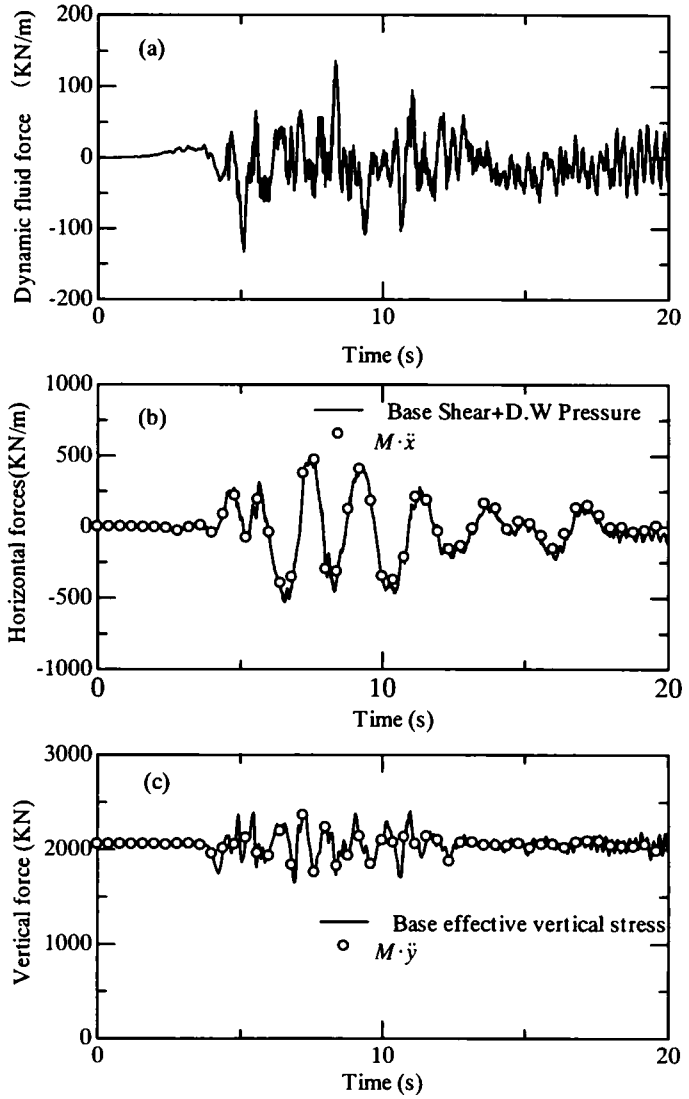

Fig. 6.15 Predicted time histories of (a) dynamic fluid force; (b) horizontal force; (c) vertical force in Case KB2-1 with M_f=0.48 (Dr=40%)

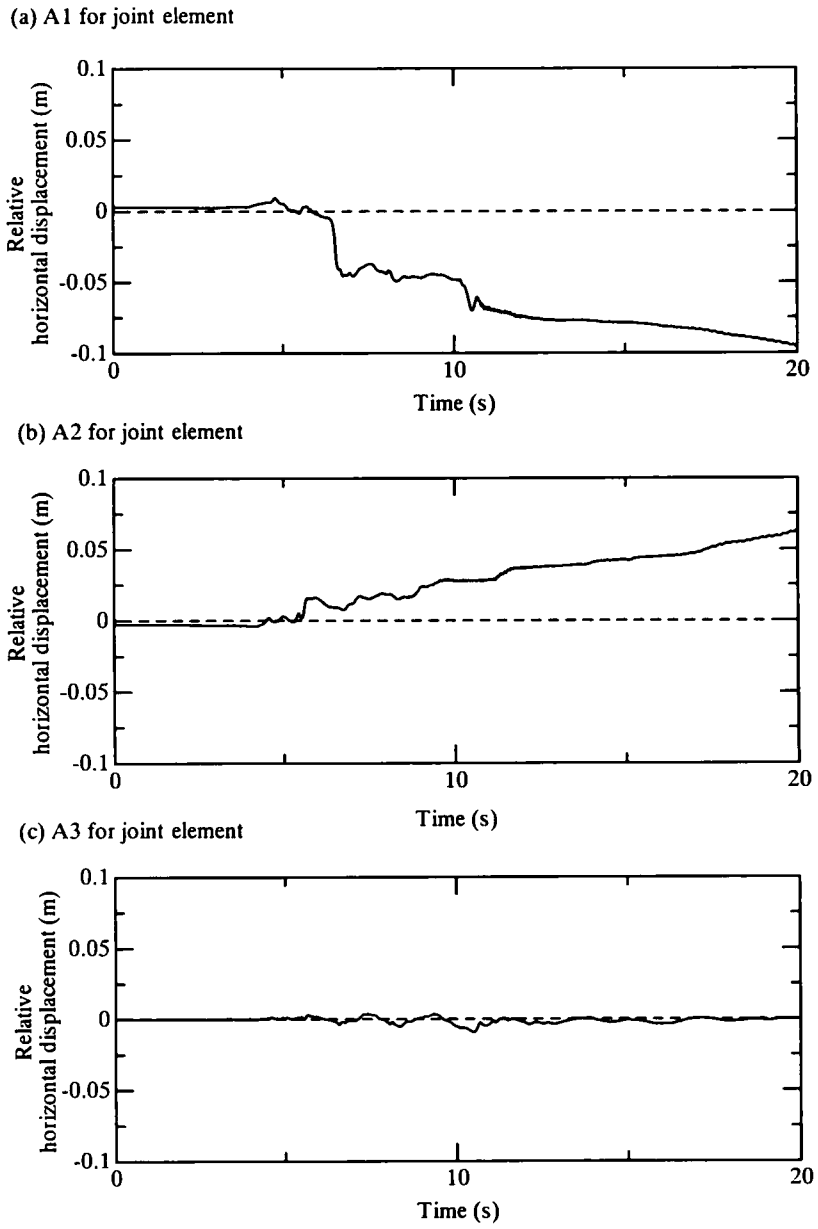

Fig. 6.16 Predicted relative horizontal displacements for joint element in Case KB2-1 with M_f=0.48 (Dr=40%)

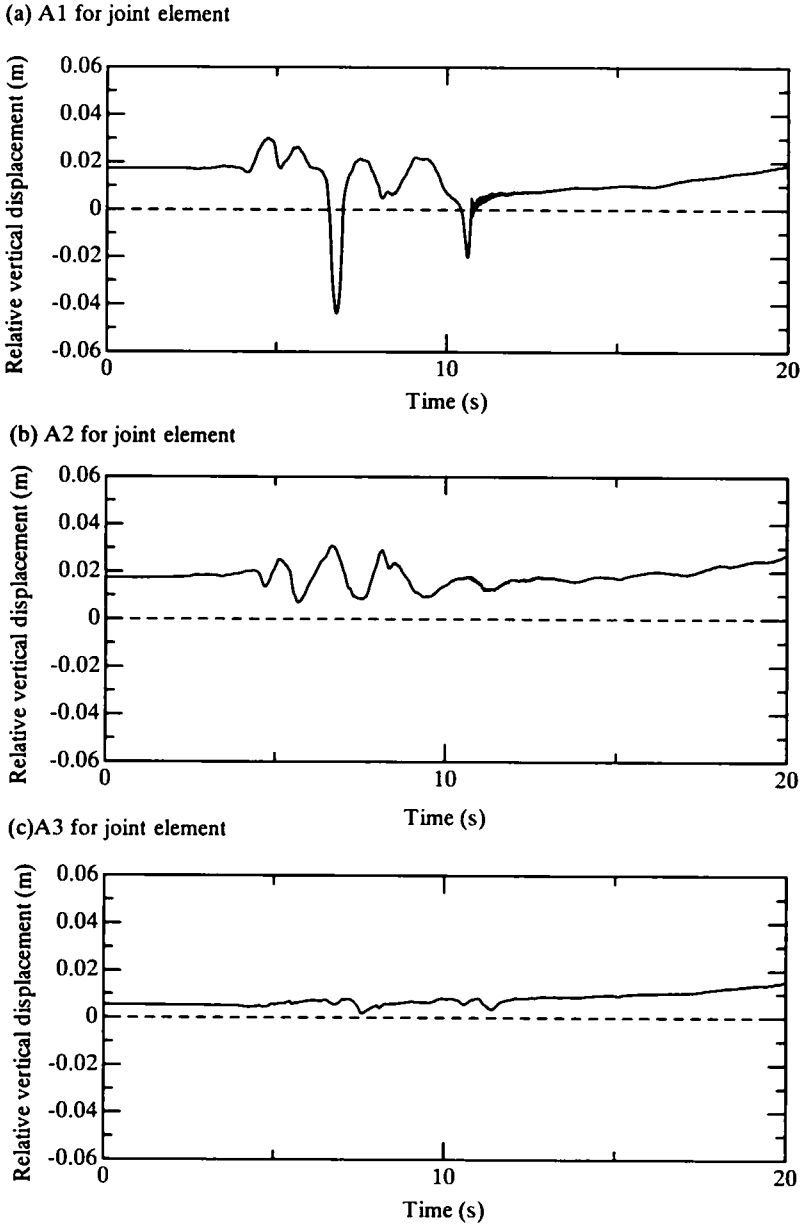

Fig. 6.17 Predicted relative vertical displacements for joint element in Case KB2-1 with M_f=0.48 (Dr=40%)

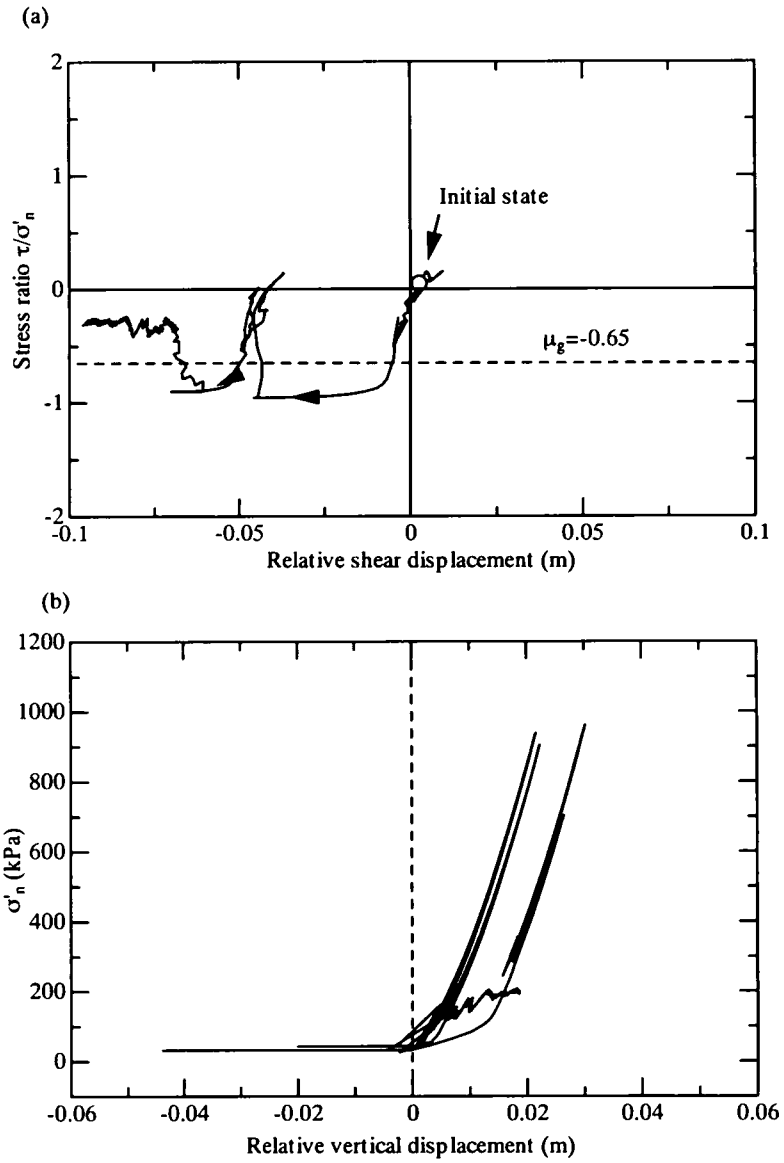

Fig. 6.18 Stress path for joint element A1 (refer to Fig. 6.2) in Case KB2-1 with M_f=0.48 (Dr=40%)

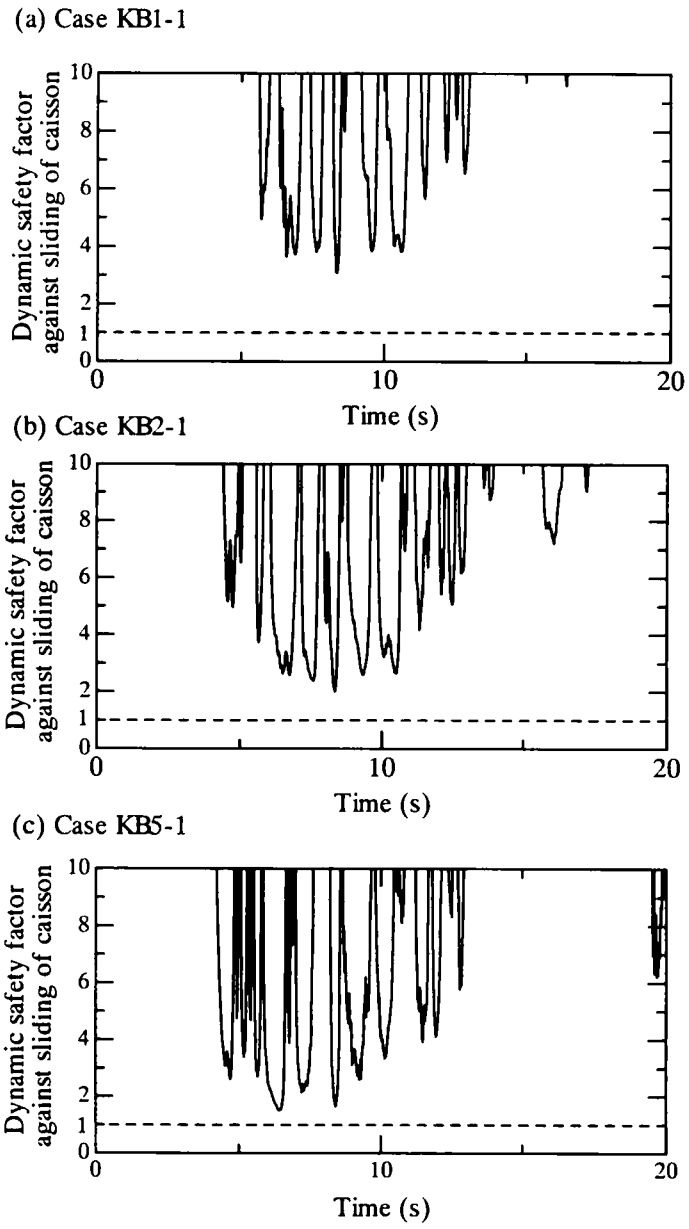

Fig. 6.19 Time histories of dynamic safety factors against sliding of caisson

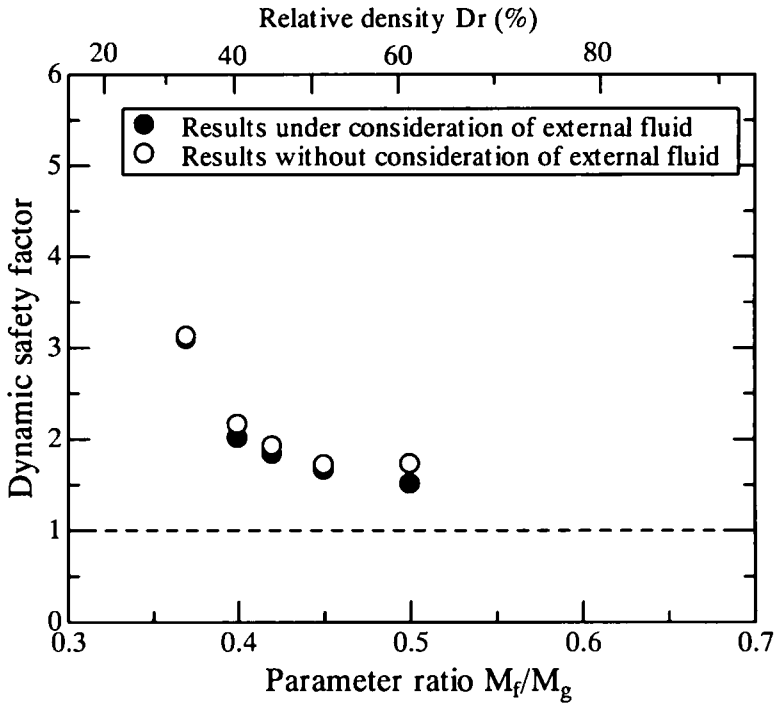

Fig. 6.20 Predicted dynamic safety factors plotted against parameter ratio M_f/M_g

CHAPTER 7

Predicted performance of composite breakwaters subjected to strong earthquakes with long-duration shaking

7.1 Introductory remarks

Concern about future strong earthquakes with long duration shaking has been expressed in many sectors for promoting preparedness against Tokai, Tonankai or Nankai earthquake. Since the most devastating type of earthquake has not occurred for about 150 years from the Ansei Tokai earthquake (1854), consequences of future Tonankai or Nankai earthquake or combined may go beyond previous experience.

Indeed, when Tokai, Tonankai and Nankai earthquakes occur together, large areas of Japan will be subjected to strong shaking over a prolonged period of time and high tsunami waves will hit the coast lines (Central Disaster Prevention Council, 2003). Distribution of the Japanese seismic intensity scale when Tokai, Tonankai and Nankai earthquakes occur together is shown in Fig. 7.1(Central Disaster Prevention Council, 2003).

An oil storage tank was severely damaged by the 2003 Tokachi-oki earthquake, coming fire disaster. It is pointed out that the cause may be related to a long-period earthquake shaking (River Bureau Ministry of Land, Infrastructure and Transport, 2004). Sloshing occurred in several oil storage tanks in Chiba Prefecture by the 2004 Kii-Hanto Oki earthquake with the long period ground motions (Hatayama et al. 2004).

Needs for prediction of accurate strong-ground motions prediction are acute. Irikura et al. (2004), for instance, examined by the recipe the validity of the earthquake source models comparing simulated and observed strong ground motions in recent large earthquakes such as the 1995 Hyogoken-Nambu earthquake and the 2003 Tokachi-oki earthquake.

The purpose of this chapter is to example the performance of composite breakwaters on

granular soils subjected to strong earthquakes with long-duration shaking, with particular emphasis seismic plastic deformation.

7.2 Accelerograms of long duration earthquakes

Tokaido-oki earthquake occurred on September 5, 2004, and a prolonged ground motion was in the Rokko Island. A typical accelerogram is shown in Fig. 7.2. Total Fourier spectrum and running spectra of the observed acceleration waveform of Rokko-G40 are presented in Fig. 7.3. The predominant period was total spectrum probed to amount to 6 seconds or so. The running spectra show that the predominant period is 2 seconds in the first part (1-100s) of acceleration waveform but 6 seconds for the second part (101-240s).

In order to investigate performance of composite breakwater when future earthquakes of long-period shaking, the present study constructed scenario ground motion in such a way that the intensity of Rokko-G40 accelerogram was increased for the peak acceleration to have 100 gal with duration of 60s. Indeed, Kobe city assume more than five or less on the seismic intensity with duration of one minute or more in the region of Kobe city when Tonankai and Nankai earthquakes occur together (Kobe city, 2004). Input horizontal acceleration constructed in the present study is shown in Fig. 7.4.

7.3 Predicted responses

The target breakwater is essentially the same as breakwater No.7 in the port of Kobe that stood prior to the 1995 Hyogoken-Nambu earthquake. A finite-element mesh used for the present dynamic analyses of breakwater No.7 is the same as shown Fig. 6.2.

The material parameter M_f was assumed 0.48 and other parameters used are same to Table 6.1 in chapter 6.

The predicted horizontal and vertical accelerations of the caisson top are shown in Fig. 7.5. The response horizontal accelerations on the caisson top amplify significantly in the early stage of shaking, but the degree of amplification became moderate in the later stage of shaking compared with the trace of the input horizontal accelerations.

The predicted plastic deformation of the composite breakwater system after shaking is shown in Fig. 7.6. The caisson settled and significantly tilted. Also, the rubble mound deformed although the impose peak acceleration only 100 gal.

The predicted time histories of vertical and horizontal displacements of the caisson top are shown in Fig. 7.7. The caisson rocked and settled significantly with shaking cycles over a long duration of 60s, exhibiting the average settlement as large as caisson top underwent and maximum amplitude reached.

The predicted distributions with depth, of the vertical strain ε_{yy}, the lateral strain ε_{xx} and the volumetric strain ε_v in foundation soil along the centerline of the caisson after shaking (t=60s) are shown in Fig. 7.8. The soil elements below the caisson structure underwent significant amounts of vertical compression (Fig. 7.8 (a)) that were accompanied by equally significant lateral expansion (Fig. 7.8(b)). The plastic deformation of foundation soil occurred under partial drainage condition (Fig. 7.8 (c)).

The predicted stress paths and time history of excess pore pressure below the caisson are shown in Fig. 7.9, Fig. 7.10 and Fig. 7.11. At the deepest level (EK1) and mid level (EK2) in the foundation soil below the caisson, excess pore pressure increased rapidly in the early stages of the main earthquake shaking. However, excess pore pressure gradually dissipates during main shaking. Excess pore pressure at the shallow level (EK3) indicated negative value due to dilatancy.

The predicted stress paths and time history of excess pore pressure in the foundation soil of seabed (EK4) are shown in Fig. 7.12. The predicted stress states reached the phase transformation line and presented dilatancy behavior. The predicted excess pore pressure in the sand backfill of seabed was very closed to on initial effective vertical stress s'_{v0} values.

7.4 Subjects for future study

In this chapter, the effect of scenario earthquakes of moderate shaking yet having a prolonged duration has been investigated. The caisson significantly settled and tilted although the impose peak acceleration only 100 gal. Furthermore, constitute relation under complex effective stress paths that are difficult to imagine to occur under field condition happened, unless integrated partial-drainage analyses such as those adapted in this study. In such an earthquake shaking having a prolonged duration, deformation of foundation soil may be received the effect of partial drainage condition and dilatancy during cyclic shearing.

A more detailed analyses in the future is necessary to investigate complex stress paths and excess pore pressure development, depending on the importance of such factors as:

- Initial state of stress
-Dilatancy
- Partial drainage or undrained condition
-Constitutive relations

Future will see above-mentioned factors by experimental work and numerical study.

7.5 Conclusions

The influence of scenario earthquakes of moderate shaking yet having a prolonged duration has been investigated. The caisson settled and significantly tilted. Also, the rubble mound deformed although the impose peak acceleration only 100 gal. Furthermore, constitute relation under complex effective stress paths that are difficult to imagine to occur under field condition happened, unless integrated partial-drainage analyses such as those adapted in this study. Also, it refers to some responsible factors that need further future studies.

References

Kobe city (2004). Preparation for Nankai, Tonankai earthquakes and tsunami, *http://www.city.kobe.jp.*

Special Board of Investigation for Tonankai and Nankai earthquakes. (2003). Report for Tonankai and Nankai earthquakes, *Central Disaster Prevention Council*, No. 2-2.

River Bureau Ministry of Land, Infrastructure and Transport (2004). Long period earthquake Disaster islands 2004, JAPAN, 40.

Hatayama K., Zama S., Yamada, H. Nishi, H and Hirokawa, M. (2004). Sloshing of oil tank and long period wave motion by 2004 Kii-Hanto Oki earthquake and Tokaido-Oki earthquake, *Official Home page(http://www.fri.go.jp),National Research Institute of Fire and Disaster*.1-11.

Irikura, K., Miyake, H., Iwata, T. Kamae, K., Kawabe, H. and Dalguer, L. A. (2004). Decipe for predicting strong ground motions from future large earthquakes, *13th World conference on earthquake engineering*, Vancouver, B.C., Canada, Paper No. 1371

Strong Earthquake Observation System for Port Area, Roko-G40 (2004). *Port and Airport Research Institute.*

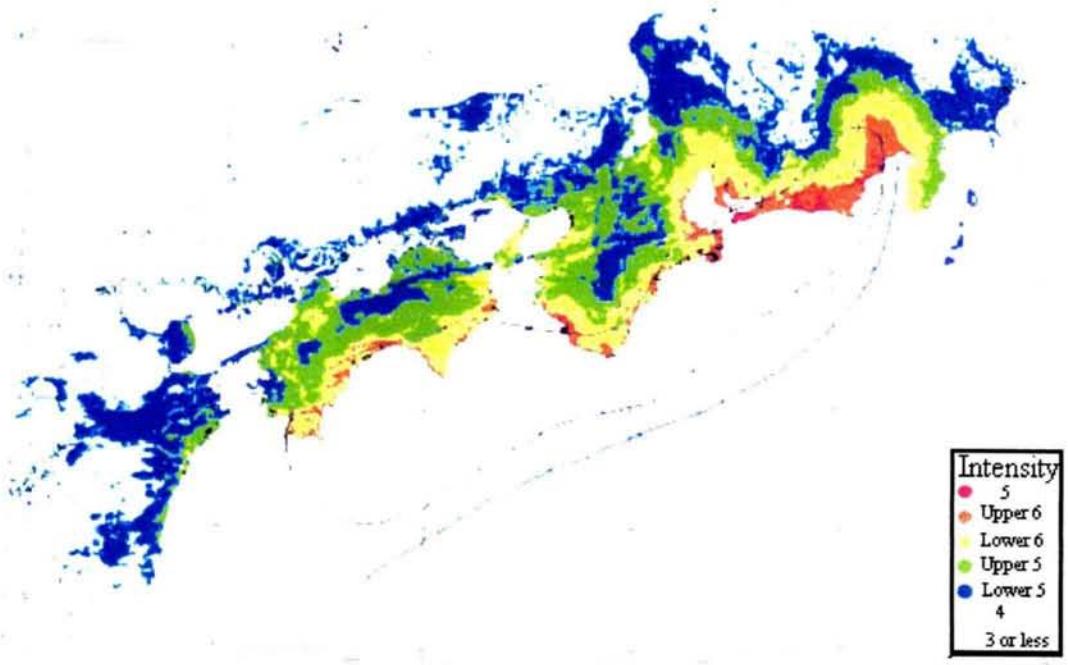

Fig. 7.1 Distribution of the Japanese seismic intensity scale when Tokai, Tonankai and Nankai earthquakes occur together (Central Disaster Prevention Council, 2003)

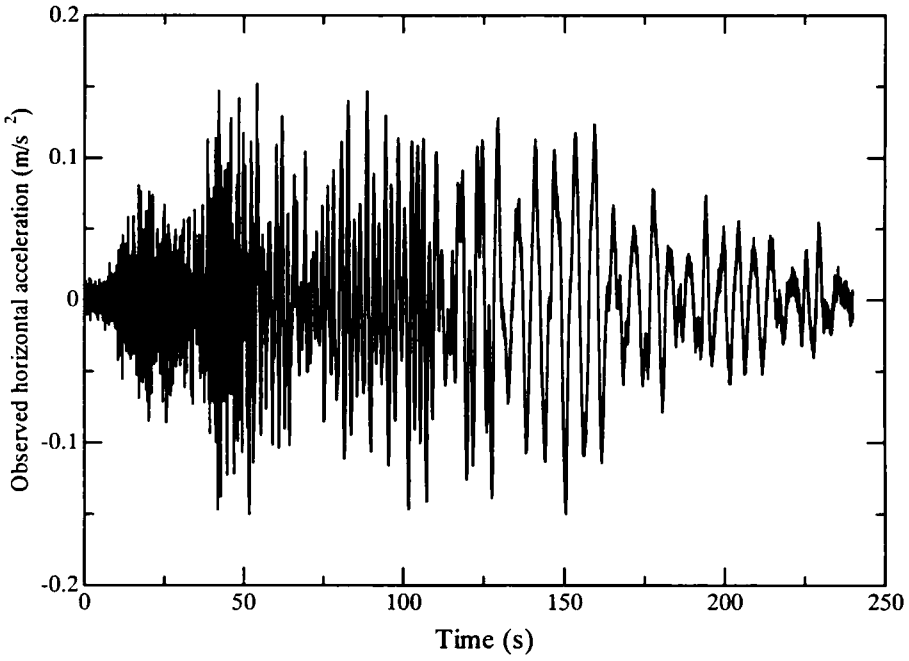

Fig. 7.2 Observed acceleration waveform, designated Roko-G40, of the 2004 Tokaido-oki earthquake (Port and Airport Research Institute, 2004)

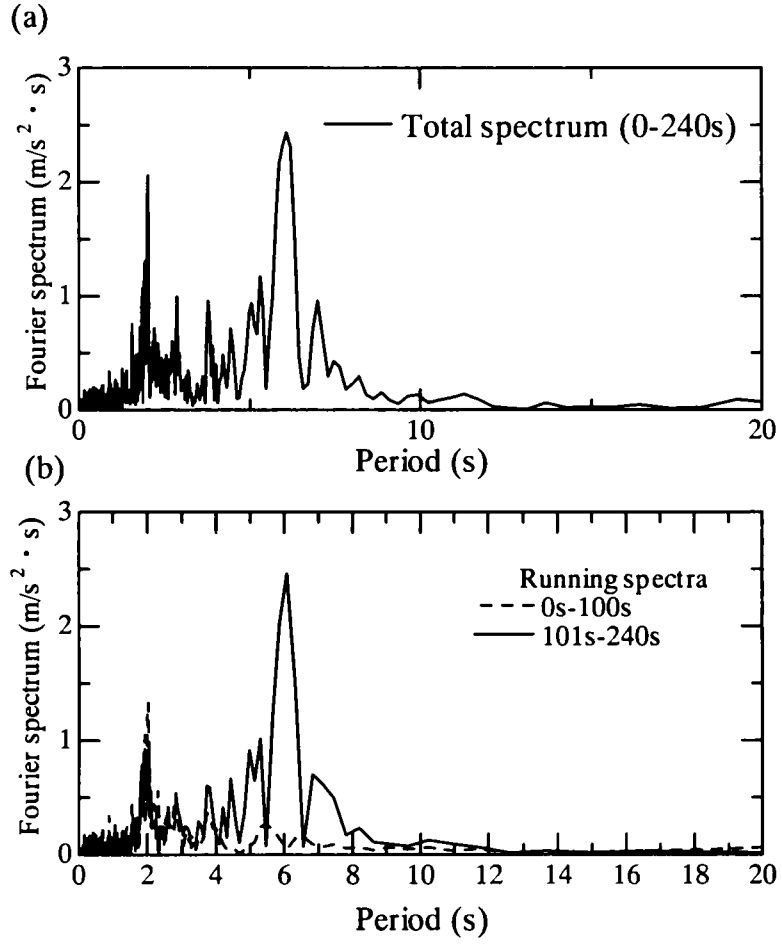

Fig. 7.3 Running spectra for observed acceleration waveform of Roko-G40

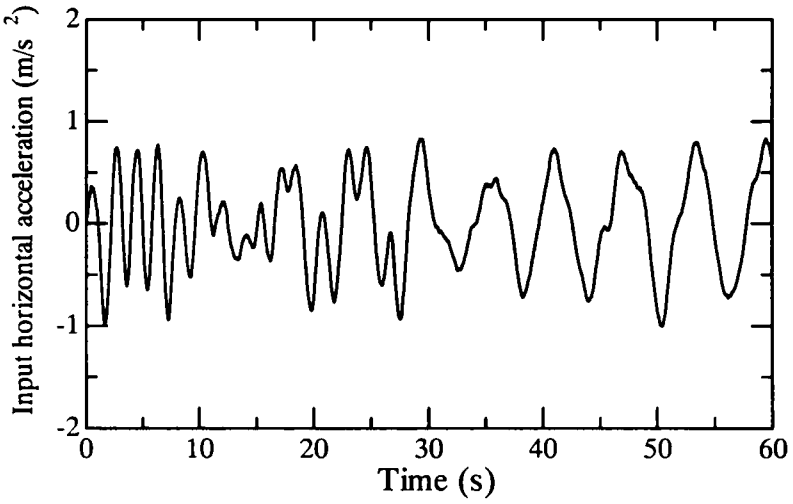

Fig. 7.4 Input horizontal acceleration with prolonged period of shaking with a peak accelerate intensified to have 100 gal

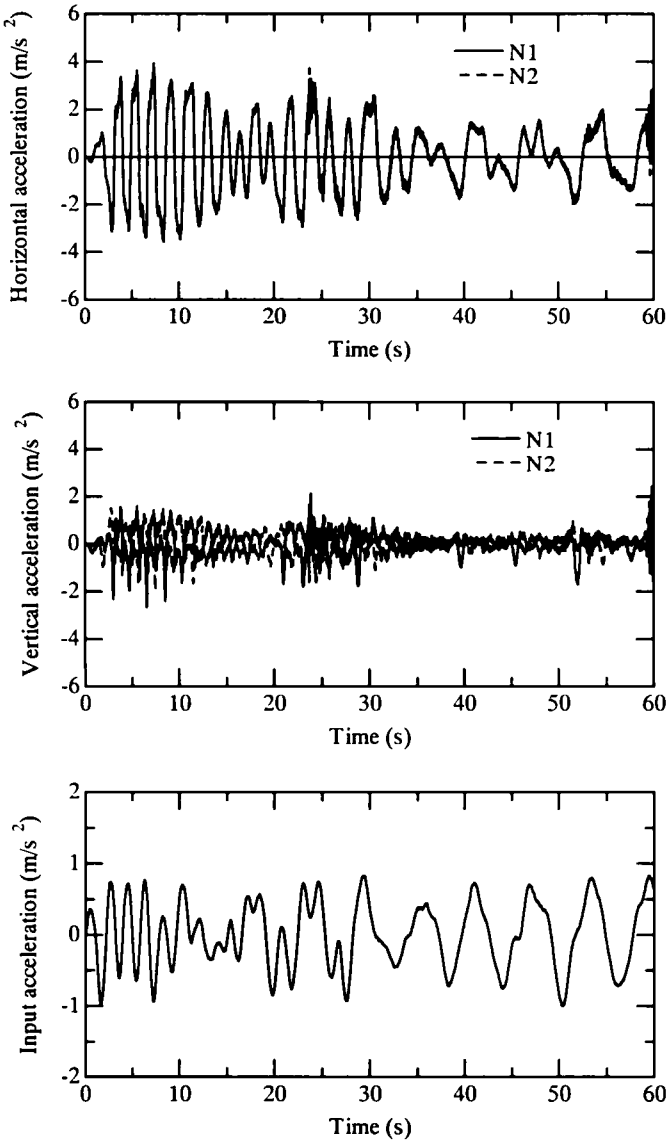

Fig. 7.5 Predicted horizontal and vertical accelerations on top of the caisson structures, together with input horizontal acceleration

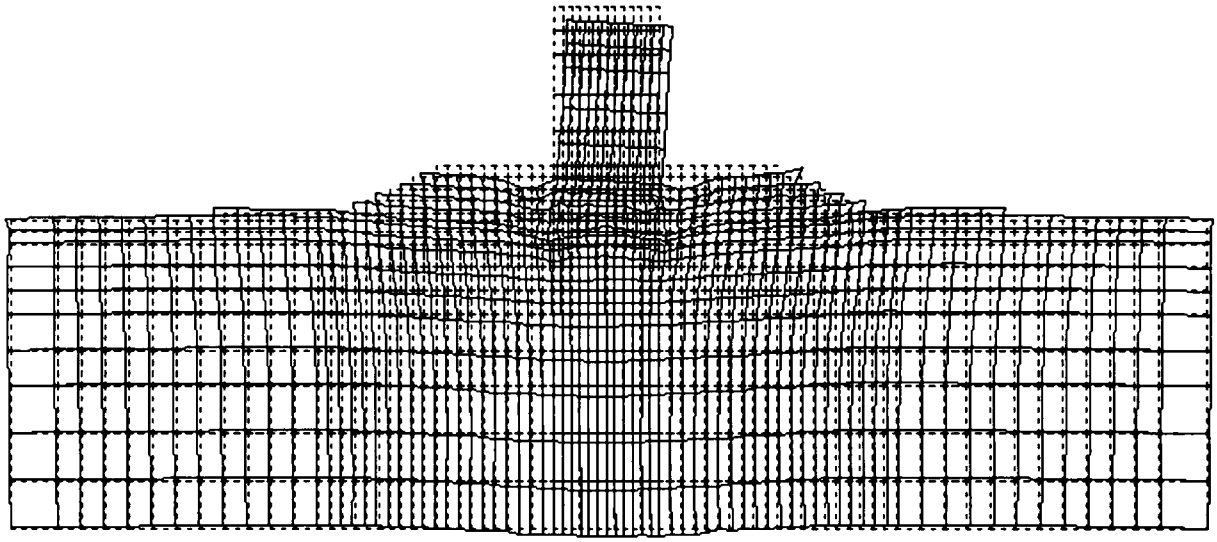

Fig. 7.6 Predicted plastic deformation of the composite breakwater No. 7 after shaking

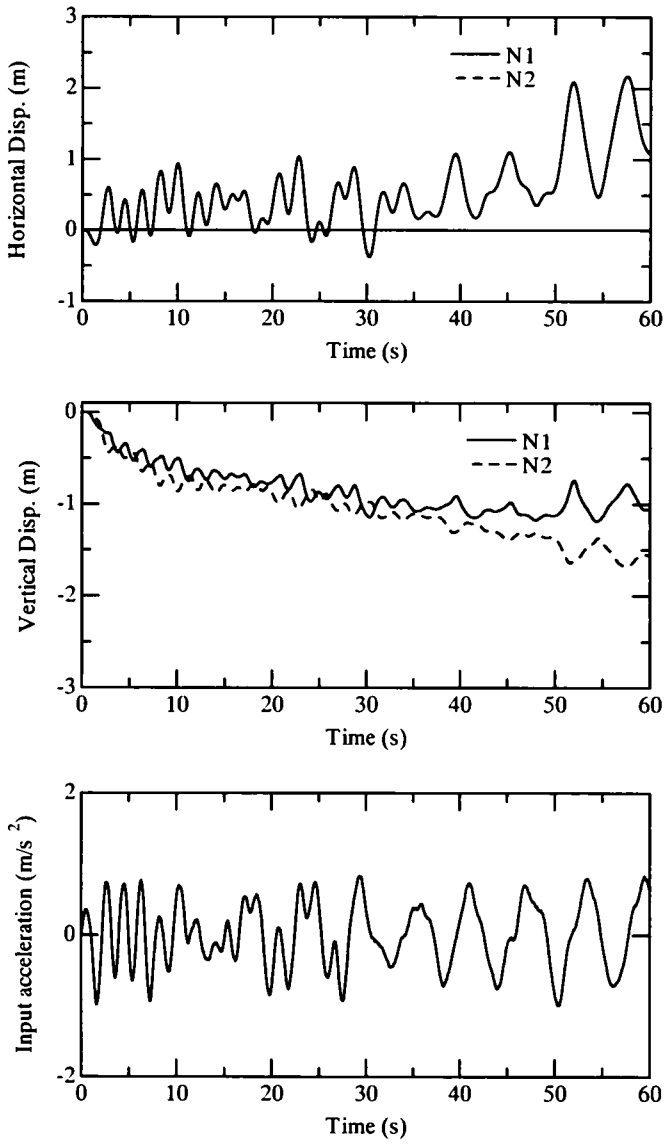

Fig. 7.7 Predicted time histories of horizontal and vertical displacements of the caisson top, together with input acceleration time history

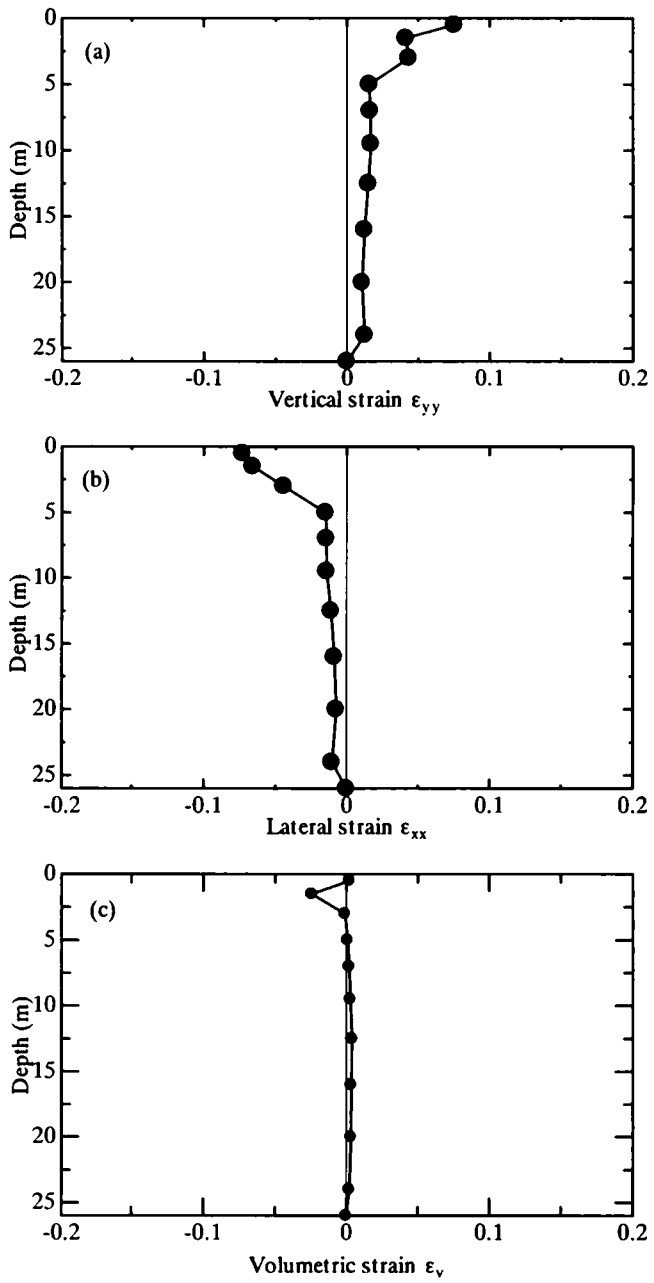

Fig. 7.8 Predicted distributions with depth of (a) vertical strains, (b) lateral strains and (c) volumetric strains in the foundation soil along the centerline of the caisson after shaking (t=60s)

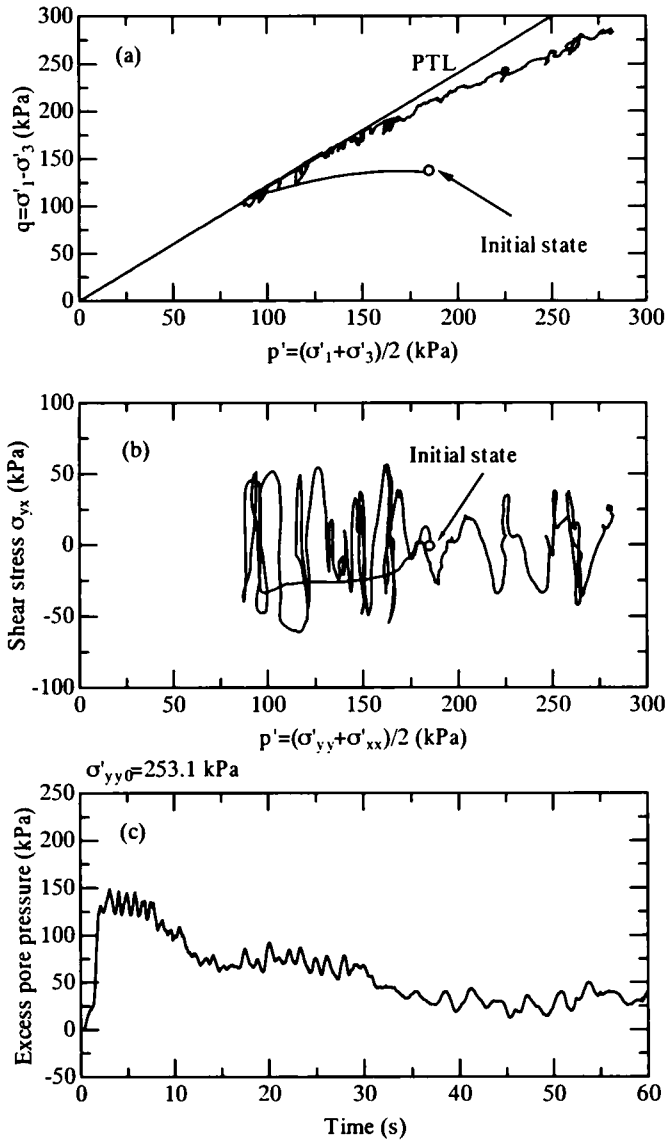

Fig. 7.9 Predicted stress paths and time history of excess pore pressure in element EK1 below the caisson

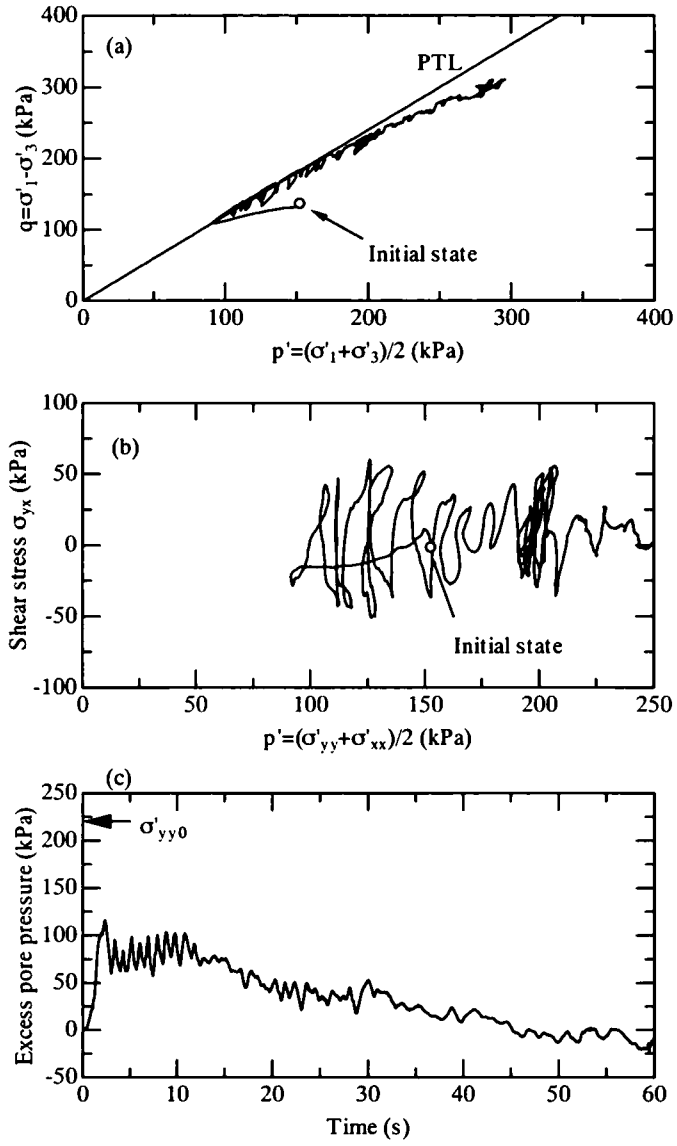

Fig. 7.10 Predicted stress paths and time history of excess pore pressure in element EK2 below the caisson

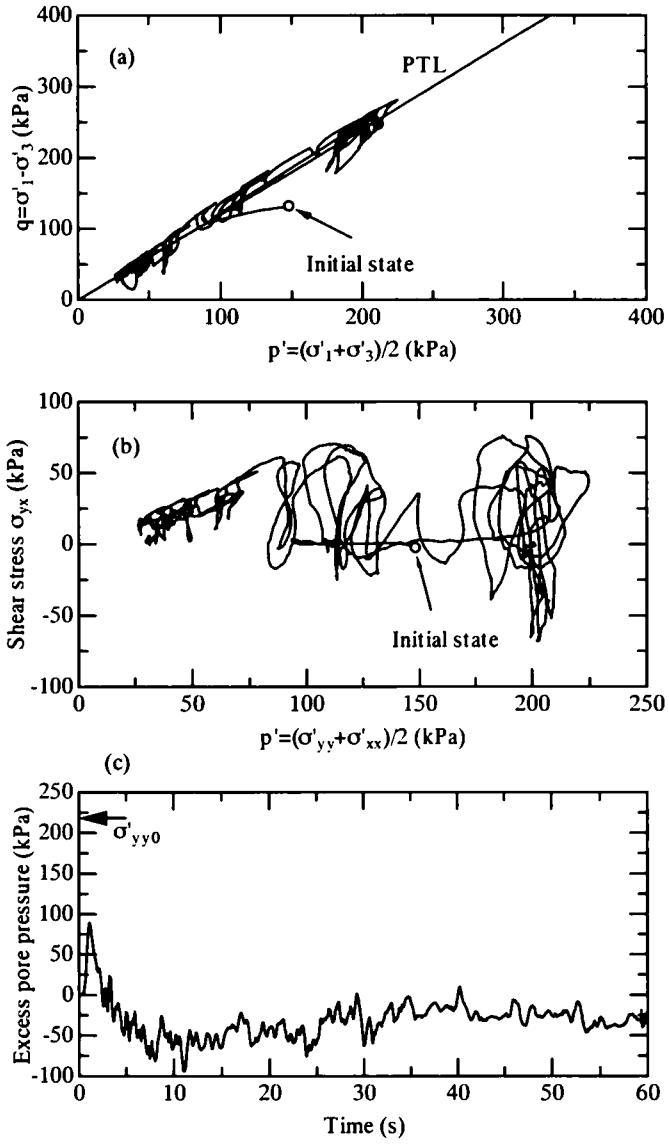

Fig. 7.11 Predicted stress paths and time history of excess pore pressure in element EK3 below the caisson

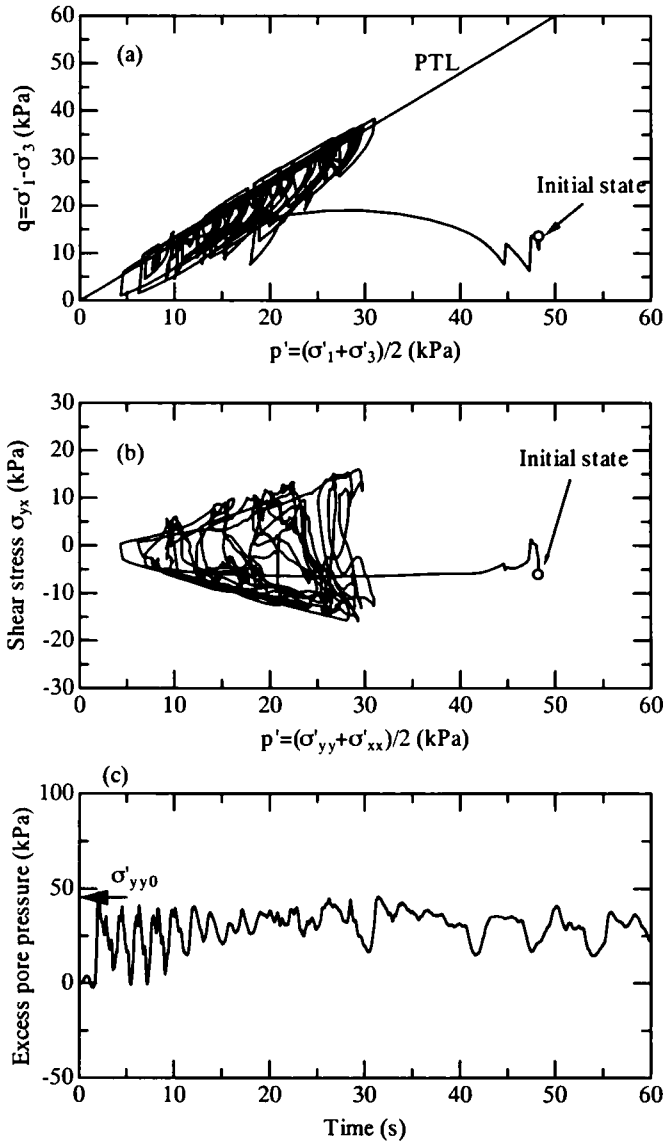

Fig. 7.12 Predicted stress paths in element EK4

PART III

PERFORMANCE OF CONTROLLED DISPOSAL SITE UNDER DYNAMIC LOADING

CHAPTER 8

Predicted seismic behavior of controlled disposal site with special reference to the performance of water-shielding sheets

8.1 Introductory remarks

The construction of disposal facilities in inland areas has become increasing difficult in view of comprehensive environmental requirements. In contrast, the construction and maintenance of disposal facilities in nearshore areas are conceived as being more favorable from environmental and engineering standpoints (Miyake, 1997; Waterfront Vitalization and Environment Research Center, 2000). Thus the performance of wave-resistant structures and water-shielding sheets has recently received much attention regarding the design of controlled disposal sites in waterfront areas. The author considers that more developments are necessary in the studies of water-shielding sheets subjected to wave-pressure related fluctuations in pore pressures in controlled disposal sites (Baba et al., 2002; Kotake et al., 2004a; 2004b). Also, the performance of such water-shielding sheets need a critical examination in view of high seismicity in most of the nearshore areas in Japan.

Koerner and Daniel (2004) discussed the stability of a cover soil layer over a water-shielding sheet in terms of a conventional seismic-intensity method, but did not make any study of the earthquake-resistant performance of the water-shielding sheet itself. Kano et al. (2004) carried out a range of laboratory tests that focused on the deformability of water-shielding sheets under earthquake shaking. However, their experimental procedure has limitations in the sense that only the static localized loading was applied on to the water-shielding sheets without any adjacent soil.

In what follows, the author attempts to apply the proposed analysis procedure to assessing the seismic behavior of a controlled disposal site in the waterfront area, with special reference to the performance of water-shielding sheets installed.

8.2 Ground conditions and material parameters

Plan view of controlled disposal site in Shikogu-Chuo city, Aichi prefecture is shown in Fig. 8.1 (Kotake et al. 2004c). This controlled disposal site was built on seashore and paper slag ashes of 300,000m^3 will be mainly disposed (Photo 8.1) (Website of Toyo construction., 2004).

Cross section of controlled disposal site is shown in Fig. 8.2. Coarse-gravel (1-200kg) was used for the rubble mound supporting the caisson and for rubble backfill. A hybrid-slotted type caisson with a low reflection ratio rested on the mound. Converter furnace slag was used for backfill soil. A water-shielding sheet on surface of backfill soil was covered and converter furnace slag was put on the water-shielding sheet to restrain of it.

Finite-element mesh on caisson type seawalls for controlled disposal site is shown in Fig. 8.3. This model targets controlled disposal site where wastes is not disposed. In this condition, overburden soil on backfill soil is small and then it is thought to be severe conditions for deformation of backfill soil.

The side boundaries and base boundaries were set to be viscous boundary. Since hybrid-slotted type caisson was used, external fluid and joint element are not taking into consideration in finite-element model. The water-shielding sheet was set up as undrained boundary. However, the modeling of the water-shielding sheet was not done. It is because of the idea that the water-shielding sheet is deformed with soil.

Constitutive model parameters selected are summarized in Table 8.1. Basically, all the constitutive model parameters were determined from a range of parametric finite-element analyses, in such a way that the predicted performance was in general agreement with what has been observed in the drum-centrifuge wave testing (Baba et al., 2002).

Input acceleration in the present analysis is observed acceleration record at Port Island (GL. -32m), in NS direction (refer to Fig. 6.3 in Chapter 6).

8.3 Predicted seismic behavior of controlled disposal site

8.3.1 Seismic deformation of controlled disposal site

The predicted deformation of controlled disposal site after shaking is shown in Fig. 8.4. Overall deformation was small, whereas foundation soil under the slope of cover soil indicated deformation into a land-side. There is no reason to think that the functional damage could be occurred by deformation.

The predicted time histories of displacements of the caisson top are shown in Fig. 8.5. Caisson represented small values of horizontal and vertical displacements.

8.3.2 Predicted effective stress states and excess pore pressures

The predicted shear stress and shear strain curve, effective stress path, and time history of excess pore pressure in element EM1 are shown in Fig. 8.6. The shear strain was not accumulated and the mean effective stress fluctuated in the range closer to the phase transformation line during the shaking and excess pore pressure was far away from initial effective vertical stress.

The predicted shear stress and shear strain curve, effective stress path, and time history of excess pore pressure in element EM2 of free field are shown in Fig. 8.7. The shear strain indicated one percentage or less. Also, mean effective stress decreased in the early stage and fluctuated in the range closer to the phase transformation on reaching to phase transformation line during the shaking. The excess pore pressure increased during the shaking, but did not indicate the occurrence of the liquefaction.

The predicted shear stress and shear strain curve, effective stress path, and time history of excess pore pressure in elements EM3 and EM4 of backfill soil are shown in Fig. 8.8 and Fig. 8.9. The element EM3 represented small value of maximum shear strain. However, the shear strain was accumulated to 3 percentages. The mean effective stresses in elements EM3 and EM4 fluctuated in the range closer to the phase transformation on reaching to phase transformation line during the shaking. The excess pore pressure in elements EM3 and EM4 indicated markly negative value due to dilatancy during the shaking.

8.3.3 Performance of water-shielding sheets

Let us suppose that local coordinates of water-shielding sheet may be shown in Fig. 8.10, and translate global coordinates into local coordinates. Note that the deformation of water-shielding sheet means deformation of backfill soil.

The axial strains in water-shielding sheet 1 and sheet 2 with respect to tangential direction are shown in Fig. 8.11. Here, positive strain means extension of sheet. Water-shielding sheets 1 and 2 indicated cyclic extension and compression strains during shaking. The maximum strains became almost 2.2 and 2.4 percentages at the shallow position S1 of sheet1 and sheet 2, respectively.

The residual strain distributions of sheet 1 and sheet2 after shaking are shown in Fig. 8.12. The residual strains of sheet 1 and sheet 2 are concentrating at shallow position. In contrast, the residual strain at the mid position indicated very small value, although the residual strain distribution was uneven.

8.4 Discussions

It is important to note deformation properties of water-shielding sheets in controlled disposal site due to the earthquake. It is because that changing of permeability with deformation of water-shielding sheet could be resulted in outflow of waste from controlled disposal site.

The predicted performance of water-shielding sheets indicated small value of residual strain. However, comparising predicted strain between shallow position and other positions, predicted strain at the shallow domain showed remarkable extension strain. It is correspond to observed results of Kano et al. (2004) that investigated deformation properties of water-shielding sheets due to earthquake.

On the other hand, extension ratio of water shielding-sheet used was 200 percentages or more (Maeda et al., 2004). Therefore, it is assumed that the predicted strain of water shielding-sheet is not what affects the soundness of sheet. However, the author must point out that it is careful enough to extension performance of water-shielding sheet at the shallow domain.

8.5 Conclusion

The behavior of the controlled disposal site in the waterfront area subjected to strong earthquake shaking has been discussed based on the proposed analysis procedure in terms of the finite-element method. The calculations show that extensional straining of the order of 2% can develop in the water-shielding sheet during strong shaking, and that the extensional straining tends to concentrate on the section with shallow soil cover. The latter finding is in qualitative agreement with the experimental results of Kano et al. (2004).

References

Baba, S., Miyake, M., Tsurugasaki, K., Kim, H. (2002). Development of wave generation system in a drum centrifuge, *ICPMG2002, Canada, 265-270.*

Kano, S., Oda, K., Yoshida, M. and Mitoh, M. (2004). Deformation properties of waterpoof sheets due to the earthquake damage deformation of seawalls for controlled waste disposal site, *Annual journal of coastal engineering* , Vol. 51, JSCE, 796-800

Kotake, N., Kitade, N., Turugasaki, K., Baba, S. (2004a). Strain measurement of geomembrane with strain gauges, *Proc. of the 39th Japan national conf. on geotechnical engineering*, 2305-2306.

Kotake, N., Kitade, N., Turugasaki, K., Baba, S., Nishino, Y., Tokunaga, K. and Morita, K.

(2004b). Strain measurement of liner sheet in a coastal wate disposal site, *Proc. of the 39th Japan national conf. on geotechnical engineering*, 2307-2308

Kotake, Y., Turugasaki, K., Baba, S., Miyake, M., Fujiwara, R., Kaneko, K., Tezuka, T., Tokunaga, K. and Moriya, K. (2004c). Field observation of pore water pressure in the backfill space of a caisson-type bulkhead for wast dispose, *Annual journal of coastal engineering* , Vol. 51, JSCE, 681-685

Koerner, R. M. and Daniel, D. E. (2004). "Final covers for solid waste landfills and abandoned dumps", Gihodo, 205-211(Japanese translation by Kamon, M., Katsumi, T. and Kondo, M.).

Maeda, S., Yamamura, K., Ueda, M., Inoue, T., Asada, H., Sakamoto, A., Akai, T. and Kamon, M. (2004). Performance evaluation in analysis on the waste disposal sites in the sea using triple liner system with polyurethane elastomer grouted between double geomembrane sheets, *Proc. of the 39th Japan national conf. on geotechnical engineering*, 2233-2234.

Miyake, M. (1997) Amagasaki offshore refuse landfill in Osaka bay phoenix project, *Bulgarian-Japanese seminar on geotechnics of soft soils*, 87-102.

Waterfront Vitalization and Environment Research Center, (2000). Manual for Design, construction and management of controlled disposal site,.1-86(in Japanese).

Website of Toyo construction. (2004). *http://www.toyo-const.co.jp/tech/kankyou/18.html*.

Table 8.1 Constitutive model parameters used

Material	Mg	M_f	α	β_0	β_1	H_0^*	Hu0 (kPa)	γ_u	γ_D	K_0	k m/s
Backfill soil	1.2	0.8	0.35	20.0	0.04	1500	8000	4	3	0.56	0.00025
Rubble mound	1.2	0.9	0.35	20.0	0.04	1500	8000	4	3	0.56	1.0
Seabed	1.2	0.8	0.35	20.0	0.04	1500	8000	4	3	0.56	0.0005

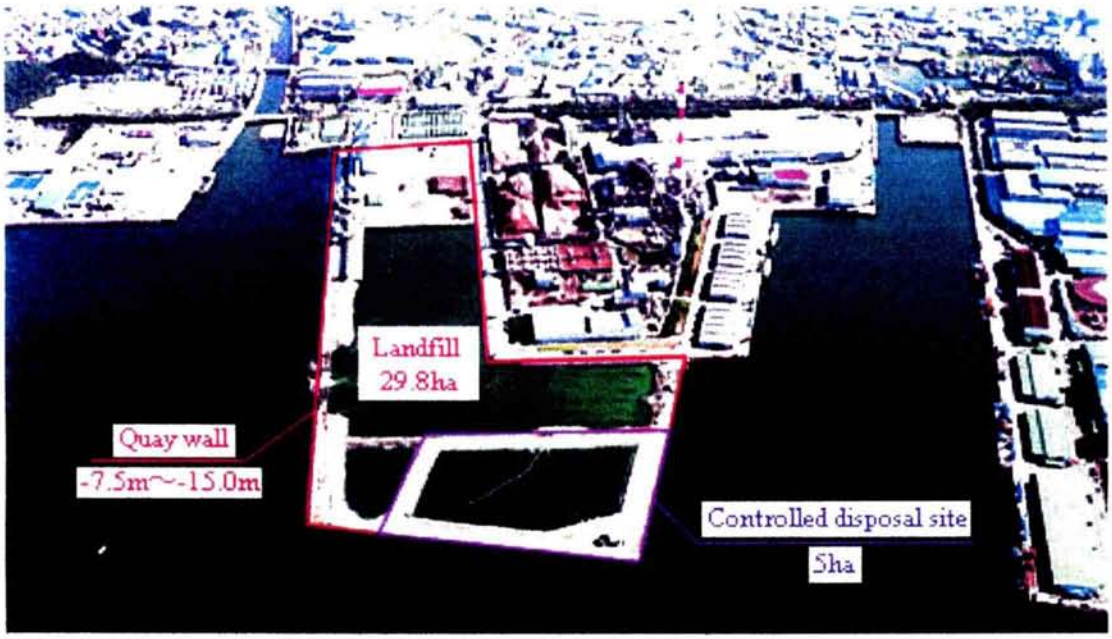

Photo 8.1 Aerophotograph of controlled disposal site in Shikogu-Chuo city (Website of Toyo construction., 2004)

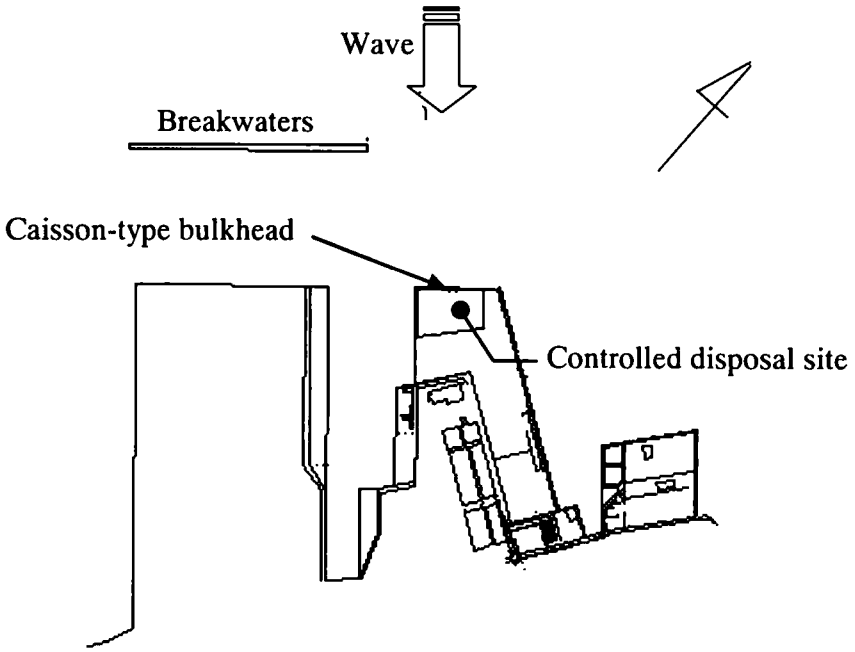

Fig. 8.1 Plan view of controlled disposal site in Shikogu-Chuo city (Kotake et al., 2004c)

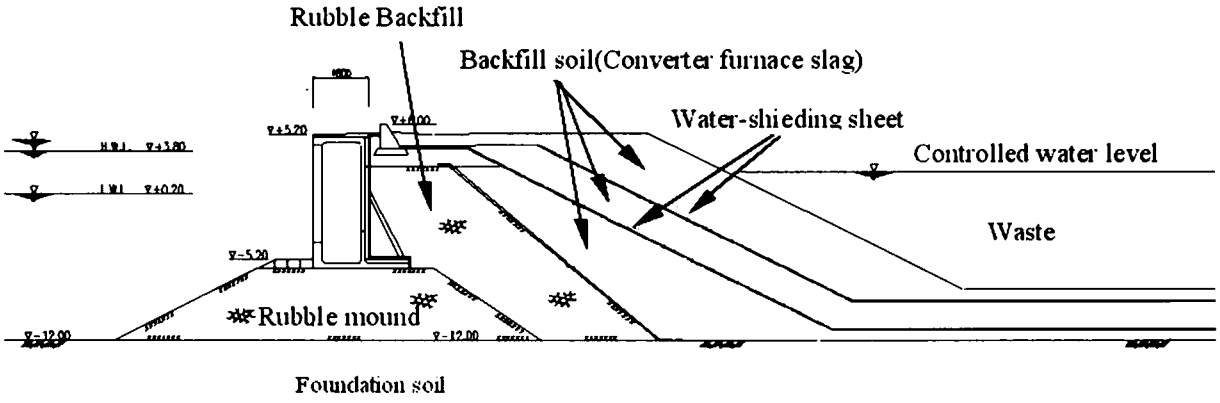

Fig. 8.2 Cross section of controlled disposal site (Kotake et al., 2004c)

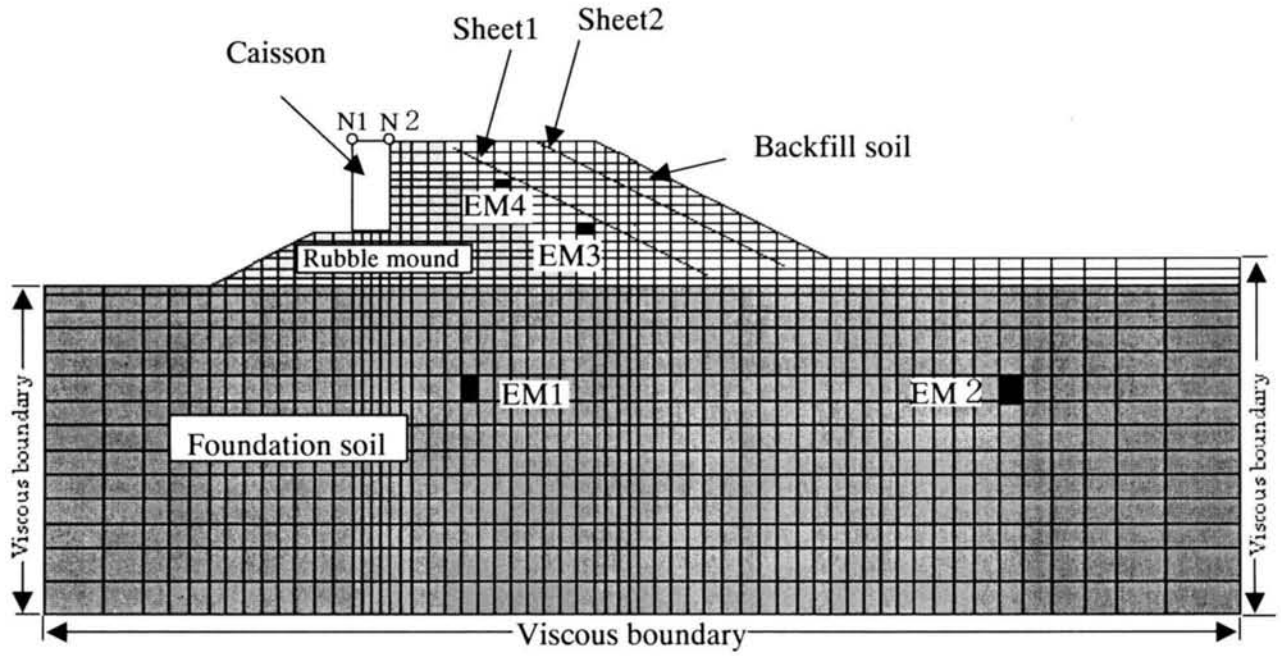

Fig. 8.3 A finite-element mesh used for analysis

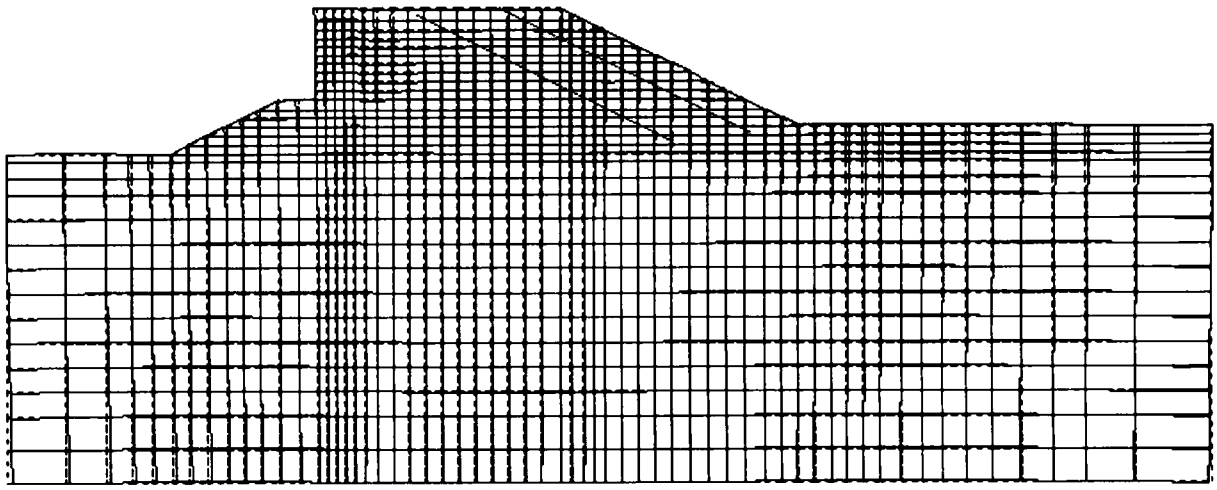

Fig. 8.4 Predicted deformation of controlled diposal site

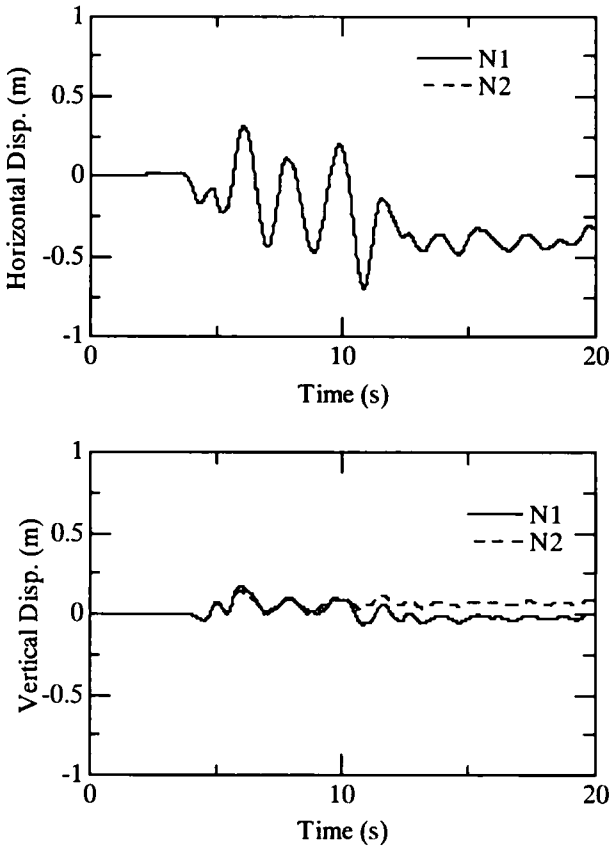

Fig. 8.5 Predicted time histories of horizontal and vertical displacements of the caisson top

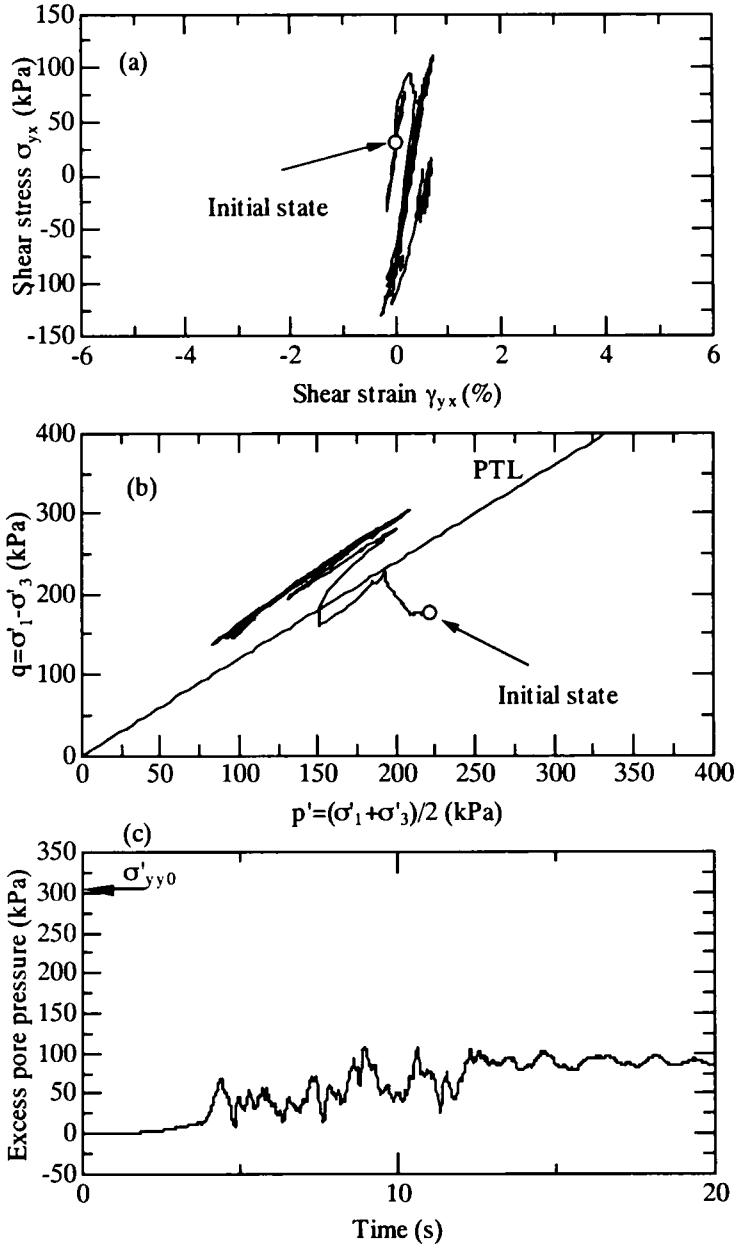

Fig. 8.6 (a) Shear stress and shear strain curve, (b) effective stress path, and (b) time history of excess pore pressure in element EM1

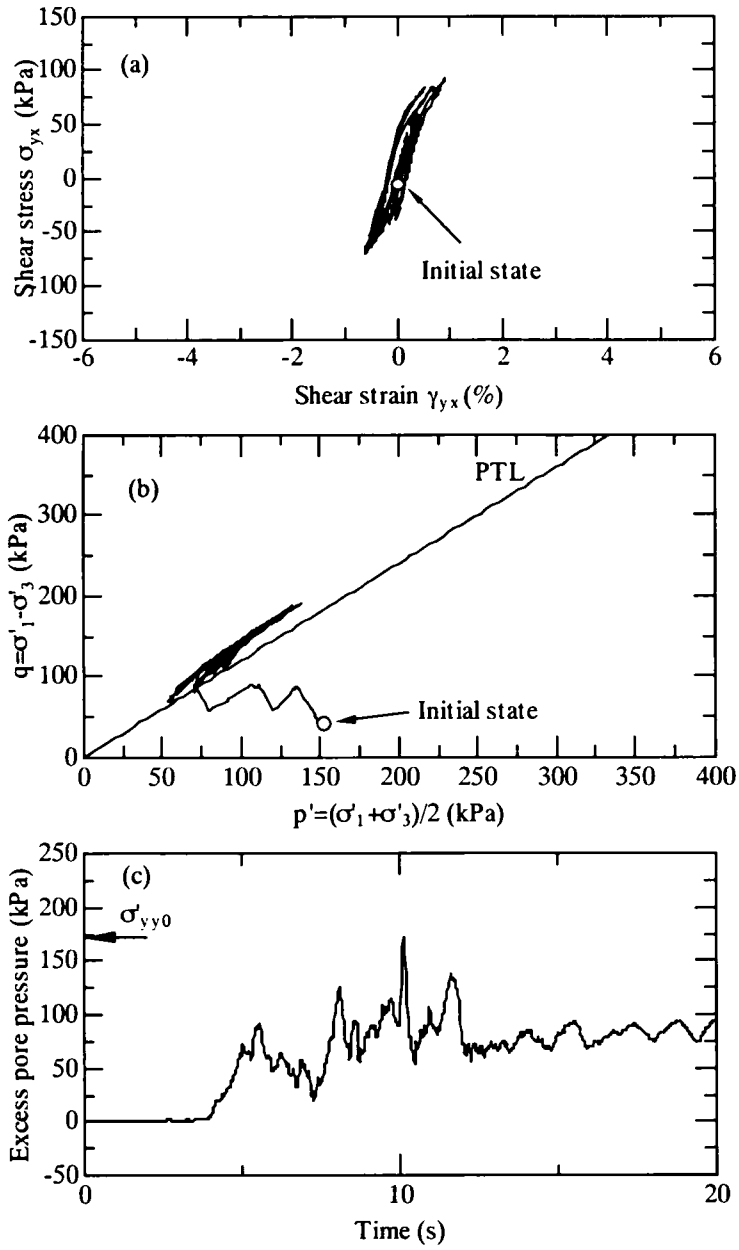

Fig. 8.7 (a) Shear stress and shear strain curve, (b) effective stress path, and (b) time history of excess pore pressure in element EM2

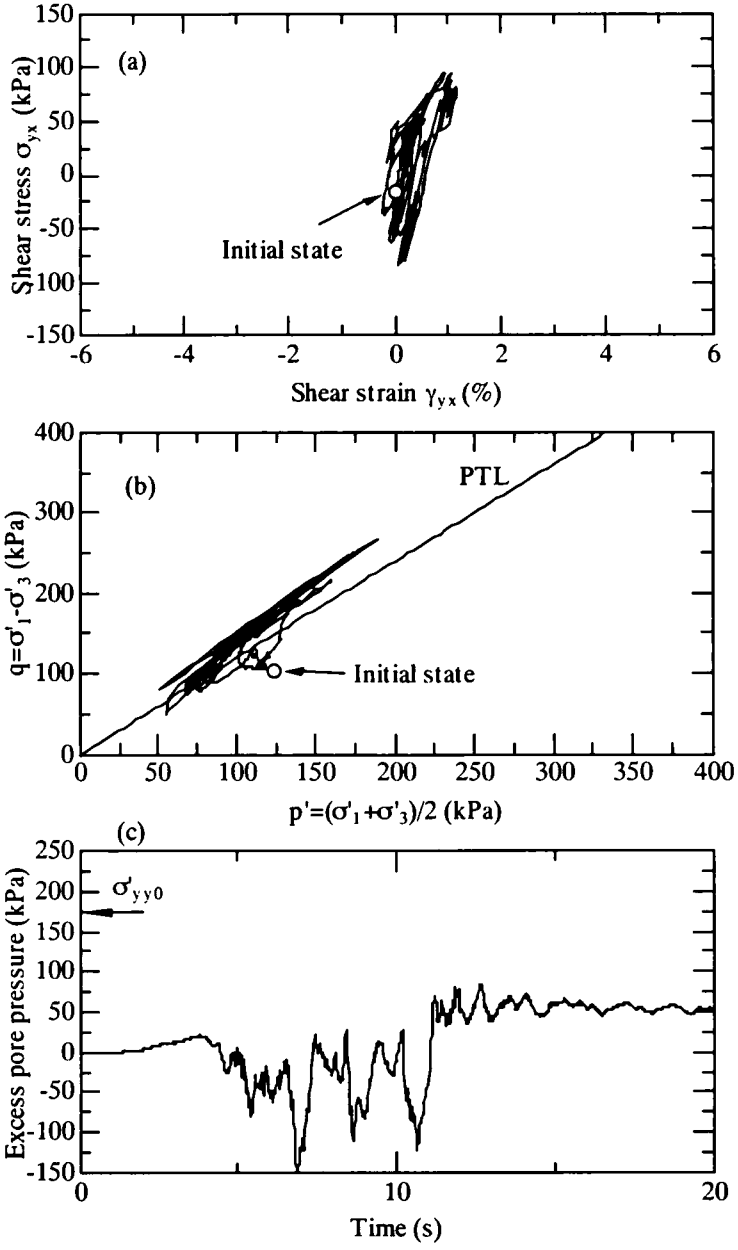

Fig. 8.8 (a) Shear stress and shear strain curve, (b) effective stress path, and (b) time history of excess pore pressure in element EM3

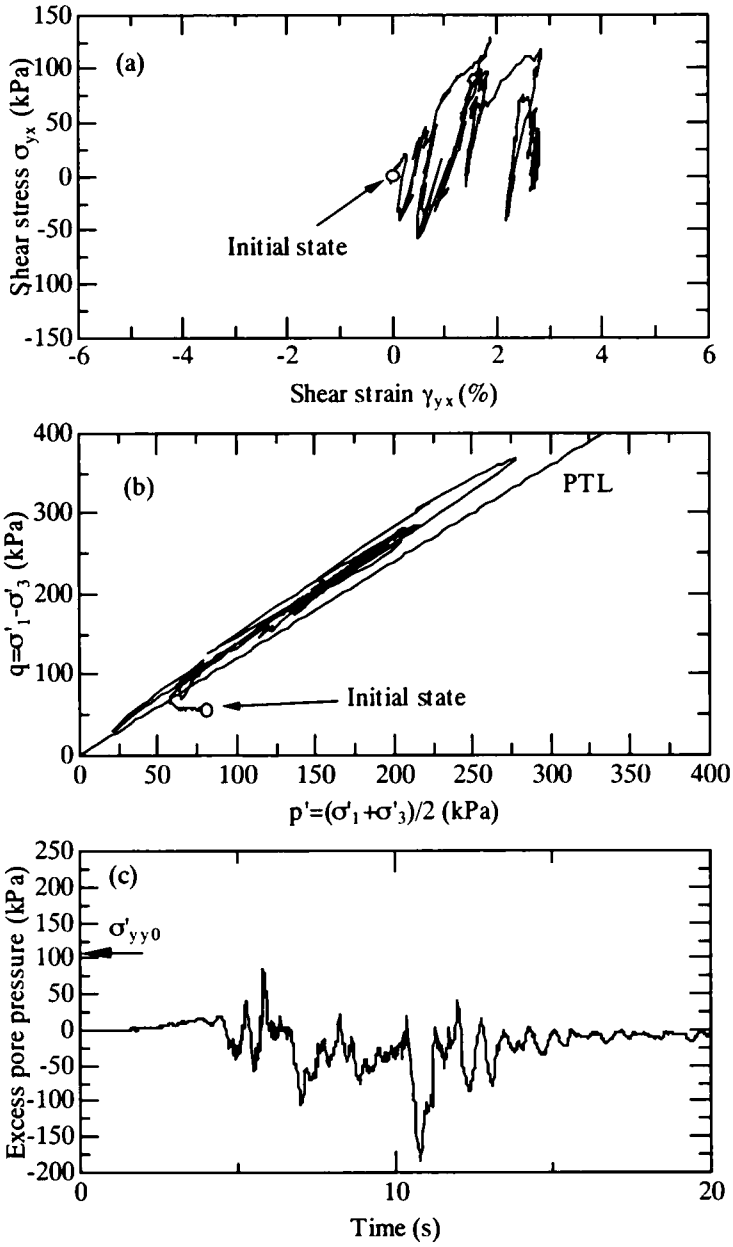

Fig. 8.9 (a) Shear stress and shear strain curve, (b) effective stress path, and (b) time history of excess pore pressure in element EM4

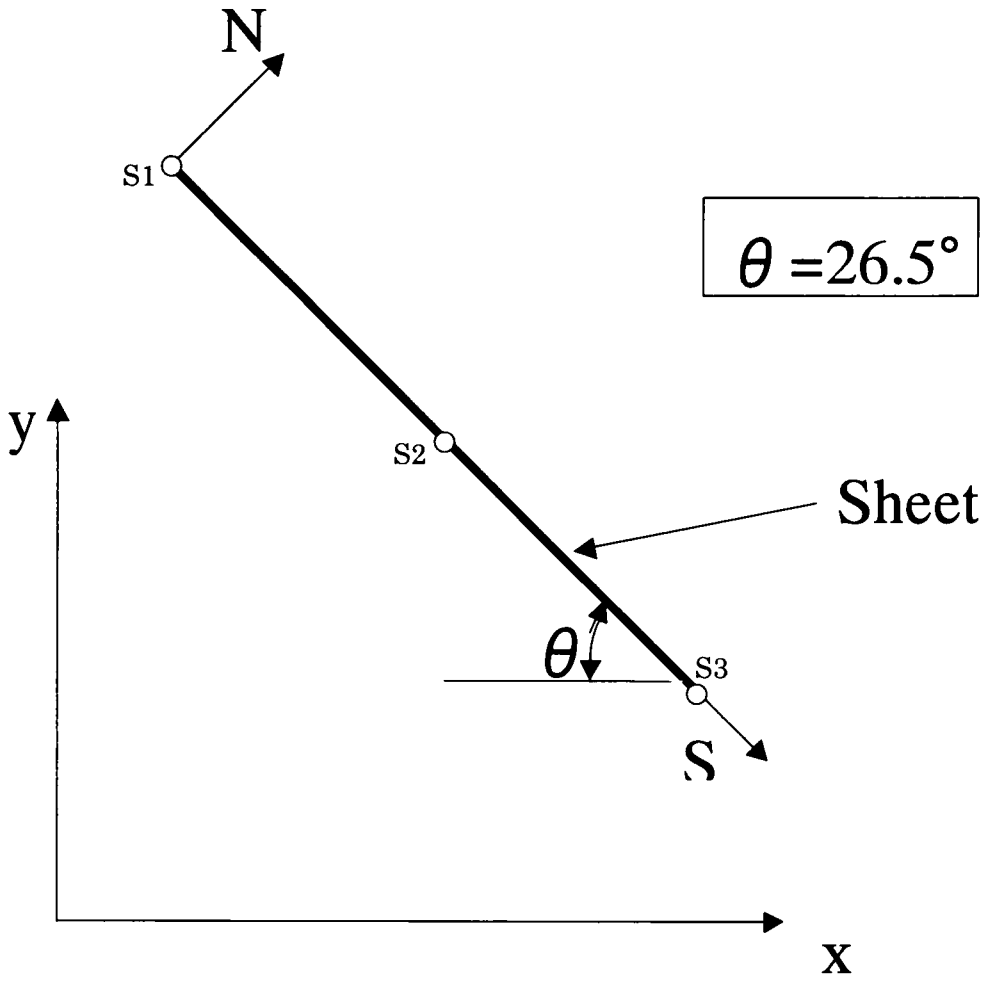

Fig. 8.10 Local coordinates of water-shielding sheet

(a) Water-shielding sheet 1

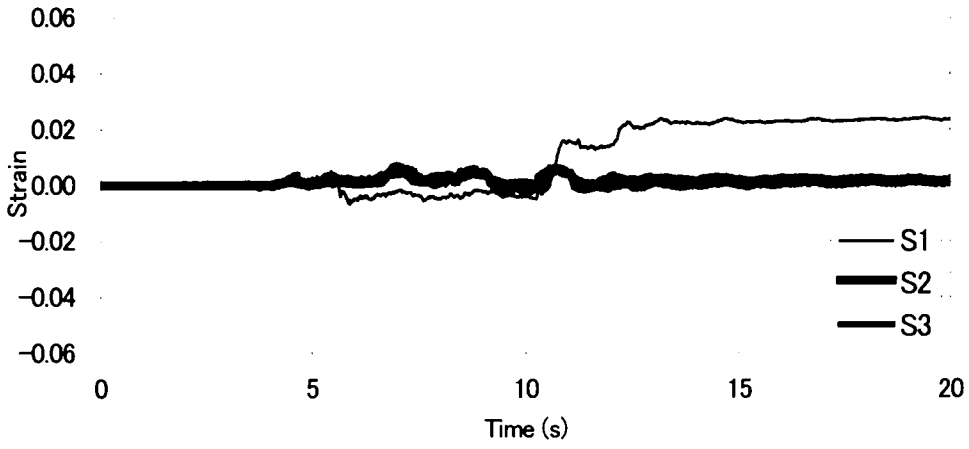

(b) Water-shielding sheet 2

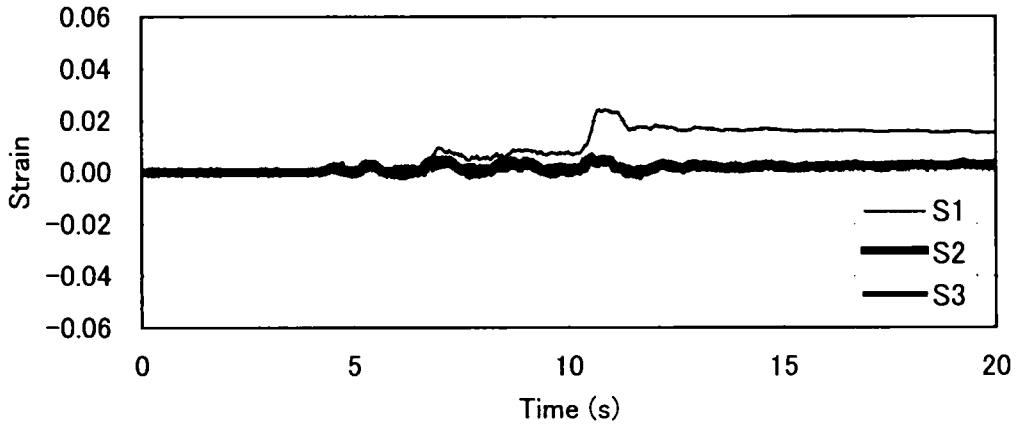

Fig. 8.11 Predicted axial strains in water-shielding sheets during shaking

(a) Water-shielding sheet 1

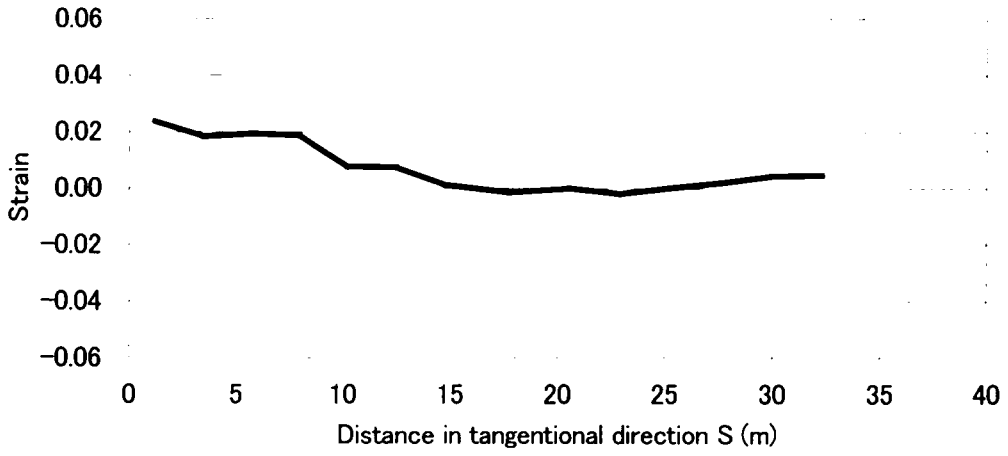

(b) Water-shielding sheet 2

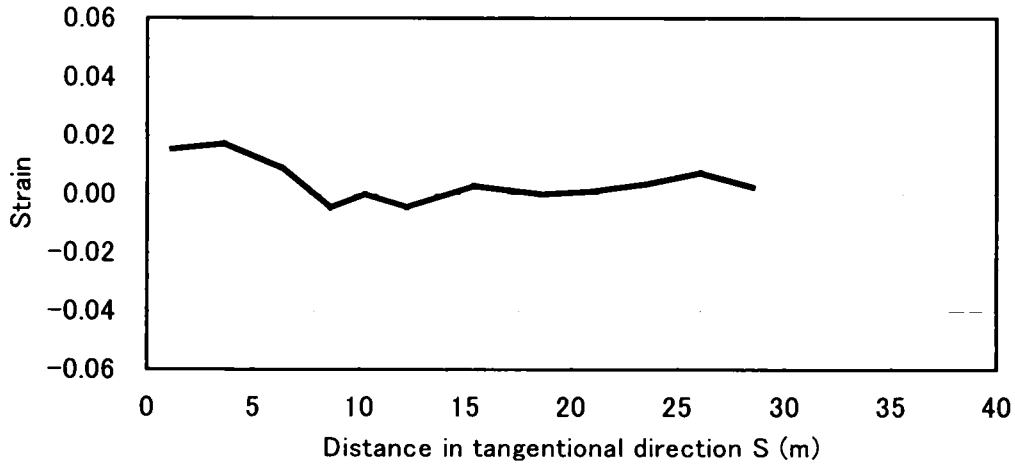

Fig. 8.12 Residual axial strain distributions of sheet 1 and sheet2 after shaking

CHAPTER 9

Effect of wave-induced pore pressure fluctuations on the performance of controlled disposal site

9.1 Introductory remarks

This chapter applies the proposed finite-element analysis procedure to assessing the effect of wave-induced pore pressure fluctuations in a controlled disposal site. The emphasis of the discussion will be placed on looking at the effect on the performance of the water-shielding sheets in it.

Before going into details of the analysis, let us briefly review related, previous works on wave-seabed interactions. Analytical approaches based on poro-elasticity (Madsen, 1978; Yamamoto et al., 1978 among others) have provided a useful picture of wave-seabed interactions, although there remain a few inherent limitations regarding modeling of real particulate sediments. Finite-element analyses were performed for looking at complex interactions between wave, soil and marine structures (Mase et al, 1991; Kuwahara et al, 1992). Sassa (2000) developed a finite-element code that incorporated a cyclic-plasticity model and applied it to reproducing liquefaction of beds of loosely packed, saturated sand subjected to either progressive or standing wave loading. Baba et al. (2002) performed a series of fluid-wave experiments using a drum centrifuge and discussed the resistance of a water-shielding sheet to wave-induced pore pressure fluctuations in the backfill soil. Kotake et al. (2004) made extensive field observation of pore pressure fluctuations in the backfill soil and in the rubble mound for a controlled disposal site in Shikogu-Chuo city.

In what follows, detailed discussion will be made of the predicted effect of wave-induced pore pressure fluctuations in the controlled disposal site from the present analysis, in light of the filed observations of Kotake et al. (2004).

9.2 Analytical procedure

In order to investigate effect of wave-induced pore pressure fluctuations in controlled disposal site, Coupled analysis of "CADMAS-SURF (Coastal Development Institute of Technology, 2001) and finite element method" is performed. CADMAS-SURF is analytical method incorporated VOF(Volume of Fluid) that was method of dealing with complicated free surface wave (Appendix 1). In this chapter, finite element method developed in chapter 1 is applied. Flow chart of presented analysis for assessing the performance of water-shielding sheet in controlled disposal site is shown in Fig. 9.1.

9.3 Wave conditions and finite-element mesh adopted

A finite-element mesh used for analysis with representative elements is shown in Fig. 9.2. Constitutive model parameters used is same to Table 8.1 in chapter 8.

Wave conditions used in present study was 17m of water level, 3m of wave height and 5s of period observed field (Kotake et al, 2004). Time-history of pressure fluctuation U_{toe} at toe of the caisson calculated by CADMAS-SURF is shown in Fig. 9.3. Maximum pressure obtained was 9 kPa.

9.4 Predicted and observed responses

9.4.1 Comparison of predicted and observed pore pressure fluctuations

In order to compare predicted and observed pore pressure fluctuations, let us first look at the field-observed pore pressure fluctuations. Field observation time histories of maximum pore pressure fluctuations observed in backfill soil and rubble mound for controlled disposal site in Shikogu-Chuo city (Kotake et al., 2004) are shown in Fig. 9.4. Observed period of waves was 5s and wave height was 3m. In February 5, 2004, response ratio of maximum pore pressure fluctuation (U_{heel}) in element EN2 at heel of the caisson with respect to maximum pore pressure fluctuation (U_{toe}) in EN1 at toe of the caisson was 20 percentages. Also, response ratio (U_x/U_{toe}) of maximum pore pressure fluctuation U_x in backfill soil was almost 5 percentages. In backfill soil, pore pressure fluctuation indicated remarkably decreasing of pore pressure fluctuation. Here, response ratio means ratio of pressure fluctuation (U_x) at each position with respect to pressure fluctuation (U_{toe}) at toe of the caisson.

The predicted time-history pore pressure fluctuation U_{heel} in element EN2 at heel of the caisson is shown Fig. 9.5. The predicted wave-induced pore pressure fluctuation at heel of the caisson with respect to toe of the caisson significantly decreased. Response ratio ($U_{heel}/(U_{toe}$) of pore pressure fluctuation was 23 percentages.

The predicted and observed distribution of response ratio of pressure fluctuation nearby

water-shielding sheet is shown in Fig. 9.6. The predicted and observed response ratios U_x/U_{toe} of pressure fluctuations was considerably small in value.

Overall, the predicted distribution of pressure fluctuation compare well with the field-observed results(Kotake et al. 2004).

9.4.2 Predicted behavior of backfill soil with reference to the performance of water-shielding sheets

In order to discuss the details of the soil behavior, the predicted shear stress and shear strain curve in backfill soil EN3 nearby the water-shielding sheet are shown in Fig. 9.7(a). Accumulation of the shear strain was very small in value. The effective stress state was below the phase transformation line (Fig. 9.7(b)), and accumulation of excess pore pressure (Fig. 9.7(c)) was very small in value. The predicted performances in backfill soil EN4(Fig. 9.8) was almost same with those in backfill soil EN3.

The predicted residual axial strain distributions in tangential direction of sheet 1 and sheet 2 after wave loading (t=100s) are shown in Fig. 9.9. Residual axial strains were small in value at every position. This predicted result correspond to small response ratio of pore pressure fluctuations nearby water-shielding sheet (refer to Fig. 9.6). It is indicated that the influence of wave-induced pore pressure fluctuations are small on the water-shielding sheet.

9.4.3 Pore pressure fluctuations under long period of wave

In order to discuss pore pressure fluctuations under long period of wave, a additional finite-element analysis was performed for controlled disposal site under the wave period of 12 seconds. The values of all other parameters for wave and soil parameters in the analyses were held unchanged.

Predicted horizontal distributions of response ratio of pressure fluctuation under the wave period of 12 seconds in rubble mound and backfill soil, together with predicted and observed results(Kotake et al., 2004) under the wave period of 5 seconds are shown in Fig. 9.10. The predicted response ratios U_x/U_{toe} of pore pressure fluctuations under the wave periods of 5 seconds and 6 seconds significantly decay in the course of propagation through the backfill soil. However, the predicted response ratios of pore pressures under the wave period of 12 seconds increased more than those under the wave period of 5 seconds. The predicted response ratio of pore pressure fluctuations under the wave period of 5 seconds were compared favorably with field-observed results(Kotake et al., 2004).

The predicted distributions of response ratios of pressure fluctuations with wave periods

nearby water-shielding sheet are shown in Fig. 9.11. The predicted response ratios of pressure fluctuations nearby toe of water-shielding sheet were smaller than 10 percentage in all the case. However, at distance 8.4m from shoulder, the predicted response ratios of pressure fluctuation indicated peak value in the case of wave period of 12 seconds. It is likely that low-permeable soil layer used for backfill soil was thin at shallow depth.

9.5 Discussion

Note that manual for Design, construction and management of controlled disposal site (Waterfront Vitalization and Environment Research Center, 2000) supposed impermeability of backfill soil behind caisson and no effect of decreasing of pore pressure fluctuations in backfill soil considered. However, backfill soil behind of caisson used gravel of good permeability for controlled disposal site in Shikogu-Chuo city (Kotake et al. 2004) and for finite-element analyses.

Consider now the predicted results of wave-induced pore pressure fluctuations in the backfill soil under a wave period of 5s. The predicted response ratios of pore pressure fluctuations proved to significantly decay in the course of propagation through the backfill, exerting only limited impact upon the water-shielding sheet(see Fig. 9.6). Also, the predicted residual strain of water-shielding sheet indicated small value (see Fig. 9.9).

Let us consider the effect of wave period on response ratio of pore pressure fluctuations (see Fig. 9.11). The predicted response ratio of pore pressure fluctuation at shallow depth significantly increased with increasing wave period. Field-observed maximum wave height and wave period for controlled disposal site in Shikogu-Chuo cit (Kotake et al., 2004) were 3m and 5s, respectively. However, care is needed when markedly long periods of waves will hit the semi-permeable seawall system for a controlled disposal site, since the present analyses demonstrate that the effect of wave pressures can penetrate deep into the backfill soil and affect the water-shielding sheet system there.

9.6 Conclusions

Characteristics of wave-induced pore pressure fluctuations in the backfill of the controlled disposal site have been discussed based on the range of analyses in terms of the present analysis procedure.. The principal conclusions obtained in this chapter may be summarized as follows:

1. The characteristics of propagation of wave pressures through the rubble mound and backfill soil are well captured by the present analysis procedure. In fact, the predicted pore pressure

fluctuations compare favorably with the field observations made by Kotake et al. (2004).

2. The wave-induced pore pressure fluctuations under a wave period of 5s proved to significantly decay in the course of propagation through the backfill, exerting only limited impact upon the water-shielding sheet.

3. However, care is needed when markedly long periods of waves will hit the semi-permeable seawall system for a controlled disposal site, since the present analyses demonstrate that the effect of wave pressures can penetrate deep into the backfill soil and affect the water-shielding sheet system there.

References

Baba, S., Miyake, M., Tsurugasaki, K., Kim, H. (2002). Development of wave generation system in a drum centrifuge, *ICPMG2002, Canada, 265-270.*

Coastal Development Institute of Technology, (2001). Research and development of [Super Roller Flume for Computer Aided Design of Maritime Structure(CADMAS-SUR)], Library No. 12.

Kotake, Y., Turugasaki, K., Baba, S., Miyake, M., Fujiwara, R., Kaneko, K., Tezuka, T., Tokunaga, K. and Moriya, K. (2004). Field observation of pore water pressure in the backfill space of a caisson-type bulkhead for wast dispose, *Annual journal of coastal engineering* , Vol. 51, JSCE, 681-685.

Kuwahara, H. and Ohmaki, M. (1992). Elastoplastic behaviour of soil ground nearby composite breakwaters due to wave loading, *Proc. of coastal engineering, JSCE*, Vol. 39, 861-865.

Mase, H. Kawasako, J. and Sakai, T. (1991). Study of wave response on foundation soil of composite breakwaters, *Proc. of coastal engineering, JSCE*, Vol. 38, 821-825.

Sassa, S. (2000). Fundamental studies of wave-induced liquefaction of sand beds, *Doctoral thesis*, 88-126.

Special board of investigation for Tonankai and Nankai earthquakes. (2003). Report for Tonankai and Nankai earthquakes, *Central Disaster Prevention Council*, No. 2-2.

Yamamoto, A., (1993). Study of application of coastal groundwater level theory for seacoast and coastal reclaimed ground, *Doctoral thesis, Kyoto University*,1-151

Yamamoto, T., Koning, H. L., Sellmeijer., H. and Hijium, E. (1978). On the response of a pore-elastic bed to water waves, *J. Fluid Mech.* Vol.87, No. 1, 193-206.

Yamamoto, T. (1981). Wave-induced pore pressures and effective stresses in inhomogeneous seabed foundations, *Ocean Engng.* Vol. 8, 1-16.

Waterfront Vitalization and Environment Research Center (Wave), (2000). Manual for Design, construction and management of controlled disposal site, 58-62 (in Japanese).

Appendix 1 Feature of the CADMAS-SURF

The CADMAS-SURF (Super Roller Flume for Computer Aided Design of Maritime structure) code was developed by a joint project of several Japanese institutes(Coastal Development Institute of Technology, 2001). With this code, two-dimensional Navier-Stokes equations of incompressible fluid are solved implicitly, fluid surface is evaluated by the VOF (Volume Of Fluid) method, bottom configuration in a grid cell is determined by a porous-body media method, and a $k-\varepsilon$ model is used for turbulence closure.

Continuity and Navier-Stokes equations based on porous model, and Advection equation on fluid surface may be expressed as

Continuity equation

$$\frac{\partial \gamma_x u_f}{\partial x}+\frac{\partial \gamma_y w_f}{\partial y}=0 \tag{A.1}$$

Navier-Stokes equations

$$\lambda_v \frac{\partial u_f}{\partial t}+\frac{\partial \lambda_x u_f u_f}{\partial x}+\frac{\partial \lambda_y w_f u_f}{\partial y}=-\frac{\gamma_v}{\rho}\frac{\partial p}{\partial x}-R_x+\frac{\partial}{\partial x}\left(\gamma_x \nu_e\left[2\frac{\partial u_f}{\partial x}\right]\right)+\frac{\partial}{\partial y}\left(\gamma_y \nu_e\left[\frac{\partial u_f}{\partial y}+\frac{\partial w_f}{\partial x}\right]\right) \tag{A.2}$$

$$\lambda_v \frac{\partial w_f}{\partial t}+\frac{\partial \lambda_x u_f w_f}{\partial x}+\frac{\partial \lambda_y w_f w_f}{\partial y}=-\frac{\gamma_v}{\rho}\frac{\partial p_f}{\partial y}-\gamma_v g-R_y+\frac{\partial}{\partial x}\left(\gamma_x \nu_e\left[\frac{\partial w_f}{\partial x}+\frac{\partial u_f}{\partial y}\right]\right)+\frac{\partial}{\partial y}\left(\gamma_y \nu_e\left[2\frac{\partial w_y}{\partial y}\right]\right) \tag{A.3}$$

Advection equation on fluid surface

$$\gamma_v \frac{\partial F}{\partial t}+\frac{\partial \gamma_x u_f F}{\partial x}+\frac{\partial \gamma_y w_f F}{\partial y}=0 \tag{A.4}$$

in which t : time; u_f and w_f: horizontal and vertical velocity of fluid, respectively; ρ : fluid density; p_f : pressure; ν_e : combination of kinematic partical viscosity and eddy viscosity; g : gravity acceleration; γ_v : Porosity; γ_x and γ_y : horizontal and vertical area transmission factor, respectively; CM: inertia coefficient ($\lambda_v=\gamma_v+(1-\gamma_v)CM$ $\lambda_x=\gamma_x+(1-\gamma_x)CM$, $\lambda_y=\gamma_y+(1-\gamma_y)CM$); R_x and R_y: Horizontal and vertical resistant force by porous media, respectively.

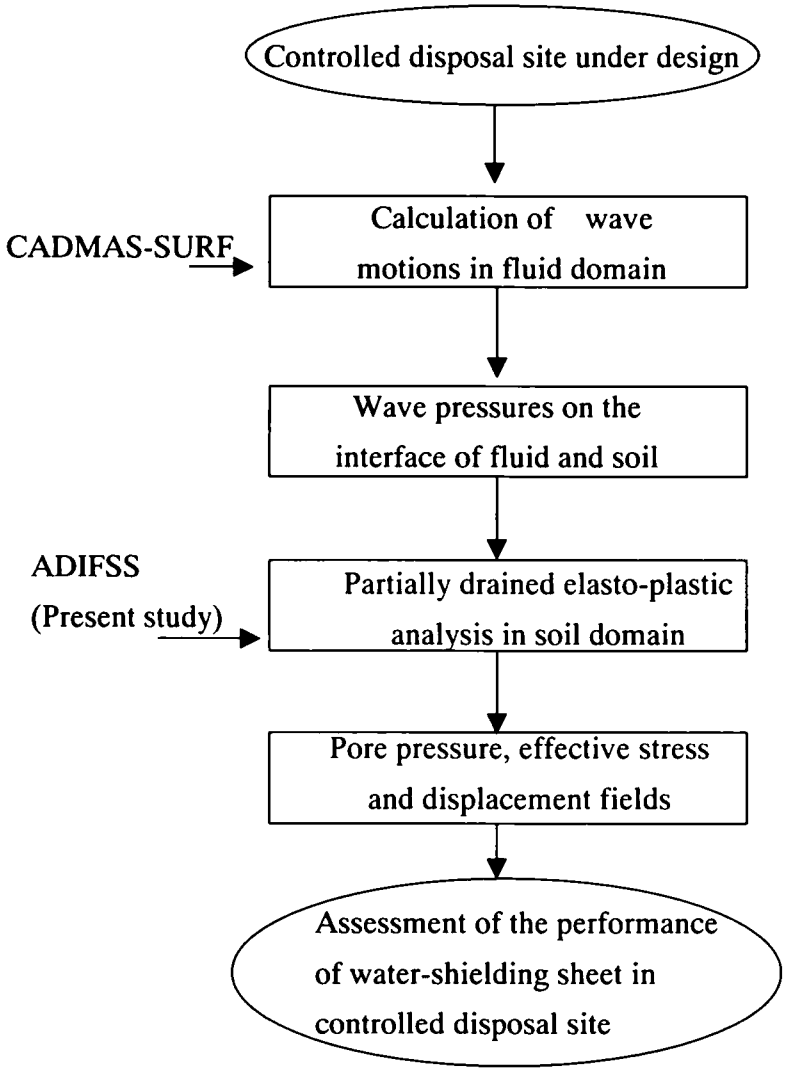

Fig. 9.1 Flow chart of presented analysis for assessing the performance of water-shielding sheet in controlled disposal site

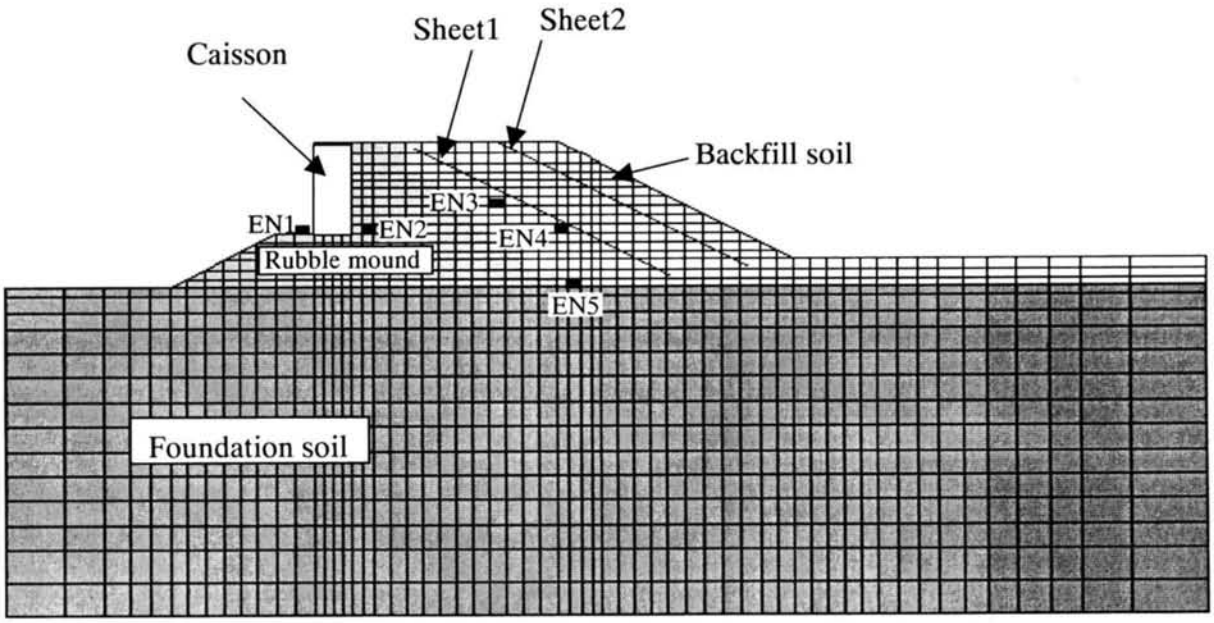

Fig. 9.2 A finite-element mesh used for analysis with representative elements

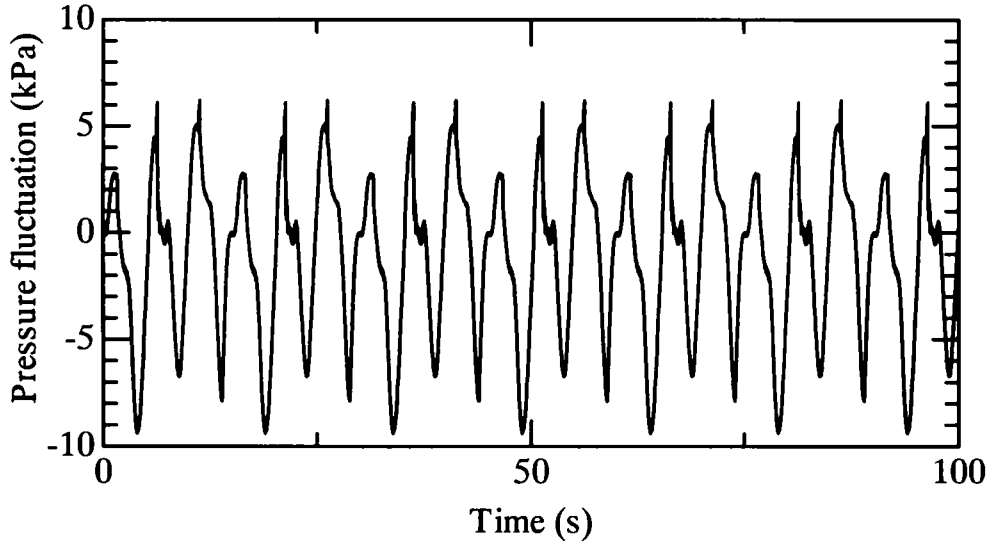

Fig. 9.3 Predicted time-history of pressure fluctuation at toe of the caisson (EN1)

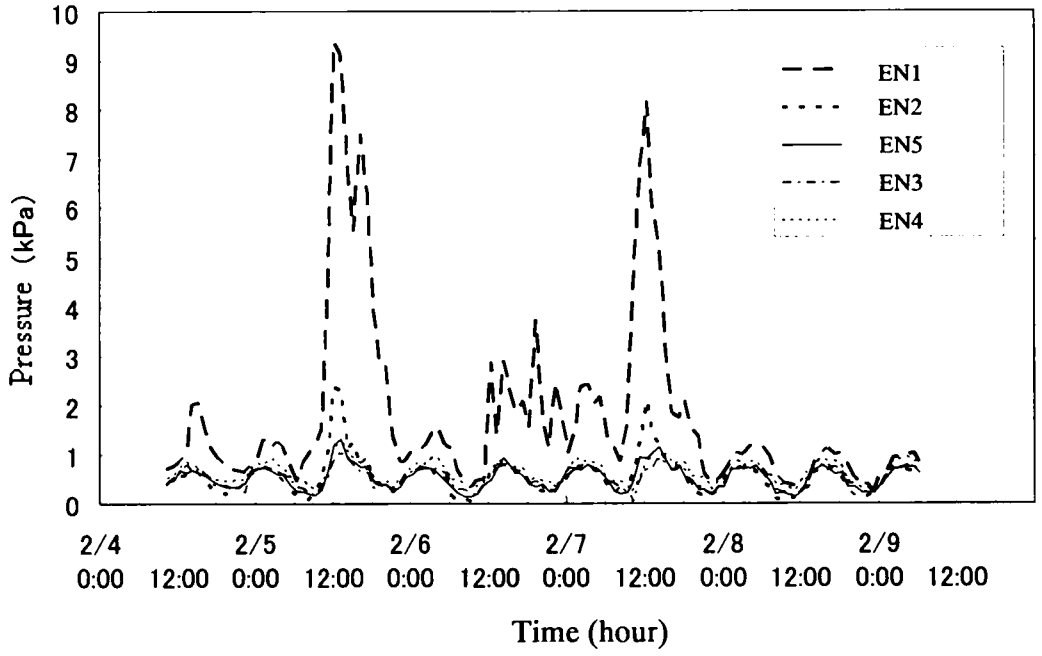

Fig. 9.4 Observed time histories of maximum pore pressure fluctuation(Kotake et al. 2004)

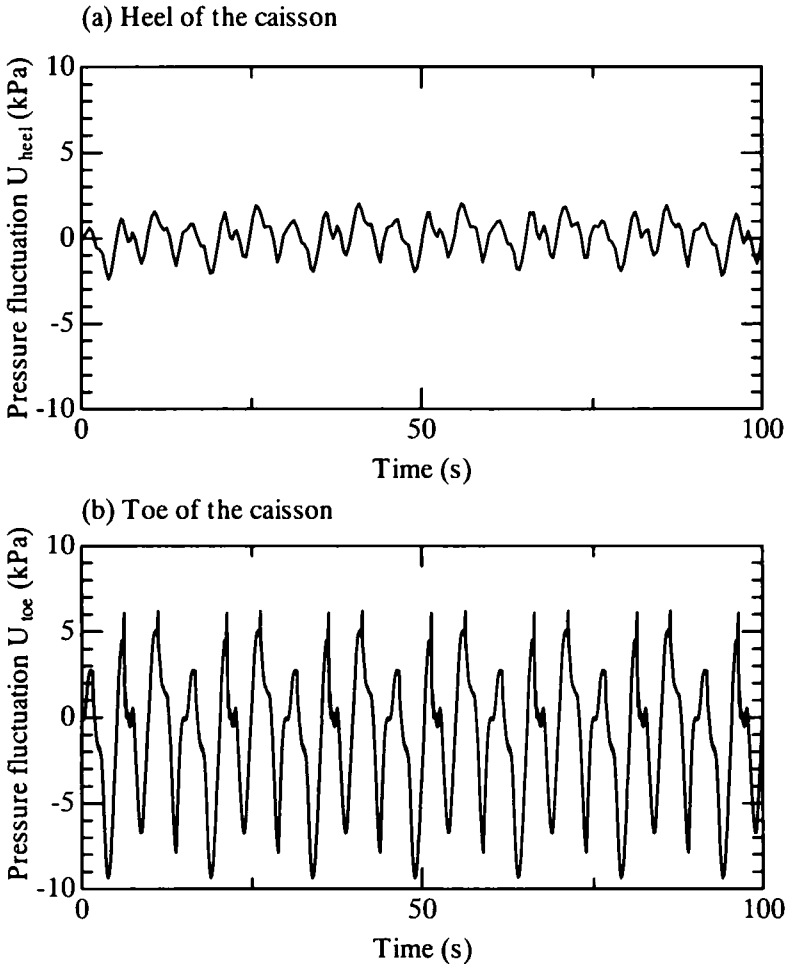

Fig. 9.5 Predicted time history of pressure fluctuations (a) at heel of the caisson and (b) at toe of the caisson

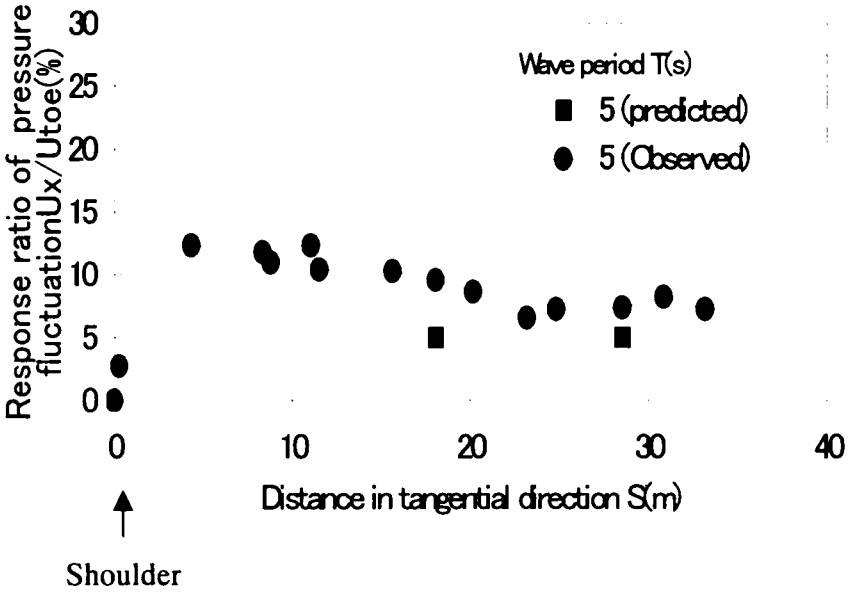

Fig. 9.6 Distribution of response ratio of pressure fluctuation nearby water- shielding sheet

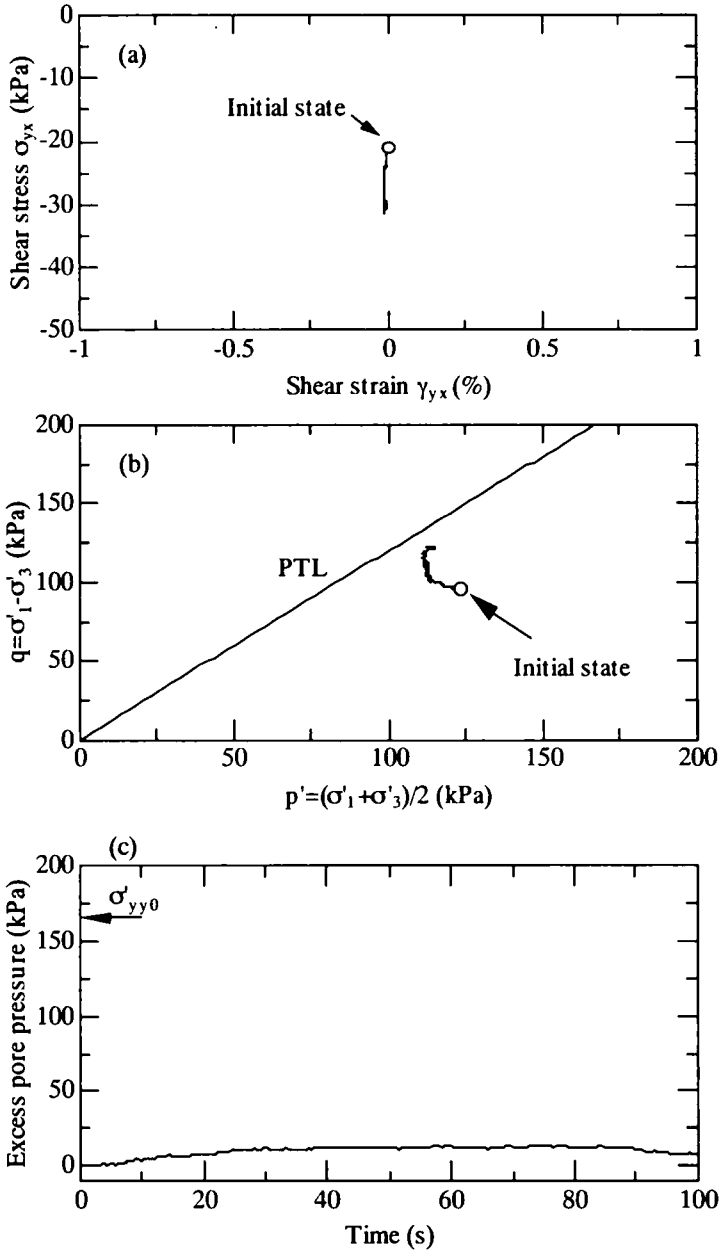

Fig. 9.7 (a) Predicted stress and strain curve, (b) effective stress path, and (c) excess pore pressure in backfill soil EN3

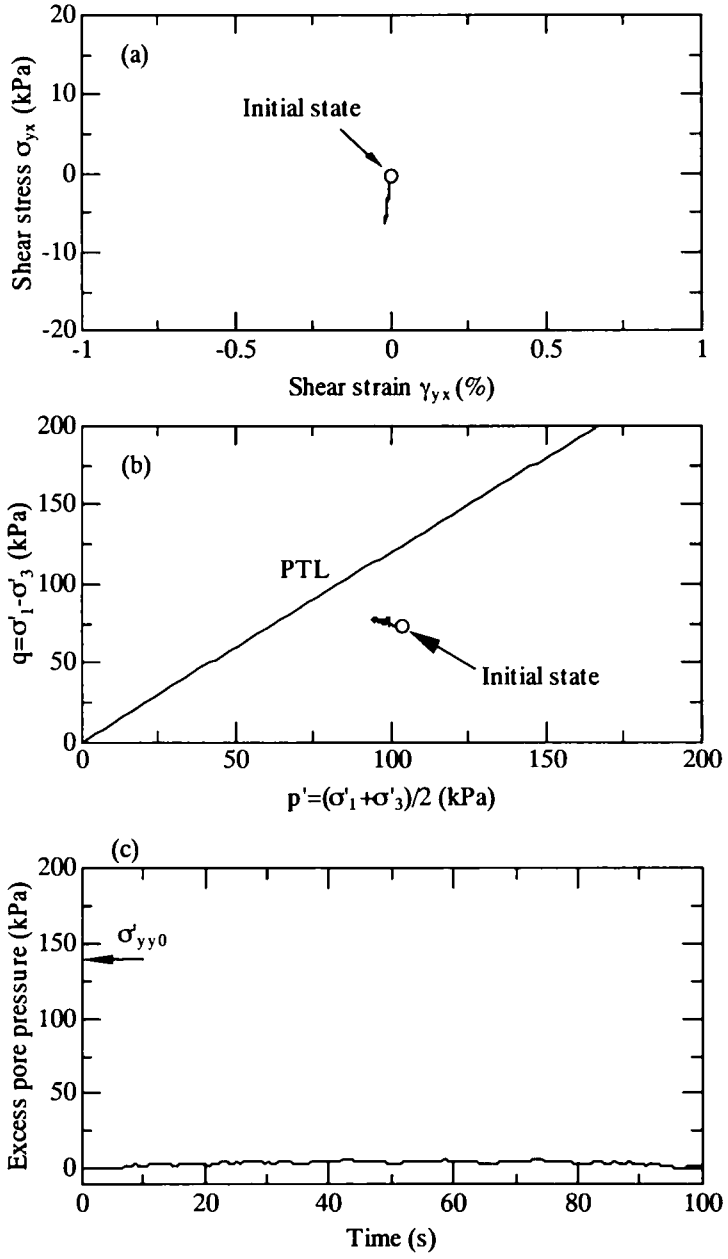

Fig. 9.8 (a) Predicted stress and strain curve, (b) effective stress path, and (c) excess pore pressure in backfill soil EN4

(a) Water-shielding sheet 1

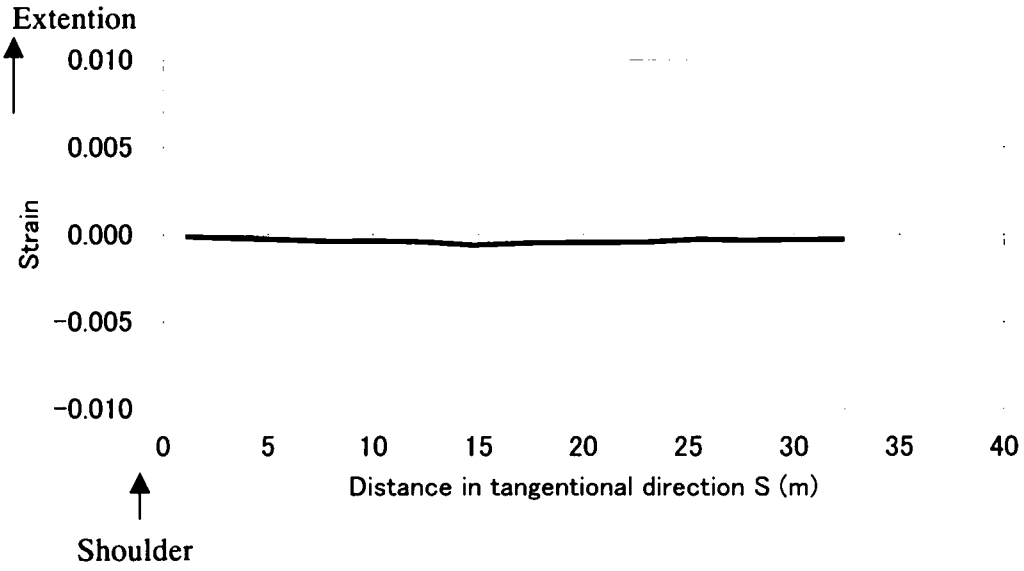

(b) Water-shielding sheet 2

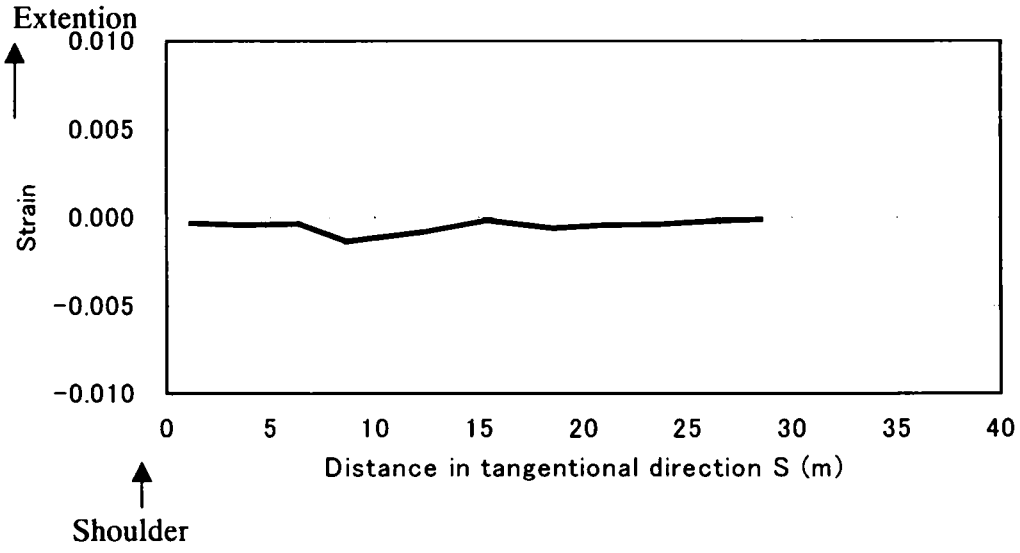

Fig. 9.9 Residual axial strain distributions of sheet 1 and sheet2 after wave loading (t=100s)

(a) Location of horizontal distribution of response ratio of pressure fluctuation

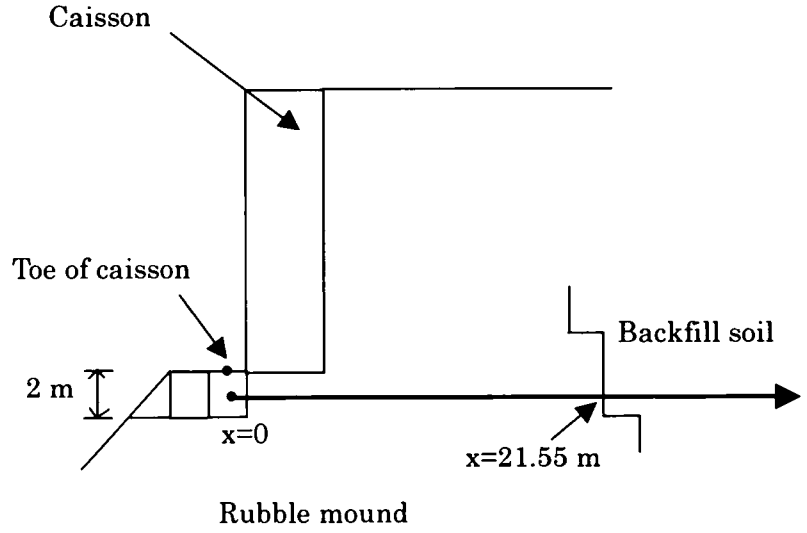

(b) Horizontal distribution of predicted and observed response ratios of pressure fluctuation

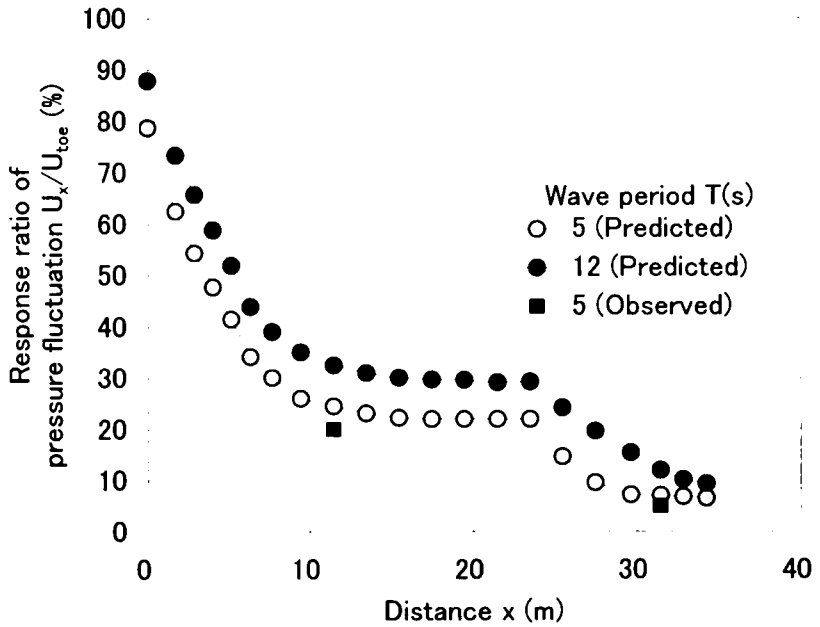

Fig. 9.10 (a) Location of horizontal distribution of response ratios of pressure fluctuation, and (b) horizontal distribution of response ratios of pressure fluctuation

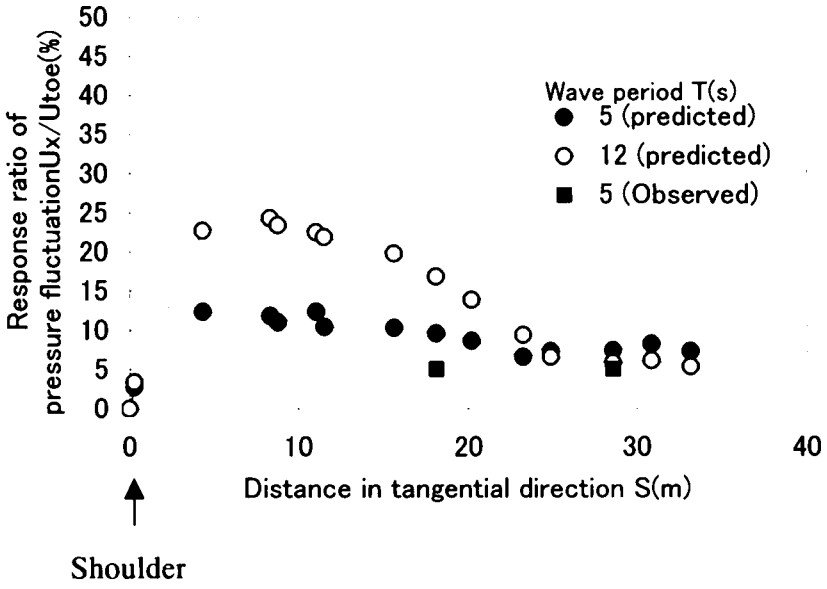

Fig. 9.11 Distribution of response ratio of pressure fluctuation with wave periods nearby water-shielding sheet

CONCLUDING REMARKS

The conclusions obtained in the foregoing Chapters may be summarized as follows, under the headings of Parts 1, 2 and 3 involved.

PART I ANALYSIS FRAMEWORK

Chapter 1 describes the features of a fully coupled, dynamic finite-element program for plane-strain deformation that was developed in the present study. The validity of the analysis code was verified through comparisons of the predictions with the closed-form analytical solutions in the three classes of elastodynamic problems, specifically the solutions by Simon et al. (1984), by Idriss and Seed (1968) and by Graham and Rodriguez (1952).

In chapter 2, a plane-strain version of the elastoplastic constitutive model by Pastor et al. (1990) was reformulated, with consideration of generalized loading criteria. This permitted parameter M_g, related to the angle of the phase-transformation line, to be a true material constant in the sense that the value is independent of the shearing mode (compression or extension) and may be determined for a given soil. The introduction of generalized loading criteria permitted a consistent description of softening behavior in the present framework as being a loading process. Furthermore, particular emphasis was placed for developing a workable yet physically sound procedure for determining the plastic constitutive parameters concerned. The outcome of this approach is such that the non-associativeness parameter M_f/M_g correlates well with the degree of compaction or relative density Dr of sand, providing a useful equation of correlation as represented by $M_f / M_g = \exp(1.07Dr - 1.35)$.

Chapter 3 was devoted to formulating a new elastoplastic constitutive model for joint elements that represented interfaces between soil and solid structures. The formulation was made in such a way that the joint-element model became a counterpart of the previously formulated, plane-strain version of the elastoplastic constitutive model for soil. The performance of the joint-element modeling was favorably tested in light of the monotonic and cyclic shearing tests on sand-steel interfaces that were reported by Fakharian and Evgin (1997).

Chapter 4 discussed the characteristics of the dynamic fluid pressures that developed through

interactions between saturated soil and the adjacent fluid column. The outcome of the discussion includes the following:

(a) The elastoplastic finite-element modeling for the submerged deposit of sand captured the build-up of seismically induced residual pore pressures leading up to liquefaction, and clarified the nature of the dynamically induced pore pressure fluctuations that occurred following liquefaction.

(b) There occurred a marked interaction between the liquefied sand and the overlying fluid column, enhancing the dynamic pressure changes at the fluid-soil interface.

(c) The predicted dynamic pressure changes from the finite-element analyses and the two-layer-fluid theory compare favorably with what has been measured in the centrifugal shaking-table tests on the fluid/saturated sand systems.

PART II PERFORMANCE OF COMPOSITE BREAKWATERS UNDER SHAKING

Chapter 5 applied the proposed analysis procedure to assessing the deformability of composite breakwater models subjected to a range of centrifugal shaking-table tests. The particular emphasis placed on investigating into the effect of the degree of compaction of the foundation sand below the caisson structure. The outcome of the discussion includes the following findings:

(a) The soil elements below the caisson structure underwent significant amounts of vertical compression that were accompanied by equally significant lateral expansion. The deformation mode was accentuated when the effective stress path crossed the phase transformation line from below and accounted for a significant portion of the accumulated settlement of the caisson structure during shaking.

(b) The predicted performance of caisson settlements compares favorably with the measured performance when the M_f/M_g versus Dr relationship proposed in Eq. (2.34) is allowed for in the procedure of determination of the material parameters.

A revisit was made in Chapter 6 to the seismic performance of Kobe port breakwater No.7 during the 1995 Hyogoken-Nambu earthquake, in terms of the proposed finite-element analysis procedure. The outcome of the analyses performed may be summarized as follows.

(a) The best prediction in terms of the final caisson settlement proved to be the case where the non-associativeness parameter M_f/M_g was equal to 0.48. This prediction is of considerable practical interest, since the identified case points to the relative density Dr of the sand fill being equal to 40%, provided that Eq. (2.34) holds true for the deposits of decomposed granite soil.

(b) The large settlements of the order of 2m in the composite breakwater system may be

ascribed to a sort of repeated shear failure in the foundation soil whose effective stress state was far from being the state of liquefaction.
(c) The factors of safety against sliding at the interface of the caisson and rubble mound during shaking could be assessed by closely examining the effective stress states in the joint elements incorporated. The factor of safety against sliding tends to take a smaller minimum in the course of shaking in the cases where parameter M_f (or Dr) takes a larger value, suggesting an adverse effect of increased degree of compaction in the sandfill.

Chapter 7 points out the consequences of scenario earthquakes of moderate intensity yet having a prolonged duration of shaking upon the plastic deformability of composite breakwater systems. Also, it refers to some responsible factors that need further future studies.

PART III PERFORMANCE OF CONTROLLED DISPOSAL SITE UNDER DYNAMIC LOADING

Chapter 8 deal with the seismic performance of a controlled disposal site under strong shaking. The predictions in terms of the present analysis procedure show that extensional straining of the order of 2% can develop in the water-shielding sheet during the strong shaking anticipated, and that the extensional straining tends to concentrate on the section with shallow soil cover. The latter finding is in qualitative agreement with the experimental results of Kano et al. (2004).

In Chapter 9 the characteristics of wave-induced pore pressure fluctuations in the backfill of a controlled disposal site were predicted using the present analysis procedure and compared with the filed observations available. The outcome of the discussion includes:
(a) The predicted performance of propagation of wave pressures through the rubble mound and backfill soil compares favorably with the field observations of Kotake et al. (2004).
(b) The wave-induced pore pressure fluctuations under a wave period of 5s proved to decay significantly in the course of propagation through the backfill, exerting only limited impact upon the water-shielding sheet in the backfill.
(c) However, care is needed when markedly long periods of waves are anticipated to hit the semi-permeable seawall system for a controlled disposal site. This statement arises from the following observation: namely, the present analyses demonstrate that the effect of wave pressures can penetrate deep into the backfill soil and affect the water-shielding sheet system there to some extent.

Overall, the present thesis demonstrates the capability of the proposed analysis procedure for dealing with the important classes of dynamic fluid-soil-structure interactions, encouraging its wider application to nearshore geotechnics and waterfront geohazards reduction.